- 9. Tanodekaew, S.; Prasitsilp, M.; Swasdison, S.; Thavornyutikarn, B.; Pothsree, T.; Pateepasen, R. Biomaterials 2004, 25, 1453.
- Sahu, K.; Verma, Y.; Sharma, M.; Rao, K. D.; Gupta, P. K. Skin Res Tech 2010, 16, 428.
- 11. Tang, C.; Chen, N.; Zhang, Q.; Wang, K.; Fu, Q.; Zhang, X. Polym Degrad Stabil 2009, 94, 124.
- 12. Wang, X.; Du, Y.; Luo, J.; Yang, J.; Wang, X.; Shi, X.; Hu, Y. Polymer 2006, 47, 6738.
- 13. Wang, X.; Du, Y.; Luo, J.; Yang, J.; Wang, W.; Kennedy, J. F. Carbohydr Polym 2009, 77, 449.
- 14. Xie, Y.; Wang, A.; Liu, G. Polym Compos 2010, 3, 89.
- 15. Wang, X.; Du, Y.; Luo, J.; Lin, B.; Kennedy, J. F. Carbohydr Polym 2007, 69, 41.
- 16. Meng, N.; Zhou, N.; Zhang, S.; Shen, J. Appl Clay Sci 2009, 42, 667.
- 17. Bozhilov, K. N.; Xu, Z.; Dobrzhinetskaya, L. F.; Jin, Z-M.; Green II, H. W. Lithos 2009, 109, 304.
- Tjong, S. C. Synthesis and structure-property characteristics of clay-polymer Nanocomposites, Nanocrystalline Materials; Oxford: Elsevier, 2006; Chapter 10; p. 311.
- 19. Hsu, S.; Tseng, H.; Hung, H.; Wang, M.; Hung, C.; Li, P.; Lin, J. Appl Mater Interfaces 2009, 1(11), 2556.
- 20. Li, P.; Wei, J.; Chiu, Y.; Su, H.; Peng, F.; Lin, J. Appl Mater Interfaces 2010, 2, 1608.
- 21. Patil, D. R., Fanta, G. F. J Appl Polym Sci 1993, 47, 1765.
- 22. Lanthong, P.; Nuisin, R.; Kiatkamjornwong, S. Carbohydr Polym 2006, 66, 229.

- 23. Mun, G. A.; Nurkeeva, Z. S.; Dergunov, S. A.; Nama, I. K.; Maimakov, T.P.; Shaikhutdinov, E. M.; Lee, S. C.; Park, K. React Funct Polym 2008, 68, 389.
- 24. Sun, T.; Zhou, D.; Xie, J.; Mao, F. Eur Food Res Technol 2007, 225, 451.
- 25. Zhang, J.; Wang, Q.; Wang, A. Carbohydr Polym 2007, 68, 367.
- 26. Singha, V.; Sharmaa, A. K.; Tripathi, D. N.; Sanghib, R. J Hazard Mater 2009, 161, 955.
- 27. Huacai, G.; Wan, P.; Dengke, L. Carbohydr Polym 2006, 66, 372.
- 28. Mishra, D. K.; Tripathy, J.; Srivastava, A.; Mishra, M. M.; Behari, K. Carbohydr Polym 2008, 74, 632.
- 29. Casimiroa, M. H.; Botelho, M. L.; Leal, J. P.; Gil, M. H. Radiat Phys Chem 2005, 72, 731.
- 30. Semenzato, S.; Lorenzetti, A.; Modesti, M.; Ugel, E.; Hrelja, D.; Besco, S.; Michelin, R. A.; Sassi, A.; Facchin, G.; Zorzi, F.; Bertani, R. Appl Clay Sci 2009, 44, 35.
- 31. Dai, H.; Li, H.; Wang, F. Surf Coat Technol 2006, 201, 2859.
- 32. Bayramoğlu, G.; Arica, M. Y. Colloids Surf A 2002, 202, 41.
- 33. Wang, J. P.; Chen, Y. Z.; Zhang, S. J.; Yu, H. Q. Bioresour Technol 2008, 99, 3397.
- 34. Luckachan, G. E.; Pillai, C. K. S. Carbohydr Polym 2006, 64, 254.
- 35. Kittur, F. S.; Kumar, A. B. V.; Tharanathan, R. N. Carbohydr Res 2003, 338, 1283.
- 36. Krishna Rao, K. S. V.; Chung, I.; Ha, C. S. React Funct Polym 2008, 68, 943.
- 37. Sivudu, K. S.; Thomas, S.; Shailaja, D. Appl Clay Sci 2007, 37, 185.
- 38. Sperling, L. H. Introduction to Physical Polymer Sciences. 4th ed.; New York: John Wiley & Sons, 2006; p. 477.

- 39. Zhou, Y.; Yang, D.; Gao, X.; Chen, X.; Xu, Q.; Lu, F.; Nie, J. Carbohydr Polym 2009, 75, 293.
- 40. Mohan, Y. M.; Lee, K.; Premkumar, T.; Geckeler, K. E. Polymer 2007, 48, 158.
- 41. Oh, S. T.; Han, S. H.; Ha, C. S.; Cho, W. J. J Appl Polym Sci 1996, 59, 1871.
- 42. Je, J.; Kim, S. J Agric Food Chem 2006, 54, 6629.



Table 1. The water absorbency of hydrogels derived from CS, AA and /or HEMA grafted-CS copolymers and CS-g-poly(AA-co-HEMA)/mica nanocomposites.

D.L	AA: HEMA	Mica	Water absorbency
Polymer	(mol ratio)	(w w ⁻¹ of monomer)	$(g g^{-1})^1$
CS			10 <u>+</u> 2
CS-g-poly(AA)			101 <u>+</u> 4
CS-g-poly(HEMA)			11 <u>+</u> 1
CS-g-poly(AA-co-HEMA)	3:1		64 <u>+</u> 2
	1:1		54 <u>+</u> 3
	1:3		20 <u>+</u> 2
	1:1	5	45 <u>+</u> 3
	1:1	7	44 <u>+</u> 1
	1:1	10	46 <u>+</u> 2
	1:1	15	35 <u>+</u> 5

¹Data are shown as the mean \pm 1 SD and are derived from 5 repeats. Means within the column are significantly different (p<0.05).

Table 2. Total plate counts (replication competent cells) and the relative inhibition of growth of *S. aureus* in the presence of sodium ampicillin and the hydrogels of CS, AA and/or HEMA grafted-CS copolymers and CS-*g*-poly(AA-*co*-HEMA)/mica nanocomposites with various mica loadings.

		6 h cu	lture time	8 h cult	ture time
Sample type	Mica (% w w ⁻¹)	CFU ml ⁻¹ (x 10 ⁹) ¹	Relative inhibition (%)	CFU ml ⁻¹ (x 10 ⁹) ¹	Relative inhibition (%)
Negative control ²	0	6.95 <u>+</u> 1.51	-	8.15 <u>+</u> 1.25	-
Positive control ³		0	100	0	100
CS ⁴		2.7 <u>+</u> 0.25	61	6.4 <u>+</u> 1.68	21
CS-g-poly(AA) ⁴		0.52 <u>+</u> 0.48	93	0.91 <u>+</u> 0.85	89
CS-g-poly(HEMA) ⁴		2.18 <u>+</u> 0.28	69	5.95 <u>+</u> 1.25	27
CS-g-poly(AA-co-HEMA) ⁴		1.90 <u>+</u> 0.19	73	2.92 <u>+</u> 0.07	64
CS-g-poly(AA-co-HEMA) ⁴	7	1.4 <u>+</u> 0.37	81	3.6 <u>+</u> 0.55	57
CS-g-poly(AA-co-HEMA) ⁴	10	1.5 <u>+</u> 0.34	81	3.9 ± 0.31	54
CS-g-poly(AA-co-HEMA)	15	5.0 <u>+</u> 1.68	36	5.9 <u>+</u> 2.4	30

 $^{^{1}}$ CFU ml $^{-1}$ is shown as the mean \pm 1 SD and are derived from 6 repeats. Means within a column or across a row are significantly different (p<0.05).

²Negative control contains only the MHB medium and *S. aureus*.

³Positive control contains 250 mg of the sodium ampicillin, MHB medium and *S. aureus*.

⁴All hydrogel samples were co-cultured with S. aureus in MHB media at 250 mg ml⁻¹.

Table 3. Minimum inhibition concentration of hydrogels derived from CS, AA and/or HEMA grafted-CS copolymers and CS-g-poly(AA-co-HEMA)/mica nanocomposites with various mica loadings.

Sample test	Mica (% w w ⁻¹)	CFU ml ⁻¹ $(x \ 10^8)^1$	MIC (mg ml ⁻¹) ²
Negative control ³	-	18 <u>+</u> 1.0	-
CS ⁴		10 <u>+</u> 0.6	25
CS-g-poly(AA) ⁴		3.0 <u>+</u> 0.4	1.56
CS-g-poly(HEMA) ⁴		6.6 <u>+</u> 3.5	> 25
CS-g-poly(AA-co-HEMA) ⁴		1.2 <u>+</u> 0.5	12.5
CS-g-poly(AA-co-HEMA) ⁴	5	1.1 <u>+</u> 0.4	12.5
CS-g-poly(AA-co-HEMA) ⁴	7	5.1 ± 0.6	12.5
CS-g-poly(AA-co-HEMA) ⁴	10	4.6 <u>+</u> 0.4	12.5
CS-g-poly(AA-co-HEMA) ⁴	15	4.9 <u>+</u> 4.9	12.5

 $^{^{1}}$ CFU ml $^{-1}$ is shown as the mean \pm 1 SD and is derived from 3 repeats. Means within the column are significantly different (p<0.05).

²MIC are shown as mg ml⁻¹ for a 2% (v v⁻¹) seeding of a late log phase culture of *S. aureus* in MHB media and evaluated at late stationary phase (24 hr of culture).

³Negative control contains only the MHB medium and *S. aureus*.

⁴All hydrogel samples were co-cultured with S. aureus in MHB media at 250 mg ml⁻¹.

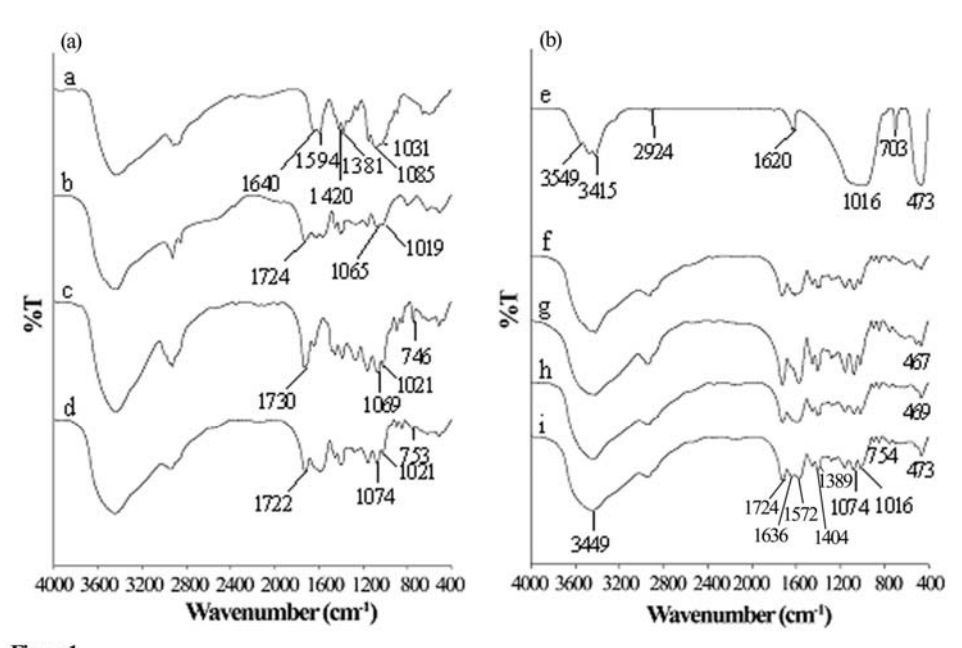


Figure 1

Representative FT-IR spectra of (A): (a) CS, and (b) CS-g-poly(AA), (c) CS-g-poly(HEMA) and (d) CS-g-poly(AA-co-HEMA) hydrogels, the last being synthesized with an AA: HEMA, N-MBA: CH, APS: CH and TEMED: CH molar ratios of 1, 0.11, 0.07 and 0.58, respectively; (B): (e) mica, and CS-g-poly(AA-co-HEMA)/mica nanocomposite hydrogels with mica loadings of: (f) 5%, (g) 7%, (h) 10% and (i) 15% w w-1 based on the monomer. 104x72mm (600 x 600 DPI)

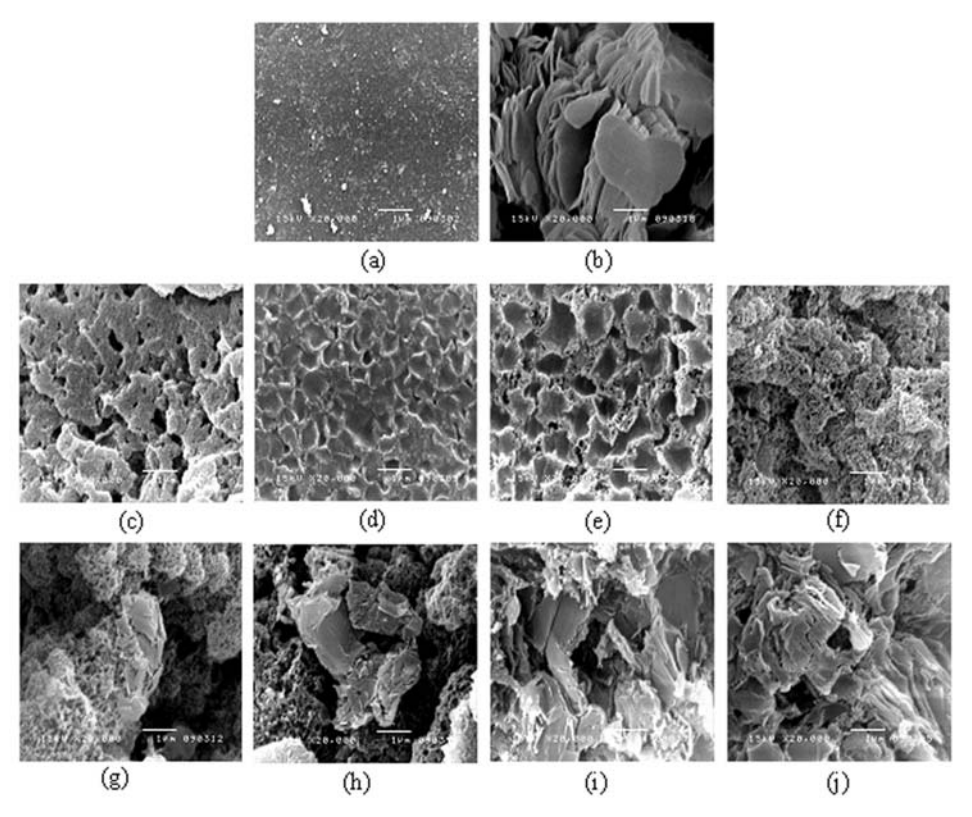
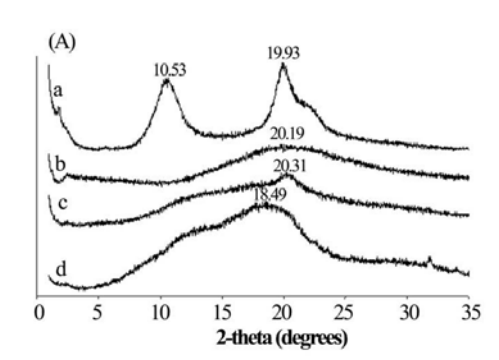


Figure 2

Representative SEM micrographs of (a) CS, (b) mica, (c) CS-g-poly(AA), (d) CS-g-poly(HEMA), (e, f) CS-g-poly(AA-co-HEMA), and CS-g-poly(AA-co-HEMA)/mica composite hydrogels synthesized with mica loading levels of (g) 5%, (h) 7%, (i) 10% and (j) 15% w w-1 of the monomer. 158x140mm (400 x 400 DPI)



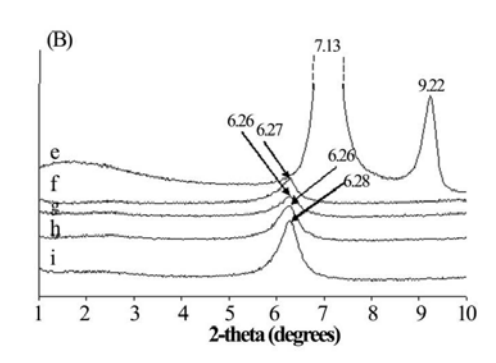


Figure 3

Representative XRD patterns of hydrogels synthesized from (A): (a) CS, (b) CS-g-poly(AA) synthesized with 1 g CS, 54 mmol AA, and N-MBA, APS and TEMED at 10%, 10% and 40% w w-1 of CS, respectively, (c) CS-g-poly(AA-co-HEMA) and (d) CS-g-poly(HEMA); (B): (e) mica, and CS-g-poly(AA-co-HEMA)/mica nanocomposite hydrogels synthesized with mica loadings of (f) 5%, (g) 7%, (h) 10% and (i) 15% w w-1 based on the monomer, 1 g CS, an AA: HEMA molar ratio of 1:1, and N-MBA, APS and TEMED at 10%, 10% and 40% w w-1 of CS, respectively.

60x24mm (600 x 600 DPI)

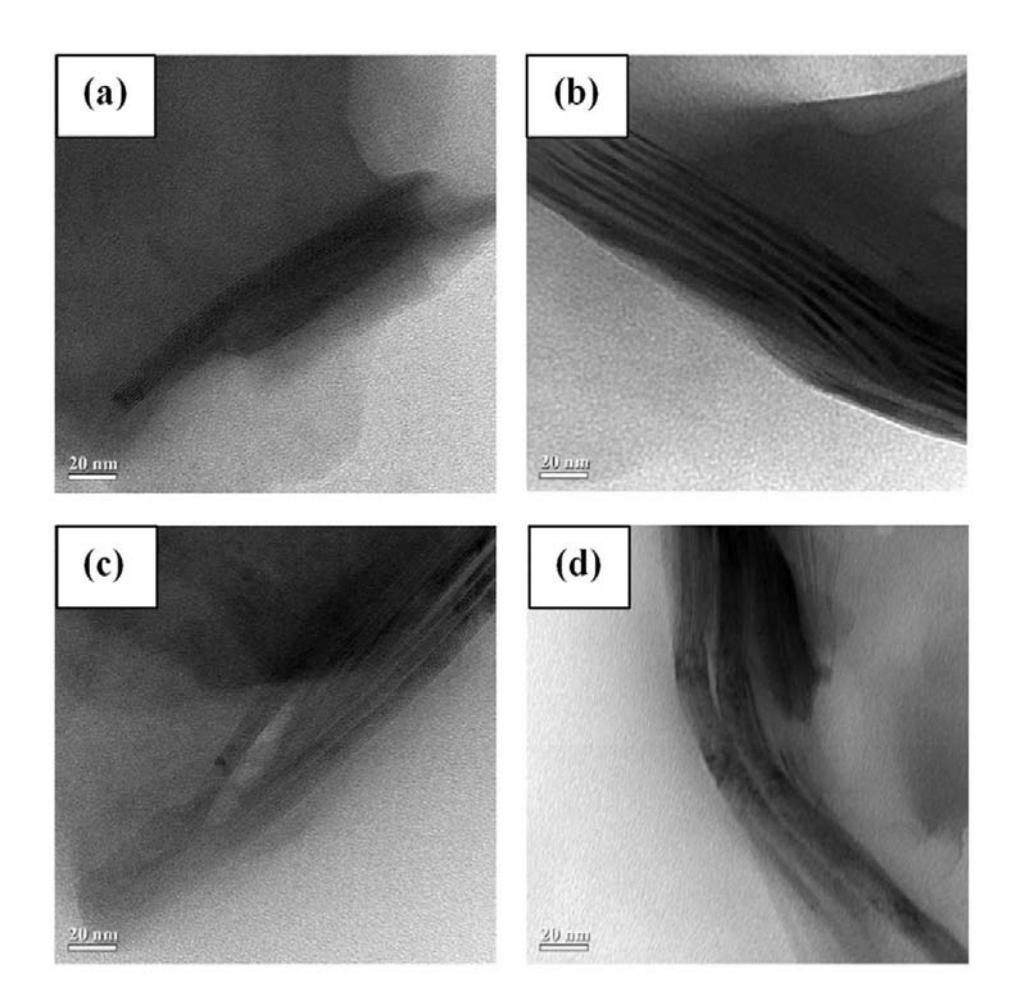


Figure 4

Representative TEM micrographs of CS-g-poly(AA-co-HEMA)/mica composite hydrogels synthesized with mica loadings of (a) 5%, (b) 7%, (c) 10% and (d) 15% w w-1 based on the monomer. $104x115\text{mm} \ (300 \ x \ 300 \ \text{DPI})$

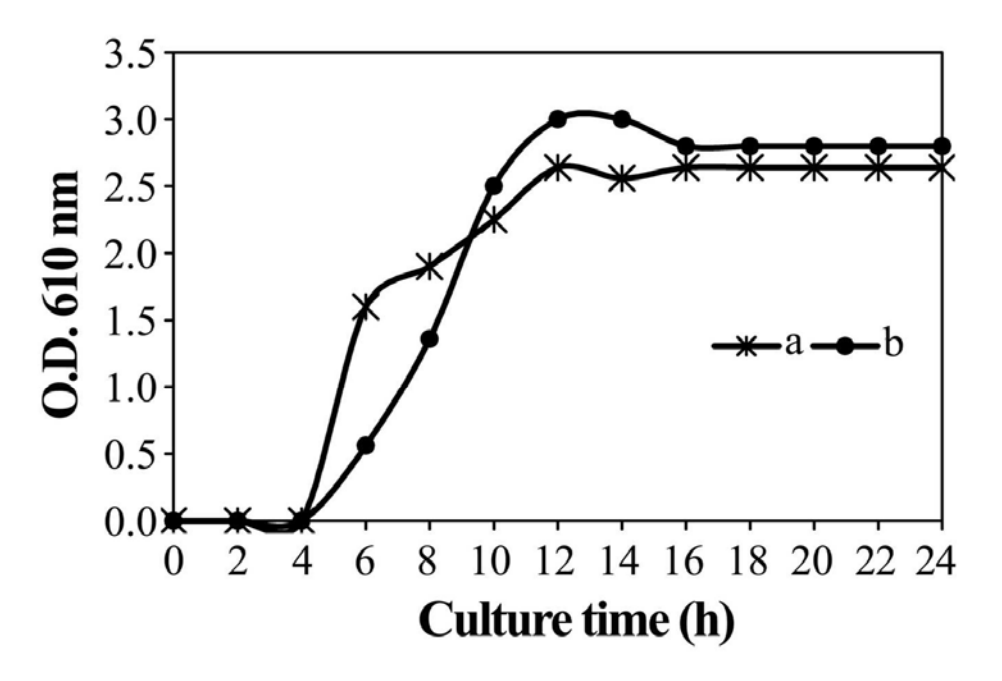


Figure 5

The optical density at 610 nm of S. aureus cultured in HMB media at various culture times with (a) the negative control, or 250 mg ml-1of (b) CS-g-poly(AA-co-HEMA) hydrogel prepared with 1 g CS, a AA: HEMA molar ratio of 1:1, and N-MBA, APS and TEMED at 10%, 10% and 40% w w-1 of CS, respectively, with polymerization performed at 250 pm and 60 °C for 60 min. 59x45mm (600 x 600 DPI)

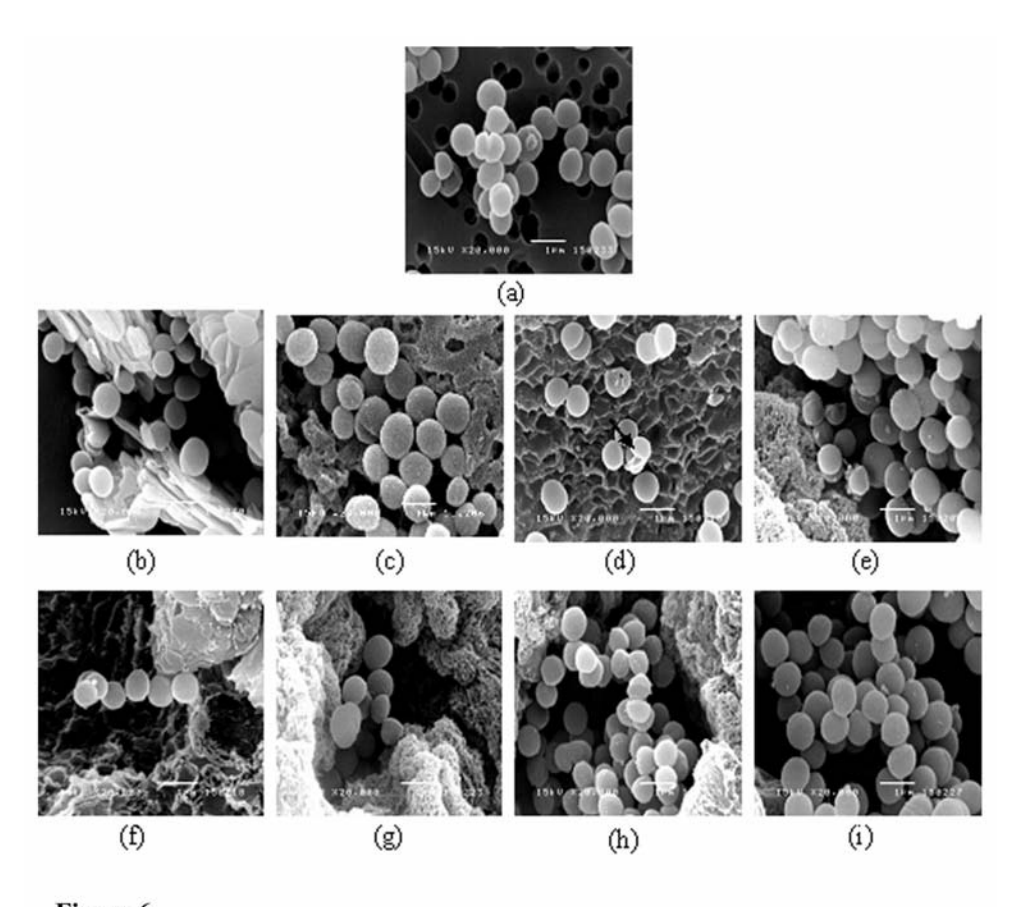


Figure 6

Representative SEM micrographs of S. aureus after co-culture for 24 h with (a) negative control, (b) mica, (c) CS-g-poly(AA), (d) CS-g-poly(HEMA), (e) CS-g-poly(AA-co-PHEMA) and CS-g-poly(AA-co-PHEMA)/mica nanocomposites with mica loadings of: (f) 5%, (g) 7%, (h) 10% and (i) 15% w w-1 based on the monomer. The arrow in (d) highlights a damaged cell. 152x142mm (600 x 600 DPI)

KAPOK I: CHARACTERISTCS OF KAPOK FIBER AS A POTENTIAL PULP SOURCE FOR PAPERMAKING

Somporn Chaiarrekij,* Apiporn Apirakchaiskul, Kuntinee Suvarnakich, and Suda Kiatkamjornwong

The potential use of kapok fiber for pulping and papermaking has been investigated. The kapok fibers were cooked using the optimal dosage of sodium hydroxide determined from the experiments. Then, the pulp was refined twice using a disc refiner with a disc gap of 1/100 inch and this kapok pulp was mixed with commercial hardwood pulp and/or softwood pulp at different blend ratios to make papers. Addition of the kapok pulp to the mixed pulps improved the tensile and burst strengths of the sheets but decreased the tear resistance and elongation. Brightness and opacity of the sheets were also dropped with the addition of kapok pulp to the mixed pulps. Water repellency of the sheets prepared from the kapok pulp mixed with the commercial pulps was also improved. These results indicate that kapok fiber can be a quality pulp source for papermaking, especially for packaging paper.

Keywords: Kapok fiber; Properties; Raw material; Papermaking

Contact information: Department of Imaging and Printing Technology, Faculty of Science, Chulalongkorn University, Phayathai Road, Bangkok, 10330 Thailand; *Corresponding author: Huaja@hotmail.com

INTRODUCTION

The kapok tree, Ceiba pentandra (L.) Gaertn. (Malvales: Malvaceae), formerly Bombacaceae family, is cultivated widely in Southeast Asia, as well as other parts of East Asia and Africa. The kapok fiber is an agricultural product obtained from the fruits of the kapok tree (Tang et al. 2008; Qiuling and Lin 2009). Kapok fibers have a hollow structure with a thin fiber wall and large lumen (Hong et al. 2005; Lim and Huang 2007). The diameter including the fiber wall is $16.5 \pm 2.4 \, \mu m$. The lumen diameter is $14.5 \pm 2.4 \, \mu m$ μ m and the fiber length is 25 \pm 5 μ m (Huang and Lim 2006). Kapok fibers are fluffy, light-weight and too inelastic to be spun, and so are good for stuffing beds, pillows and cushions. Chemical compositions of kapok fiber were differently reported by two groups of researchers. The first one mentioned that kapok fiber is chemically composed of 64% cellulose, 13% lignin and 23% pentosan on a weight basis (Kobayashi et al. 1977) while the other stated that it comprises of 35% cellulose, 21.5% lignin, 22% xylan and 13% of acetyl groups on a weight basis (Hori et al. 2000). Besides all those mentioned chemical compositions, they also contain a waxy cutin on the fiber surface which makes them water repellent and oil absorbent. Thus, they are also useful in oil removal applications (Hori et al. 2000; Khan et al. 2004; Huang and Lim 2006; Rengasamy et al. 2011).

There are few reports on utilizing blended kapok fibers for papermaking, such as, the blend of 75:25 (w/w) kapok fibers: bamboo pulp was treated with detergent and

sodium hydroxide before being used to produce paper (Malab et al. 2001). In this case, the combination of the two non-wood fibers significantly reduced the volume of the bamboo pulp, and the amounts of chemical reagents and energy consumption, without adversely affecting the paper strength properties. Another study has indicated that kapok fibers could potentially be pulped to produce paper (Chaiarrekij et al. 2008), but this claim has not been established and any products have not been further characterized. However, it has been observed that paper sheets made from kapok pulp seemed to demonstrate superior water resistant behavior even without any sizing agents being added.

Consequently, the optimum set of pulping conditions for the kapok fibers to give the best strength properties was investigated. This optimal set of pulping conditions was then employed to produce kapok pulp. The influence of kapok pulp on paper properties when the kapok pulp was mixed with commercial hardwood pulp and softwood pulp was also determined. The hypothesis being tested was that kapok pulp might increase the strength properties of the hybrid paper prepared from mixtures of kapok pulp with conventional commercial softwood pulp and/or hardwood pulp. It was thought that as well as providing better strength, paper made of kapok pulp might possess superior water resistance, which is generally required for a packaging paper.

EXPERIMENTAL

Materials

Before pulping, the kapok fibers (sourced from the north eastern part of Thailand) were washed, cleaned, and immersed in water for three weeks prior to manually squeezing out the excess water and cutting to 3-5 cm in length. The moisture content was determined using the moisture balance (FD-600, Kett Electric Laboratory, Japan). The commercial softwood (SW) pulp from Pine and hardwood (HW) pulp from Eucalyptus were obtained from the Crofton Pulp & Paper Mill, Canada and the Phoenix Pulp & Paper Public Co., Ltd, Thailand, respectively.

Methods

The experiment was divided into 2 parts. The first part was about determination of optimal pulping condition for kapok fiber, while the second part was about examining the effects of kapok pulp addition to commercial softwood and hardwood pulps on the properties of the resultant pulp and paper.

Determination of optimal pulping condition for kapok fiber

Kapok fibers were separately pulped using 10, 15, 20, and 25% (w/w) NaOH, based on the oven-dried pulp weight. The liquor-to-wood ratio was 17:1. The pulping was carried out in an autoclave digester, (UEC-2017A, Universal Engineering, India) with an initial digesting temperature at 40 °C. The pulp matrix was then gradually heated to 120 °C over 30 min. Pulping was proceeded at this temperature for another 120 min. The pulp was then extensively washed with tap water to remove the alkalinity from the pulp by controlling with a pH meter (Hanna HI 98128, Hanna Instrument, U.S.A.).

Kapok pulps were refined twice through a disc refiner, using a 1/100 inch disc gap (Andritz Sprout, U.S.A.). The degree of refining was determined following the Canadian Standard Freeness (CSF) standard, using a freeness tester (CF/A, Regmed, Brazil) according to TAPPI Standard Method T227 om-04. Kapok pulps were disintegrated in a standard disintegrator (Formax T-100, Adirondack, U.S.A.) for 100,000 revolutions in hot water (80 °C) to remove latency. The average length of 5,000 fibers per sample was automatically determined using a fiber quality analyzer (FQA, Optest, Canada) according to the TAPPI Standard Method T271 om-98 using the following equations.

The arithmetic average length of individual fibers (L) is calculated from equation (1):

$$L = \underbrace{\sum n_i l_i}_{\sum n_i} \tag{1}$$

The length-weighted average length of the fibers (L_1) is calculated from equation (2):

$$L_1 = \frac{\sum n_i l_i^2}{\sum n_i l_i} \tag{2}$$

The weight-weighted average length of the fibers $(L_{\rm w})$ is calculated from equation (3):

$$L_{\rm w} = \frac{\sum n_i l_i^3}{\sum n_i l_i^2} \tag{3}$$

where the number of fibers (n_i) is the number of fibers in each class of length (l_i) .

The chemical composition of each pulp was determined using TAPPI Standard Method T222 om-98 for lignin determination, TAPPI Standard Method T203 cm-99 for alpha cellulose (α -cellulose) determination, and Browning's method for holocellulose determination (Browning 1963). The amount of hemicellulose was calculated from the difference between the holocellulose content and the alpha cellulose content.

Kapok pulp was also made into 60 g/m² handsheets on a Rapid-Köthen sheet former (RK-2A KWT, PTI, Austria) according to the ISO Standard Method 5269-2. The brightness and opacity of the handsheets were measured using an optical tester (Color Touch PC, Technidyne, U.S.A.), based on ISO Standard Methods 2470 and 2471, respectively. The tensile, burst, tear, and zero-span tensile strengths were measured using a tensile strength tester (Strograph E-S, Toyo Seiki, Japan), a burst strength tester

(SE002P, Lorentzen & Wettre, Sweden), a tear strength tester (Protear, Thwing-Albert, U.S.A.), and a modified tensile strength tester (Pendulum Tensile Strength Tester with special clamps adjustable to zero, Toyo Seiki, Japan), according to TAPPI Standard Method T494 om-01, T403 om-02, T414 om-04 and T231 cm-96, respectively. The contact angle of water in contact with surface of handsheet was automatically measured using the Pocket Goniometer PG-3 (Fibro System, Sweden) by capturing and processing the water droplet images. The dynamic mode was used to measure the rate of change of the contact angle as a function of time. The test was done following TAPPI standard T558 om-06.

The effects of the addition of kapok pulp to commercial softwood pulp and hardwood pulps on the properties of the resultant paper samples

Kapok pulp produced by using the set of optimal conditions previously described was bleached using 3% (w/w) aqueous hydrogen peroxide at a 1.5% consistency and 80 °C for 120 min. The product was disintegrated using a disintegrator (Formax T-100, Adirondack Machine, U.S.A.) for 100,000 revolutions in hot water (80 °C) to remove latency. Each commercial pulp was beaten in a valley beater (UEC-2018A, Universal Engineering, India) in which 360 g of the oven-dried pulp in 23 L of water was accommodated, according to TAPPI Standard method T200 sp-01. The softwood pulp and hardwood pulp were separately beaten to meet the Canadian Standard Freeness of 350 mL and 300 mL, respectively. Then, the bleached kapok pulp was mixed with the commercial beaten hardwood pulp, softwood pulp and mixed pulp (25:75 (w/w) softwood: hardwood) to make handsheets. These procedures of papermaking and paper characterization were repeated in the manner as described.

Statistical analysis

Parametric data were analyzed using the analysis of variance (ANOVA). In all cases, a p-value smaller than or equal to 0.05 was accepted as being a statistically significant difference. For all of the experiments, three replicates were performed.

RESULTS AND DISCUSSION

Determination of Optimal Pulping Condition

Chemical composition of kapok pulp

The effects of the sodium hydroxide solution on the chemical composition of the kapok pulp are summarized in Table 1. Analysis of the chemical composition of the pulps showed that an increased amount of sodium hydroxide in cooking liquor resulted in lower percentages of lignin, higher percentages of holocellulose and alpha cellulose, with lower percentages of hemicellulose. It should be noted that holocellulose is composed of alpha cellulose and hemicellulose. This finding was to be expected, since sodium hydroxide solution dissolves lignin. Carbohydrates, especially hemicellulose, can also be easily destroyed by sodium hydroxide, leaving a higher ratio of alpha cellulose behind. Since all of the P-values of the chemical compositions were lower than 0.05, the effects of sodium

hydroxide solution on kapok pulp chemical compositions were thus statistically significant.

 Table 1. Effects of Sodium Hydroxide Concentration on the Chemical

Composition of the Kapok Pulp

Pulp Chemical Composition		NaOH Dosage (% w/w)			
	10	15	20	25	P-value
Lignin (%)	19.20	18.27	17.57	17.53	0.0109*
Holocellulose (%)	76.12	76.53	78.49	78.50	0.0005*
Alpha cellulose (%)	65.63	69.87	69.65	69.96	0.0002*
Hemicellulose (%)	10.49	6.66	8.84	8.54	0.0007*
* Statistically significant since P-va	alue is lower	than 0.05			

Kapok pulp and fiber characteristics

The effects of sodium hydroxide treatment level on pulp yield, freeness and the average fiber length, characterized in terms of arithmetic, length-weighted, and weight-weighted criteria are summarized in Table 2, along with the percentage of fines.

Table 2. Pulp and Fiber Characteristics of the Kapok Pulp after Soda Pulping

Pulp and Fiber Properties		NaOH Dosage (% w/w)		
	10	15	20	25
Pulp yield (%)	62.40	51.25	44.69	40.46
Freeness (CSF, mL)	401	362	296	277
Average fiber length-Arithmetic (mm)	0.91	0.91	0.83	0.81
Average fiber length-Length weighted (mm)	1.51	1.49	1.32	1.28
Average fiber length-Weight weighted (mm)	2.26	2.17	1.93	1.83
Fines (%)	21.5	21.6	22.7	23.7

The results in Table 2 indicate that high sodium hydroxide concentration could also result in a lower pulp yield because of the removal of lignin and extractives. Also, high sodium hydroxide dosage could lead to carbohydrate degradation, especially with the hemicellulose, due to a peeling reaction. This might also contribute to the lower pulp yield.

Table 2 shows that increasing the concentration of sodium hydroxide significantly decreased the degree of the pulp freeness. Thus, there was a decrease in the pulp's drainage capacity. This was probably due to an increasing amount of fines which would have a significantly greater surface area than fibers for water absorption. Also relevant are the removal of hydrophobic lignin, the dissolution of hemicellulose and possibly the saponification of the cutin wax by the alkali with "solvation" of the cellulose. The latter two possibilities were supported by the results from contact angle studies in which the contact angle with water decreased when the amount of alkali was increased (Fig. 1).

Figure 1 also shows that the handsheets in the dry state (at a zero contact time) had the greater water contact angles. However, after contact with the water, the contact angles decreased due to wetting, absorption, penetration, and spreading of the water under the influence of the cellulosic hydrophilic interactions.

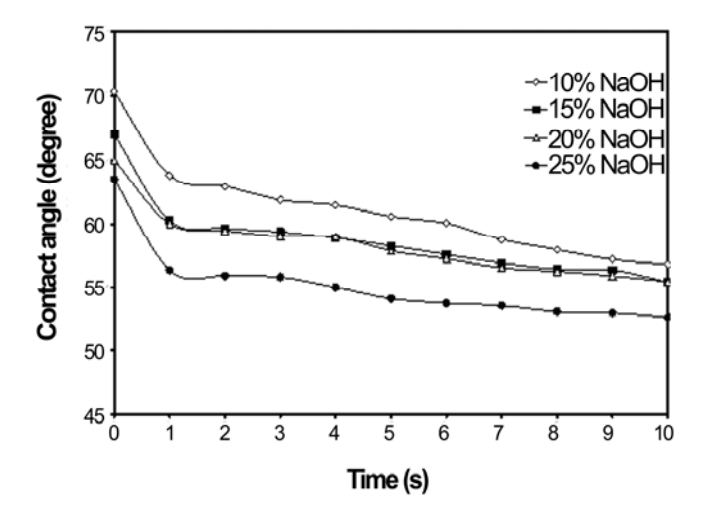


Fig. 1. The effects of different sodium hydroxide concentrations on water contact angles of the kapok fiber sheets.

It should be noted that weight weighted average fiber length is one of the average fiber length values, but it emphasizes more on the content of long fibers as compared to the length weighted fiber length and the arithmetic average fiber length, respectively. When the amount of sodium hydroxide increased, the average fiber length significantly decreased, whilst the fines content was increased (Table 2). This was likely to have occurred because the fibers were damaged by a peeling reaction under the strong alkali conditions leading to carbohydrate degradation (Sjöström 1993). Thus, the greater the amount of carbohydrate that was degraded by the alkali, the lower would be the mean fiber length and the greater would be the amount of fiber fines.

Kapok handsheet properties

The effects of the sodium hydroxide solution on the kapok handsheet properties are summarized in Table 3.

Table 3. Effects of Sodium Hydroxide Concentration on the Kapok Handsheet Properties

Pulp and Paper Properties	NaOH Dosage (% w/w)				
	10	15	20	25	P-value
Apparent density (g/cm ³)	0.68	0.80	0.82	0.88	0.1264
ISO opacity (%)	97.9	97.5	97.4	97.0	0.0235*
ISO brightness (%)	21.3	19.1	18.6	18.1	0.1917
Tensile index (N m/g)	80.3	100.4	111.5	101.3	0.0002*
Elongation (%)	1.75	2.01	2.10	2.05	0.0335*
Burst index (kPa m ² /g)	4.44	5.73	5.96	5.98	0.0348*
Tear index (mN m ² /g)	1.78	1.68	1.60	1.59	0.4005
Zero span tensile index (N m/g)	59.5	58.2	56.7	55.9	0.9801
* Statistically significant since P-va	lue is lower	than 0.05	•		•

Increasing the amount of sodium hydroxide solution led to an increase in the apparent density of the sheets which was defined as handsheet grammage divided by

handsheet thickness, but a lower opacity (Table 3). Such effects are likely to be due to the role of sodium hydroxide solution in breaking up lignin molecules within the fiber cell wall. As the hydrophobic lignin was removed, the fiber surface became more hydrophilic, encouraging fiber swelling and conformability. This would result in a more compacted sheet that in turn, which could lead to fewer air-to-fiber interfaces and a lower opacity. In addition, the increasing content of fines and the greater amount of fiber contact areas would help to improve fiber bonding, leading to denser sheets, as indicated by the higher apparent density. Shorter fibers and a greater amount of fines also provided a basis for more effective filling of existing voids, which might also have contributed to lower opacity of the sheet. However, the effect of sodium hydroxide solutions on the apparent density appeared in this case to be statistically insignificant while its effect on opacity was statistically significant.

Pulp brightness would be expected to increase when greater amounts of sodium hydroxide solution were used, since more lignin would be removed. However, the observed trend was the opposite of this expectation, as indicated by the statistical evaluation (Table 3). However, greater concentrations of sodium hydroxide solution might reduce pulp brightness through an alkali darkening reaction, resulting in structural changes of the chromophoric groups in the residual lignin. These groups could also absorb light and thus cause the brightness of the pulp to decrease. An additional plausible explanation might be that the sodium hydroxide solution mediated the removal of lignin and caused greater sheet compactness with a resultant reduced level of light scattering of the sheet, whilst the greater amount of fines might also lead to sheet compactness.

The tensile index defines the tensile strength of paper. It is the tensile strength divided by the grammage. The burst index defines the burst strength of the paper and is equal to the burst strength divided by the grammage. Fiber bonding is highly likely to affect the tensile strength and burst strength. Increasing sodium hydroxide dosage provided higher tensile and burst strengths due to increasing fiber bonding, since lignin was removed and fibers became more conformable (Table 3). Increased fiber bonding caused by the greater sodium hydroxide dosage also led to the higher elongation. However, it should be noticed that using too high dosage of sodium hydroxide was detrimental to tensile and burst strengths as a result of carbohydrate degradation by peeling reaction at a strong alkali condition. The effects of the sodium hydroxide concentration in cooking liquor on the tensile index, the elongation and the burst index were statistically significant.

The tear index, the tear resistance value divided by the grammage, defines the tear resistance of the paper. Tear resistance is affected by many factors, such as the intrinsic fiber strength, the fiber length, and fiber bonding. The most important factor for well-bonded sheets is the fiber strength. The zero span tensile index is defined by the zero-span tensile strength divided by the grammage. Generally, zero span tensile index is a function of both the intrinsic fiber strength and the fiber bonding; however, the intrinsic fiber strength is a major contributing factor. The tear index decreased when the sodium hydroxide concentration increased (Table 3). The same observation was found for the zero span tensile index. This effect could be caused by the peeling reaction that destroys endwise, the chains of cellulose and hemicellulose and by the alkaline hydrolysis that leads to a drop in the degree of polymerization of the fibers (Shatalov and Pereira 2005).

The decrease in tear resistance might also be caused by the shorter fiber length and the greater amount of fines that are created. However, the effects of sodium hydroxide dosage on the tear and zero span tensile index values were so small that they were statistically insignificant.

Overall, the optimum condition for kapok fiber pulping was that of the cooking liquor containing 20% (w/w) of sodium hydroxide, which gave the maximum tensile properties as discussed. Thus, kapok pulp that was prepared using a 20% (w/w) sodium hydroxide dosage was used in subsequent experiments. However, the pulp was bleached before being mixed with commercial pulps.

Effects of Kapok Pulp Addition to Commercial Softwood and Hardwood Pulps on the Properties of the Resultant Pulp and Paper

Fiber length distributions of kapok, softwood and hardwood pulps

The fiber length distributions of the kapok pulp that was produced using the cooking liquor of 20% (w/w) sodium hydroxide and the commercial softwood pulp and hardwood pulp are shown in Fig. 2.

The kapok pulp had an intermediate amount of short fibers that was less than that of the hardwood pulps. The softwood pulp gave the lowest short fiber content. The kapok pulp was also intermediate in the amount of both medium and long fibers. These were lower than that from the hardwood pulp. The softwood pulp contained the greater amount of long fibers.

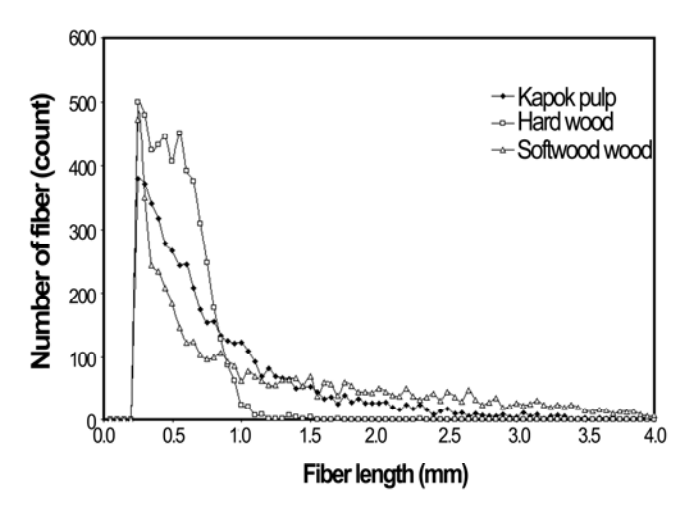


Fig. 2. Fiber length distributions of the kapok, hardwood and softwood pulps.

Fiber length, fines content and zero span tensile index of kapok, softwood and hardwood pulps

Fiber length, fines content and zero span tensile index of kapok, softwood and hardwood pulps are compared and illustrated in Table 4.

Table 4. Fiber Length, Fines Content and Zero Span Tensile Index of Kapok and the Commercial Pulps

4.10 0011111101010111 011110			
Pulp Properties	Pulp Types		
	Kapok	Softwood (SW)	Hardwood (HW)
Average fiber length-Arithmetic (mm)	0.83	1.25	0.50
Fines (%)	22.7	43.2	34.0
Zero span tensile index (N m/g)	56.7	82.6	44.2

After being refined to the freeness of 300 mL as shown in Table 4, the average fiber length of the kapok pulp (0.834 mm) was between those of the softwood pulp (1.253 mm) and hardwood pulp (0.496 mm). The kapok pulp also had the lowest level of fines, followed by the hardwood pulp and softwood pulp, respectively.

As shown in Table 4, the sheets made from the softwood and hardwood pulps had the greatest and least zero-span tensile index at 82.6 and 44.2 N m/g, respectively. That made from kapok pulp was 56.7 N m/g. Since kapok fiber was brittle, this led to the lower zero span tensile index of kapok pulp.

Apparent density

The apparent densities of the sheets that were prepared from different ratios of the kapok pulp to the commercial softwood (SW), hardwood (HW) and softwood-hardwood mixed pulps, are shown in Fig. 3.

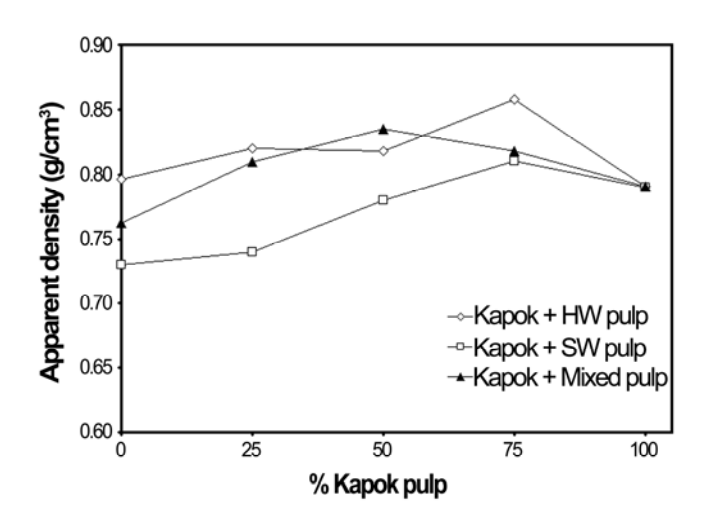


Fig. 3. Apparent density of the sheets made from kapok pulp mixed with the commercial hardwood (HW) pulp and softwood (SW) pulp at the indicated percentages.

The sheets made from the hardwood pulp had a greater apparent density than those containing either the softwood pulp or the kapok pulp. That is because the shorter fibers of the hardwood pulp fill the voids and pores in the sheet structure, making the sheets more compact. The inclusion of kapok pulp increased the apparent density of the sheets in all of the pulp mixtures. This could be because the kapok fibers have very thin cell wall, being easily collapsed, making more compact sheets. However, sheets derived

from the pure kapok pulp were not greater in apparent density, as seen by the fact that the kapok fibers become easily entangled. Thus, pure kapok sheets gave poor sheet formation and an irregular sheet surface.

Tensile index and burst index

The sheets made from kapok pulp gave the highest tensile index (Fig. 4). This could be because the kapok fibers were long and the lumens were easily collapsed when forming paper, producing highly bonded regions and denser sheets with a resulting superior sheet tensile index.

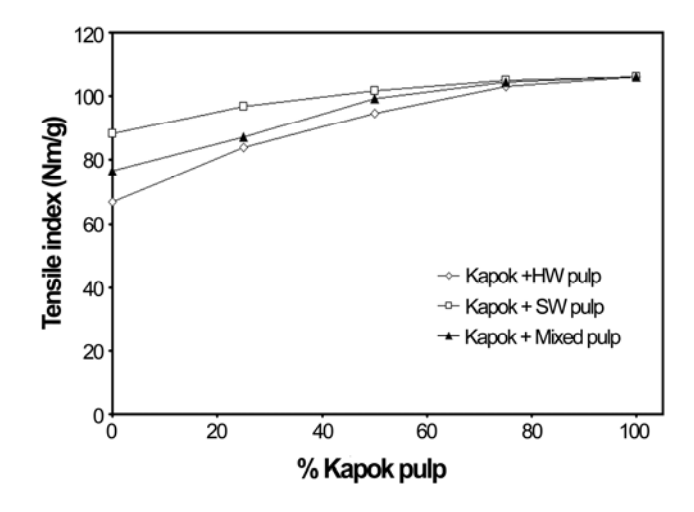


Fig. 4. Tensile index of the sheets made from kapok pulp mixed with the commercial hardwood (HW) pulp and softwood (SW) pulp at the indicated percentages.

The sheets made from the hardwood pulp produced the lowest tensile index. Those made from a 75:25 (w/w) blend of the hardwood: softwood pulps had a medium tensile index. Those made from the pure softwood pulp gave the greatest tensile index. With respect to kapok-commercial pulp mixtures, as the ratio of kapok pulp increased, the tensile index also increased (Fig. 4). However, the results were more prominent when the kapok pulp was mixed with the hardwood pulp than with the softwood pulp.

The sheets derived from the pure kapok pulp gave the highest burst index, the values being somewhat similar to those of the sheets made from the softwood pulp (Fig. 5). This is because both kapok fiber and the softwood fiber are long and have extensive contact areas that are available for fiber bonding. The sheets made from the hardwood pulp had the lowest burst index. This is because the hardwood pulp contained a greater amount of short fibers, resulting in poor bonding. As the ratio of the kapok pulp in mixtures with the hardwood pulp or the 75:25 ratios (w/w) of hardwood pulp: softwood pulp increased, the burst indexes of the resultant paper significantly increased, because fiber bonding was greatly improved.

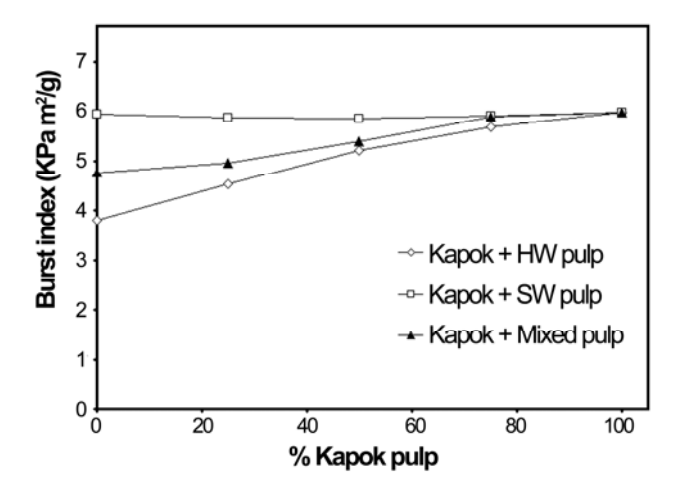


Fig. 5. Burst index of the sheets made from kapok pulp mixed with the commercial hardwood (HW) pulp and softwood (SW) pulp at the indicated percentages.

Tear index and elongation

One of the key characteristics of kapok fibers is their brittleness. Thus, the sheets made from the kapok pulp had the lowest tear index relative to those made from the commercial softwood pulp, the hardwood pulp, and the softwood-hardwood mixed pulp. For kapok-commercial pulp mixtures at different ratios, it was clearly observed that as the ratio of kapok pulp increased, the tear index significantly decreased (Fig. 6).

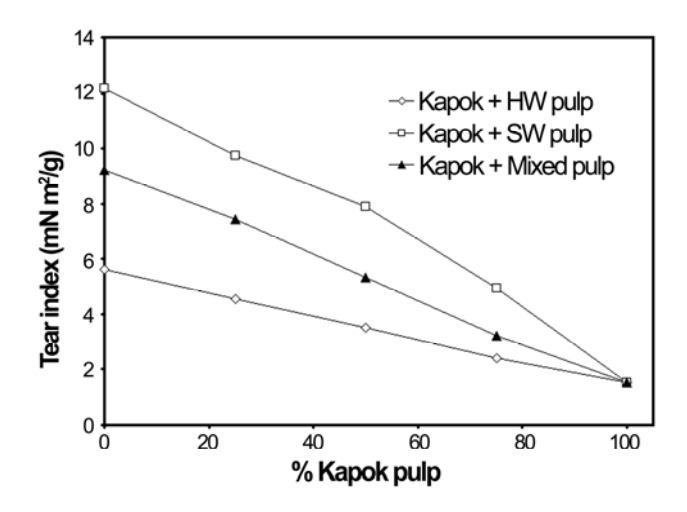


Fig. 6. Tear index of the sheets made from kapok pulp mixed with the commercial hardwood (HW) pulp and softwood (SW) pulp at the indicated percentages.

The elongation of the sheets that were prepared from different ratios of the kapok pulp is compared in Fig. 7. Sheets made from kapok pulp had the lowest elongation. This is because the key characteristics of kapok fibers are their brittleness and inelasticity, which might reduce the elongation of the sheets when a load was applied. Thus, as the

ratio of the kapok pulp was increased, the elongation significantly decreased in all pulp mixtures.

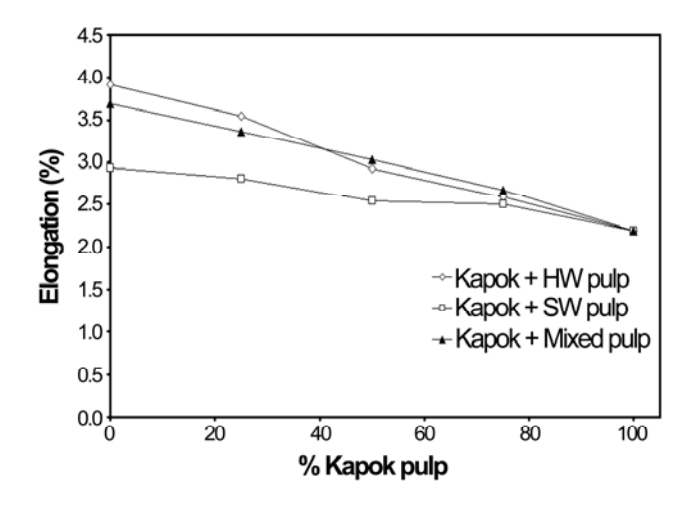


Fig. 7. Elongation of the sheets made from kapok pulp mixed with the commercial hardwood (HW) pulp and softwood (SW) pulp at the indicated percentages.

Water contact angle

The water contact angles of the sheets made from kapok pulp mixed with the commercial softwood pulp and hardwood pulp are shown in Fig. 8. As seen in Fig. 8, K 100 represented handsheets made from 100% kapok pulp. HW100 indicated handsheets made from 100% hardwood pulp while SW100 illustrated handsheets made from 100% softwood pulp. M100 designated handsheets made from mixed pulp (25:75 (w/w) softwood pulp: hardwood pulp). Handsheets prepared from kapok pulp mixed with hardwood, softwood and mixed pulps with different percentages characterized by K: HW, K: SW and K: M with the percentage indicated in parenthesis.

The results indicated that as the time of contact increased, the water contact angles decreased because of absorption and penetration of the water droplets into the sheet. Those made from 100% kapok pulp gave the greatest values for the water contact angle. This effect was due to the unique characteristics of the kapok fibers having a wax coating on the surface. Although the kapok fibers were pulped, some of the wax was still present. When mixed with the commercial pulps (softwood, hardwood and mixed pulps), as the ratio (w/w) of the kapok pulps increased, the water contact angle values increased.

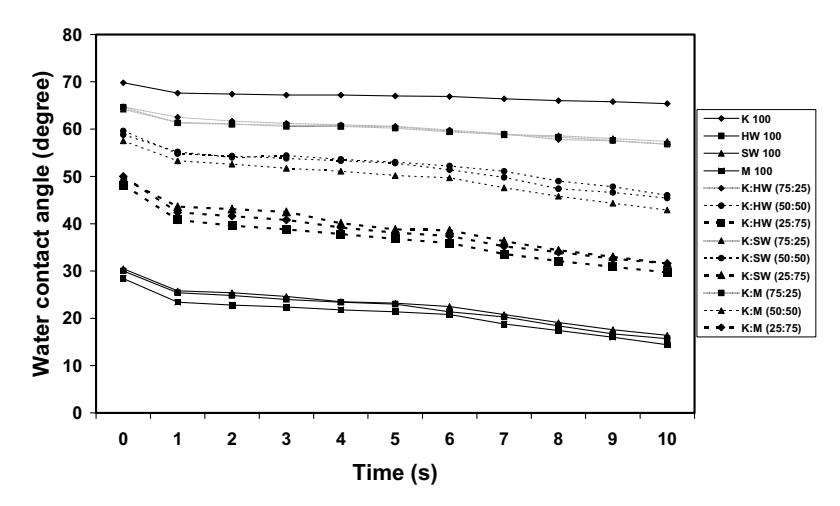


Fig. 8. Water contact angles of the sheets from the kapok (K) pulp mixed with the commercial hardwood (HW) pulp, softwood (SW) pulp and mixed (M) pulp at the indicated percentages.

CONCLUSIONS

- 1. When kapok pulp was mixed with the commercial softwood pulp and/or hardwood pulp, the tensile and burst strengths of the blended sheets increased but with the lower tear resistance and elongation due to the excellent tensile strength and brittleness of kapok pulp.
- 2. Brightness and opacity of the blended sheets decreased when higher amounts of kapok pulp were added in the pulp mixture due to the yellowness of the kapok pulp.
- 3. Handsheets containing kapok pulp gave greater water contact angles due to the hydrophobic nature of kapok fibers.
- 4. Thus, kapok pulp can potentially be mixed with the commercial softwood pulp and/or hardwood pulp to produce commercial packaging paper when the strength and light weight characteristics are required.

ACKNOWLEDGMENTS

This research was financially supported by a Research Team Aid Grant from the Thailand Research Fund and Commission of Higher Education under the contract number RTA5080004. The authors would like to thank the Department of Imaging and Printing Technology of Chulalongkorn University, and the Product and Technology Development Center of Siam Cement Group Paper Company Limited for providing relevant research facilities.

REFERENCES CITED

Browning, B. L. (1963). *Methods in Wood Chemistry*, Interscience Publishers, New York.

- Chaiarrekij, S., Wongsaisuwan, U., and Watchanakit, S. (2008). "Papermaking from Kapok fiber," *Thai Petty Patent*, 4279, June 13, 2008.
- Hong, X., Wei-dong, Y., and Mei-wu, S. (2005). "Structure and Performances of the Kapok Fiber," *Journal of Textile Research* 26(4), 4-6.
- Hori, K., Flavier, M. E., Kuga, S., Lam, T. B. T., and Liyama, K. (2000). "Excellent oil absorbent kapok [*Ceiba pentandra (L.) Gaertn.*] fiber: Fiber structure, chemical characteristics, and application," *J. Wood Sci.* 46(5), 401-404.
- Huang, X. F., and Lim, T. T. (2006). "The performance and mechanism of hydrophobic—oleophilic kapok filter for oil/water separation," *Desalination* 190(1-3), 295-307.
- Khan, E., Virojnagud, W., and Ratpukdi, T. (2004). "Use of biomass sorbents for oil removal from gas station runoff," *Chemosphere* 57, 681-689.
- Kobayashi, Y., Matsuo, R., and Nishiyama, M. (1977). "Method for adsorption of oils," *Japanese Patent*, 52,138,081, November, 17, 1977.
- Lim, T.-T., and Huang, X. (2007). "Evaluation of Kapok (*Ceiba pentandra* (L.) Gaertn.) as a Natural Hollow Hydrophobic-Oleophilic Fibrous Sorbent for Oil Spill Cleanup," *Chemosphere* 66, 955-963.
- Malab, S. C., Agrupis, S., Cabalar, L., and Ballesteros, R. (2001). "Paper sheets from bamboo and kapok," *PCARRD Press Release* No.153, December, 14, 2001.
- Qiuling, C., and Lin, W. (2009). "Structure and Property Contrast of Kapok Fibre and Cotton Fibre," *Contton Textile Technology* 37(11), 668-670.
- Rengasamy, R.S., Dipayan, D., and Karan, P.C. (2011). "Study of Oil Sorption Behavior of Filled and Structured Fiber Assemblies Made from Polypropylene, Kapok and Milkweed Fibers," *Journal of Hazardous Materials* 186(1), 526-532.
- Shatalov, A. A., and Pereira, H. (2005). "Kinetics of polysaccharide degradation during ethanol-alkali delignification of giant reed-Part 1. cellulose and xylan," *Carbohydr. Polym.* 59(4), 435-442.
- Sjöström, E. (1993). *Wood Chemistry-Fundamentals and Applications*, 2nd ed., Academic Press, San Diego.
- Tang, A.-m., Sun, Z.-h., Fu, X., Zi, M., Zhang, H.-w., Chen, G., and Lin, Y. (2008). "Chemical and Structural Characteristics of Kapok Fibers," *Zhongguo Zaozhi Xuebao/Translations of China Pulp and Paper* 23(3), 1-5.

Article resubmitted: July 31, 2011;

Elsevier Editorial System(tm) for Journal of Chromatography A Manuscript Draft

Manuscript Number:

Title: Comparative study of the mesostructure of natural and synthetic polyisoprene by SEC-MALS and AF4-MALS

Article Type: Full Length Article

Keywords: Field flow fractionation; size exclusion chromatography; polyisoprene; multi angle light

scattering; rubber

Corresponding Author: Mr. Stéphane Dubascoux,

Corresponding Author's Institution: Montpellier SupAgro

First Author: Stéphane Dubascoux

Order of Authors: Stéphane Dubascoux; Chalao Thepchalerm; Eric Dubreucq; Suwaluk Wisunthorn;

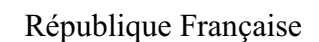
Laurent Vaysse; Suda Kiatkamjornwong; Charoen Nakason; Frédéric Bonfils

Suggested Reviewers: Stepan Podzimek stepan.podzimek@synpo.cz expert in AF4 and polymer science

Bruno Grassl bruno.grassl@univ-pau.fr expert in polymer science

Yacine Hemar y.hemar@auckland.ac.nz expert in physico-chemistry of colloidal system

Opposed Reviewers:





CENTRE INTERNATIONAL D'ETUDES SUPERIEURES EN SCIENCES AGRONOMIQUES

DEPARTEMENT DES SCIENCES POUR LES AGRO-BIOPROCEDES

UMR INGENIERIE DES AGROPOLYMERES ET TECHNOLOGIES EMERGENTES (UMR 1208 IATE, CIRAD-INRA-MONTPELLIER SUPAGRO-UM2)

Dr. Stéphane Dubascoux Tel: +33 (0) 499613016

Email: stephane.dubascoux@supagro.inra.fr

Montpellier, 05th July 2011

Cover letter

Dear Managing Editor,

Please find enclosed the submission of our regular research paper entitled: "Comparative study of the mesostructure of natural and synthetic polyisoprene by SEC-MALS and AF4-MALS". In this article, we present the first original results about natural and synthetic rubber characterization by asymmetrical flow field flow fractionation (AF4). Mesostructure evaluation by AF4 is compared with that obtained with size exclusion chromatography.

Up to now, there is a real lack of information concerning natural rubber mesosctructure and more precisely about the presence and the nature of microaggregates (gel content) among the linear polyisoprene chains. AF4 allows assessing simultaneously both the distribution of polyisoprene chains and gel content. Results obtained allow to validate the AF4 fractionation (compared to SEC results) and to consider the gel part of polyisoprene samples.

For these reasons, we think that our article matches with the topic of your journal and is appropriate for publication in journal of chromatography A.

Sincerely yours,

The authors: Stephane Dubascoux, Chalao Thepchalerm, Eric Dubreucq, Suwaluk Wisunthorn, Laurent Vaysse, Suda Kiatkamjornwong, Charoen Nakason, Frederic Bonfils

1 Comparative study of the mesostructure of natural and synthetic

- 2 polyisoprene by SEC-MALS and AF4-MALS.
- 3 Stephane Dubascoux*¹, Chalao Thepchalerm^{1,2,6}, Eric Dubreucq¹, Suwaluk Wisunthorn³,
- 4 Laurent Vaysse⁴, Suda Kiatkamjornwong⁵, Charoen Nakason², Frederic Bonfils*⁶
- 6 ¹ Montpellier SupAgro, UMR IATE 1208, 2 Place Viala, 34060 Montpellier, France
- ² Center of Excellence in Natural Rubber Technology, Faculty of Science & Technology,
- 8 Prince of Songkla University, Pattani campus, Thailand
- 9 ³ Faculty of Science and Industrial Chemistry, Prince of Songkla University, Surat Thani
- 10 campus, Thailand

5

15

- 11 ⁴ CIRAD, UMR IATE 1208, KU-CIRAD laboratory, Agroindustry building 3, 7th Floor,
- 12 Kasetsart University, Bangkok 10900, Thailand
- 13 ⁵ Faculty of Science, Chulalongkorn University, Bangkok, Thailand
- 14 ⁶ CIRAD, UMR IATE 1208, 2 Place Viala, 34060 Montpellier, France

Abstract

This paper presents results from the first analyses of the mesostructure of natural rubber (NR) by asymmetrical flow field flow fractionation (AF4). The results are compared with those obtained by size exclusion chromatography (SEC) in terms of average molar masses, radius of gyration and insoluble part (or gel quantity). Comparable results were obtained for the sample not containing gel. Conversely, for samples with gel, significant differences were found due to the presence of microaggregates. In fact, contrary to SEC, AF4 fractionation enables partial fractionation of polyisoprene chains and microaggregates in a single run without preliminary treatment. The results presented here also highlight the special structure (very compact spheres) of microaggregates in NR compared to chemical crosslinked microaggregates in synthetic polyisoprene. The advantages and drawbacks of both techniques for analysing NR samples are also discussed.

Introduction

30

31 For natural rubber (NR), as for numerous biopolymers, it is rather simplistic to speak about 32 macromolecular structure. Indeed, biopolymers often exhibit a complex associative structure, 33 a mixture of macromolecular chains, microaggregates and macroaggregates [1,2]. Because of 34 that, the term mesoscopic structure or mesostructure, which includes both macromolecular 35 structure and aggregate characterization, is increasingly being used. Although NR 36 mesostructure has been studied for many years, the origins of its unique properties are not yet 37 fully clear. Recently, Kim et al. [3,4] revisited the mesostructure of NR. Kim et al. [3,4] analysed NR samples with SEC-MALS and showed that the soluble part injected into a SEC 38 39 system contained very few branched macromolecules, contrary to earlier published studies [5-40 7]. Kim et al. [3,4] showed that the soluble part of NR in solution in tetrahydrofuran (THF) was composed of a mixture of linear chains and assumed compact microaggregates ($R_g \approx 110$ -41 42 130 nm). They showed that to more effectively ascertain the mesostructure of NR, as is the 43 case with most polymers, a MALS detector coupled with SEC is required to avoid a 44 misunderstanding of the structure. From a mechanistic point of view, many mechanisms have 45 been proposed to explain the associative structure of NR [8-11]. The most recent proposal is Tanaka's group scheme involving a protein and a phospholipid at each end of the poly(cis-46 47 1,4-isoprene) chain. These two reactive end chains would appear to be involved in what they 48 called the "naturally occurring network" of NR [12,13]. 49 Today, many tools are available for macromolecule analysis. Of these techniques, size 50 exclusion chromatography (SEC) and field flow fractionation (FFF) are tools of choice to 51 fractionate macromolecules according to their sizes. SEC is beyond doubt the most popular 52 and developed technique for polymer separation. However, a recent study has also highlighted 53 some difficulties for NR separation with SEC coupled with a multi-angle light scattering 54 (MALS) detector because of an abnormal elution phenomenon [3]. This abnormal elution is

due to co-elution of microaggregates with short chains. Kim et al. [3] showed that the abnormal elution occurring with NR could be overcome by treating the SEC columns with an ionic surfactant. After treatment, it was possible to separate these compact microaggregates from linear random coil polyisoprene chains [3]. However, it is difficult to be sure whether or not all microaggregates elute and the procedure is rather cumbersome. The solution to this SEC limitation for NR sample analysis might be the use of techniques based on field flow fractionation. Recent reviews have demonstrated the potentiality of FFF in various fields, such as polymer science [14], biomolecule characterization [15], nanoparticles [16] or the environment [17]. Moreover, FFF could easily be coupled on-line with different detectors, such as a refractive index detector, an ultra-violet detector, a light scattering or inductively coupled plasma mass spectrometer [18]. Recently, Messaud et al. [14] emphasized the fact that field flow fractionation techniques can provide effective simultaneous separation of polymer and microgel. The most popular FFF techniques used for polymer fractionation are thermal flow field flow fractionation (Th-FFF) and Flow Field Flow Fractionation (Fl-FFF or F4) [14]. The main difference between these two sub-techniques is the field used for the fractionation. Fractionation takes place in a channel and the field is a thermal gradient for Th-FFF, while it is a crossflow stream carried through an ultrafiltration membrane in the case of Fl-FFF [19]. Up to now, only Th-FFF has been used for NR characterization [20-23]. However, during Th-FFF, macromolecules are separated according to their size and their chemical composition. Thus, heterogeneity in the chemical composition of a given polymer can complicate the determination of macromolecular structure. Asymmetrical Fl-FFF (AsFl-FFF or AF4) is Fl-FFF where the channel is semi-permeable and asymmetric, involving less sample dilution [19]). Natural rubber has been analysed by Th-FFF using either the polyisoprene calibration curve [20,22,23] or a multi-angular light scattering detector (MALS) [21]. Lee and Molnar [23] compared the analysis of natural rubber by Th-FFF and SEC. They

55

56

57

58

59

60

61

62

63

64

65

66

67

68

69

70

71

72

73

74

75

76

77

78

used a calibration curve made with linear standards poly(cis-1,4-isoprene). The analysed NR samples (RSS1 type) had a number-average molar mass (M_n) of about 0.8 million g.mol⁻¹ and a weight-average molar mass (M_w) of about 29 million g.mol⁻¹, M_w being three times higher than that given by SEC. Lee and Molnar [23] showed that the high molar masses and microgels disappeared after mastication of a NR sample in an extruder. The range of molar masses found was between 10,000 and 10 million g.mol⁻¹ (non-masticated RSS). Filtration of the solution through filters with 5 µm pores led to a shift in the fractogram towards lower retention times. This phenomenon was observed for non-masticated rubber but not for masticated rubber. This shift to lower molar masses was attributed to the removal and/or degradation of microgels (or ultra-high molar mass species). They quantified the gel rate (as a % of total rubber, w/w) in the NR samples by Th-FFF and found slightly lower values (RSS 13%, masticated RSS 0%) than with their conventional method – i.e. filtration through a 125 μm wire mesh after 24 h in toluene (RSS 15%, masticated RSS 0%). Fulton and Groves [21] analysed two synthetic polyisoprenes (IR305, Natsyn2200), a polybutadiene (Europrene BR40) and a natural rubber (SMR5L) in cyclohexane by Th-FFF-MALS without any filtration. They showed that the IR305 sample was essentially linear with no gel, as confirmed later by Kim et al. [3] by SEC-MALS, contrary to the Natsyn2200 sample, which had a 25% gel rate and was branched for molar masses above 5.10⁵ g.mol⁻¹. While there was no steric effect in the separation process for the two synthetic polyisoprenes, they observed such an effect for the polybutadiene and the NR samples. As a consequence of this phenomenon, very large entities eluted together with the smaller molecules. Bang et al. [24] used AF4 to characterize and determine the molar mass distribution of styrene-butadiene rubber. This paper presents the first study of synthetic and natural polyisoprene fractionation by AF4 coupled with MALS in an organic solvent (tetrahydrofuran). The peak shape is discussed and the results in terms of average molar masses, radius of gyration and gel content are compared

80

81

82

83

84

85

86

87

88

89

90

91

92

93

94

95

96

97

98

99

100

101

102

103

with those obtained by SEC-MALS. The comparison of AF4-MALS with SEC-MALS also made it possible to evaluate the discrepancies between the two techniques for analysing NR samples.

Material & methods

Samples

111	In order to compare SEC and AF4 results on synthetic polyisoprene and natural rubber (NR),
112	four samples were chosen for their differences in mesostructure. The two synthetic poly(cis-
113	1,4-isoprenes) were Kraton IR 307 (Kraton polymer, Houston, USA) and Nippol 2200 (Zeon
114	Corporation, Louisville, USA). The main difference between these two synthetic
115	polyisoprenes is the gel rate: no gel in the IR307 sample and presence of microgel in Nippol
116	2200. The two natural rubbers, M160 and M121, were TSR5CV (Technically Specified
117	Rubber with a Constant Viscosity) made from monoclonal Hevea brasiliensis latex. The
118	preparation of the samples was described previously [25].
119	In order to reach a sample concentration of 1 mg.mL ⁻¹ , 30 ± 5 mg of the samples was
120	dissolved in about 30 mL of HPLC grade tetrahydrofuran (THF, VWR, West Chester, USA)
121	stabilized with 2,6-di-tert-butyl-4-methylphenol – BHT – (Sigma Aldrich, Saint Louis, USA)
122	at 250 mg.L ⁻¹ . The flasks were precisely weighed (± 0.01 mg) before and after filling with
123	THF to determine the exact concentration of the solutions. The solvent (THF + BHT) was
124	filtered at 0.1 µm before use. Each sample was analysed in triplicate to evaluate measurement
125	repeatability. All solutions were stored in the dark in a water bath at 30°C for 7 days and
126	gently shaken at 30 rpm (rotational agitator REAX 2, Heidolph, Schwabach, Germany) for 1
127	hour each day for optimum dissolution. Before injection, the macrogel and part of the
128	microgels were removed from all the solutions by filtration at a 1 μm cutoff with Acrodisc
129	glass filters (Pall, Port Washington, USA) to avoid both clogging of the column during SEC
130	analysis and a steric effect (resulting in inverse elution) on AF4 fractionation [21].
131	Two monodisperse polystyrene standards at 200 and 1460 kDa from Polymer Standard
132	Service (PSS, Mainz, Germany) were used to assess the quality of the separation/fractionation
133	and detector response for each SEC/AF4 injection series.

AF4 experiments

The AF4 system was a Postnova AF2000 MT series (Postnova Analytics GmbH, Landsberg, Germany) equipped with a channel adapted for organic solvents and a 350 µm spacer. The membrane was made of cellulose material treated for compatibility with organic solvents with a cut-off of 5 kDa (Postnova Analytics GmbH, Landsberg, Germany). The temperature setpoint of the AF4 oven containing the channel was 45°C. The detector flow was kept constant at 0.65 mL.min⁻¹. The focusing step consisted of a flow delivered by the injection port of about 0.2 mL.min⁻¹ with a crossflow of 1 mL.min⁻¹ for 6 minutes. Then, a 1 min transition time was applied to avoid a major pressure drop during the switch from the focus step to the elution step. The programme to decrease the linear crossflow during the elution step was as follows:

Table 1

An autosampler (PN 5300 model, Postnova Analytics GmbH) was used to carry out the 100 µL sample injections.

Detection was carried out with a 7-angle multi-angle light scattering detector (PN 3070 model, Postnova Analytics GmbH) in line with a refractive index detector (2414 model, Waters Corporation, Milford, USA). The data gathered were processed with AF2000 software (Postnova Analytics GmbH) after blank subtraction for the DRI signal (used as a concentration detector) and according to the Berry model with 2nd order polynomial formalism. In fact, it has been shown that this formalism is well adapted for entities with a radius up to 50 nm [26]. As the refractive index detector signal changes during transition steps due to the AF4 functioning principle, five blank (mobile phase) injections were carried out in

each injection series. The refractive index detector signal from the blank injections was subtracted for each sample injected.

For one series, each sample triplicate was injected once. Two series were carried out (i.e. a total of 6 injections was carried out for each sample) with different operators in order to evaluate the reproducibility of the analysis. Prior to each series of injections, the membrane was replaced and the detector was recalibrated.

SEC experiments

The SEC system was based on an on-line ERC 3112 degaser (ERC, Saitama, Japan), a Waters 515 pump (Waters Corporation, Milford, USA) and 3 MIXED-A columns in series: 2 styragel columns (porosity 20 μ m, 300 mm \times 7.5 mm I.D.) from Waters and 1 PLgel column (porosity 20 μ m, 300 mm \times 7.5 mm I.D.) from Varian (Varian, Walnut Creek, USA). All the columns were kept in an oven at 45°C. The detectors were an 18-angle multi-angle light scattering detector (Dawn DSP model, Wyatt Technology, Santa Barbara, USA) and a refractive index detector (Optilab rEX model, Wyatt Technology). Data from angles 5 to 16 were collected and processed with Astra software version 5.3.1 (Wyatt Technology) according to the Berry method with a 2nd order polynomial model. Similarly to the AF4 injection series, each sample triplicate was injected once. Two series were carried out (i.e. a total of 6 injections carried out for each sample).

Theory/calculation

180 Light scattering theory

- 181 For the Berry method with a 2nd order polynomial fit, $[Kc/\Delta R(\theta)]^{1/2}$ is plotted against
- $\sin^2(\theta/2)$. According to the light scattering theory, this plot makes it possible to determine M_{wi}
- and Rgi for each slice of the fractogram from AF4 or the chromatogram from SEC,
- respectively, according to equation 1.

$$\left[\frac{\kappa c}{\Delta R(\theta)}\right]_{i}^{1/2} = \left[\frac{1}{M_{wi}} + \frac{16\pi^2}{3_0^2} \frac{\langle R_g^2 \rangle_i}{M_{wi}} \sin^2\left(\frac{\theta}{2}\right)\right]^{1/2} \quad Equation \ 1$$

- where K is an optical constant
- c is the solute concentration (in g.mL⁻¹)
- 188 θ is the scattering angle
- $\Delta R(\theta)$ is the excess Rayleigh ratio, the ratio of scattered and incident light
- intensity
- M_{wi} is the weight-average molar mass of the solute
- λ_0 is the wavelength of the laser beam in a vacuum (in nm)
- R_g is the gyration radius of the solute (nm)
- 194

179

The optical constant K is given by equation 2.

$$K = \frac{4\pi^2 n_0^2}{N_A^2} \left(\frac{dn}{dc}\right)^2 \quad Equation \ 2$$

- where n_0 is the refractive index of the solvent
- 198 N_A is Avogadro's number
- 199 $\left(\frac{dn}{dc}\right)$ is the differential refractive index increment of the polymer in the solvent
- 200 used

201

For detailed information about the light scattering theory, refer to [27,28].

203

204

Molar mass and radius definitions

The different molar masses calculated and presented are defined as:

206
$$M_n = \frac{\sum_i N_i M_i}{\sum_i N_i}$$
 $M_w = \frac{\sum_i N_i M_i^2}{\sum_i N_i M_i}$ $M_z = \frac{\sum_i N_i M_i^3}{\sum_i N_i M_i^2}$ Equation 3, 4 & 5

207 Where N_i is the number of polymers with molecular weight M_i 209 The radius of gyration (<R_g> or R_z) or root mean square radius (r.m.s) is defined for a non-210 rigid particle as:

$$< R_g > = \frac{\sum_i c_i M_i \langle R_g^2 \rangle_i}{\sum_i c_i M_i} \quad Equation 6$$

Gel content calculation

In order to evaluate the amount of gel retained by the 1 μ m filter, the whole peak from the concentration detector (refractive index detector) observed in SEC or AF4 separation was integrated using 0.13 as the value of dn/dc [29]. This gel content was called the "filtrate gel on 1 μ m" or Gel_{>1 μ}. In previous papers this quantity of aggregates (macro and micro) was called "total gel". However, as shown by Kim *et al.* [3] and as we will see later in this paper, a not insubstantial quantity of microaggregates passes through the 1 μ m filter. As a consequence, the real total gel (G_T) is:

$$G_T = Gel_{>111} + Gel_{<111} \quad Equation 7$$

Gel $_{1\mu}$ is the quantity of microaggregates with a size smaller than 1 μ m. Gel $_{1\mu}$ cannot be determined by SEC-MALS, except by treating the columns with tetrabutylammonium bromide (TBABr) as shown previously [3]. This procedure is rather cumbersome, whereas it will be shown that Gel $_{1\mu}$ can easily be estimated using AF4 analysis of NR samples. Indeed, by knowing the initial concentration of the sample before filtration, it is possible to determine from the fractogram (DRI signal) the concentration of the two populations in solution after filtration: polyisoprene chains and microaggregates smaller than 1 μ m.

230 Thus:

$$Gel_{>1\mu m} = \frac{c_1 \times 100}{c_0} \quad Equation \ 8$$

 $Gel_{<1\mu m} = \frac{c_2 \times 100}{c_0} \quad Equation 9$

Where C_0 is the initial concentration of the analysed sample, C_1 the concentration of the analysed sample passing through the 1 μ m filter (polyisoprene chains + microaggregates) and C_2 the concentration of only the microaggregates passing through the 1 μ m filter. C_1 can be determined either by SEC or AF4 by integrating the whole peak of the concentration detector (DRI). C_2 can be calculated only by AF4 integrating the part of the DRI peak containing microaggregates.

Results & Discussion

Qualitative description of fractograms

SEC-MALS profiles for the different samples are presented in Figure 1. M_w variations started with a linear decrease corresponding to a normal elution from large chains to small chains but displayed a deviation of the slope of this curve for samples containing gel (i.e. Nippol, M121 and M160, figure 1B, C & D). As described in the introduction and as previously detailed [3], SEC separation of rubber generally presents this abnormal elution due to co-elution of delayed large macromolecules, assumed to be microaggregates ($GEL_{<1\mu}$), with the small chains of poly(cis-1,4-isoprene). This particular elution was highlighted when either a change or an inversion of the slope presenting the variation in weight-average molar mass versus elution volume occurred. Regarding the detectors, the differential refractive index (DRI) signal during the SEC elution profile corresponded to a main Gaussian peak (with slight backtailing) for Nippol and M121, and to a bimodal molar mass distribution for the IR307 and M160 samples. The LS signal was more unimodal with back-tailing varying depending on the sample.

Figure 1

Unlike SEC, AF4 fractionated the macromolecules from small to large ones and the peak shapes appeared quite different. For poly(*cis*-1,4-isoprene) with gel (i.e. Nippol 2200, M160 and M121), the shape of the LS fractograms did not correspond to a Gaussian peak. The fractograms displayed a long front tailing, (i.e. a long and low signal increase) and an abrupt increase in the LS signal from 25 to 30 min (corresponding to a crossflow ranging from 0.5 to

0.3 mL.min⁻¹) (Figure 2). For the IR307 sample, the fractogram exhibited a clearly less pronounced increase in the LS signal (Figure 2A). As the IR307 sample did not contain gel, unlike the Nippol 2200 sample, this abrupt increase in the signal was due to microaggregates, as observed by Andersson et al. [30] for AF4 analysis of ethylhydroxyethyl cellulose. For the refractive index detector signal, the behaviour was unfamiliar, with a first peak close to void volume (elution starting at 7 min), corresponding to small chains, followed by either a slight increase in the concentration signal (for IR 307), or a decrease (for Nippol 2200), or quite a constant signal up to the end of the peak (for the two natural samples) (Figure 2). With both the DRI and LS detectors, the fractograms gave a continuous elution whatever the entities eluting, be they random coil or compact microaggregates (sphere-like). However, the evolution of the molar masses (M_{wi}) in line with the elution time was not linear from a qualitative viewpoint (Figure 2). For the IR307 sample, Figure 2A shows a change in slope for an elution time of 17-18 min ($M_{wi} \approx 600 \text{ kg mol}^{-1}$). A clear decrease in the variability of the measured R_{gi} was observed from this elution time ($t_e = 17-18$ min) (Figure 2). Indeed, for the first 18 minutes of the fractogram, Rgi values were very dispersed whatever the samples analysed using Berry 2 formalism (Figure 2), compared to SEC-MALS. This high dispersion of R_{gi} may have occurred because the concentrations of the injected solutions were too low (\approx 1 mg.mL⁻¹) for LS detection or because there was a lack of resolution for small molecule fractionation under our AF4 conditions. This initial slope change in M_{wi} was observed for other samples at times that varied depending on the sample (from 13 up to 17 min). With the Nippol sample, a second marked change appeared in the Mwi slope at an elution time of about 31 min (Figure 2B). This abrupt slope change was accompanied by a dramatic increase in the LS signal due to huge entities eluting ($250 < R_{gi} < 1000$ nm). This second change in the M_{wi} slope in line with the elution time was not visible for the other synthetic polyisoprene

267

268

269

270

271

272

273

274

275

276

277

278

279

280

281

282

283

284

285

286

287

288

289

290

(IR307), but was visible to a lesser extent for the two NR samples (M121 and M160) at an elution time of about 26-27 min (Figure 2C & D).

293

291

292

294 *Figure 2*

295

296

297

298

299

300

301

302

303

304

305

306

307

308

309

310

311

312

313

314

315

The M_{wi} AF4 profile for IR 307 confirmed the presence of only one population of chains with a M_{wi} ranging from 60,000 g.mol⁻¹ to 5 million g.mol⁻¹ (Figure 2A). Conversely, the Nippol AF4 profile clearly showed the presence of 2 distinct populations (Figure 2B). The first population was composed of isolated polyisoprene chains and the second one (starting at 32 min) was composed of microaggregates with sizes under 1 µm (Gel<14) with a drastic increase in the M_{wi} slope. For the two NR samples (M121 and M160) (Figure 2C and 2D), the M_{wi} profiles were quite different from that for Nippol. Isolated polyisoprene chains seemed to elute first up to about 27 min. After this elution time, the M_{wi} profile exhibited an increase in slope (from 27 to about 35 min), reaching a quasi-plateau (from 35 min). This behaviour suggests that this population was quite monodisperse. These two parts could be attributed to co-elution of isolated polyisoprene chains and $Gel<_{1\mu}$ in the first case and $Gel<_{1\mu}$ only for the plateau. Large differences were observed for the Mwi=f(Ve) and Rgi=f(Ve) slopes, the sizes (Rgi) and the molar masses (M_{wi}) of the second populations for Nippol compared to the two natural polyisoprene samples (Figure 2). These results tend to confirm that the gel was not intrinsically the same for natural and synthetic polyisoprene. Indeed for NR, the radius for the $Gel \le_{1\mu}$ was about 150 nm for a molar mass close to 15 million g.mol⁻¹ whereas for Nippol for the same molar mass the radius was about 240 nm (i.e. 60% higher), as illustrated in Figure 3. Moreover, there was no "plateau effect" for Nippol compared to the NR samples. Thus, with a lower Rgi for the same Mwi, the microaggregates in the NR samples seemed more compact than in the Nippol synthetic polyisoprene. However, some of the difference observed in the slopes may have been due to an underestimation of $M_{\rm wi}$ for the microaggregates of the NR samples. Indeed, it cannot be ruled out that the dn/dc of NR microaggregates is not constant. Changes in the non-isoprene composition (lipids and/or proteins) of microaggregates cannot be excluded. A change in the proportion of non-isoprene compounds versus polyisoprene in the microaggregates could lead to a change in the dn/dc and so in the $M_{\rm wi}$ determined.

Figure 3

One of the main difficulties encountered with AF4 fractionation is to define a correct and unbiased integration range. For our data, the integration range for average molar mass and radius of gyration assessment was started when the Mwi and Rgi signals were stabilized (out of void peak influence) and stopped just before the end of the peak (shown as the red box in figure 4 for M160, for example). This choice of integration area was made in order to have results including almost all the peak surface and to avoid a decrease in repeatability for the AF4 results due to pre- and post-peak radius and mass dispersion and heterogeneity because of a low LS signal. This method was applied for the AF4 signals from IR307, M160 and M121. On the other hand, the treatment for Nippol 2200 was different. Indeed, the variation in M_{wi} in the second part of Nippol 2200 fractionation was quite high due to the presence of microaggregates with ultra high molar masses (over 10¹⁰ g mol⁻¹). Moreover, this final M_w increase was quite noisy and unrepeatable, probably due to the low associated RID signal. In fact, as presented in table 2 for example, increasing the Nippol 2200 integration range (from 9.5 - 35 min to 9.5 - 40 min), drastically increased the average molar masses, but also the standard deviation. Lastly, a 7% increase in RID integration area (hence in quantity) led to an increase of 4 orders of magnitude for the Mw and resulted in an increase in the standard

deviation from 25% to 71%. Consequently, for Nippol, the integration range was shortened, compared to the other samples, to avoid excessive variability in the results.

Table 2

In order to quantify aggregates exceeding 1 μ m (Gel $_{^{-1}\mu}$) (estimation of C_1 in eq. 9), the whole peak was integrated (green box in figure 4). The quantity of microaggregates smaller than 1 μ m (Gel $_{^{<1}\mu}$) (estimation of C_2 in eq. 10) was calculated according to a third integration range (the blue box in figure 4) starting from the middle of the zone we considered as a mixture of polyisoprene chains and microaggregates (data R_g =f(V_e)) up to the end of the peak.

Figure 4

Comparison of data between SEC-MALS and AF4-MALS

Average molar masses

 M_n , M_w and M_z were calculated from the SEC and AF4 results for each sample. The results are presented in Figure 5.

Figure 5

The number average molar mass M_n did not present significant differences whether determined by SEC or AF4 (Figure 5). The ratio of M_n obtained by AF4 to that obtained by SEC was ranged between 0.85 and 1.0. Unlike M_n , M_w and M_z were different, with a higher M_w and M_z obtained for AF4. As described previously, these larger M_w and M_z can be

explained by the presence of large microaggregates not observed with SEC. This observation is confirmed by the fact that for IR 307 (poly(*cis*-1,4-isoprene) without gel), M_w and M_z exhibited no significant difference between SEC and AF4 results. The difference between AF4 and SEC in terms of average molar masses was, as expected, higher for M_z than for M_w. The M_w ratios (M_{w-AF4}:M_{w-SEC}) ranged from 1.0 to 4.3 (for IR 307 and M121 respectively) whereas the M_z ratios (M_{z-AF4}:M_{z-SEC}) ranged from 1.0 to 18.6 (for IR 307 and Nippol respectively). For the three average molar masses considered (i.e. M_n, M_w or M_z), the AF4 results showed greater heterogeneity than for the SEC results, with high standard deviations. This lower reproducibility and repeatability was mainly due to the difficulty in defining the integration range, as previously explained, but also to the substantial variability generated by the refractive index detector baseline position. Indeed, the AF4 principle resulted in some noise, deviations and jumps in the DRI baseline and thus to some doubts / uncertainties on the baseline position, despite the blank subtraction. The large M_z difference (from AF4 to SEC) and RSD for Nippol was due to the large amount of microaggregates with ultra high molar masses and to the poor repeatability in the high mass range, as explained later on.

Determination of gel rates

The gel rates in the samples were calculated after SEC and AF4 analysis. $Gel_{>1\mu}$ was calculated for both the SEC and AF4 analyses whereas $Gel_{<1\mu}$ was only calculated after AF4 analysis. Figure 6 presents the $Gel_{>1\mu}$ rate after SEC and AF4 analyses. For the IR 307 and Nippol samples, the $Gel_{>1\mu}$ rate did not display any significant difference (no gel for IR307 and average $Gel_{>1\mu}$ slightly higher for Nippol with AF4). For the two NR samples, only M160 exhibited a significant difference in the $Gel_{>1\mu}$ rate between SEC and AF4 determination (23.8% for SEC and 17.2% for AF4). For M121, the lack of significant difference was due to the high variance of the AF4 result. The $Gel_{<1\mu}$ calculation was estimated at 9.5% for Nippol,

27% for M160 and 29% for M121 (no Gel $_{<1\mu}$ for IR 307). These large quantities of Gel $_{<1\mu}$ explained the large differences observed for M_w and M_z in the NR samples and the Nippol sample (higher M_w and M_z for AF4 analyses compared to SEC). However, as a result of such a large quantity of Gel $_{<1\mu}$ for the NR samples, assumed to be "lost" in not insubstantial proportions in SEC, the Gel $_{>1\mu}$ rate should have been much lower with AF4 compared to SEC for Nippol, M160 and M121. The slight difference observed between AF4 and SEC for the Gel $_{>1\mu}$ rate could be explained either by the large measurement variability for AF4, or by an overestimated Gel $_{>1\mu}$ calculation in AF4 analysis (potentially due to concentration peak area determination and therefore to blank subtractions). For the Gel $_{<1\mu}$ calculation, Kim *et al.* [3] obtained Gel $_{<1\mu}$ values close to 10% (calculated by SEC after ionic surfactant treatment of the columns) for NR samples similar to M160 and M121, meaning a difference with our Gel $_{<1\mu}$ values of about 15%.

Figure 6

Comparison of radii of gyration

As for the average molar masses, the R_g values obtained with AF4 were higher than those obtained with SEC, except for the IR307 sample, whose R_g was the same for both separation techniques (see table 3). Nevertheless, the differences in R_g obtained with the two techniques were less pronounced than for M_z . This was due to the narrower radius of gyration size range observed (typically varying from 20 to 200 nm) compared to the 10^2 - 10^3 order of magnitudes for the masses over the whole fractionation (up to 10^5 for Nippol). The variation in R_{gi} depending on the elution time with AF4 displayed a similar behaviour to that for M_{wi} (Figure 2). As the variation in R_{gi} was less significant than for M_{wi} , it implies that the material was becoming increasingly compact (greater increase for masses than for radii) towards the

end of the elution, especially for the second population, as previously illustrated in figure 3.
This observation confirms the presence of compact microaggregates highlighted by Kim *et al*.
[3].
Table 3

Conclusions

This work demonstrates the ability of AF4 to fractionate natural and synthetic poly(cis-1,4-isoprene). Distinct populations (characterized by a clear slope change in M_{wi} variation) corresponding to isolated polyisoprene chains and microaggregates smaller than 1 μ m (Gel $_{<1}\mu$) were detected. Average molar masses were determined and compared with those obtained by SEC. Similar M_n values were obtained but large differences were observed for M_w and M_z . These differences could be explained by a microgel population observed in AF4 but not during SEC separation. Moreover, microaggregates in the NR samples exhibited quite a different structure, appearing more compact than the microaggregates in the Nippol synthetic polyisoprene. Some problems (difficulties in defining the baseline, DRI signal jumps, etc.) due to the use of DRI with AF4 were encountered, in particular for gel rate determination. It seems obvious that some analytical developments are needed to optimize fractionation, increase the resolution for small polyisoprene chains and enable better reproducibility. However, these results are promising and microgel (Gel $_{<1}\mu$) can be considered for further individual studies and physico-chemical characterization.

Acknowledgements

The authors gratefully thank Emilie Croizat and Christine Char for their valuable contribution to this project. A4F-MALS and SEC-MALS analyses were carried out on the LipPol-Green platform (http://www.supagro.fr/plantlippol-green/). We kindly thank CIRAD DRS and Agropolis fondation (http:// http://www.agropolis-fondation.fr) for financial support, and the Hubert Curien Programme for funding Miss Chalao Thepchalerm's scholarship.

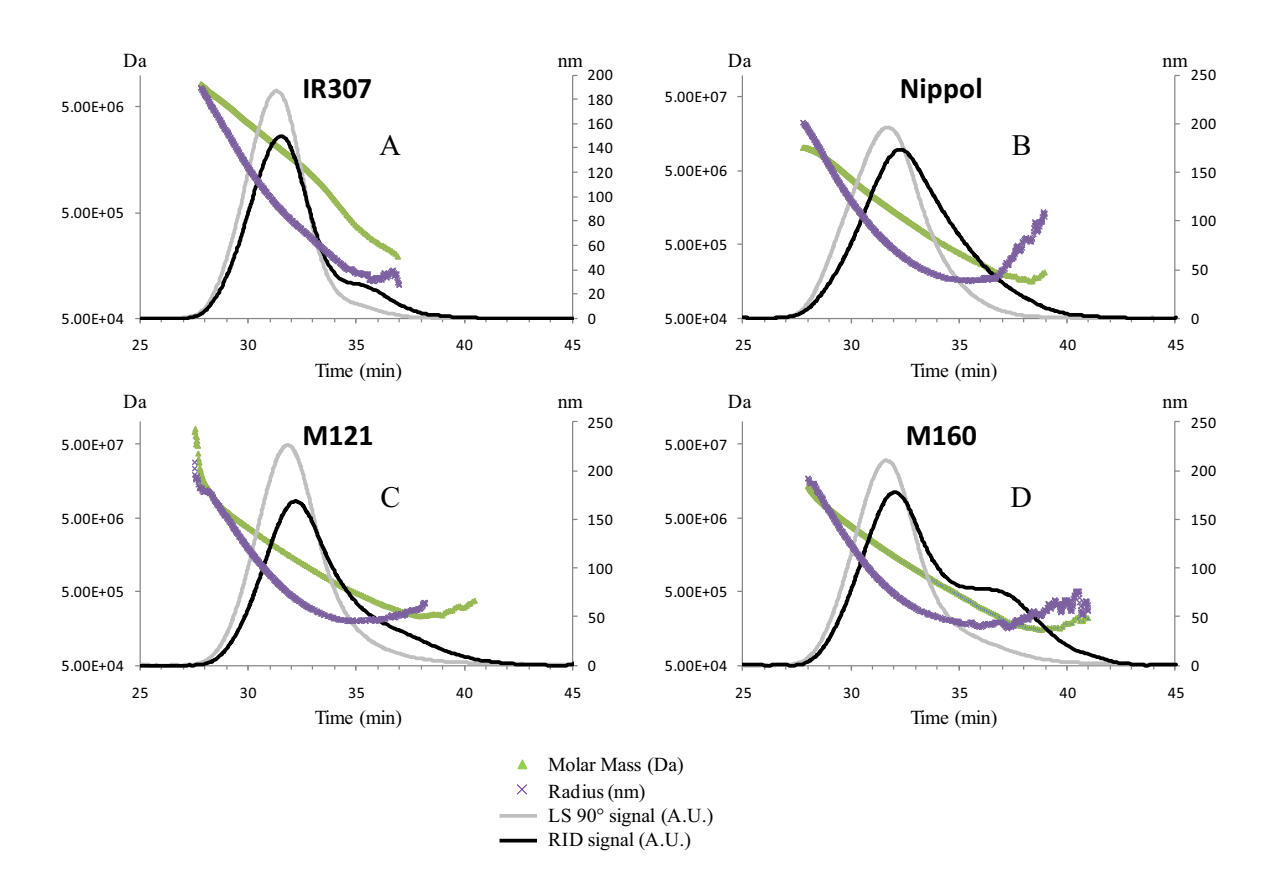
445 **References**

- 446
- 447 [1] Hongsheng Liua, Fengwei Xiea, Long Yua, Ling Chena, L. Li, Prog. Polym. Sci. 34
- 448 (2009) 1348.
- 449 [2] L. Vaysse, F. Bonfils, P. Thaler, J. Sainte Beuve, in D.R. Höfer (Editor), Sustainable
- Solutions for Energy Generation, Royal Society of Chemistry, Cambridge, 2009, p.
- 451 335.
- 452 [3] C. Kim, M. Morel, J. Sainte Beuve, A. Collet, S. Guilbert, F. Bonfils, J. Chromatogr.
- 453 A 1213 (2008) 181.
- 454 [4] C. Kim, J. Sainte Beuve, S. Guilbert, F. Bonfils, Eur. Polym. J. 45 (2009) 2249.
- 455 [5] Angulo-Sanchez JL, Caballero-Mata P, Rubber Chem. Technol. 54 (1981) 34.
- 456 [6] K.N.G. Fuller, W.S. Fulton, Polymer 31 (1990) 609.
- 457 [7] J. Tangpakdee, Y. Tanaka, J. Rubber Res. 1 (1998) 14.
- 458 [8] S.N. Gan, J. Membrane Sci., Pure Applied Chemistry A33 (1996) 1939.
- 459 [9] J. Tangpakdee Sakdapipanich, T. Kowitteerawut, K. Suchiva, Y. Tanaka, Rubber
- 460 Chem. Technol. 72 (1999) 712.
- 461 [10] F. Ngolemasango, E. Ehabe, C. Aymard, J. Sainte-Beuve, B. Nkouonkam, F. Bonfils,
- 462 Polym. Int. 52 (2003) 1365.
- 463 [11] Y. Tanaka, L. Tarachiwin, Rubber Chem. Technol. 82 (2009) 283.
- 464 [12] S. Amnuaypornsri, J. Sakdapipanich, S. Toki, B.S. Hsiao, N. Ichikawa, Y. Tanaka,
- 465 Rubber Chem. Technol. 81 (2008) 753.
- 466 [13] J. Carretero-Gonzalez, T. A. Ezquerra, S. Amnuaypornsri, S. Toki, R. Verdejo, A.
- Sanz, J. Sakdapipanich, B.S. Hsiaod, M.A. Lopez–Manchadoa, Soft Matter 6 (2010)
- 468 3636.

- 469 [14] F.A. Messaud, R.D. Sanderson, J.R. Runyon, T. Otte, H. Pasch, S.K.R. Williams,
- 470 Prog. Polym. Sci. 34 (2009) 351.
- 471 [15] R. Qureshi, W. Kok, Anal. Bioanal. Chem. 399 (2011) 1401.
- 472 [16] G. Lespes, J. Gigault, Anal. Chim. Acta 692 (2011) 26.
- 473 [17] L.J. Gimbert, K.N. Andrew, P.M. Haygarth, P.J. Worsflod, Trends Anal. Chem. 22
- 474 (2003) 615.
- 475 [18] S. Dubascoux, I. Le Hecho, M. Hassellov, F. Von der Kammer, M.P. Gautier, G.
- 476 Lespes, J. Anal. At. Spectrom. 25 (2010) 613.
- 477 [19] M.E. Schimpf, K.D. Caldwell, G.J. C., Field Flow Fractionation Handbook, Wiley
- 478 Interscience, 2000.
- 479 [20] W.-S. Kim, C.H. Eum, A. Molnar, J.-S. Yu, S. Lee, Analyst 131 (2006) 429.
- 480 [21] W.G. Fulton, SA, J. Nat. Rubber Res. 12 (1997) 154.
- 481 [22] S. Lee, C. Eum, A. Plepys, B. Korean Chem. Soc. 21 (2000) 69.
- 482 [23] S. Lee, A. Molnar, Macromolecules 28 (1995) 6354.
- 483 [24] D.Y. Bang, D.Y. Shin, S. Lee, M.H. Moon, J Chromatogr. A 1147 (2007) 200.
- 484 [25] C. Kim, M. Morel, J. Sainte Beuve, S. Guilbert, F. Bonfils, Polym. Eng. Sci. 50 (2010)
- 485 240.
- 486 [26] M. Andersson, B. Wittgren, K.-G. Wahlund, Polymer 46 (2003) 4279.
- 487 [27] I. Teraoka, Polymer Solutions: An Introduction to Physical Properties, New York,
- 488 2002.

492

- 489 [28] P.J. Wyatt, Anal. Chim. Acta 272 (1993) 1.
- 490 [29] C. Kim, A. Deratani, F. Bonfils, J. Liq. Chromatogr. Relat. Technol. 33 (2010) 37.
- 491 [30] M. Andersson, B. Wittgren, K.G. Wahlund, Anal. Chem. 73 (2001) 4852.



 $\label{eq:Figure 1: Chromatograms (from the RID and LS detector at 90°) and variation in R_g and M_i \\ depending on the elution time during SEC analysis$

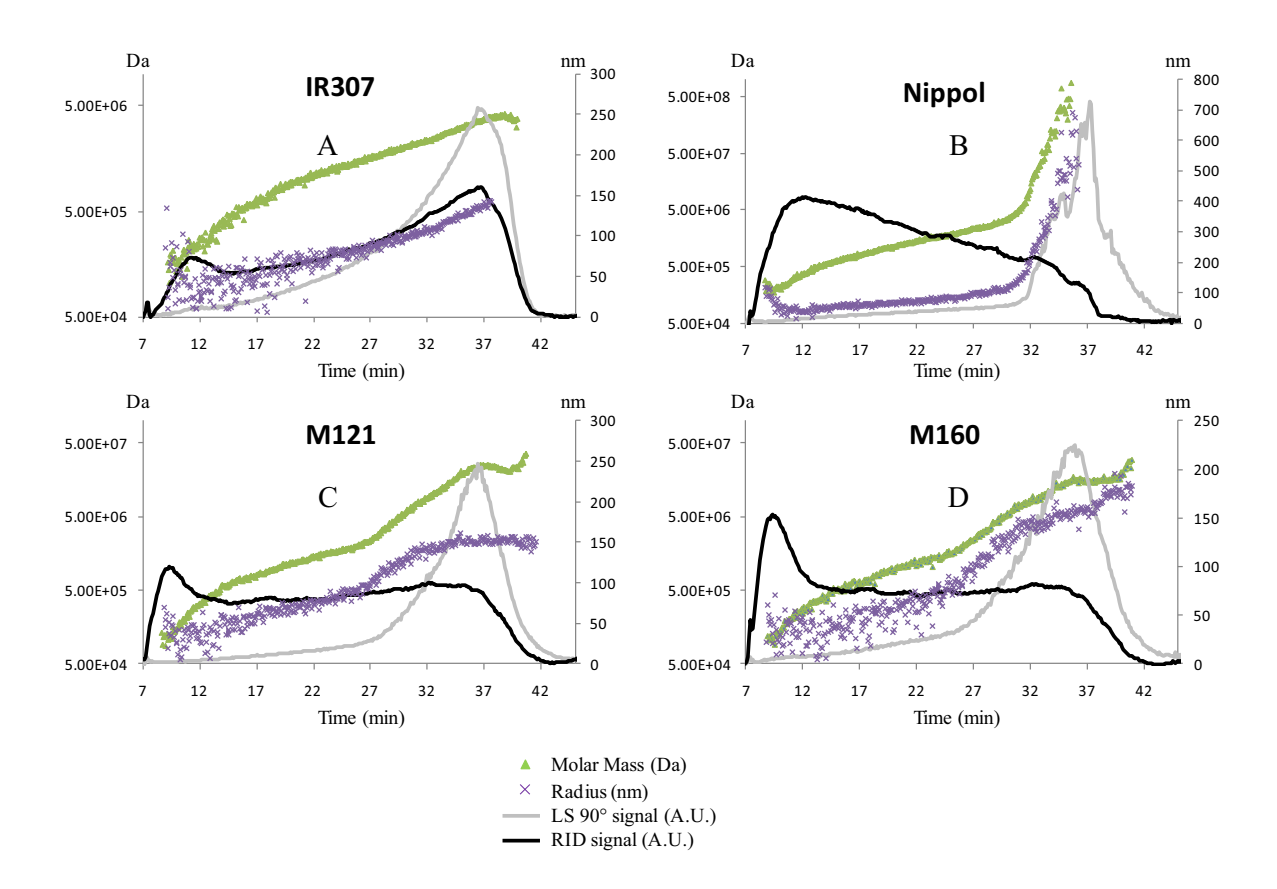


Figure 2: Fractograms (from the RID and LS detector at 90°) and variation in R_g and M_i depending on the elution time during AF4 analysis

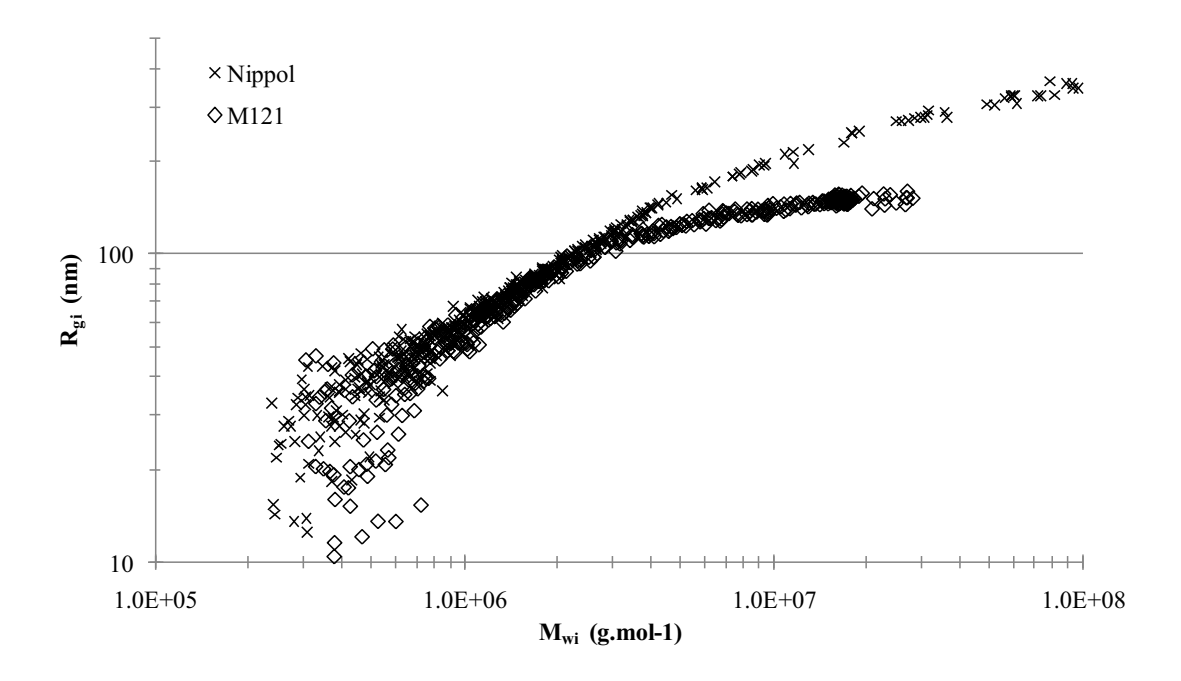


Figure 3: Variation of the radius of gyration (R_{gi}) depending on molar masses (M_{wi}) for the Nippol 2200 and M121 samples.

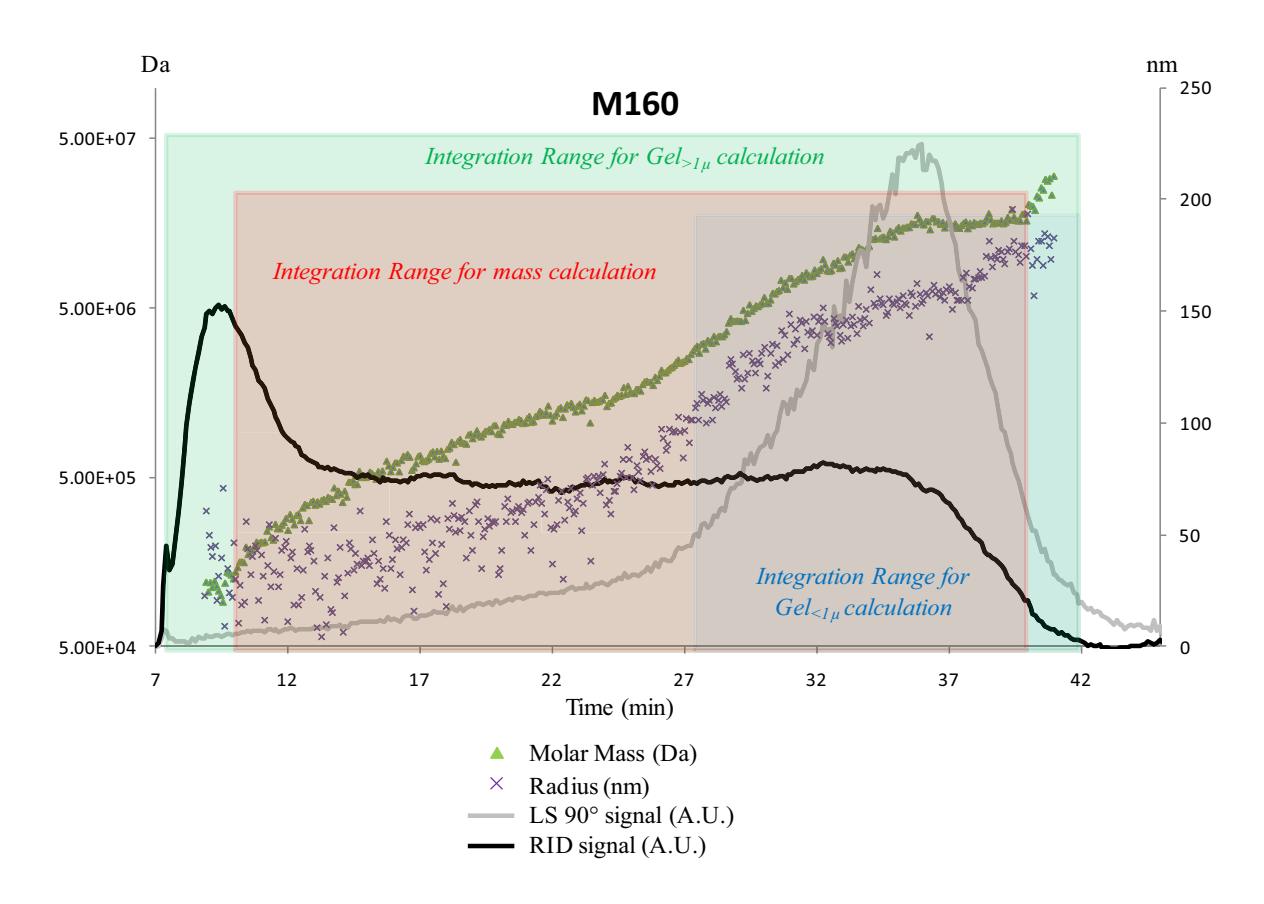


Figure 4: Determination of the AF4 integration range for the M160 sample

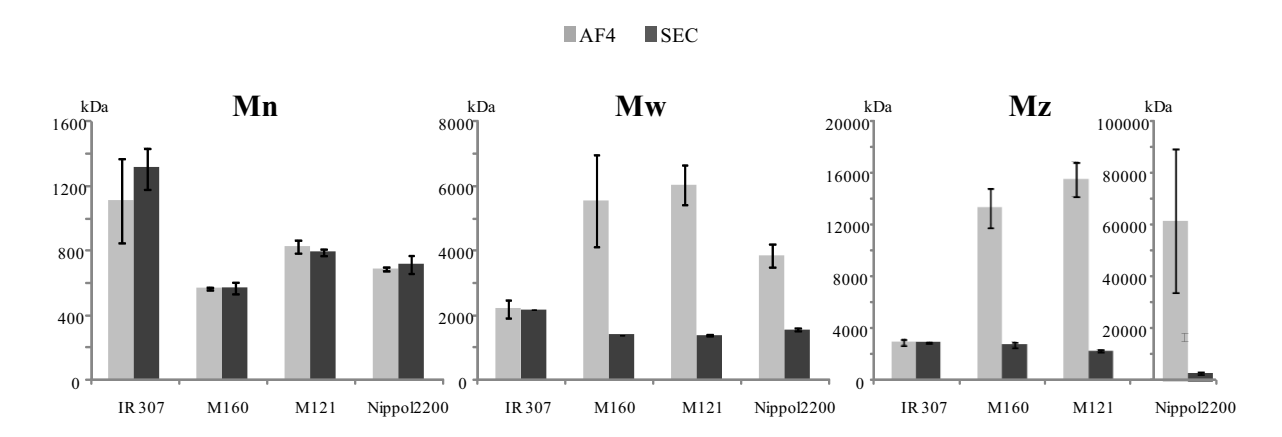


Figure 5: Comparison of masses obtained by SEC and AF4

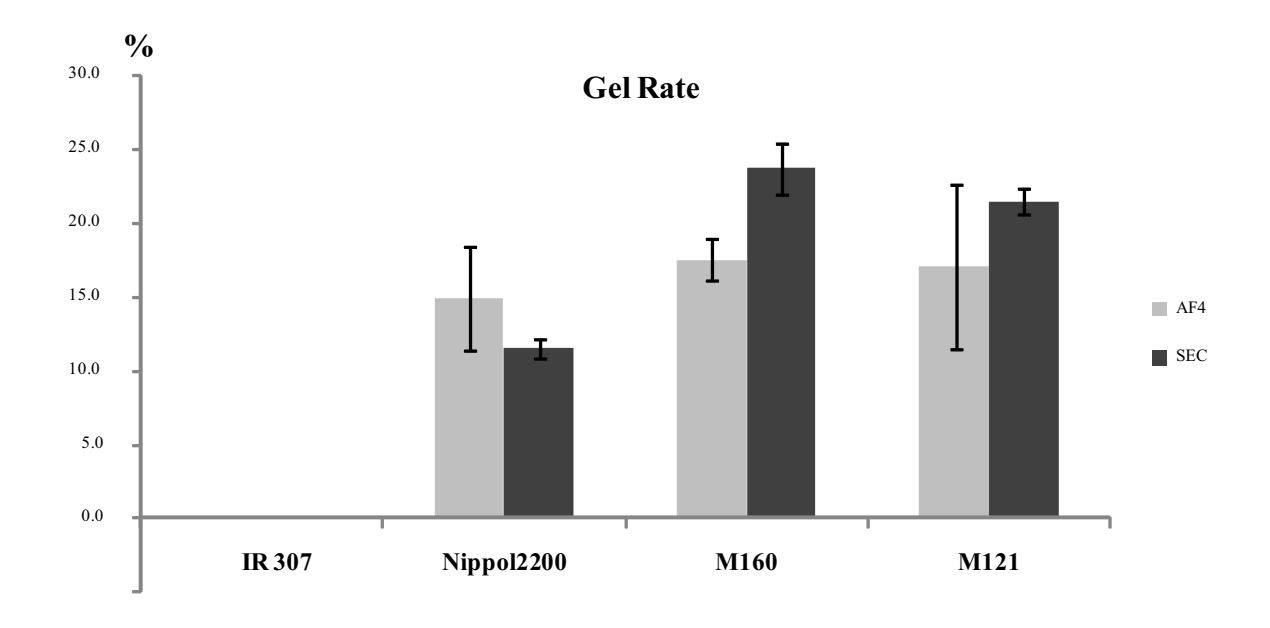


Figure 6: Comparison of filtrate gel on 1 μm (Gel $_{^{>1}\mu}$) rate calculated by AF4 and SEC

Step	Duration (min)	Crossflow (mL.min ⁻¹)	Type of rate		
1	1.5	1	Constant		
2	30	From 1 to 0.08	Linear		
3	9	0.08	Constant		
4	7	0	Constant		

 Table 1: AF4 crossflow programme during elution

Tables 2

	integration start	integration end	M _n (Da)	RSD	M _w (Da)	RSD	Mz (Da)	RSD	
Nippol	9.5 min	35 min	6.95E+05	4%	3.61E+06	25%	4.24E+07	62%	Integration :+7%
2200	9.5 min	40 min	7.48E+05	4%	9.36E+10	71%	1.40E+14	81%	of surface area

Table 2: Nippol 2200 mass calculation (M_n , M_w and M_z with respective RSD from one AF4 series) with different integration ranges

		R _g (nm)	SD (nm)	CV
ID207	AF4	115.8	3.8	4.0%
IR307	SEC	112.1	1.4	1.3%
Nippol	AF4	249.9	28.8	28.8%
	SEC	108.5	4.2	3.9%
M160	AF4	136.5	7.0	4.3%
	SEC	102.8	2.3	2.2%
M121	AF4	133.5	7.8	3.4%
	SEC	92.5	2.4	2.6%

⁽¹⁾ SD: standard deviation, CV: coefficient of variation ((SD/mean) x 100)

Table 3: $R_{\rm g}$ determined by AF4 and SEC

Elsevier Editorial System(tm) for Colloids and Surfaces B: Biointerfaces Manuscript Draft

Manuscript Number:

Title: Surface-quaternized chitosan particles as an alternative and effective organic antibacterial filler

Article Type: Full Length Article

Keywords: chitosan; particle; heterogeneous quaternization; minimum inhibitory concentration.

Corresponding Author: Dr. Voravee Hoven, Ph.D.

Corresponding Author's Institution: Chulalongkorn University

First Author: Oraphan Wiarachai, MS

Order of Authors: Oraphan Wiarachai, MS; Nuttha Thongchul, PhD; Suda Kiatkamjornwong, PhD; Voravee Hoven, Ph.D.

Abstract: Taking advantage of the large surface area that is covered with permanent positive charges of quaternary ammonium entities, this research aimed to develop environmentally friendly, organic antibacterial fillers from quaternized chitosan particles that may be applicable for biomedical devices, health and textile industries. The particles were formulated by ionic crosslinking of chitosan with tripolyphosphate followed by quaternization that was conducted under heterogeneous condition via either direct methylation or reductive N-alkylation with a selected aldehyde followed by methylation. Sub-micron, spherical, and positively charged quaternized chitosan particles were formed, as determined by 1H-NMR, FT-IR, PCS, and TEM analysis. Antibacterial activity tests performed by viable cell counts suggested that all quaternized chitosan particles exhibited superior antibacterial activity against the model Gram-positive bacteria, S.aureus, as compared to the native chitosan particles at neutral pH. Only some quaternized chitosan particles, especially those having a high charge density and bearing large alkyl substituent groups, were capable of suppressing the growth of the model Gramnegative bacteria, E. coli. The inhibitory efficiency of the quaternized chitosan particles was quantified in terms of the minimum inhibitory concentration (MIC).



June 12, 2011

Dear Sir/Madam:

I would like to send a manuscript, entitled "Surface-quaternized chitosan particles as an alternative and effective organic antibacterial filler" to be considered for publication as a full paper in Colloids and Surfaces B: Biointerfaces. On behalf of all authors, namely, Oraphan Wiarachai, Nuttha Thongchul, Suda Kiatkamjornwong, Voravee P. Hoven, I hereby confirm that this manuscript or its contents in some other form has not been published previously by any of the authors and/or is not under consideration for publication in another journal at the time of the submission.

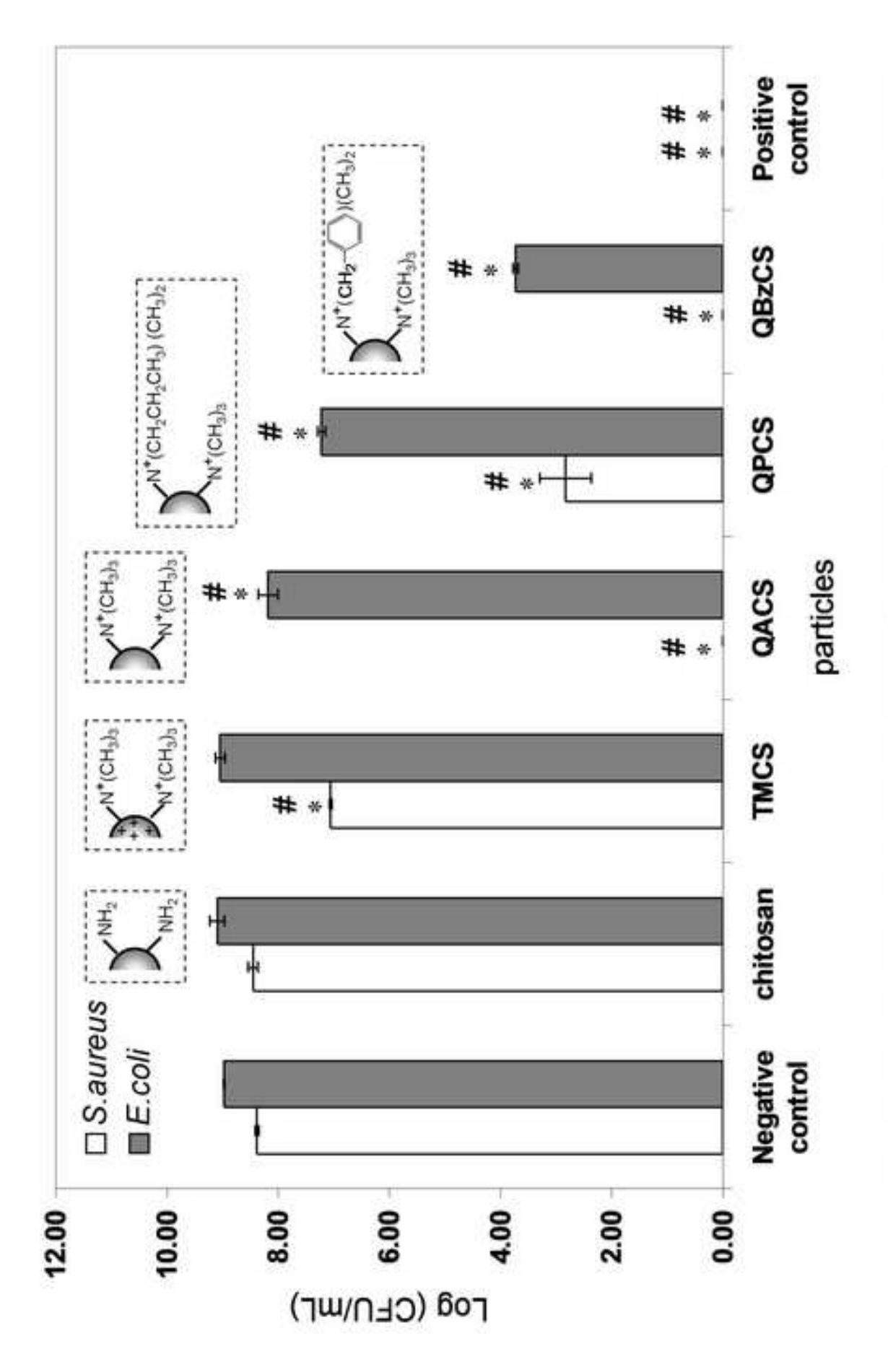
This work introduces surface-quaternized chitosan particles as an effective, environmentally friendly, organic antibacterial filler that may be incorporated into materials that require antibacterial activity. Based on the minimum inhibitory concentration, it was found that some surface-quaternized chitosan particles are more effective in inhibiting the bacterial growth than the quaternized chitosan solution. The fact that the heterogeneous quaternization used for the preparation of surface-quaternized chitosan particles can simply be done without the requirement for tedious purification process opens up an opportunity to produce such effective antibacterial filler at a large scale and that is very beneficial from industrial perspective.

The authors believe that the content of this contribution would be of interest to **Colloids and Surfaces B: Biointerfaces** audiences. Should there be any further information which may be required or if any problems arise, please contact me at the address shown below.

Sincerely yours,

Vp. Horeen

Voravee P. Hoven, Ph.D. Corresponding Author



[*p < 0.01 (compared with the negative control), "p < 0.01 (compared with the chitosan particles)]

Research highlights

- Quaternized chitosan particles prepared by heterogeneous quaternization exhibited significantly higher antibacterial activity against *S. aureus* (Gram positive bacteria) and *E. coli* (Gram negative bacteria) than the particles prepared by homogeneous quaternization.
- Only some quaternized chitosan particles, especially those having a high charge density and bearing a large alkyl substituent, were capable of suppressing the growth of *E. coli*, the Gram-negative bacteria.

Surface-quaternized chitosan particles as an alternative and effective organic antibacterial filler

Oraphan Wiarachai^{a,b}, Nuttha Thongchul^c, Suda Kiatkamjornwong^d, Voravee P. Hoven^{e*}

^a Program in Petrochemistry and Polymer Science, Faculty of Science, Chulalongkorn University, Phayathai Road, Pathumwan, Bangkok 10330, Thailand

^b Center for Petroleum, Petrochemicals, and Advanced Materials, Chulalongkorn University, Phayathai Road, Pathumwan, Bangkok 10330, Thailand

^c Institute of Biotechnology and Genetic Engineering, Chulalongkorn University, Phayathai Road, Pathumwan, Bangkok 10330, Thailand

^d Department of Imaging and Printing Technology, Faculty of Science, Chulalongkorn University, Phayathai Road, Pathumwan, Bangkok 10330, Thailand

^e Organic Synthesis Research Unit, Department of Chemistry, Faculty of Science, Chulalongkorn University, Phayathai Road, Pathumwan, Bangkok 10330, Thailand

* Corresponding author. Tel: +66-2218-7626-7 ext 102; fax: +66-2218-7598 E-mail address: vipavee.p@chula.ac.th.

ABSTRACT

Taking advantage of the large surface area that is covered with permanent positive charges of quaternary ammonium entities, this research aimed to develop environmentally friendly, organic antibacterial fillers from quaternized chitosan particles that may be applicable for biomedical devices, health and textile industries. The particles were formulated by ionic crosslinking of chitosan with tripolyphosphate followed by quaternization that was conducted under heterogeneous condition via either direct methylation or reductive Nalkylation with a selected aldehyde followed by methylation. Sub-micron, spherical, and positively charged quaternized chitosan particles were formed, as determined by ¹H-NMR. FT-IR, PCS, and TEM analysis. Antibacterial activity tests performed by viable cell counts suggested that all quaternized chitosan particles exhibited superior antibacterial activity against the model Gram-positive bacteria, S.aureus, as compared to the native chitosan particles at neutral pH. Only some quaternized chitosan particles, especially those having a high charge density and bearing large alkyl substituent groups, were capable of suppressing the growth of the model Gram-negative bacteria, E. coli. The inhibitory efficiency of the quaternized chitosan particles was quantified in terms of the minimum inhibitory concentration (MIC).

Keywords: chitosan; particle; heterogeneous quaternization; minimum inhibitory concentration

1. Introduction

Incorporation of antibacterial fillers is an efficient approach to introduce antibacterial activity to materials. There are many types of filler that can be incorporated into the materials to induce their antibacterial activity such as antibiotic [1], nitric oxide [2], halogen species [3, 4], biocide [5] and heavy metal [6-8]. From several types of antibacterial fillers, heavy metal in the form of silver nanoparticles (AgNPs), are well recognized to exhibit an effective antibacterial activity and are widely used in many applications such as medical devices [9], paint [10], coating [11] and textiles [12]. Recently, it has been reported that the AgNPs could affect human tissues from diverse routes of exposure including the respiratory system, skin, and gastrointestinal tract [13]. It has been proposed that AgNPs may interact with thiol groups of proteins and enzymes within mammalian cells, some of which are key components in the antioxidant defense mechanism of the cell. Inhibition of this mechanism would then result in an increase in the concentration of reactive oxygen species that can alter or damage the function of the cells. Also, it has been found that the AgNPs can be released from commercial clothing (socks) into the wash water [14], and so could increase the risk of environmental contamination. Therefore, it is highly desirable if the antibacterial fillers can be developed from natural, nontoxic and environmentally friendly material.

Chitosan is a natural biopolymer derived from the deacetylation of chitin, an abundantly available biopolymer found in the exoskeletons of insects, the shell of crustaceans, and fungal cell walls. It is nontoxic, biodegradable, biocompatible and possesses antibacterial properties [15]. In fact, the potential of chitosan particles as an effective antibacterial agent/filler has been realized and continuously reported. Early work by Qi and co-workers demonstrated that chitosan in the form of nanoparticles exerted a higher antibacterial activity against *E. coli, S. choleraesis, S. typhimurium, and S. aureus* than chitosan solution, and it was proposed that the greater surface area of the particles provided a

more intimate contact with the surface of bacterial cells [16]. Ye and co-workers, on the other hand, have shown that cotton fabrics coated with core-shell particles, having poly(*n*-butyl acrylate) as the core and chitosan as the shell, exhibited an excellent antibacterial activity against *S. aureus* with a reduction in viable bacteria numbers of more than 99% [17].

In general, chitosan would exhibit its antibacterial activity only in acidic medium, due to the poor solubility of chitosan above its pKa (pH 6.5). Quaternization of the amino groups to introduce permanent positively charged quaternary ammonium groups has been recognized as a potential way to enhance the antibacterial activity of chitosan over a broader pH range. The reaction can simultaneously introduce the permanent positive charge and hydrophobicity, the two parameters that are believed to affect the antibacterial activity [18-20]. Synthetic routes and applications of quaternized derivatives of chitosan have been recently reviewed and published [21, 22], whilst the application of quaternized chitosan particles has been reported. For example, particles fabricated from chitosan that was formerly quaternized by hexyl bromide were incorporated as bactericidal fillers in poly(methyl methacrylate) bone cement and tested against *S. aureus* and *S. epidermidis* under a neutral pH environment [23].

In order to promote ionic interactions with the negatively charged components of the bacterial cell membrane, the incorporation of metal ions [24-26] or cationic polymer [27] into chitosan particles has also been recently reported as an alternative approach. Qi and coworkers have suggested that the antibacterial activity can be enhanced by incorporating Cu²⁺ into chitosan particles [25]. Later, Du and co-workers have shown that chitosan particles loaded with various metal ion such as Ag⁺, Cu²⁺, Zn²⁺, Mn²⁺, Fe²⁺, exhibited higher antibacterial effect against *E. coli*, *S. choleraesuis*, and *S. aureus* than chitosan particles [24, 26]. In addition, Inphonlek and coworkers have found that core-shell nanoparticles having poly(methyl methacrylate) core coated with polyethyleneimine, and chitosan-mixed-

polyethyleneimine shells exhibited higher antibacterial activity against *S. aureus* and *E. coli* than chitosan nanoparticles [27].

Here in this research, we attempt to develop an environmentally friendly, organic antibacterial filler from chitosan particles. The permanent positive charges in the form of quaternary ammonium groups were introduced to the surface of pre-fabricated chitosan particles under heterogeneous condition via direct methylation or reductive *N*-alkylation using two different aldehydes, propionaldehyde and benzaldehyde, followed by methylation with methyl iodide. This method has the advantage that it can be performed conveniently in the absence of tedious purification process that is generally required for homogeneous quaternization. The success of this type of method for enhancing antibacterial activity especially in a neutral pH environment has been previously reported for the chitosan films [28]. And the fact that the addition of cationic metal species or polymers is no longer necessary truly simplifies the fabrication method.

2. Materials and methods

2.1. Materials

Chitosan flake (DAC 85%, $M_V = 45,000$ Da) was purchased from Seafresh Chitosan (Lab) Co., Ltd (Thailand). Propionaldehyde, methyl iodide (CH₃I), sodium borohydride (NaBH₄), sodium chloride (NaCl), sodium hydroxide (NaOH), sodium iodide (NaI) and tripolyphosphate (TPP) were purchased from Fluka (Switzerland). Acetic acid, benzaldehyde, ethanol (EtOH), and methanol (MeOH) were purchased from Merck (Germany). Dialysis membrane (cut-off molecular weight of 12,400 g/mol) was purchased from Sigma (USA). All reagents and materials were of analytical grade and used without further purification. *E. coli* and *S. aureus* were provided by National Center for Genetic Engineering and Biotechnology (BIOTEC), Thailand. Mueller-Hinton agar (MHA) and Mueller-Hinton broth (MHB) were

purchased from Difco (USA). Mueller Hinton agar plates were supplied by Department of Medical Science, Ministry of Public Health, Thailand. Ultrapure distilled water was obtained after purification using a Millipore Milli-Q system (USA) that involves reverse osmosis, ion exchange, and a filtration step.

2.1. Preparation of surface-quaternized chitosan particles

Chitosan particles were prepared using TPP as a crosslinking agent according to the published procedure by Qi *et al.* [16] Preparation of quaternized *N*-alkyl chitosan particles were done following the method of Vallapa *et al.* [28]. In brief, an anhydrous methanol solution of a selected aldehyde (10 mL) having a desired concentration was added into a flask containing chitosan particles (0.03 g). After stirring for a given time at ambient temperature (~28-30°C), NaBH₄ (0.3 g, 0.8 mol) was added into the reaction mixture and the solution was stirred for 24 h. The resulting *N*-alkyl chitosan particles were then isolated by centrifugation at 12,000 rpm for 30 min. The supernatant was discarded and the particles were centrifugally washed as above with methanol three times and then dried *in vacuo*. An anhydrous methanol solution (10 mL) containing NaI (0.30 g, 2 mmol) and NaOH (0.13 g, 3 mmol) was then added into a flask containing chitosan or *N*-alkyl chitosan particles (0.03 g) and CH₃I was then added via syringe. The reaction mixture was stirred at 50°C for a given time. The particles were isolated and purified as above mentioned.

2.2. Characterization of surface-quaternized chitosan particles

Fourier Transform-Infrared (FT-IR) spectra were collected using a Nicolet Impact 410 FT-IR spectrometer. All samples were prepared as KBr pellets. All ¹H NMR spectra were recorded in a 1% (v/v) solution of CF₃COOH/D₂O or D₂O using a Varian model Mercury-400 nuclear magnetic resonance spectrometer (USA) operating at 400 MHz. Chemical shifts

(δ) are reported in parts per million (ppm) relative to tetramethylsilane (TMS) or using the residual protonated solvent signal as a reference. The size and the morphology of all particles were examined by transmission electron microscope (TEM, Model JEM-2100, Japan) with the average diameter calculated using Semafore software and reported from the measurement of 100 randomly selected particles. The ζ -potential values of the particles were determined using a Nanosizer Nano-ZS (Malvern Instruments, UK) at 25°C with a scattering angle of 173°. All data are displayed as the mean \pm one standard deviation and are derived from at least three independent experiments. The data were calculated using the Helmholtz-Smoluchowski equation.

2.8. Evaluation of antibacterial activity

All glasswares used for the tests were sterilized in an autoclave at 121 °C for 15 min prior to use. All particles were sterilized by exposing to UV radiation for 60 min prior to the tests. The antibacterial test was performed according to a modified method of Qi *et al.* [16]. Chitosan and quaternized chitosan particles (2.5 mg) were added to 5 mL of MHB in test tubes and aseptically inoculated with 50 μ L of the freshly prepared bacterial suspension in distilled water (OD₆₀₀ = 0.5). The pH of the broth was about 7.4. The negative and positive controls were a broth solution alone and a broth solution with ampicillin (50 mg/mL), respectively. After mixing, broth cultures were incubated at 37 °C in a shaking incubator (Model G-25, New Brunswick Scientific Co., Inc., USA), at 110 rpm for 24 h. Then, 100 μ L of the bacterial solution was removed and 10-fold serially diluted down to 10⁶-fold the original level. A 100 μ L aliquots of each diluted bacterial suspension was then spreaded onto the MHA plates for total plate counting. After incubating at 37 °C for 18 h, the number of colonies, and thus replication competent bacteria, were then counted as a measure of the

assumed viable number of bacteria. The results after correction for the dilution factor were expressed as mean colony forming units per volume (CFU/mL).

To determine the minimum inhibitory concentration (MIC) of all particles, the particles were first suspended in 5 mL of MHB and two-fold serial dilutions prepared. Each set of serial dilutions was then inoculated under aseptic conditions with 50 μ L of the freshly prepared bacterial suspension in distilled water (OD₆₀₀ = 0.5). After incubating at 37 °C for 24 h, the total plate count enumeration of the CFU/mL was evaluated as described above. The lowest concentration of the particles that inhibited the growth of bacteria was considered as the minimum inhibitory concentration (MIC).

All tests of antibacterial activity were performed in triplicate per sample, upon at least three independent samples and expressed as mean \pm standard deviation (SD). Statistical analysis was performed using the Statistical Package for the Social Science (SPSS) version 17.0 software. Statistical comparisons made by One-Way Analysis of Variance (ANOVA) with the Least Square Difference (LSD) tests were used for post hoc evaluations of differences between groups. The threshold level for accepting statistical significance was set at p < 0.01.

3. Results and Discussion

3.1. Preparation and characterization of surface-quaternized chitosan particles

Chitosan particles were first fabricated by ionic crosslinking between positively charged chitosan and negatively charged TPP. The process was conducted at ambient temperature in the absence of any surfactant or oil phase. The resulting chitosan particles appeared as fine white powder after drying and were insoluble in water, dilute acidic and alkali solutions. As outlined in Scheme 1, chitosan particles were then surface-modified by heterogeneous reductive *N*-alkylation with selected aldehyde, namely propionaldehyde and

benzaldehyde which yielded N-propyl chitosan particles and N-benzyl chitosan particles, respectively. Subsequent methylation with CH₃I thus formed quaternized N-propyl chitosan (QPCS) particles and quaternized N-benzyl chitosan (QBzCS) particles, respectively. Furthermore, the quaternization (Scheme 1) was also conducted directly on chitosan particles by methylation with CH₃I and gave quaternary ammonium-containing chitosan (QACS) particles as products. The optimized conditions for the preparation of each surfacequaternized chitosan particles via heterogeneous quaternization, so as to yield the highest degree of quaternization in terms of reaction time and reagent concentration were empirically identified (Table S1, Supplementary Material) based on the results from water contact angle and ζ-potential measurements following the criteria as previously described [28]. Another type of quaternized particles designated as N,N,N-trimethylchitosan (TMCS) particles were prepared for comparison. Although the quaternary ammonium entity (trimethyl, -N(CH₃)₃) of the TMCS particles is similar to that of the QACS particles, the TMCS particles were prepared differently by ionic gelation of N,N,N-trimethylchitosan synthesized homogeneously from chitosan according to the method reported by Sieval et al. [29]. In other words, TMCS particles should not only bear positive quaternary ammonium groups at the particles' surface which is the case for the QACS particles, but also inside the particles.

Chemical functionalities of all quaternized chitosan particles were first identified by FT-IR analysis. As shown in Fig. 1, absorption peaks at 1650 and 1544 cm⁻¹ can be assigned to the C=O stretching (Amide I) and N-H bending (Amide II) of the glucosamine unit of chitosan, respectively. The decrement of the N-H bending signal at 1544 cm⁻¹ and the appearance of the C-H deformation signal in a range of 1470-1460 cm⁻¹ in the spectra of all quaternized chitosan particles implied that the amino groups were functionalized by alkyl substituents introduced by either reductive *N*-alkylation/methylation or direct methylation. Nonetheless, the C-H deformation peak belonging to the TMCS particles was obviously weak

as opposed to those observed for other particles implying that there was smaller content of quaternary ammonium groups in the TMCS particles.

The degree of success in the quaternization of chitosan particles was also confirmed by ^{1}H NMR analysis. As illustrated in Fig.2, the multiplet in the range of $\delta 3.3$ - 4.4 ppm comes from the six carbon atoms at the 2', 3, 4, 5, 6, and 6' positions, while the two singlets at $\delta 1.9$ and $\delta 2.9$ ppm are due to the methyl protons from the acetyl groups (position A) and at the 2 position of N-acetyl glucosamine unit, respectively. For the QPCS and QBzCS particles, it should be emphasized that not all of the amino groups of chitosan were alkylated in the first step of reductive N-alkylation. As a consequence, the signals of the methyl protons appearing in Fig.2(d-e) would come from methyl groups attached to both alkylated and nonalkylated amino functionalities. The signal at $\delta 3.1$ -3.3, $\delta 3.0$, and $\delta 2.7$ ppm can be assigned to the methyl protons of the trisubstituted $(-N^+(C\underline{H}_3)_3)$ or $NR^+(C\underline{H}_3)_2$, position B), disubstituted (- $N(C\underline{H}_3)_2$ or $-NR(C\underline{H}_3)$, position C) and monosubstituted (-NH(C \underline{H}_3), position D) amino groups, respectively. The trace signals of methylene protons ($\delta 1.0$ ppm) and methyl protons $(\delta 0.85 \text{ ppm})$ observed on the spectrum of QPCS particles (Fig.2(e)) can be used as additional evidences confirming the attachment of propyl groups at the amino moieties of chitosan in the step of reductive N-alkylation. For the QBzCS particles (Fig.2(f)), the signals of aromatic protons at δ 7.4 ppm together with the benzylic protons at 1.0 ppm could be used to verify the attachment of benzyl groups at the amino positions of chitosan.

Based on the ^{1}H NMR analysis, the degree of quaternization (%DQ) can also be estimated. To simplify the calculation, it was assumed that the majority of quaternary ammonium groups existed in the form of $^{-}N^{+}(C\underline{H}_{3})_{3}$ and only a few were present in the form of $NR^{+}(C\underline{H}_{3})_{2}$. This assumption is based on the fact that the non-alkylated or free amino groups (-NH₂) left after the *N*-reductive alkylation step are less bulkier than the alkylated amino group (-NHR) and should thus be more accessible for nucleophilic substitution of $CH_{3}I$. Such

characteristics should favor the formation of $-N^+(C\underline{H}_3)_3$ as opposed to that of the $NR^+(C\underline{H}_3)_2$. The %DQ can thus be calculated from the relative ratio between the integration of the nine protons from the three methyl groups of the quaternized *N*-alkyl chitosan at the position $\delta 3.1$ -3.3 ppm and the peak integration of the six protons of chitosan ($\delta 3.3$ -4.4 ppm). Accordingly, the calculated %DQ value based on the content of $N^+(C\underline{H}_3)_3$ was 2.1, 7.1, 4.2, and 5.7 % for TMCS, QACS, QPCS, and QBzCS particles, respectively. It should be taken into account that the quaternized chitosan particles were not completely soluble in the CF₃COOH/D₂O, the solvent used for NMR analysis. As a result, the %DQ values obtained from 1H NMR analysis are not capable of reflecting the actual degree of surface quaternization, they can only be used as a qualitative measure of the extent of surface substitution. The fact that %DQ of TMCS particles was the lowest agrees quite well with the data formerly described based on FT-IR analysis (Fig.1).

TEM analysis revealed that all particles were quite spherical in shape and had average diameters in a sub-micron range of 260 -490 nm (Fig. 3). The dimension of QACS particles was quite comparable to that of the TMCS particles implying that the preparation method did not have significant impact on the particle size and morphology. On the other hand, the size of chitosan particles seemed to be greater when being modified by a larger alkyl substituent (propyl, benzyl) which came from the aldehyde used in the reductive *N*-alkylation step. The charge characteristic of the quaternized chitosan particles was determined by photon correlation spectroscopy (PCS). As shown in Fig. 3, all particles prepared by heterogeneous quaternization via reductive *N*-alkylation followed by methylation (QPCS and QBzCS particles) or direct methylation (QACS particles) exhibited greater zeta potential values than those of chitosan and TMC particles. Indeed, comparing TMCS and QACS particles, it seems that the heterogeneous quaternization approach was more efficient in enhancing positive charges of the chitosan particles than the homogeneous one. This may stem from the fact that some positive charges of

TMC were neutralized following ionic crosslinking with the negatively charged TPP upon the particle formation. In accord with this notion is that the TMCS particles formed by the crosslinking of TMC and TPP were not completely soluble in CF₃COOH/D₂O. As a result, the %DQ of TMC particles (2.1%) was much lower than that of the originally synthesized TMC (%DQ = 11.8%) indicating the consumption of the positive charges during crosslinking. Unlike the TMCS particles, the introduction of trimethyl groups to chitosan particles via direct methylation to yield the QACS particles was performed after the particle formation. Thus, the positive charge density generated thereafter was not depleted by the crosslinking. A similar explanation can be applied for the QPCS and QBzCS particles, where again the quaternization was applied after the particle formation. Interestingly, the presence of the larger alkyl substituents (propyl and benzyl) somewhat promoted the subsequent methylation accounting for why the ζ -potential was raised above +35 eV for both the QPCS and QBzCS particles. It is postulated that the more hydrophobic environment created by the propyl and benzyl substituents may increase a chance of CH₃I, a small organic molecule of low polarity, to reach the amino active sites of chitosan chain during methylation. Previous work has also demonstrated that the degree of surface quaternization can be tailored by adjusting the CH₃I concentration used in the methylation step [28].

3.2 Antibacterial efficacy of surface-quaternized chitosan particles

The antibacterial activity of surface-quaternized chitosan particles were tested against the representative Gram-positive and Gram-negative bacteria, *S. aureus* and *E. coli*, respectively, and reported as the total number of replication competent (viable) cells as mean colony forming units per volume (CFU/mL). In the case of *S. aureus*, all quaternized chitosan particles, TMCS, QACS, QPCS and QBzCS particles, exhibited significantly higher antibacterial ratio (> 95%) than the chitosan particles at pH 7.4 (Fig. 4), supporting that the

introduction of the positive charges via quaternization can effectively improve the antibacterial activity of chitosan particles especially in neutral media. In contrast, the antibacterial action of chitosan particles cannot be detected given that their viable counts closely resembled those of the negative control. This outcome is in line with our previous observation on chitosan film implying that chitosan particles would exhibit its potential in suppressing the bacterial growth only when they are in acidic media in which they are positively charged [28]. This also further suggested that the chelation of the amino groups of chitosan as proposed by others [30, 31] is definitely not the major mechanism that controls the antibacterial activity at this particular condition. These evidences support that the superior antibacterial activities of some quaternized chitosan particles, especially QPCS and QBzCS particles, to the chitosan particles are mainly due to their higher charge density in near neutral pH condition than the latter (See Fig. 3 for ζ -potential data). Overall, this trend is in accordance with previously observed data reported by Qi and coworkers [16], who proposed that the positively charged chitosan particles should interact favorably with negatively charged cell membranes, causing an increase in membrane permeability and eventually rupture and leakage of intracellular components. This proposed mechanism is particularly reasonable in the case of the Gram-positive bacteria, such as S. aureus since their outer membrane consists of negatively charged teichoic acid, that is believed to be responsible for the electrostatic binding with the positively charged particles.

Although the TMCS particles exhibited a slightly lower ζ -potential than the chitosan particles, they still inhibited the growth of *S. aureus*, potentially suggesting that the inhibition did not solely rely on the contact-inhibitory mechanism which should be charge density-dependent, but may also be influenced by the charge inside the particles or the ability to dissolve in the media considering that TMC is water soluble and not all of the TMC molecules were crosslinked by TPP during the particle formation. In fact, this release-inhibitory

mechanism involving surface leaching of soluble chitosan and/or its quaternized derivatives has been recently proposed by Fernandez-Saiz and co-workers [32] and also in our earlier work on the surface-quaternized chitosan films [28]. Similar explanations may also be applied in the case of QACS particles whose charge density (ζ -potential = +29.3 mV) was slightly higher than those of both chitosan particles (ζ -potential = +27.1 mV) and TMCS particles (ζ -potential = +23.2 mV). Having the same type of quaternary ammonium groups (-N(CH₃)₃), the QACS particles exhibited better antibacterial action against *S. aureus* than the TMCS particles indicating that the heterogeneous quaternization was potentially a more effective route to promote the antibacterial activity of chitosan particles than the homogeneous one. This is extremely important considering that the higher charge density can be achieved via heterogeneous route without sacrificing the positive charges to the crosslinking process. The lowering of the ζ -potential upon ionotropic crosslinking of TMC by TPP has also been reported by Sadeghi and co-workers [33]. It is also conceivable that the uncrosslinked surface-modified quaternized layer on the surface of QACS particles may leach out easier than the quaternary entities trapped or crosslinked by TPP inside and/or on the surface of TMCS particles.

The trend observed for the representative Gram-negative bacteria, $E.\ coli$ is quite different from that seen with the Gram-positive $S.\ aureus$ described above. In comparison with the negative control and chitosan particles, the quaternized chitosan particles with only slightly higher charge density, namely TMCS, and QACS particles, did not possess significant antibacterial activity against $E.\ coli$ (Fig. 4). QACS particles exhibited % antibacterial activity of 82.9% whereas the detrimental action of TMCS cannot be detected. On the other hand, the quaternized chitosan particles with larger alkyl groups having higher charge density, namely QPCS and QBzCS particles, exerted much higher antibacterial action against the $E.\ coli$. With a similar ζ -potential, the QBzCS particles displays a greater inhibitory action than the QPCS particles which is reasonable considering that the uppermost

layer of the outer membrane of *E. coli* contains lipopolysaccharide that should interact favorably with hydrophobic entities of the particles. In addition, the fact that QACS film was reported to exhibit much lower % antibacterial activity against *S. aureus* (26%antibacterial ratio) and *E.coli* (29% antibacterial ratio) [28], in comparison with the QACS particles apparently suggests that the antibacterial efficacy can be magnified by the enhanced surface area of the particles.

Comparatively, as outlined in Fig. 4, it was found that $E.\ coli$ had a greater resistance to quaternized chitosan particles than the $S.\ aureus$. This can be explained by three reasons. Firstly, the absence of an outer membrane and the presence of negatively charged teichoic acid within a thick peptidoglycan layer (20-80 nm) on the surface of $S.\ aureus$ should make them more attractive to the positively charged, quaternized chitosan particles and more specific to be damaged by positively charged molecules than $E.\ coli$. Secondly, the presence of a number of small channels of porins within the outer membrane of $E.\ coli$ may help block the entrance of the particles into the bacterial cell, making them more difficult to inhibit than $S.\ aureus$. Finally, the smaller dimension of $S.\ aureus$ (sphere, i.d. ~ 0.5 -1 μ m) may partly account for more intimate contact with the quaternized chitosan particles, making the antibacterial activity more effective than the $E.\ coli$ (rod, 0.3-1.0 \times 1.0-6.0 μ m).

Minimum inhibitory concentration (MIC) is the lowest concentration of an antimicrobial agent that can inhibit the growth of the target microorganism. From a practical perspective, this value is a key indication of the inhibitory efficiency of the substance against the microorganism. In this study, the MIC values of chitosan, TMCS, QACS, and QBzCS particles were evaluated by viable cell counting methods. The MIC values for each type of particle were identified by comparing the viable cell counts (log (CFU/mL)) between the suspension having the designated particles and the negative control). Results for all quaternized chitosan particles are displayed in Table 1. The fact that the concentration of as

high as 1000 mg/mL was neccessary for chitosan particles to express their inhibitory power explained why no inhibitory action was detected when previously tested with 0.5 mg/mL or 500 μg/mL chitosan particles (Fig.4). To start suppressing the growth of *E. coli* by chitosan particles demanded a concentration as high as 2000 μg/mL. These results support the previous assumption that *E. coli* is more tolerant than *S. aureus*. However, using the same growth media for bacteria, MHB, much lower MIC values of 234 and 117 μg/mL against *S. aureus* and *E. coli*, respectively have been reported for the chitosan particles also prepared by ionotropic crosslinking by TPP [24]. It is suspected that this difference may be a result of their particles having a much smaller size (~54 nm) and so possess a greater available surface area than ours (~320 nm). Therefore, a significantly lower quantity of chitosan particles was required in their case. In contrast, Sadeghi and co-workers [33] reported a two-fold higher MIC value for the TPP-crosslinked chitosan particles against *S. aureus*. This is reasonable given that their particles had a comparable size (~250 nm) to ours but with less ζ- potential (+15.9 eV).

As anticipated, the QACS particles with lower MIC were more potent in prohibiting bacterial growth than the TMCS particles. This MIC value (62.5 µg/mL) was apparently lower than those reported for TMC solutions with various degree of quaternization (%DQ) [33, 34] indicating their superior antibacterial efficacy. This outcome truly indicated the potential of heterogeneous route for the preparation of quaternized chitosan particles as opposed to the conventional homogeneous one which is obviously suffered from the drawback of a deteriorated antibacterial activity because the particles have to be formed after quaternization. The data demonstrated by Sadeghi and co-workers (also shown in Table 1) can be used as a good example [33]. The variation in experimental parameters such as molecular weight and degree of deacetylation of chitosan, %DQ, growth media, pH, initial bacteria concentration, bacterial source, method used for determination of the antibacterial

activity (i.e. optical density (OD), total plate counts for viable cells) should be taken into account when comparing the results. Eventhough a greater quantity of QPCS and QBzCS particles was required to start their detrimental effect on both bacterial strains as compared with the QACS particles, their antibacterial action was more effective when the quantity of all particles were as equal to or above the MIC values of the QPCS and QBzCS particles. This can be evidenced from the data shown in Fig.4 (tested with 500 μ g/mL particles). Interestingly, the MIC values of both QACS and QBzCS particles were independent on the bacterial strain.

4. Conclusions

Quaternized chitosan particles having different alkyl substitutents can be successfully prepared by heterogeneous direct methylation or reductive N-alkylation/methylation as verified by 1 H NMR and FT-IR analyses. The particles were spherical in shape, having an average diameter in a range of 230-490 nm and carried positive charges with ζ -potential ranging from +23.2 to +46.8 mV. As determined by viable count method, it was found that all quaternized chitosan particles exhibited higher antibacterial activity against S. aureus (Gram positive bacteria) than the chitosan particles in neutral media. It is believed that the electrostatic binding between the positive charges on the particles and the negatively charged teichoic acid on the outer membrane of S. aureus was responsible for their superior antibacterial activity. In contrast, only the QPCS and QBzCS particles, which have a high charge density and relatively large alkyl groups, were capable of suppressing the growth of E. coli (Gram-negative bacteria). The fact that E. coli had greater resistance to all quaternized chitosan particles than the S. aureus may be explained as a result of their difference in shape and outer membrane properties. The minimum inhibitory concentration (MIC) data led to two important conclusive remarks: (1) the antibacterial efficiency of each particle was dose-

dependent and (2) having the same alkyl substituent as TMCS particles, QACS particles were a more potent antibacterial material indicating that the heterogeneous quaternization was a more effective method than the homogeneous one. The results obtained from this research suggested that the surface-quaternized chitosan particles may potentially be used as effective antibacterial fillers for biomedical applications.

Acknowledgments

This research was financially supported by Research Team Promotion Grant from the Thailand Research Fund (RTA50800004). The authors appreciated a language editing service provided by Dr. Robert Butcher, the Publication Counselling Unit (PCU), Faculty of Science, Chulalongkorn University.

References

- [1] M. Changez, V. Koul, A. K. Dinda, Efficacy of antibiotics-loaded interpenetrating network (IPNs) hydrogel based on poly(acrylic acid) and gelatin for treatment of experimental osteomyelitis: in vivo study, Biomaterials 26 (2005) 2095-2104.
- [2] B. J. Nablo, A. R. Rothrock, M. H. Schoenfisch, Nitric oxide-releasing sol-gels as antibacterial coatings for orthopedic implants, Biomaterials 26 (2005) 917-924.
- [3] Y. Y. Sun, G. Sun, Novel refreshable *N*-halamine polymeric biocides: *N*-chlorination of aromatic polyamides, Ind. Eng. Chem. Res. 43 (2004) 5015-5020.
- [4] Y. Sun, G. Sun, Synthesis, characterization, and antibacterial activities of novel *N*-halamine polymer beads prepared by suspension copolymerization, Macromolecules 35 (2002) 8909-8912.

- [5] S. M. Iconomopoulou, G. A. Voyiatzis, The effect of the molecular orientation on the release of antimicrobial substances from uniaxially drawn polymer matrixes, J. Control. Release 103 (2005) 451-464.
- [6] N. Cioffi, L. Torsi, N. Ditaranto, G. Tantillo, L. Ghibelli, L. Sabbatini, T. Bleve-Zacheo, M. D'Alessio, P. G. Zambonin, E. Traversa, Copper nanoparticle/polymer composites with antifungal and bacteriostatic properties, Chem. Mater. 17 (2005) 5255-5262.
- [7] M. Rai, A. Yadav, A. Gade, Silver nanoparticles as a new generation of antimicrobials, Biotechnol. Adv. 27 (2009) 76-83.
- [8] V. K. Sharma, R. A. Yngard, Y. Lin, Silver nanoparticles: Green synthesis and their antimicrobial activities, Adv. Colloid Interf. 145 (2009) 83-96.
- [9] F. Furno, K. S. Morley, B. Wong, B. L. Sharp, P. L. Arnold, S. M. Howdle, R. Bayston, P. D. Brown, P. D. Winship, H. J. Reid, Silver nanoparticles and polymeric medical devices: A new approach to prevention of infection, J. Antimicrob. Chemoth. 54 (2004) 1019-1024.
- [10] A. Kumar, P. K. Vemula, P. M. Ajayan, G. John, Silver-nanoparticle-embedded antimicrobial paints based on vegetable oil, Nat. Mate. 7 (2008) 236-241.
- [11] M. Wagener, Antimicrobial coatings, Polym. Paint Colour J. 196 (2006) 34-37.
- [12] N. Duran, P. D. Marcato, G. I. H. De Souza, O. L. Alves, E. Esposito, Antibacterial effect of silver nanoparticles produced by fungal process on textile fabrics and their effluent treatment, J. Biomed. Nanotechnol. 3 (2007) 203-208.
- [13] X. Chen, H. J. Schluesener, Nanosilver: A nanoproduct in medical application, Toxicol. Lett. 176 (2008) 1-12.
- [14] T. M. Benn, P. Westerhoff, Nanoparticle silver released into water from commercially available sock fabrics, Environ. Sci. Technol. 42 (2008) 4133-4139.

- [15] M. N. V. R. Kumar, R. A. A. Muzzarelli, C. Muzzarelli, H. Sashiwa, A. J. Domb, Chitosan chemistry and pharmaceutical perspectives, Chem. Rev. 104 (2004) 6017-6084.
- [16] L. F. Qi, Z. R. Xu, X. Jiang, C. H. Hu, X. F. Zou, Preparation and antibacterial activity of chitosan nanoparticles, Carbohyd. Res. 339 (2004) 2693-2700.
- [17] W. J. Ye, M. F. Leung, J. Xin, T. L. Kwong, D. K. L. Lee, P. Li, Novel core-shell particles with poly(*n*-butyl acrylate) cores and chitosan shells as an antibacterial coating for textiles, Polymer 46 (2005) 10538-10543.
- [18] X. L. Ye, X. G. Li, L. J. Yuan, L. H. Ge, B. S. Zhang, S. B. Zhou, Interaction of houttuyfonate homologues with the cell membrane of gram-positive and gramnegative bacteria, Colloid Surf. A-Physicochem. Eng. Asp. 301 (2007) 412-418.
- [19] M. E. I. Badawy, Structure and antimicrobial activity relationship of quaternary *N*-alkyl chitosan derivatives against some plant pathogens, J. Appl. Polym. Sci. 117 (2010) 960-969.
- [20] C. H. Kim, K. S. Choi, Synthesis and antibacterial activity of quaternized chitosan derivatives having different methylene spacers, J. Ind. Eng. Chem. 8 (2002) 71-76.
- [21] W. Sajomsang, Synthetic methods and applications of chitosan containing pyridylmethyl moiety and its quaternized derivatives: A review, Carbohyd. Polym. 80 (2010) 631-647.
- [22] V. K. Mourya, N. N. Inamdar, Trimethyl chitosan and its applications in drug delivery, J. Mater. Sci.-Mater. Med. 20 (2009) 1057-1079.
- [23] Z. L. Shi, K. G. Neoh, E. T. Kang, W. Wang, Antibacterial and mechanical properties of bone cement impregnated with chitosan nanoparticles, Biomaterials 27 (2006) 2440-2449.

- [24] W. L. Du, S. S. Niu, Y. L. Xu, Z. R. Xu, C. L. Fan, Antibacterial activity of chitosan tripolyphosphate nanoparticles loaded with various metal ions, Carbohyd. Polym. 75 (2009) 385-389.
- [25] L. F. Qi, Z. R. Xu, X. Jiang, Y. Li, M. Q. Wang, Cytotoxic activities of chitosan nanoparticles and copper-loaded nanoparticles, Bioorg. Med. Chem. Lett. 15 (2005) 1397-1399.
- [26] W. L. Du, Y. L. Xu, Z. R. Xu, C. L. Fan, Preparation, characterization and antibacterial properties against *E. coli* K88 of chitosan nanoparticle loaded copper ions, Nanotechnology 19 (2008) 085707.
- [27] S. Inphonlek, N. Pimpha, P. Sunintaboon, Synthesis of poly(methyl methacrylate) core/chitosan-mixed-polyethyleneimine shell nanoparticles and their antibacterial property, Colloid Surf. B-Biointerfaces 77 (2010) 219-226.
- [28] N. Vallapa, O. Wiarachai, N. Thongchul, J. S. Pan, V. Tangpasuthadol, S. Kiatkamjornwong, V. P. Hoven, Enhancing antibacterial activity of chitosan surface by heterogeneous quaternization, Carbohyd. Polym. 83 (2011) 868-875.
- [29] A. B. Sieval, M. Thanou, A. F. Kotze, J. C. Verhoef, J. Brussee, H. E. Junginger, Preparation and NMR characterization of highly substituted *N*-trimethyl chitosan chloride, Carbohyd. Polym. 36 (1998) 157-165.
- [30] M. Kong, X. G. Chen, C. S. Liu, C. G. Liu, X. H. Meng, L. J. Yu, Antibacterial mechanism of chitosan microspheres in a solid dispersing system against *E. coli*, Colloid Surf. B-Biointerfaces 65 (2008) 197-202.
- [31] R. G. Cuero, G. Osuji, A. Washington, *N*-Carboxymethylchitosan inhibition of aflatoxin production: Role of zinc, Biotechnol. Lett. 13 (1991) 441-444.

- [32] P. Fernandez-Saiz, J. M. Lagaron, M. J. Ocio, Optimization of the biocide properties of chitosan for its application in the design of active films of interest in the food area, Food Hydrocolloids 23 (2009) 913-921.
- [33] A. M. M. Sadeghi, F. A. Dorkoosh, M. R. Avadi, P. Saadat, M. Rafiee-Tehrani, H. E. Junginger, Preparation, characterization and antibacterial activities of chitosan, *N*-trimethyl chitosan (TMC) and *N*-diethylmethyl chitosan (DEMC) nanoparticles loaded with insulin using both the ionotropic gelation and polyelectrolyte complexation methods, Int. J. Pharm. 355 (2008) 299-306.
- [34] W. Sajomsang, P. Gonil, S. Saesoo, Synthesis and antibacterial activity of methylated *N*-(4-*N*,*N*-dimethylaminocinnamyl) chitosan chloride, Eur. Polym. J. 45 (2009) 2319-2328.

List of Figure and Scheme Captions

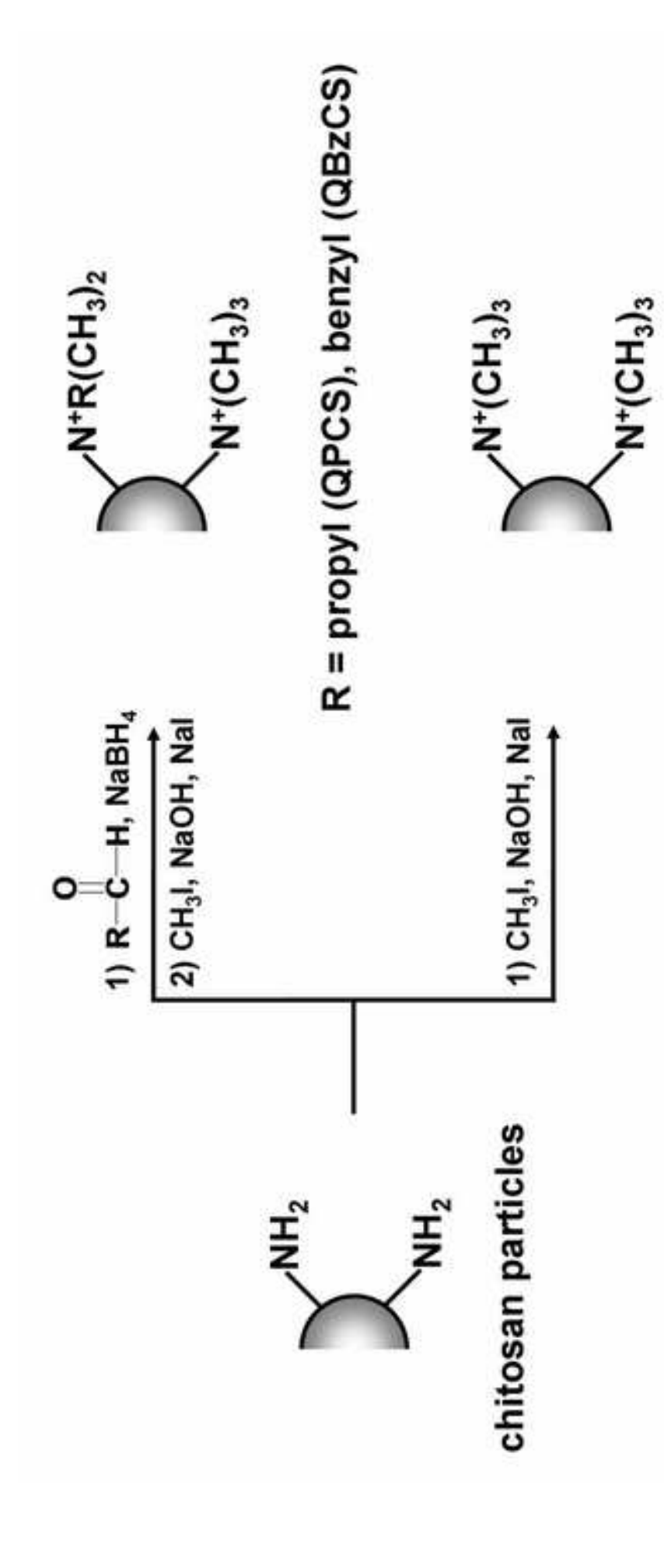
Scheme 1 Preparation of surface-quaternized chitosan particles by reductive *N*-alkylation/methylation (top row) and direct methylation (bottom row).

Fig. 1. FT-IR spectra of (a) chitosan particles, (b) TMCS particles, (c) QACS particles, (d) QPCS particles, and (e) QBzCS particles.

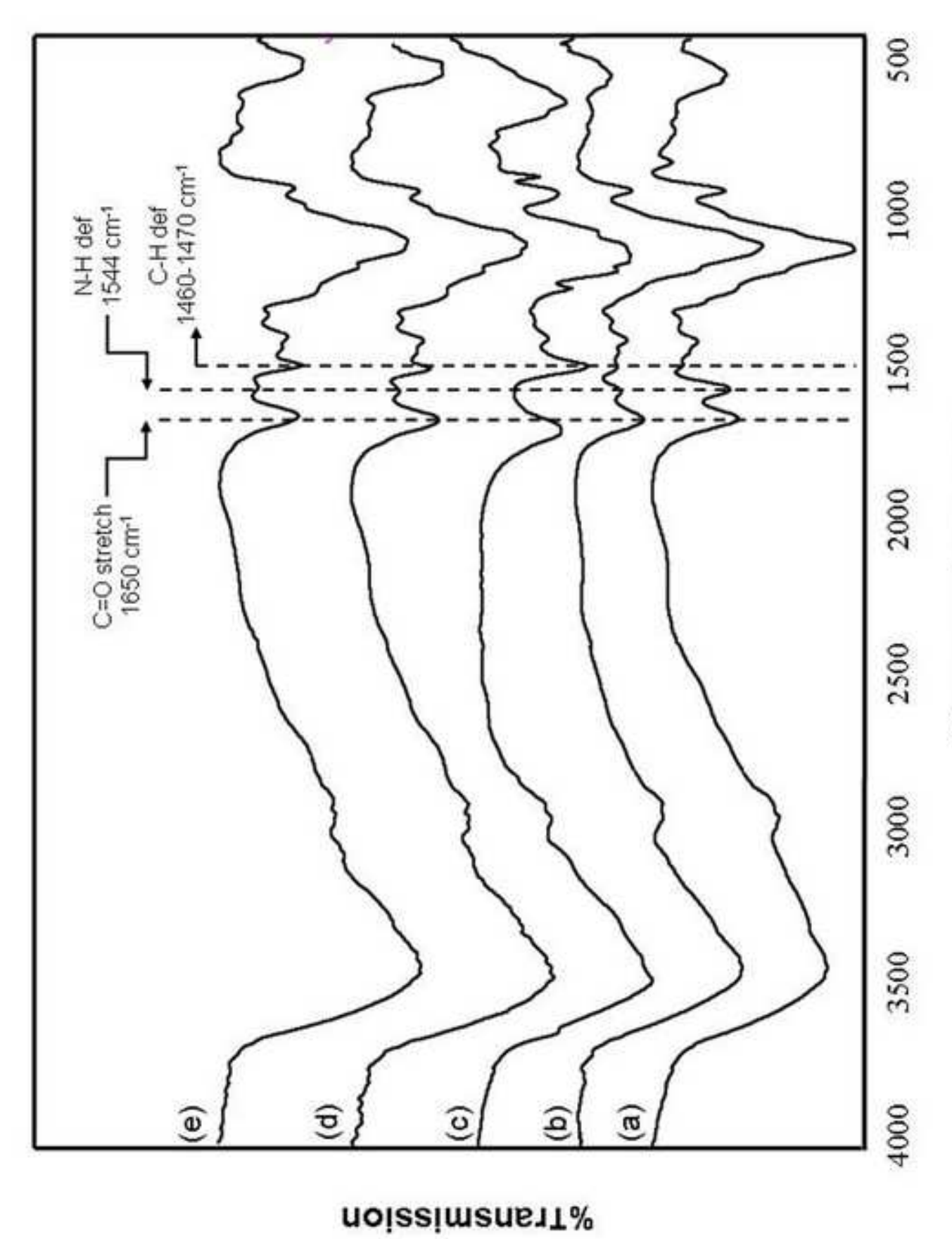
Fig. 2. ¹H-NMR spectra of (a) chitosan particles, (b) TMCS particles, (c) QACS particles, (d) QPCS particles, and (f) QBzCS particles.

Fig. 3. Representative TEM micrographs (x 12,000), average particles sizes and ζ - potentials of chitosan and quaternized chitosan particles. Micrographs shown are representative of at least 10 such fields of view per sample and 3 independent samples.

Fig. 4. Total replication competent (viable) cell counts of *S. aureus* and *E. coli* in suspension after incubation with different chitosan particles (0.5 mg/mL) for 24 h. Statistical significance with p < 0.01 of the viable count is compared with the negative control (*) and the chitosan particles (#). Below in the table is the corresponding antibacterial ratio.

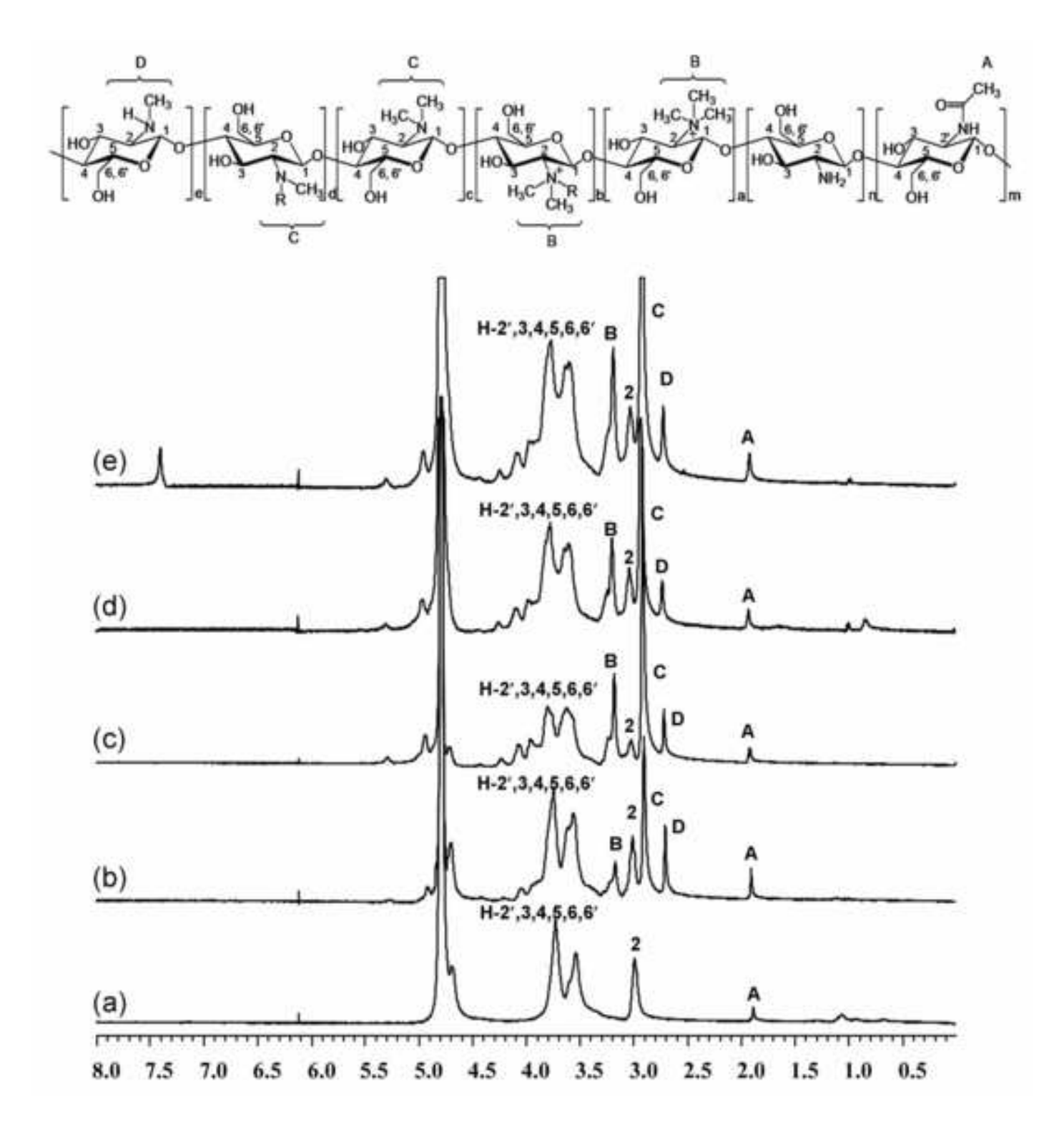


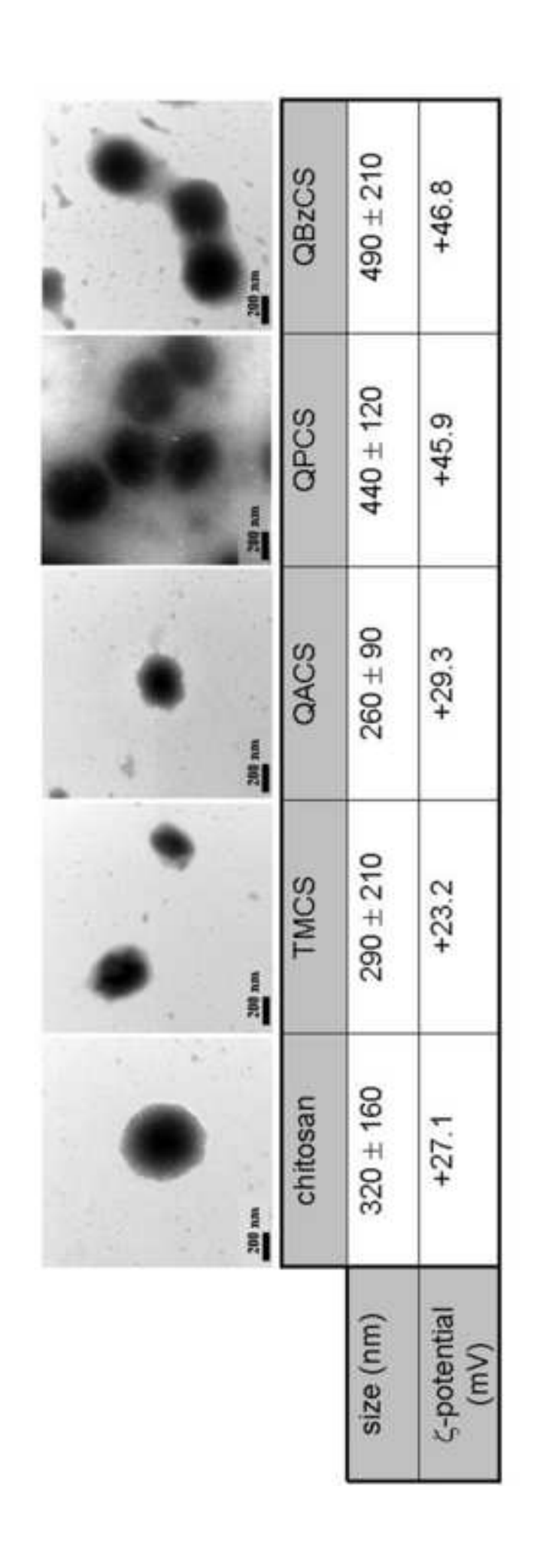
QACS

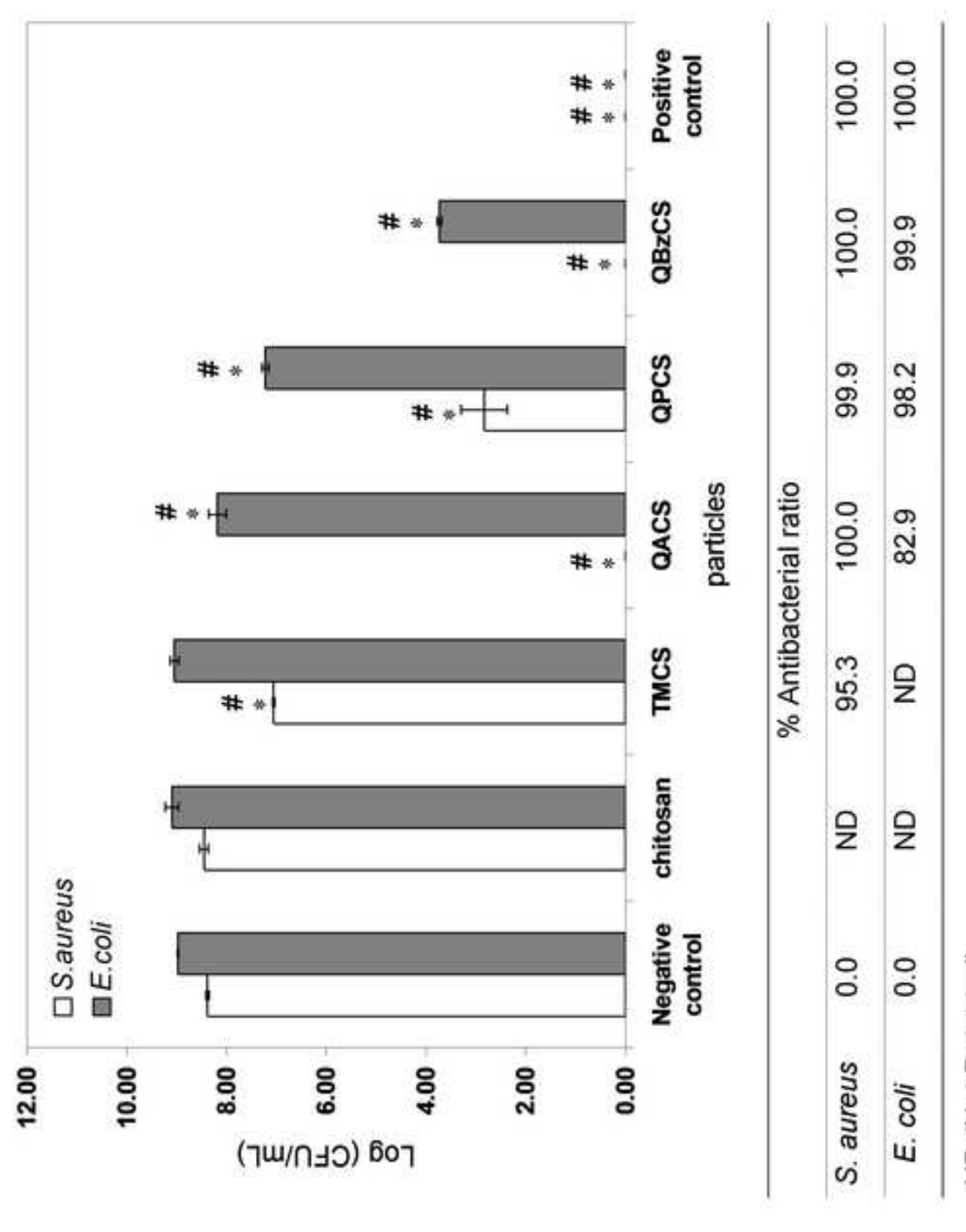


Wavenumbers (cm⁻¹)

Figure(s) Click here to download high resolution image







ND (Not Detected)

Table 1. MIC values of chitosan and quaternized chitosan particles prepared in this work against *S. aureus* and *E. coli* in comparison with those of chitosan particles and quaternized chitosan both in the form of solution and particles as reported in the literatures

	MIC (μg/mL)	
Materials	S. aureus	E. coli
chitosan particles; size = 320 ± 160 nm [TS]	1000	2000
chitosan particles; size = 54 nm [24]	234	117
chitosan particles; size = 250 nm [33]	2000	N/A
TMCS particles; size = $290 \pm 210 \text{ nm}$ [TS]	250	125
QACS particles; size = $260 \pm 90 \text{ nm}$ [TS]	62.5	62.5
TMC particles; size = 215 nm [33]	500	N/A
TMC solution; 55±5%DQ [33]	250	N/A
TMC solution; MW = 120 kDa, 64%DQ [34]	125	250
TMC solution; MW = 200 kDa, 28%DQ [34]	500	1000
QPCS particles; size = 440 ± 120 nm [TS]	125	250
QBzCS particles; size = 490 ± 210 nm [TS]	125	125

[TS] = this study; N/A = not available

Supplementary Material Click here to download Supplementary Material: Wiarachai_CSB_Supplementary_Final.doc

Polymer International



Improvement of tensile modulus and tear strength of natural rubber dipped films by vinylated silica generated in situ

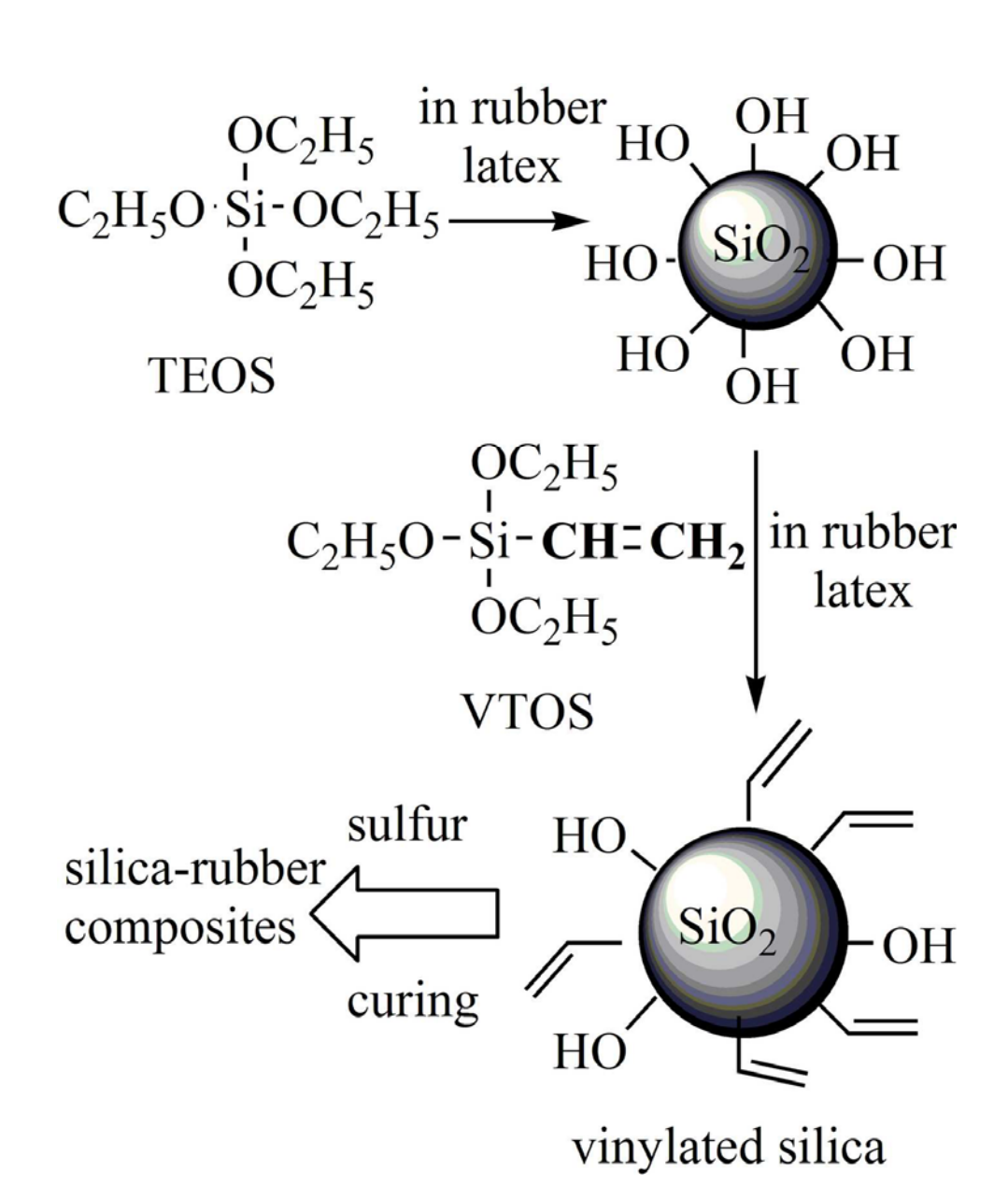
Journal:	Polymer International
Manuscript ID:	PI-11-0382
Wiley - Manuscript type:	Original Article
Date Submitted by the Author:	06-Jun-2011
Complete List of Authors:	Rachanark, Navagan; Chulalongkorn University, Program of Petrochemistry and Polymer Science Tangpasuthadol, Varawut; Chulalongkorn University, Chemistry Kiatkamjornwong, Suda; Chulalongkorn University, Department of Imaging and Printing Technology
Key Words:	composite, silica, sol-gel process, natural rubber

SCHOLARONE™ Manuscripts

Improvement of tensile modulus and tear strength of natural rubber dipped films by vinylated silica generated in situ

Navagan Rachanark, Varawut Tangpasuthadol*, Suda Kiatkamjornwong

Vinylated silicas were generated in natural rubber latex. The silica-rubber vulcanizates showed high tensile modulus and tear strength, possibly due to vinyl group participation in the sulfur curing of rubber.



59x71mm (600 x 600 DPI)

Improvement of tensile modulus and tear strength of natural rubber dipped films by vinylated silica generated in situ

Navagan Rachanark¹, Varawut Tangpasuthadol²,*, Suda Kiatkamjornwong³ ¹Program of Petrochemistry and Polymer Science, Faculty of Science, Chulalongkorn University, Bangkok, Thailand 10330

²Organic Synthesis Research Unit, Department of Chemistry, Faculty of Science,

Chulalongkorn University, Bangkok, Thailand 10330

³Department of Imaging and Printing Technology, Faculty of Science, Chulalongkorn

University, Bangkok, Thailand 10330

*Corresponding author: Tel. 66-2218-7626, Fax. 66-2218-7598

E-mail address: varawut.t@chula.ac.th

Email: navagan@hotmail.com, suda.k@chula.ac.th

Abstract

Alkylated silica particles were generated in dipped natural rubber films by sol-gel process of tetraethoxysilane (TEOS) and alkyltrialkoxysilane that were mixed with rubber latex before dipping process. Vinyltriethoxysilane (VTOS), ethyltriethoxysilane (ETOS), and methacryloxypropyltrimethoxysilane (MPS) were three alkyltrialkoxysilanes investigated as surface-treating reagents for the silica formed in the system. After heating the mixed alkaline latex at 80°C, the conversions from the silane to silica were in the range of 38-77% by mole of the total added silanes, depending on the size and polarity of the alkyl group in the silane. By TEM, the in situ silica particles were observed around rubber particles in the latex. Among the three

silanes, only the addition of VTOS in the TEOS-mixed latex led to significantly increases of tensile modulus and tear strength of the vulcanized films as compared to the addition of TEOS alone, possibly due to the participation of vinyl groups in the curing process.

Keywords: composite; silica; sol-gel process; natural rubber



Introduction

Natural rubber (NR) latex is used to produce thin film products such as gloves and condoms, which require high elongation and excellent resilience. Nevertheless, NR has some weak characteristics, such as low tensile strength and modulus. A conventional technique to reinforce NR products is to physically mix fine silica powder with solid rubber or to mix aqueous slurry of silica with NR latex. However, in the mixing process, silica particles tend to aggregate and agglomerate due to intermolecular hydrogen bonding between the hydroxyl groups on the silica surface. This often results in poor particle dispersion in the rubber matrix and high viscosity during mixing. Silica can also adsorb or react with curing agents and accelerators on its surface which results in the reduction of curing efficiency.

A method for overcome these problem is to generate silica particles right in the NR matrix. *In situ* silica formation is achieved by the sol–gel process of a silica precursor, such as tetraethoxysilane (TEOS), within the rubber matrix. There have been many reports on the *in situ* silica formation methods in solid rubber sheet, ^{3,4} rubber solution, ^{5,6} and rubber latex. ⁷⁻¹⁰ However, the use of TEOS alone as the silica precursor results in silica with polar hydroxyl groups on its surface. These polar groups potentially cause incompatibility between silica and rubber. One way to reduce the number of hydroxyl groups on the silica surface was to utilize alkyltrialkoxysilane to form 'alkylated' silica. The alkyltrialkoxysilane is a compound that carries three alkoxy groups and an alkyl substituent. The three alkoxy arms are required for bonding with silica, while the alkyl substituent is designated for *bonding* or *interacting* with the rubber matrix. They were regularly used under the name 'coupling agent' in rubber processing industry to chemically modify silica powder, in order to improve the filler

dispersion and prevent adsorption of curing agents on the silica surface. Some functional groups such as alkyl, phenyl, amine, and vinyl groups can be introduced by selecting the right choice of alkyltrialkoxysilanes.^{11,12}

The mixing of TEOS and alkyltrialkoxysilanes in NR latex for the preparation of *in situ* silica reinforced rubber vulcanizates were reported recently. The composite containing *in situ* silica had higher tensile modulus and tear strength than the composite prepared by conventionally mixing with silica powder. A combination of bis-(3-triethoxysilylpropyl)tetrasulfide (TESPT) and TEOS that was mixed with the latex was shown to improve the mechanical properties and sulfur curing rates during milling and compression process. Triethoxysilanes carring either vinyl, ethyl, and iso-butyl group were reportedly used to generate silica in sulfur-cured NR sheets obtained by melt-compression process. Among them, vinyltriethoxysilanes was the most promising silane that was able to enhance the tensile modulus and resistance to tear of the rubber vulcanizates.

In this work, the focus was to utilize a mixed silane system in the reinforcement of natural rubber films that were prepared by 'latex-dipping' process. TEOS was used in combination with either VTOS or methacryloxypropylmethoxysilane (MPS) to prepare *in situ* silica having carbon-carbon double bonds on the particle surface. ETOS was also used in the film preparation for the purpose of investigating the role of C=C double bond in the reinforcement capability of the resulting silica. The structures of TEOS, VTOS, ETOS, and MPS are shown in Fig. 1. It was hypothesized that the *in situ* 'vinylated' silica particles can improve the dispersibility and mechanical properties of the NR/silica dipped films.

Experimental

Materials

Concentrated natural rubber latex with 60% weight content of dry rubber (DRC) incorporated 0.7% NH₃ was purchased from the Rubber Research Institute of Thailand. Liquid dispersion of vulcanizing agents was donated from Polymer Innovation Co., Ltd., Nonthaburi, Thailand. Tetraethoxysilane (TEOS, >98%), vinyltriethoxysilane (VTOS, >98%), ethyltriethoxysilane (ETOS, >97%), methacryloxypropyltrimethoxysilane (MPS, >98%) were purchased from Aldrich, Germany.

Preparation of pre-vulcanized NR latex

The concentrated NR latex was diluted with 0.7% v/v ammonia solution to obtain 30% DRC latex. It was then mixed with the dispersion of vulcanizing agents formulated as shown in Table 1. Then a predetermined amount of TEOS was added to the latex compound with stirring. After maturated at room temperature for 24 hr, a predetermined amount of VTOS, ETOS, or MPS was mixed with the latex mixture as listed in Table 2. The homogeneous milky mixture of silane-latex was maturated for an additional 24 hr before it was used in the dipping process. During the maturation period, the reaction of silane slowly took place in the presence of water and base in the latex. The total amount of alkoxysilanes added into the latex was limited to 30 phr, because the latex tended to be unstable if a higher amount of the silanes was added.

Table 1 Composition of vulcanization reagents in the form of dispersed liquid used in the latex dipping process

Ingredients	Amount (phr ^a)
Natural rubber	100
Sulfur	2.5
$ZMBT^b$	0.5
$ZDEC^{c}$	1.5
ZnO^d	2.0

^a part per hundred part of rubber by weight, ^bzinc salt of 2-mercaptobenzothiazole, ^czinc-diethyldithiocarbamate, ^dzinc oxide

Table 2 Variation of alkoxysilane amounts mixed into NR latex for *in situ* silica-NR composites preparation

	Silane amount (phr)			
	Shalle amount (pm)			
Entry	TEOS	VTOS	ETOS	MPS
VNR	-	-	<u>-</u>	-
30T	30	-	0	-
25T	25	-	- 7	_
25T5V	25	5	-	-
20T10V	20	10	-	-
25T5E	25	-	5	-
20T10E	20	-	10	-
25T5M	25	-	-	5
20T10M	20	-	-	10

Dipping process

In situ silica-NR vulcanized films were prepared by dipping glass cylinders (pre-dipped in Ca(NO₃)₂ solution, 40 mm in diameter) in the prepared latex-silane-vulcanizing agent mixtures. The coated former was then heated in an oven at 80°C for 24 hr to initiate the vulcanization and sol-gel process of the added silanes. On average, the film thickness obtained was 0.15 mm.

Determination of silica content in the *in situ* silica-NR dipped films

The silica content was determined by cutting the NR/silica dipped films into small pieces (~50 mg). After an exact weight was determined, the sample was heated at 850°C for 15 min in an oven. The weight of the remaining ash was calculated for the silica content in the composite by equations 1 and the conversion of the alkyltrialkoxysilane to silica was calculated using equation 2,

Silica Content (phr) =
$$100 (W_1/W_2)$$
 (1)

Conversion (%) =
$$100 (W_3/W_4)$$
 (2)

where, W_1 is the weight of silica in the sample, W_2 is the weight of the organic rubber, W_3 is the obtained amount of the *in situ* generated silica in the sample, and W_4 is the theoretical amount of silica generated from the added amount of alkoxysilane in the latex. The calculation of W_4 was based on the chemical equation shown in Fig. 2 by assuming a quantitative conversion of TEOS and alkyltriethoxysilane to silica and alkylated silica, respectively. The results reported were averaged from three specimens.

Microscopic Analysis

A scanning electron microscope (JOEL JSM-6480LV SEM) was used to analyze silica distribution in the NR matrix at 15 keV. The analysis was performed on the fractured surface of silica-NR dipped films prepared by breaking the film specimens while it was immersed in liquid nitrogen. Energy dispersive X-ray spectrometric (EDX) detector was carried out at an elevation angle of 35° in order to determine atomic types on the analyzed surface. A transmission electron microscope (JOEL JEM-2100) was used to examine the morphology of rubber and silica particles in the latex mixed with the silane precursors. The silane-latex mixture was diluted with distilled water to obtain a DRC of 0.75%. The substrate was stained by exposure to RuO₄ vapor before TEM analysis.

Mechanical properties

Tensile properties were measured with an H10KS universal testing machine (Hounsfield, Redhill, UK), according to JIS K6251-8 at a grip length of 10 mm, and a crosshead speed of 500 mm/min. Each data point was an average value obtained from four replicates of specimens. Tear properties were measured using a Hounsfield H10KS universal testing machine, following ASTM D624-91. The die C-cut specimens were tested at a gauge length of 70 mm and a crosshead speed of 500 mm/min. The values reported for each sample were averaged from three specimens.

Tension set measurement

All dipped film samples were cut into the size of 5×60 mm. Two lines about 10 mm apart were marked at the center of the sample strip. The sample was extended until the distance between the two lines was twice that of the original length, and was held for 10 min. After that, the sample was allowed to retract for 10 min. The final distance

between the two lines was then measured. All measurements were made by using a vernier caliper. The tension set was calculated using equation 3 where L_i and L_f were the initial and final distances between the two lines.

Tension set (%) =
$$((L_f - L_i)/L_i) \times 100$$
 (3)

Results and Discussions

Silica content and percentage conversion of silanes to silica

Earlier, we reported a cross-condensation of TEOS and alkyltrialkoxysilanes that were mixed together in the NR latex to form 'alkylated' silicas *in situ*. ⁹ In this work, TEOS was first mixed into the latex in order to form the silica particles during the maturation period. Then one of the alkyltrialkoxysilanes was added so that it could condense with the pre-formed silica, resulting in silica particles with selected alkyl groups (R) on the surface (Fig. 3).

The amounts of silicas formed in the rubber matrix are listed in Table 3. The conversion of TEOS to silica in the silica-NR dipped film was the highest at 77%, resulting in 6.7 phr of silica. Although the sol-gel process of the silane took place preferably in an alkaline latex, the conversion obtained here for TEOS was somewhat lower than our previous reports of >90%. In those reports, the concentration of NR latex was 60% DRC but in this work the latex was diluted to 30% to suit the dipping process. The diluted latex contained a large amount of water, possibly suppressing the chemical equilibrium back to silicic acid, and thus reducing the silicon dioxide network formation. At various ratios of TEOS and alkyltrialkoxysilanes (Table 3), the degree of silane-to-silica conversions in the rubber vulcanizates decreased when the relative amount of alkyltrialkoxysilane was increased. This was because each of the selected

alkyltrialkoxysilanes contained only three hydrolysable siloxane arms as compared to four siloxanes in the structure of TEOS. In addition, the degree of silane-to-silica conversion was also affected by the structure and polarity of the alkyl substituent in the silanes used, i.e. TEOS-VTOS > TEOS-ETOS > TEOS-MPS. In highly polar aqueous medium, a polar and small alkyl group on the silane molecule should allow higher access of water and another silanol group (-Si-OH) at condensation site than does the non-polar and bulky substituent. In this case, the vinyl group (in VTOS) is more polarized than the ethyl (in ETOS), the mixed VTOS-TEOS silanes therefore results in a higher conversion than the ETOS-TEOS. In the case of MPS, the methacryloxypropyl group is long and bulky. It therefore partially inhibits the sol-gel process, resulting in slightly lower silica formation than does the VTOS system. This result is in fact in good agreement with our earlier finding.⁹

Table 3 Silica content and degree of conversion from alkoxysilane to silica in rubber.

Entry	Silica content (phr)	Conversion (%)
30T	6.7 ± 0.3	77 ± 3.0
25T	5.1 ± 0.1	70 ± 1.0
25T5V	5.6 ± 0.3	61 ± 3.5
20T10V	5.2 ± 0.1	52 ± 0.6
25T5E	5.0 ± 0.2	54 ± 2.2
20T10E	4.8 ± 0.2	48 ± 2.2
25T5M	5.2 ± 0.4	48 ± 3.2
20T10M	4.9 ± 0.1	38 ± 0.8

Moreover it was believed that the alkoxysilane precursors could evaporate from the mixed latex during the dipping and drying steps. To overcome the loss of starting silane reagents, the silane-mixed latex was maturated (or stored) at room temperature for 1-2 days in order to allow partial sol-gel process to take place. This hypothesis was tested with results shown in Fig. 4, in which the degree of conversion was determined after one and two days of maturation. Without the maturation, the conversion of TEOS to silica in the rubber matrix was only 25% but increased dramatically to almost 80% (or about 7 phr) after one day of storage at room temperature.

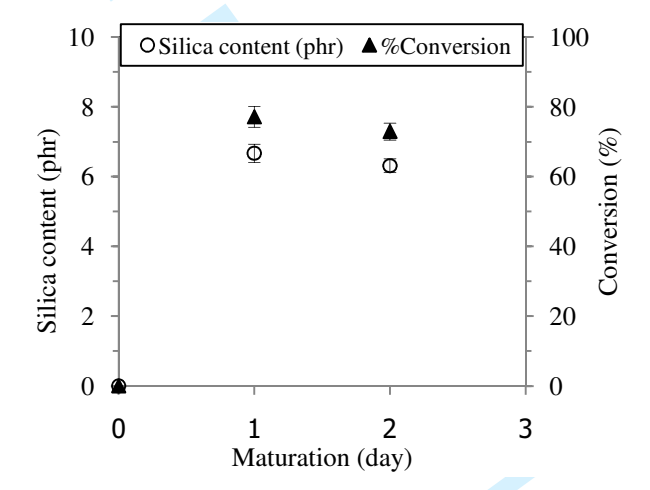


Figure 4 Changes of silica content and degree of conversion of TEOS (30 phr) mixed in the NR latex (30% DRC) as a function of latex maturation time

Morphology of the in situ silica and NR

The image from transmission electron microscope (TEM) was used to locate the silica particles in the rubber latex (Fig. 5). Analysis of the ruthenium-stained latex sample showed that the shape of NR particles appeared to be spherical with size ranging from 0.1-1 µm (Fig. 5a). The *in situ* generated silica were observed as dark irregular-shaped

submitted to 'Polymer International'

particles, with the size of about 100 nm or less, surrounding the rubber particle in the latex compound mixed with TEOS (Fig. 5b), TEOS-VTOS (Fig. 5c), and TEOS-MPS (Fig. 5d).

The distribution of silica particles in the fractured surface of the composite films was analyzed by scanning electron microscope (SEM) (Fig. 6). The silica formed in the vulcanizate was visualized as aggregates among ZnO particles, an activator used in the vulcanization process (Fig. 6a). The identity of silicon atoms was confirmed by its characteristic peak at 1.7 keV in the EDX spectrum, while the ZnO was identified by the signal at 1.0 keV (Fig. 6b).

Comparison of the characteristic of *in situ*-formed silica generated from the mixed silanes was made as shown in Fig. 7. The silica particles of all precursor types form aggregates with sizes ranging from <1 to several µm and are dispersed throughout the rubber matrix. The particles obtained appear to be quite similar in terms of size and shapes, regardless of its precursor type.

Mechanical properties

In order to investigate the effect of alkyltrialkoxysilane types on the tensile properties of the *in situ* silica-NR dipped films, four rubber samples filled with approximately equal amounts of *in situ* generated silica $(5.0 \pm 0.4 \text{ phr})$ were prepared and named as 25T, 20T10V, 20T10E, and 20T10M. Their analyses for modulus value at 300% & 500% elongation and tensile strength at break were performed in comparison with the silica-free vulcanized film (VNR) as shown in Fig. 8. The modulus at 500% elongation of the 20T10V was significantly higher than the others. The use of mixed TEOS-ETOS and TEOS-MPS were slightly less effective in reinforcing the rubber film than using TEOS-

VTOS or only TEOS. It seemed that MPS, also containing the vinyl group, was not as efficient as a reinforced precursor as VTOS for the dipped system.

The elongations at break of these selected vulcanizates, with or without the *in situ* silica, were between 630-690% (Fig. 9). No relation between the ultimate elongation and the type of silane precursor was observed. Tear testing of all NR/silica composites was performed on cast rubber sheets (~0.6 mm thick) that were prepared from the same latex compound as used for the dipping process. From the results shown in Fig. 10, only two samples, 20T10V and 20T10E, had significantly higher tear strength than did the VNR. The highest tear strength belonged to 20T10V.

From the tensile and tear test results of the *in situ* silica-NR vulcanizates, the vinyl group in VTOS that was mixed with TEOS in the ratio of 1:2 (VTOS:TEOS) plays an important role in the mechanical properties of the rubber films. The vinyl group on the *in situ* generated vinylated silica can most likely take part in the sulfur vulcanization process. In other words, the sulfur crosslinking takes place not only among the isoprene units of NR chains but possibly also with the vinylated silica particles. Unfortunately using a spectroscopic method such as IR to detect the disappearance of vinyl group after sulfur cure step would be inconclusive, since the NR matrix also contains a large number of double bonds. Nevertheless this type of participation was reported in other works, such as the preparation of wood fiber/PE and PP composites, in which the vinyl group was reportedly bonded with polyolefin backbone via radical grafting while the ethoxy silyl group on the other end of VTOS reacted with the hydroxyl groups of cellulose structure. ^{13,14}

submitted to 'Polymer International'

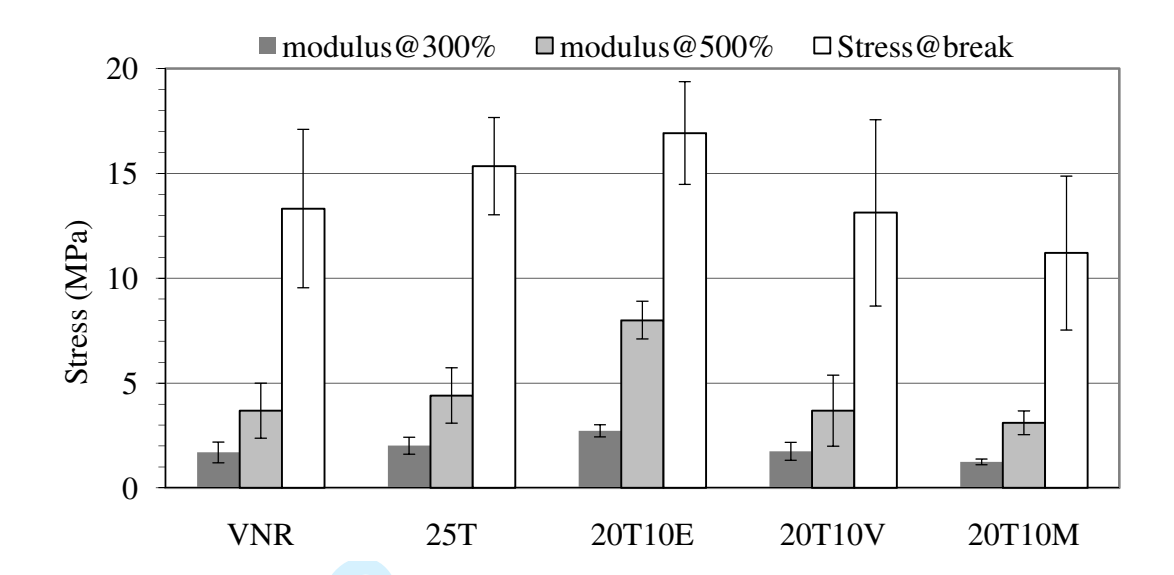


Figure 8 Modulus at 300&500% elongation and tensile strength of the dipped NR films filled with *in situ* silica generated by various types of alkoxysilane precursor, compared with silica-free dipped film (VNR).

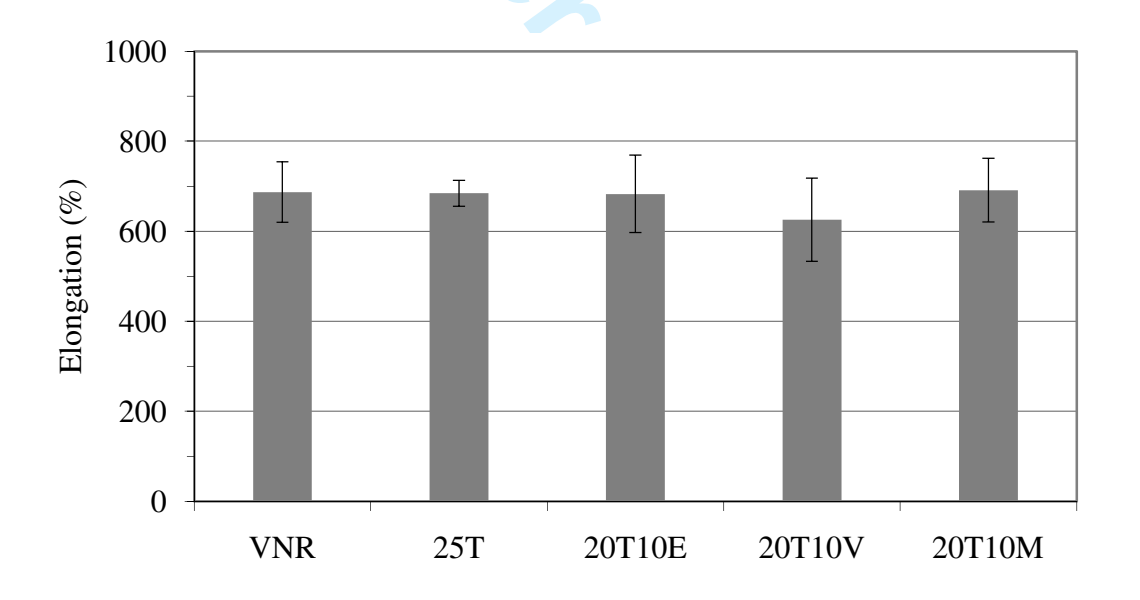


Figure 9 Elongation at break of the dipped NR films filled with *in situ* silica generated by various types of alkoxysilane precursor, compared with silica-free dipped film (VNR).

submitted to 'Polymer International'

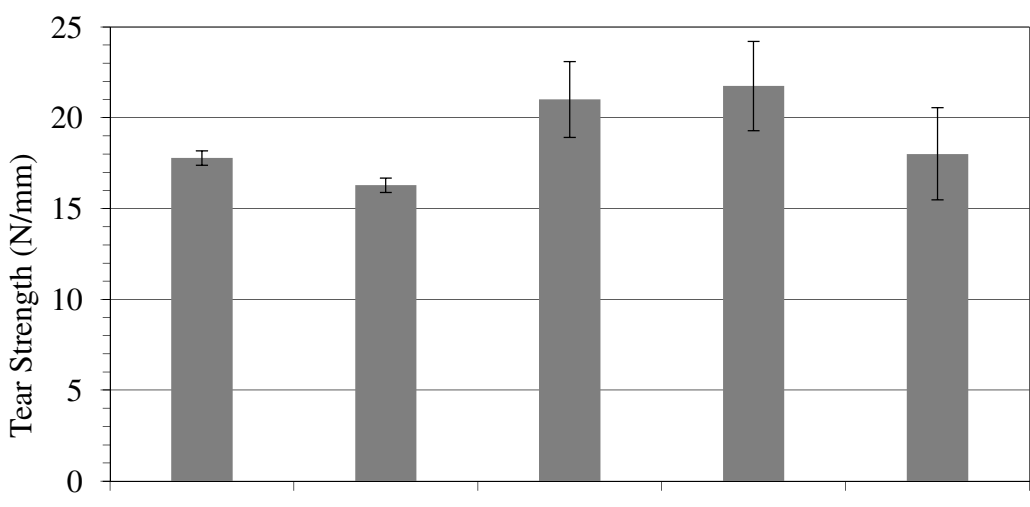


Figure 10 Tear strength of the vulcanized cast NR sheets filled with in situ silica generated by various types of alkoxysilane precursor, compared with silica-free sheets (VNR).

20T10E

20T10V

20T10M

25T

VNR

Figure 11 shows the results of tension set study. The tension set parameter, reflects the elasticity of rubber. It is the extent to which vulcanized rubber is permanently deformed after the film is stretched for a certain length and time. Here the tension set percentages of all *in situ* NR/silica dipped films were between 2.3 to 4.3%. No difference between the *in situ* silica-reinforced and non-reinforced samples was observed. The use of TEOS and other alkyltrialkoxysilanes to generate silica in the dipped film did not significantly affect to the tension set.

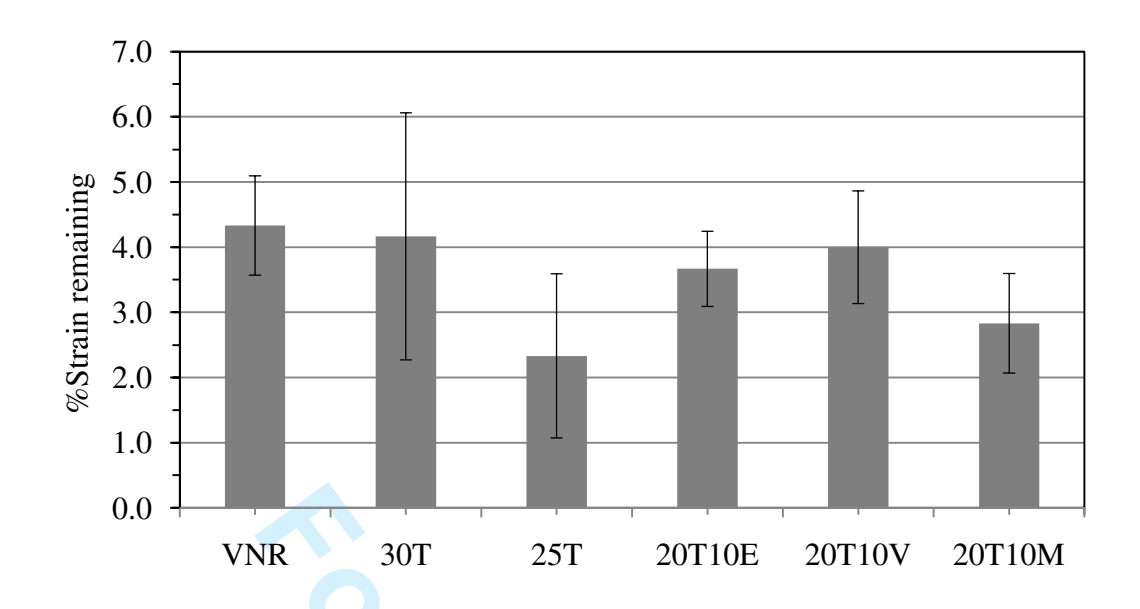


Figure 11 Result of tension set study of the dipped rubber films filled with *in situ* silica generated by various types of alkoxysilane precursor, compared with silica-free dipped rubber film (VNR).

Conclusion

Silicas with different alkyl groups were successfully generated in the vulcanized dipped NR films by the use of TEOS/alkyltriethoxysilane as precursors. Maturation of the silane-latex mixture for at 2 days was required in order to obtain high degree of silane-to-silica conversion. A single heating step was used to initiate sulfur-vulcanization of the rubber films as well as silica formation in the rubber matrix. By TEM, the *in situ* silica particles were observed around the NR particle. The size of silica particle was less than 100 nm, but it did not depend on the silane types. The SEM images and EDX analysis confirmed that the *in situ* silica particles were fairly dispersed inside the rubber matrix. The use of vinyl containing alkoxysilane to treat the surface of *in situ*-formed silica resulted in the vulcanizate that possessed higher tensile modulus than the other silanes. Based on the mechanical testing results, we believed that the unsaturation

submitted to 'Polymer International'

nature of the C=C double bond on the *in situ* formed silica could involve in the sulfur vulcanization process of the NR.

Acknowledgement

The research funding provided by Research Team Assistance Grant under Contract Number RTA5080004 from the Thailand Research Fund was highly acknowledged. Many thanks also go to Chemical Innovation Co., Ltd., Thailand, for mechanical testing facilities.

submitted to 'Polymer International'

REFERENCES

- 1. Mathew S, Varghese S, Rajammal G and Thomas PC, *J Appl Polym Sci* **104**: 58-65 (2007).
- 2. Castellano M, Conzatti L, Codta G, Falqui L, Turturro A, Valenti B and Negroni F, *Polymer* **46**: 695-703 (2005).
- 3. Kohjiya S and Ikeda Y, Rubber Chem Technol 73: 534-550 (2000).
- 4. Ikeda Y, Poompradub S, Morita Y and Kohjiya S, *J Sol-Gel Sci Technol* **45**: 299-306 (2008).
- 5. Poompradub S, Chaichua B, Kanchanaamporn C, Boosalee T and Prasassarakich P, *Kgk-Kaut Gummi Kunst* **61**: 152-155 (2008).
- 6. Chaichua B, Prasassarakich P and Poompradub S, *J Sol-Gel Sci Technol* **52**: 219-227 (2009).
- 7. Tangpasuthadol V, Intasiri A, Nantivanich D, Niyompanich N and Kiatkamjornwong S, *J Appl Polym Sci* **109**: 424-433 (2008).
- 8. Satraphan P, Intasiri A, Tangpasuthadol V and Kiatkamjornwong S, *Polym Adv Technol* **20**: 473-486 (2009).
- 9. Siramanont J, Tangpasuthadol V, Intasiri A, Na-Ranong N and Kiatkamjornwong S, *Polym Eng Sci* **49**: 1099-1106 (2009).
- 10. Watcharakul N, Poompradub S and Prasassarakich P, *J Sol-Gel Sci Technol* **58**: 407-418 (2011).
- 11. Hsiue GH, Chen JK and Liu YL, *J Appl Polym Sci* **76**: 1609-1618 (2000).
- 12. Chen G, Zhou S, Gu G, Yang H and Wu L, *J Colloid Interface Sci* **281**: 339-350 (2005).

submitted to 'Polymer International'

- 13. Bengtsson M and Oksman K, Compos Sci Technol 66: 2177-2186 (2006).
- 14. Xie Y, Hill CAS, Xiao Z, Militz H and Mai C, *Composites Part A* 41: 806-819 (2010).



$$C_{2}H_{5}O-Si-OC_{2}H_{5}$$

$$C_{2}H_{5}O-Si-OC_{2}H_{5}$$

$$TEOS$$

$$OC_{2}H_{5}$$

$$CH_{3}-CH_{2}-Si-OC_{2}H_{5}$$

$$OC_{2}H_{5}$$

$$ETOS$$

$$OC_{2}H_{5}$$

$$ETOS$$

$$OC_{2}H_{5}$$

$$ETOS$$

$$CH_{2}=CH-Si-OC_{2}H_{5}$$

$$OC_{2}H_{5}$$

Figure 1 Structures of tetraethoxysilane (TEOS), ethyltriethoxysilane (ETOS), vinyltriethoxysilane (VTOS), and methacryloxypropyltrimethoxysilane (MPS). $118 \times 154 \text{mm} \; (600 \times 600 \; \text{DPI})$

n Si
$$(OC_2H_5)_4$$
 + 2n H_2O (Si O_2)_n + 4n C_2H_5OH tetraethoxysilane silica ethanol

n R-Si(
$$OC_2H_5$$
)₃ + 1.5n H₂O (R-SiO_{1.5})_n + 3n C₂H₅OH alkyltriethoxysilane alkylated silica ethanol

Figure 2 Chemical equations of the conversion of TEOS to silica (top) and alkyltriethoxysilane to

Figure 3 Cross-condensation of alkyltrialkoxysilane (RTOS) and a silica particle from tetraethoxysilane (TEOS) precursor.

128x41mm (300 x 300 DPI)

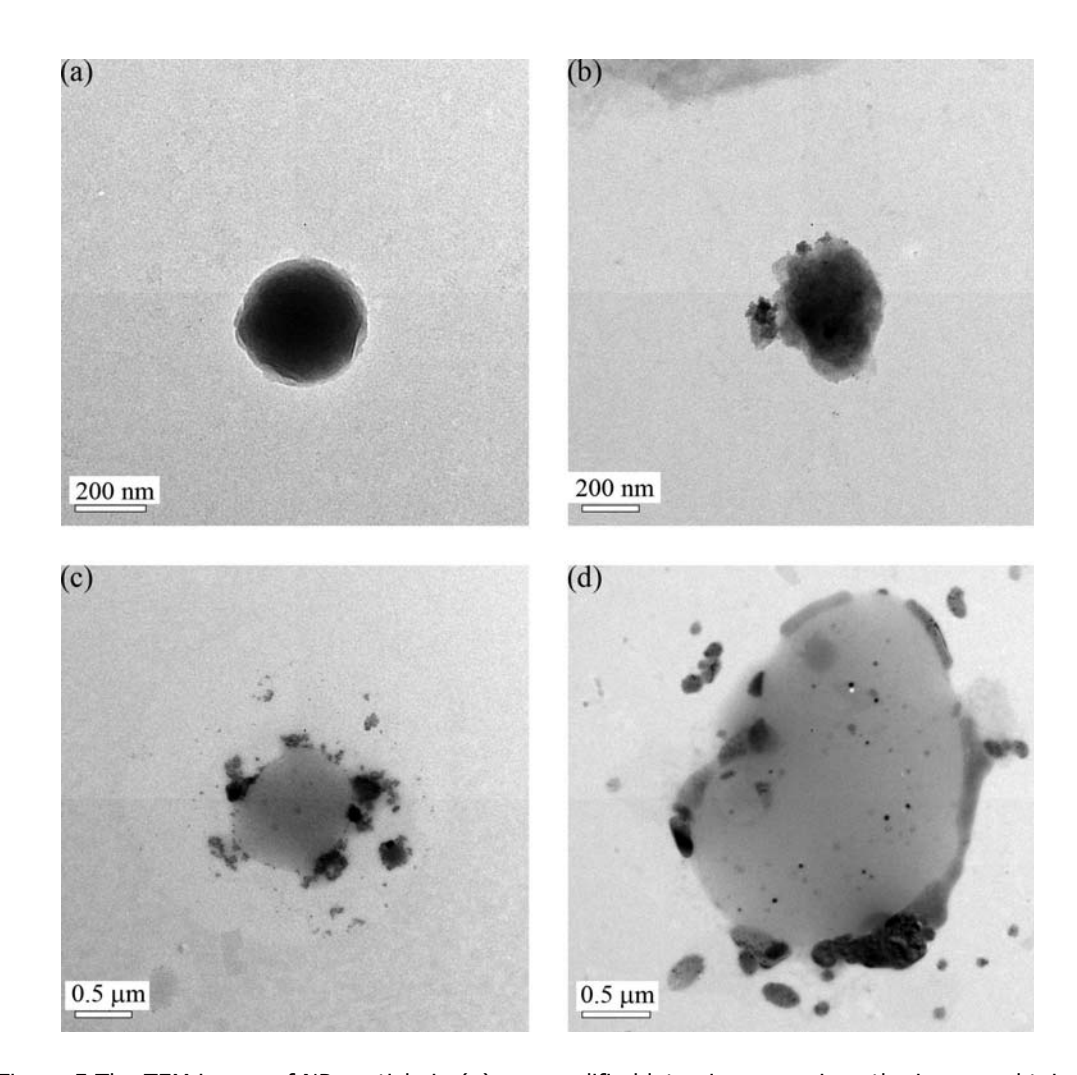


Figure 5 The TEM image of NR particle in (a)non-modified latex in comparison the images obtained from the latex that was mixed with (b)TEOS, (c)TEOS-VTOS, and (d) TEOS-MPS. The in situ-formed silica particles were seen as the dark spots surrounding the rubber core.

158x158mm (300 x 300 DPI)

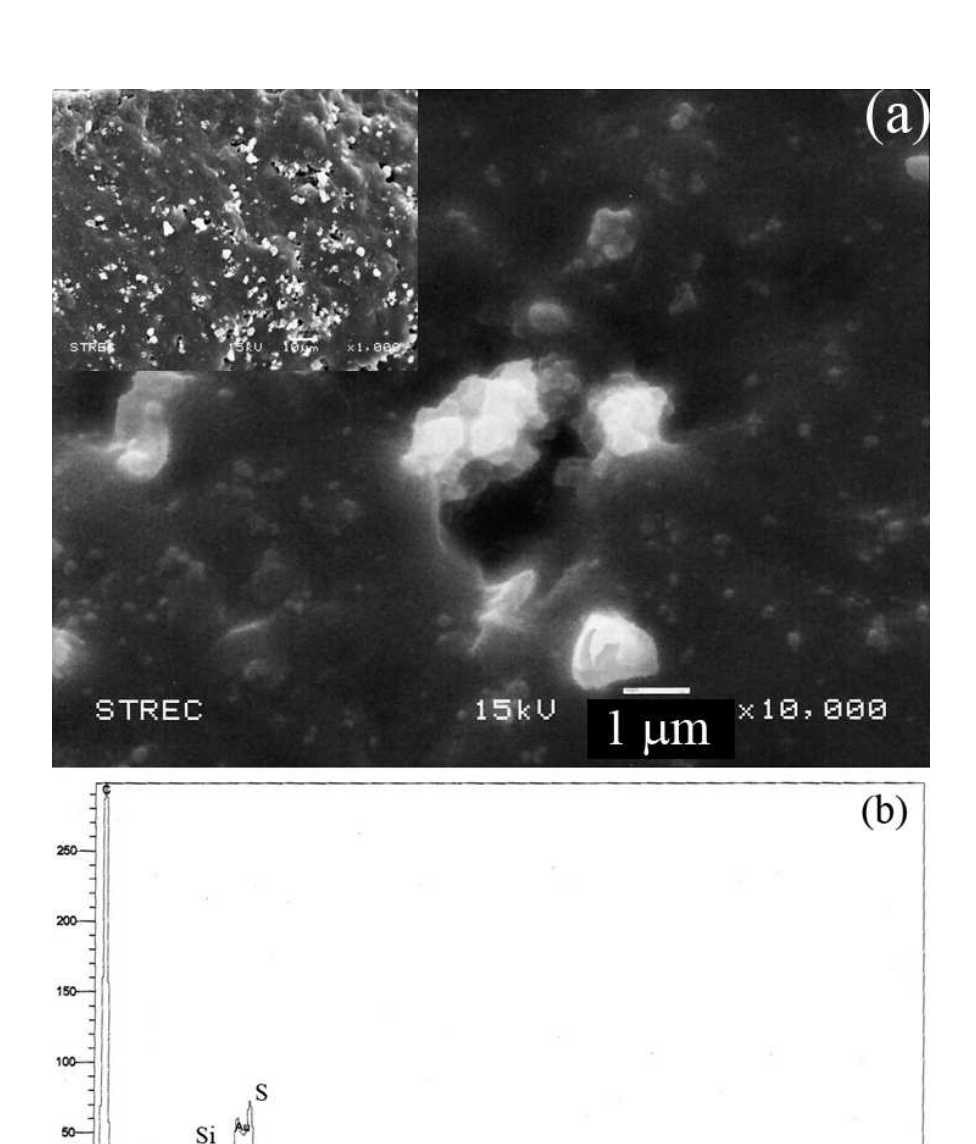


Figure 6 (a)The inset figure $(1,000\times)$ shows the distribution of in situ-formed silica obtained from the fractured surface of silica-NR vulcanizates (sample: 30T; 6.7 phr silica). The main image $(10,000\times)$ shows close-up detail of the silica aggregates. (b)The EDX spectrum of the shown area in the main image displays a series of elements, including Zn and Si. 60x81mm $(300 \times 300 \text{ DPI})$

Energy (keV)

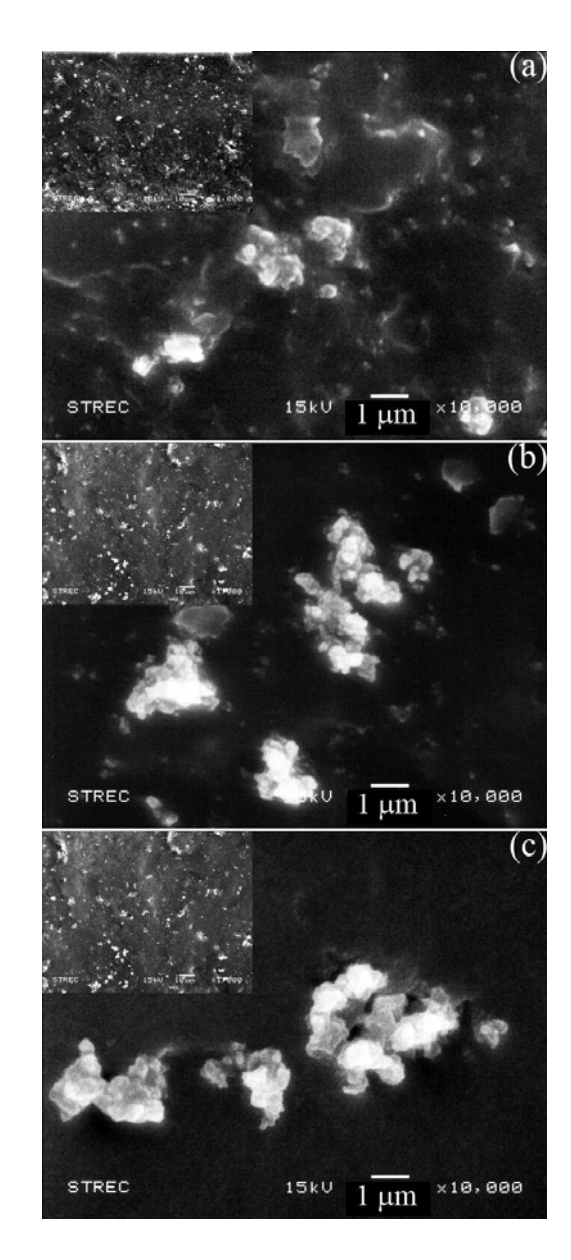


Figure 7 The SEM images show the distribution of in situ-formed silica (inset; $1,000\times$) and detailed silica aggregates (main; $10,000\times$) obtained from the fractured surface of silica-NR vulcanized films of (a)20T10V (silica: 5.2 phr), (b)20T10E (silica: 4.8 phr), and (c)20T10M (silica: 4.9 phr). 60x140mm (300 x 300 DPI)

Draft

Multilayer Film Assembled from Charged Derivatives of Chitosan: Physical Characteristics and Biological Responses

Wilaiporn Graisuwan^{1,2}, Cheeraporn Ananthanawat³, Oraphan Wiarachai^{1,2}, Songchan Puthong⁴, Suphan Soogarun⁵, Suda Kiatkamjornwong⁶, Voravee P. Hoven^{7*}

Program in Petrochemistry and Polymer Science, Faculty of Science, Chulalongkorn
University, Phayathai Road, Pathumwan, Bangkok 10330, Thailand
 Center for Petroleum, Petrochemicals, and Advanced Materials, Chulalongkorn University,
Phayathai Road, Pathumwan, Bangkok 10330, Thailand
 Program in Macromolecular Science, Faculty of Science, Chulalongkorn University,
Phayathai Road, Pathumwan, Bangkok 10330, Thailand
 The Institute of Biotechnology and Genetic Engineering, Chulalongkorn University,
Phayathai Road, Pathumwan, Bangkok 10330, Thailand
 Department of Clinical Microscopy, Faculty of Allied Health Sciences,
Chulalongkorn University, Phayathai Road, Pathumwan, Bangkok 10330, Thailand
 Department of Imaging and Printing Technology, Faculty of Science, Chulalongkorn
University, Phayathai Road, Pathumwan, Bangkok 10330, Thailand
 Organic Synthesis Research Unit, Department of Chemistry, Faculty of Science,
Chulalongkorn University, Phayathai Road, Pathumwan, Bangkok 10330, Thailand

RECEIVED DATE (to be automatically inserted after your manuscript is accepted if required according to the journal that you are submitting your paper to)

TITLE RUNNING HEAD. Multilayer film of charged chitosan

*To whom correspondence should be addressed. Tel: +66-2218-7627 ext 102. Fax: +66-2218-

7598. E-mail: vipavee.p@chula.ac.th

ABSTRACT. Polyelectrolyte multilayer films were assembled from charged derivatives of chitosan: *N*-[(2-hydroxyl-3-trimethylammonium)propyl]chitosan chloride (HTACC), *N*-succinyl chitosan (SCC), and *N*-sulfofurfuryl chitosan (SFC) and selected oppositely charged polyelectrolytes which are poly(acrylic acid) (PAA) and poly(allylamine hydrochloride) (PAH) successfully deposited on the surface-treated poly(ethylene terephthalate) (treated PET) substrates by alternate layer-by-layer adsorption. The assembly process was monitored by quartz crystal microbalance with dissipation (QCM-D). Stratification of the multilayer films was demonstrated by water contact angle data. The coverage of the assembled films was characterized by AFM. Biological responses of the assembled films were assessed in terms of *in vitro* cell adhesion and proliferation of fibroblasts, antibacterial activity, and protein adsorption. The *in vitro* cells study showed slightly alternating trend depending on the outermost layer. The multilayer film containing HTACC exhibited greater antibacterial activity against *E. coli* and *S. aureus* than the treated PET substrate and the control. The blood compatibility study suggested that (PAH/SFC) can reduce protein adsorption.

KEYWORDS. Charged derivative, Chitosan, Muitlayer film, Layer-by-layer, Cytocompatibility, Antibacterial activity, Antithrombogenicity

Introduction

The layer-by-layer (LBL) assembly technique, typically based on the alternating adsorption of oppositely charged polyelectrolytes, has been widely employed for the modification of biomaterial surfaces in order to render them bioactive, adhesive or non-adhesive for cells or specific microorganisms so that they can be used for biomedical applications. This versatile strategy, involving building up of thin multilayer film, is mostly driven by electrostatic interactions between a charged polyelectrolyte and an oppositely charged surface. The first adsorbed layer of polyelectrolyte from aqueous solution leads to the surface charge reversal and enables second adsorption of an oppositely charged polyelectrolyte. The process is simple and can be adapted for any type of substrate as long as the surface charge is present without the limitation of substrate topology. In principle, the thickness of the multilayer film can be varied as a function of adsorption variables as well as the number of deposition. Most importantly, the surface properties of the supported films are determined by the outermost layer that is last deposited.

Chitosan is considered as one of the most attractive natural polyelectrolyte often used for generating biocompatible surfaces via multilayer assembly. It is the partially deacetylated form of chitin, the second-most abundant natural polymer, mainly harvested from the exoskeleton of insects, marine crustaceans and fungal cell walls. Its favorable physico-chemical and biological characteristics such as biocompatible,² biodegradable,^{3,4} non-toxic,⁵ and antibacterial activity⁶ makes chitosan suitable for many bio-related applications. Besides, charged derivatives of chitosan exhibit diversified bioactivities. Quaternary ammonium chitosan, a positively charged derivative possesses superior antimicrobial activity^{7,8}. Succinyl chitosan, a negatively charged derivative, has favorable properties such as low toxicity and long-term retention in the body so it

was applied as a drug carrier. Sulfonated chitosan, another negatively charged derivative, on the other hand, is antithrombogenic. 10-12

Several researches have been reported on the formation of polyion complex multilayer films between chitosan and a number of anionic polyelectrolytes. Serizawa, *et al.*^{13,14} have revealed the alternating anti-vs procoagulation activity of ultrathin polymer films prepared from dextran sulfate and chitosan by the layer-by-layer assembly technique against human blood. Zhu, *et al.*¹⁵ assembled the multilayer films of poly(styrene sulfonate, sodium salt) (PSS) and chitosan to improve cytocompatibility of the poly(L-lactic acid) surface. Cai, *et al.*¹⁶ constructed a multilayer film using chitosan and gelatin on titanium in order to improve their biocompatibility. Fu, *et al.*¹⁷ generated multilayer films from heparin (anti-adhesive agent) and chitosan (antibacterial agent) on aminolyzed PET films. It was found that the multilayer films not only reduced the bacterial adhesion but also kill the bacteria adhered onto the surface. This desirable feature renders the multilayer film a powerful anti-infection coating for cardiovascular devices. Liu, *et al.*¹⁸ modified a surface of poly(ethylene terephthalate) (PET) by hydrolysis and built up multilayer films by alternative adsorption of chitosan and chondroitin sulfate. The *in vitro* cell culture revealed that the adherence of endothelial cells was enhanced on the multilayer-deposit PET film with their preserved function.

In our previous publication,¹⁹ we have demonstrated that the multilayer films can be successfully assembled from charged derivatives of chitosan (CHI), *N*-sulfofurfuryl chitosan (SFC) and *N*-[(2-hydroxyl-3-trimethylammonium)propyl]chitosan chloride (HTACC) on the plasma-treated PET. Alternate bioactivity of the multilayer assembly of three pairs of polycation/polyanion: CHI/poly(styrene sulfonate sodium salt) (CHI/PSS), poly(allylamine hydrochloride)/SFC (PAH/SFC), and HTACC/poly(acrylic acid) (HTACC/PAA) were realized

by testing against four proteins having different size and charge characteristic which are albumin, fibrinogen, γ -globulin, and lysozyme.

In the present study, we explore further on the insight into the physical characteristics of the multilayer films assembled from those charged derivatives that have been reported earlier (SFC and HTACC) as well as an additional negatively charged derivative, *N*-succinyl chitosan (SCC). For the first time, the internal structure, water content, and viscoelastic properties of the multilayer films were assessed by quartz crystal microbalance with dissipation mode (QCM-D). Three pairs of oppositely charged polyelectrolytes were investigated: HTACC/PAA, PAH/SCC, and PAH/SFC (Figure 1). Biological responses of selected multilayer systems were tested against fibroblast cells, bacteria, plasma proteins, and platelets. The consequence of this study should provide fundamental information that should be very useful for further development of these charged derivatives of chitosan for biomedical applications.

Polycations Polyanions CH₂CHCH₂N⁺(CH₃)₃Cl⁻ OH N-[(2-hydroxyl-3-trimethylammonium) propyl] chitosan chloride (HTACC) CH₂CH NH CH₂CH NH CH₂CH NH CH₂CH NH NH CH₂CH NH NH NH N-succinyl chitosan (SCC) N-sulfofurfuryl chitosan (SFC)

Figure 1. Polycations and polyanions used for multilayer assembly.

Experimental Section

Materials. Chitosan flakes (DAC of 95%, $M_{w=}$ 100,000 g·mol⁻¹) were obtained from Seafresh Chitosan (Lab) Co., Ltd. (Thailand). Succinic anhydride (SA) was purchased from May&Baker (England). 5-Formyl-2-furan-sulfonic acid, sodium salt (FFSA), poly(allylamine hydrochloride) (PAH), $M_{w} = 70,000 \text{ g·mol}^{-1}$, phosphate buffered saline (PBS), glycine, and a bicinchoninic acid assay kit (QuantiProTM BCA assay) were supplied by Sigma-Aldrich (USA). Heparin (HEP), $M_{w} = 4,000\text{-}6,000 \text{ g·mol}^{-1}$ was purchased from Fluka (USA). Triethanolamine, sodium borohydride

(NaBH₄), glycidyltrimethylammonium chloride (GTMAC), and poly(acrylic acid) (PAA), M_w = 60,000 g·mol⁻¹ were purchased from Fluka (Switzerland). Plasma-treated poly(ethylene terephthalate) films (i.d. = 14 mm) were supplied by Wako Pure Chemical Industry, Ltd. (Japan). Fibroblast L929 cells were purchased from American Type Culture Collection (ATCC) (USA). Fetal bovine serum (FBS) and RPMI medium 1640 were purchased from InVitromex (USA). Penicillin was purchased from General Drugs House Co., Ltd. Streptomycin was purchased from M&H manufactureing Co.,Ltd. (Thailand). E. coli and S. aureus were provided by National Center for Genetic Engineering and Biotechnology (BIOTEC), Thailand. Mueller-Hinton agar (MHA) and Mueller-Hinton broth (MHB) were purchased from Difco (USA). Mueller Hinton agar plate was supplied by Department of Medical Science, Ministry of Public Health, Thailand. The chemicals were of analytical grade and used as received without further purification. Ultrapure distilled water (Milli-Q water) was obtained after purification using a Millipore Milli-Q system (USA) that involves reverse osmosis, ion exchange and a filtration step. N-[(2hydroxyl-3-trimethylammonium)propyl] chitosan chloride (HTACC), N-sulfofurfuryl chitosan (SFC), and N-succinyl chitosan (SCC) were synthesized according to the method modified from that of Seong et al.⁷ Amiji.¹⁰ and Aoki et al.,²⁰ respectively. Detailed experimental procedures and chemical characteristics of all derivatives characterized by FT-IR spectrometer (Nicolet, model Impact 410, USA) and ¹H NMR spectrometer (Varian, model Mercury-400, USA) are available in Supporting Information Section.

Multilayer Assembly. Plasma-treated PET substrates were immersed in a solution of 1 M NaOH (aq) at 60°C for 1 h. After incubated for a given time, the substrates were taken out, washed with 0.1 M HCl (aq) for 10 min to rinse off NaOH. Finally, the substrates were rinsed thoroughly with Milli-Q water and air-dried at ambient temperature to obtain the surface-hydrolyzed PET films. After surface hydrolysis, the treated PET substrates were subjected to

multilayer assembly by sequentially dipping in a polycation solution (2 mg/mL of PAH, or 2 mg/mL of HTACC) and a polyanion solution (1 mg/mL of SCC, 2 mg/mL of SFC, or 2 mg/mL of PAA) for 20 min interval. The optimal concentration of each polyelectrolyte was identified by conventional QCM measurements as previously described. All polyelectrolytes were not buffered. For most of the experiments, the salt concentration of 0.1 M NaCl (aq) was added in both solutions. The pH of the solution was adjusted by using 0.1 HCl (aq) or 0.1 NaOH (aq). The substrates were rinsed thoroughly with Milli-Q water between each dipping and after the final adsorption. Three pairs of polyelectrolyte self-assemblies were fabricated: at pH 7 for HTACC/PAA and PAH/SCC, and at pH 8 for PAH/SFC.

Characterization of Deposited Multilayer Film. A contact angle goniometer model 100-00 equipped with a Gilmont syringe and a 24-gauge flat-tipped needle (Ramé-Hart, Inc., USA) was used for the determination of water contact angles. A droplet of Milli-Q water was placed on the tested surface by bringing the surface into contact with a droplet suspended from a needle on the syringe. The measurements were carried out in air at ambient temperature. The reported angle is an average of 5 measurements on different areas of each sample. The structure and morphology of the multilayer films were examined by atomic force microscopy (AFM). AFM images were recorded with a Scanning Probe Microscope; model NanoScope®IV, Veeco, USA. Measurements were performed in air at ambient temperature using a tapping mode. Silicon nitride tips with a resonance frequency of 267-298 kHz and a spring constant 20-80 N/m were used.

Analysis by Quartz Crystal Microbalance. The apparatus and the quartz crystals used for QCM measurements were obtained from Maxtek, Inc. (USA). An AT-cut quartz crystal with a fundamental resonance frequency of 5 MHz, model SC-501-1 was used. The plating crystal (1

inch in diameter) was covered by evaporated gold on both faces. The frequency shift of the goldcoated QCM plate was monitored by a Maxtek plating monitor (model PM-710) coupled with an MPS-550 sensor probe. The Data-Log Software (Maxtek) was used for data acquisition and monitoring. For QCM measurements with dissipation mode (QCM-D), a Q-Sense D300 (Q-Sense, Götenborg, Sweden) fitted with a Q-sense axial flow chamber was used for real-time simultaneous measurement of frequency and dissipation changes. An AT-cut piezoelectric crystal coated with gold electrodes on its two faces having a fundamental resonance frequency of 5 MHz (Q-Sense AB, Götenborg, Sweden) was excited at its fundamental frequency (n=1) as well as at the third, fifth, and seventh overtones (n = 3, 5, and 7, respectively) corresponding to 15, 25, and 35 MHz, respectively. The gold-coated QCM plate was cleaned by soaking in piranha solution (3:1 H₂SO₄:30% H₂O₂) for 5 min, rinsing thoroughly with Milli-Q water and drying with a light stream of nitrogen gas prior to use. The surface modification of the gold-coated QCM plate was carried out by immersion in an ethanolic solution containing 1:1 (v/v) of 10 mM 11mercaptoundecanoic acid and 10 mM 11-mercapto-1-undecanol at ambient temperature. After 24 h, the plate was rinsed with ethanol and dried with a light stream of nitrogen gas. For the QCM measurements in the conventional mode, one side of the gold-coated QCM plate was covered with a designated polyelectrolyte solution for a desired period of time, rinsed with Milli-Q water, dried with a light stream of nitrogen gas after each step of deposition and then the resonance frequency was measured in air. For the QCM-D measurements in real-time, one side of the goldcoated quartz crystal was kept in permanent contact with a designated polyelectrolyte solution and the frequency change was recorded continuously at ambient temperature.

Cell Adhesion and Proliferation Tests. The Fibroblast L929 cells were cultured in RPMI 1640 medium supplemented with 5% fetal bovine serum (FBS), penicillin (100,000 U/L) and

streptomycin (100 mg/mL). They were incubated at 37°C in atmosphere containing 5% CO_2 where the culture medium was changed every 3 days. Both the treated PET substrates with and without multilayer films were sterilized by soaking in 70% ethanol in water for 30 min and washed twice with RPMI medium 1640. The substrates were then transferred to cover the bottom of 96-well tissue culture polystyrene (TCPS) plate. Three replicated samples were used for each condition. Approximately 5×10^3 of L929 cells in 0.2 mL culture medium were pipetted into each well containing the substrates as well as blank wells made of tissue culture polystyrene (TCPS) as a control and then incubated under 5% CO_2 at 37°C. MTT assay was used to investigate cell adhesion and proliferation. After 12 h of incubation, the culture medium was removed to discard the unattached cell and the 0.2 mL fresh culture medium was pipetted into each well followed by $10 \mu L$ of 0.5 mg/mL MTT/normal saline solution. After incubation for 4 h, the supernatant solution was removed and 150 μL of DMSO was pipetted into each well to dissolve the purple crystals of formazan. Next, 25 μL of 0.1 M glycine (pH 10.5) was added. The optical density of the solution was measured using a microplate reader (MK II, Titertek Multiskan MCC/340, Finland) at the wavelength at 540 nm.

Antibacterial Activity Test. The antibacterial activity of the multilayer film of HTACC/PAA assembled on the treated PET substrates against the Gram-positive bacteria, *S. aureus* and Gramnegative bacteria, *E. coli* was assessed by viable cell-counting method. The treated PET substrates carrying multilayer films were sterilized by exposing to UV irradiation for 1 h prior to the tests. The substrates were placed one per well of a 24-well plate containing 2 mL Mueller-Hinton broth (MHB). Then 12 μ L of bacterial suspension in distilled water (OD₆₀₀ = 0.1) was pipetted into each well and the plate incubated in a shaking incubator (Model G-25, New Brunswick Scientific Co., Inc., USA) at 37°C, 110 rpm, for 24 h. A 100 μ L of each of the

bacterial suspensions was then transferred from each well and then diluted 10^4 times and $100~\mu L$ of this diluted bacterial suspension was then spread onto Mueller-Hinton agar (MHB). After incubating at $37^{\circ}C$ for 24 h, the number of colonies, and thus replication competent bacteria were then counted as a measure of assumed viability. The results, after correction for the dilution factor, were expressed as the mean number of colony forming units per volume (CFU/mL). All tests of antibacterial activity were performed in triplicate per sample and upon at least three independent samples.

Preparation of Platelet-rich Plasma (PRP) and Platelet-poor Plasma (PPP). Human whole blood (100 mL) from a healthy volunteer was collected into a sterile plastic syringe and mixed with 3.8 %(wt/v) sodium citrate in PBS (1 mL:10 mL blood). To obtain the platelet-rich plasma (PRP) for *in vitro* static platelet adhesion testing, ^{21,22} the human whole blood was centrifuged at 1,200 rpm for 10 min. After centrifugation, the red blood cells and platelets were separated into 2 layers. The PRP as yellowish solution (top layer) was carefully withdrawn via micropipette. Subsequently, a portion of PRP was taken and then centrifuged at 2,000 rpm for 15 min to obtain the platelet-poor plasma (PPP) to be used for protein adsorption test. ^{21,22}

Determination of the Total Amount of Adsorbed Human Plasma Protein. The multilayer films of PAH/SFC and PAH/HEP assembled on the treated PET substrates were placed into 24-well tissue culture plate containing deionized water and hydrated overnight to reach an equilibrium hydration before experiment. Triplicate samples were used (n = 3). Each sample was removed from deionized water and suspended into the well containing 1.0 mL of PPP and incubated at 37°C for 3 h. After incubation, the samples were removed from PPP and followed by rinsing twice with PBS to remove any loosely attached protein. The adsorbed protein on the

sample surface was detached by soaking each sample in 1.0 mL of 1 %(wt/v) aqueous solution of sodium dodecyl sulfate (SDS) for 30 min. A 100 µL of SDS solution which socked each sample was pipetted into 96-well tissue culture plate. The solution was then mixed with 100 µL of BCA working solution in each well and followed by incubation the well-plate at 37°C for 2 h. The absorbance of the solution was measured at 562 nm by UV microplate reader (Microtiter plate reader; Model Sunrise, Tecan Austria GmbH). The amount of protein adsorbed on the samples was calculated from the protein concentration in SDS solution. The data were express as mean ±standard deviation (S.D). A protein analysis kit based on the bicinchoninic acid (BCA) method was used to determine the concentration of the protein dissolved in the SDS solution.

Evaluation of Platelet Adhesion. The multilayer films of PAH/SFC and PAH/HEP assembled on the treated PET substrates were put into the 24-well TCPS and hydrated overnight in PBS. After PBS was removed, the samples were immersed in 1 mL of freshly prepared PRP and incubated at 37°C for 1 h. After incubation, samples were gently rinsed with PBS to remove loosely adherent platelets from the surface and then treated with 2.5% glutaraldehyde in PBS to fix the platelets adhered to the surfaces for 1 h at ambient temperature. Finally, the samples were washed again with PBS and then subsequently dehydrated with gradient immersion of ethanol/water solutions (50, 60, 70, 80, 90, 95, and 100 vol.-%) for 10 min each and dried *in vacuo* overnight. The substrates were then sputter-coated with gold for the scanning electron microscope characterization (JEOL Model JSM-5410LV, Japan).

Statistical Analysis. Statistical analysis of cell adhesion/proliferation tests, antibacterial activity test, and protein adsorption are expressed as the means±standard deviations (S.D.) of a representative of three similar experiments carried out in triplicate. Statistical analysis was

performed using the Statistical Package for the Social Science (SPSS) version 14.0 software. Statistical comparisons made by One-Way Analysis of Variance (ANOVA) with the Least Square Difference (LSD) tests were used for post hoc evaluations of differences between groups. The threshold level for accepting statistical significance was set at p < 0.05.

Results and Discussion

Physical Characteristics of Multilayer Assembly. QCM is an effective tool to investigate the growth of multilayer film. It is an ultrasensitive mass sensor, consisting of a piezoelectric quartz crystal sandwiched between a pair of electrodes. When a suitable RF voltage is applied across the electrodes, the quartz crystal oscillates at its resonant frequency; a small layer added to the electrodes induces a decrease in resonant frequency ($\triangle F$). If a rigid layer is deposited on one or both sides of the electrodes, the resonant frequency will decrease proportionally to the mass of the absorbed layer according to the Sauerbrey equation: ²³

$$\Delta F = \frac{-2F_0^2 \Delta m}{A \left(\rho_q \mu_q\right)^{1/2}} \tag{1}$$

In Equation (1), ΔF = measured frequency shift, F_0 = fundamental frequency of the crystal, Δm = mass change per unit area, A = piezoelectrically active area, ρ_q = density of quartz (2.648 g/cm³), and μ_q = shear modulus of quartz (2.947×10⁶ N/cm²). Typically, the relationship between the frequency shift and the adsorbed mass per unit area (Δm) is linear obeying the Sauerbrey equation, Equation (2):

$$\Delta m = -C\Delta F/n \tag{2}$$

where C is the mass sensitivity constant (17.7 ng·cm⁻² Hz⁻¹ at 5 MHz), and n is the overtone number. In addition, dissipation can be characterized by the dissipation factor D, which is defined by Equation (3):

$$D = \frac{E_{dissipated}}{2\pi E_{stored}}$$
(3)

where $E_{dissipated}$ is the energy dissipated during one oscillation and E_{stored} is the total energy stored in the oscillating system. With the QCM-D measurements, the change in dissipation factor, $\Delta D = D - D_0$ is deduced, where D_0 is the dissipation factor of the pure crystal in solvent before adsorption and D is the dissipation factor after adsorption.

In this research, QCM analysis was conducted on a thiol-modified gold-coated QCM plate containing an equal composition of COOH and OH groups which is used as a model for treated PET substrates which were later subjected to multilayer assembly and determination of biological responses. Its water contact angle of 55° being close to that of the treated PET substrate (53°) suggests that it can satisfactorily mimic the treated PET substrate. Figure 2 displays the evolution of the normalized frequency changes ($\Delta F/n$) on the 3rd, 5th, and 7th overtone numbers and the corresponding changes in energy dissipation on the 3rd overtone number versus time of three multilayer systems as measured by QCM-D. At time (t) = 0 min, a stable baseline starting with 0.1 M NaCl was first established prior to adsorption of polyelectrolyte. At t = 5 min, a polycation (HTACC or PAH) solution was injected into the measurement chamber and allowed to adsorb for

5 min before the rinsing step began. After rinsing with 0.1 M NaCl for 5 min, at t = 15 min, the polyanion (PAA, SCC, or SFC) solution was then introduced followed by the same rinsing procedure. The adsorption and rinsing cycles were repeated until 10 individual layers of the polyelectrolyte were deposited. The change in frequency (ΔF) and dissipation (ΔD) throughout the building-up process were continuously observed indicating the stepwise deposition of the polyelectrolyte molecules to the QCM substrate. The fact that the $\Delta F/n$ of all three overtones can be superimposed throughout the whole range investigated strongly indicates that the assembled films are relatively rigid, not viscoelastic and that the adsorbed mass can be calculated from the observed frequency shift following Sauerbrey relationship.

For the HTACC/PAA system, an increase in ΔD and a decrease in $\Delta F/n$ were apparently more dramatic in the step of HTACC deposition (odd layer) as opposed to those in the step of PAA adsorption (even layer) suggesting that the HTACC layer was less rigid and perhaps greater in thickness than the its negatively charged counterpart, PAA. To explain such scenario, it is conceivable to take the comparative charge density of the HTACC and PAA into consideration. With 78% degree of substitution (%DS) of positively charged quaternary ammonium entities (N(CH₃)₃⁺), HTACC should be less charged than PAA, a weak polyelectrolyte having a pKa of 4.3^{24} at pH 7. Therefore, HTACC can adopt less extended conformations at the interface with a higher proportion of loops and tails than PAA. Not only can that bring in more HTACC chains to adsorb and yielded a thicker layer than did the PAA, but such coil-like conformation should also be able to trap more water molecules within its structure. These two reasons are believed to be responsible for the substantial difference in the decrease in $\Delta F/n$ and the increase in ΔD upon the adsorption between HTACC and PAA. It was not totally unexpected to observe a collapse of the entire multilayer film towards the interface upon the adsorption PAA. Its greater charge density as compared with HTACC makes the interpenetration and complexation/crosslinking between

the oppositely charged polyelectrolytes resulting in intrinsic charge compensation at the interface much more efficient. The stiffening of the adsorbed multilayer together with the preferably extended conformation led to a thinner layer of PAA having presumably less coupled water within its structure.

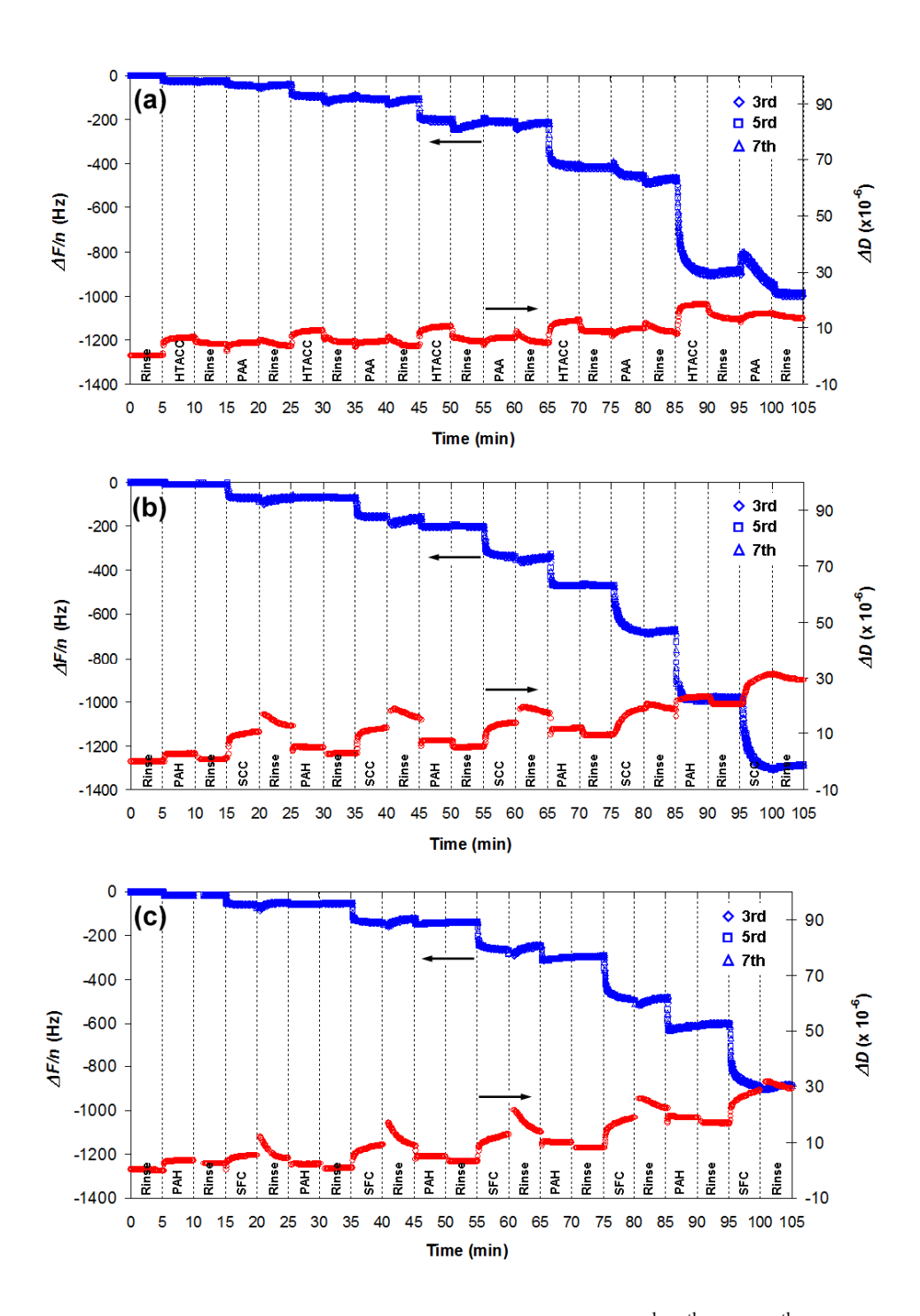


Figure 2. The change in normalized frequency $(\Delta F/n)$ on the 3rd, 5th, and 7th overtones and the energy dissipation change (ΔD) on the 3rd overtone as a function of time upon consecutive adsorption of polyelectrolytes for 3 multilayer systems: (a) HTACC/PAA, (b) PAH/SCC, and (c) PAH/SFC.

The odd-even effect in terms of $\Delta F/n$ and ΔD variation was also evidenced on other two multilayer films, PAH/SCC and PAH/SFC, both of which were assembled from the same cationic polyelectrolyte, PAH (Figure 2 (b) and (c)). The explanation based on the charge density should also be valid. As a consequence of the incomplete substitution of negatively charged entities at the NH₂ position on the chitosan backbones, SCC with 44% DS (of N-succinyl groups) and SFC with 68%DS (N-sulfofurfuryl groups) should be less charged than PAH, a weak polyelectrolyte having a pKa of 9.67.25 At pH 7-8 at which PAH/SCC and PAH/SFC multilayer films were assembled, 98-99% of -NH₃⁺ of PAH remained undissociated. This is the reason why an increase in ΔD and a decrease in $\Delta F/n$ were appreciably much greater in the step of SCC and SFC deposition (even layer) than those in the step of PAH adsorption (odd layer) suggesting that the SCC and SFC layers were thicker and presumably more water-rich than their positively charged counterpart, PAH. The higher charge density of the PAH facilitated interfacial crosslinking between the oppositely charged polyelectrolytes and so thus imparted the collapse of the film upon its deposition. This suggests that the properties of multilayer thin film depend on which the adsorbed layer in the outermost layer. Evidently, it can be concluded that all three multilayer films have a relatively compact, rigid internal structure and the differences in the observed dissipation are determined by the interfacial properties of the last deposited layer.

The water content of each individual layer for all three multilayer systems can be estimated from the mass per unit area for dry films (m_d) and wet film (m_w) following Equation (4): ²⁶ It should be emphasized that m_d and m_w were calculated based on the assumed density of the dry films (1.2 g/cm³)²⁷ by Sauerbrey equation from ΔF obtained from QCM and QCM-D measurements, respectively.

% water content =
$$\frac{m_w - m_d}{m_w} \times 100$$
 (4)

According to the results shown in Figure 3, the water contents of all three multilayer pairs are relatively high with all values being above 60%. The alternating trend of the water content between the odd and even layer was only observed at initial stage of assembly process (up to 4-7 layers). The water contents tended to level out at 85-90% between 7-10 deposited layers. Together in the same figure, the dried adsorbed mass determined by QCM was plotted to demonstrate that the odd-even effect of $\Delta F/n$ and ΔD variation analyzed by QCM-D as previously shown in Figure 2 and the m_w displayed in Figure S1 (Supporting Information) at the early stage of deposition was very much influenced by the different content of associated water within each individual layer between the odd and even layer. Once the assembly process was well established (from 5 layers onward), the odd-even fluctuation of both $\Delta F/n$ and ΔD was no longer governed by the entrapped water, but mainly dictated by the varied amount of the adsorbed polyelectrolyte which is dependent on its charge density and conformation

It is not unprecedented to see an exponential growth of deposited mass and thickness (Figure S2 in Supporting Information) in the investigated range for all three multilayer systems. Schlenoff and Dubas²⁸ described this initial nonlinear growth regime as a result of excess charge profile being truncated by the impenetrable multilayer. Ladam and co-workers²⁹, on the other hand, suggested that there are polyelectrolyte chains diffusing into and out of the film during the buildup process. It was proposed that free polyelectrolyte chains within the multilayer film diffuse out to form complexes with the oppositely charged polyelectrolytes at the surface upon the change of the bulk solution to one with polyelectrolytes of opposite charge. And that would

promote the adsorption of more material on the surface in each adsorption step than that should be expected from the regular charge compensation.

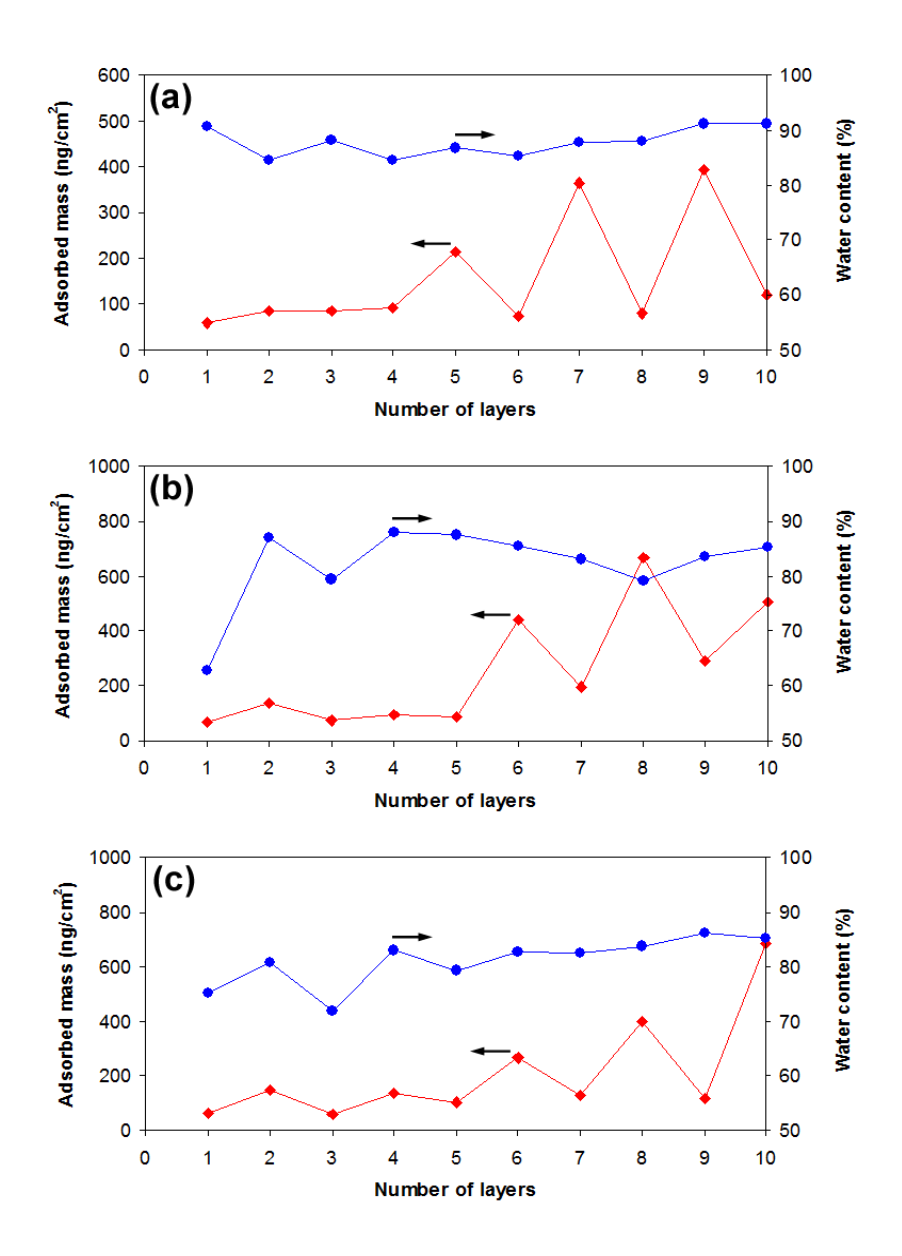


Figure 3. Water content (•) and mass per unit area for dry films (m_d) determined by QCM (◆) as a function of layer number for 3 multilayer systems: (a) HTACC/PAA, (b) PAH/SCC, and (c) PAH/SFC

Surface Coverage and Wettability of the Multilayer Films. In this research, the plasmatreated PET plates, commercially available and commonly used polymeric materials for biomedical and biomaterials applications, were employed as substrates for multilayer assembly. After the treatment by basic hydrolysis, the treated PET substrate with a water contact angle of 53° and carboxyl group density of 1.46 x 10⁻⁸ mol/cm² as estimated by Toluidine blue O assay were obtained. 19 The coverage of the deposited multilayer films was monitored by AFM analysis. Upon basic hydrolysis, the treated PET substrate became rougher as can be evidenced from the root-mean-square roughness (R_{rms}) being increased from 1.76 to 7.68 nm (micrographs not shown). As illustrated in Figure 4, the surfaces became apparently smoother after the deposition of HTACC/PAA multilayer. A similar trend was also observed for the system of PAH/SCC, except that the roughness of the even layer (having SCC as the outermost layer) seemed to be rougher than their adjacent odd layer (having PAH as the outermost layer). In contrast, the assembled PAH/SFC film became increasingly rougher upon the growth of the multilayer film implying that the defects or aggregates generated during the deposition of the first layers have been accumulated in the consecutive layer. The adsorbed polyelectrolyte that was expected to fill previously formed valleys on the surface and smoothened the film, in turn made the film rougher. This may be explained as a consequence of the loosely bound polyelectrolyte form complexes upon partial or total desorption and deposited back into the assembled layer during the adsorption process. Apparently, the interdigitation was less perfect in this particular case. The fact that the surface roughness of the film having the chitosan derivative (HTACC, SCC or SFC) as the top layer were always greater than that having its oppositely charged polyelectrolyte (PAA or PAH) as the top layer agree quite well with the QCM data which previously indicated that all chitosan derivatives with their lower charge density than their counterparts adsorbed in the less extended and more loop-like conformations and yield thicker individual layer. And that can be the origin of the odd-even topographic variation. Nonetheless, it can be assumed that the assembled films grow homogeneously when the size of the roughness and the pores is far larger than molecular sizes of polyelectrolytes and smaller than the average thickness of a single bilayer. (Table S1 in Supporting Information)

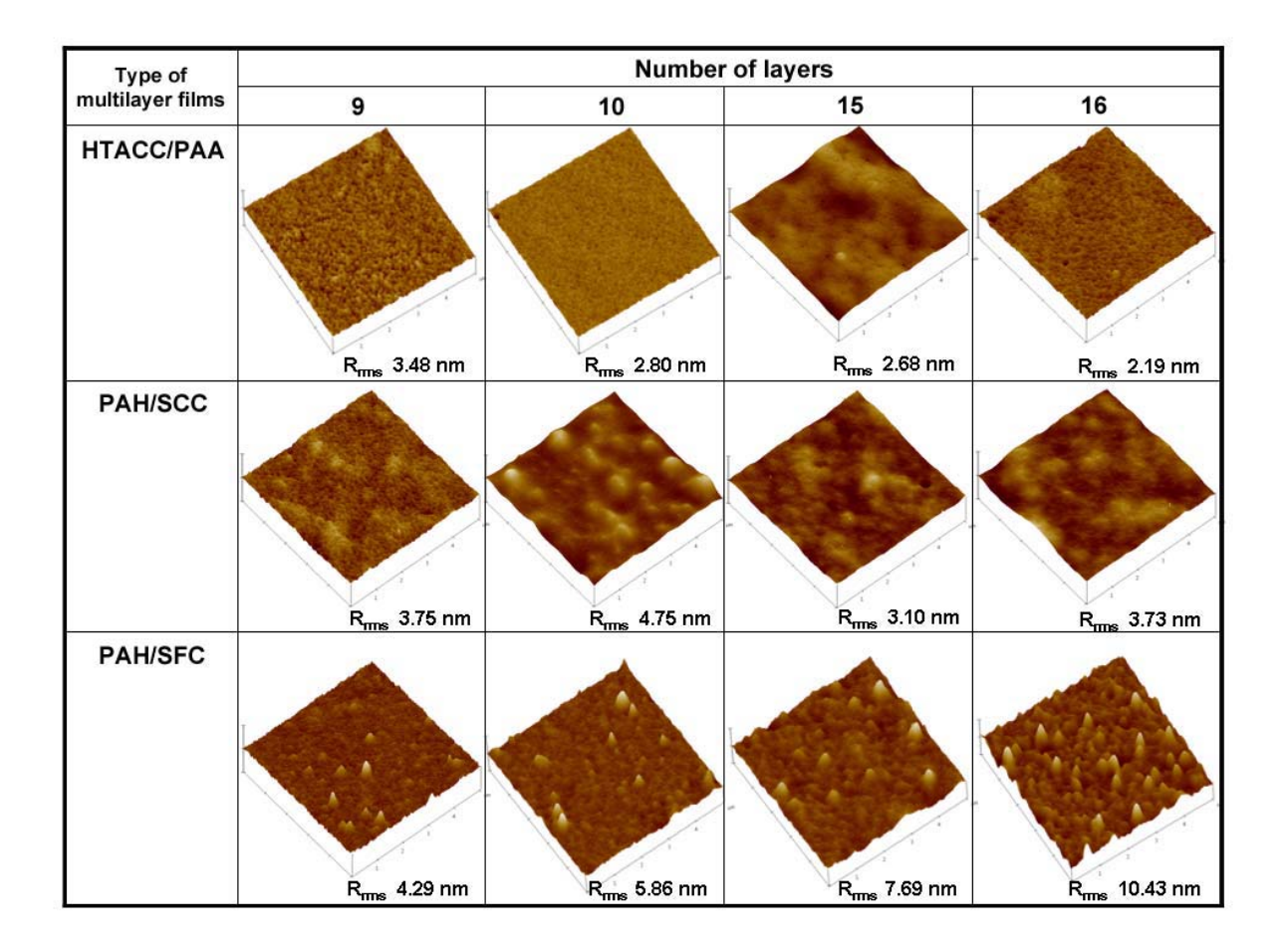


Figure 4. AFM images $(5x5 \mu m^2)$ of treated PET substrates with three multilayer systems: HTACC/PAA, PAH/SCC, and PAH/SFC. The value listed under each micrograph is the corresponding root-mean-square roughness $(R_{rms.})$ for each micrograph.

The wettability of the multilayer film was probed by water contact angle measurements. The results depicted in Figure 5 suggested that the assembled film was stratified. And the films

having the odd number of deposited layer and positively charged was more hydrophobic than those having an even number of deposited layer and negatively charged. The odd-even wetting behavior coincides with the fact that each individual layer based on QCM analysis (half of the bilayer thickness shown in Table S1) is thicker than the sampling depth of contact angle measurement (a few Å) so that the wettability of the multilayer film is strongly determined by the last layer deposited and the influence of the underlying layers was not observed.

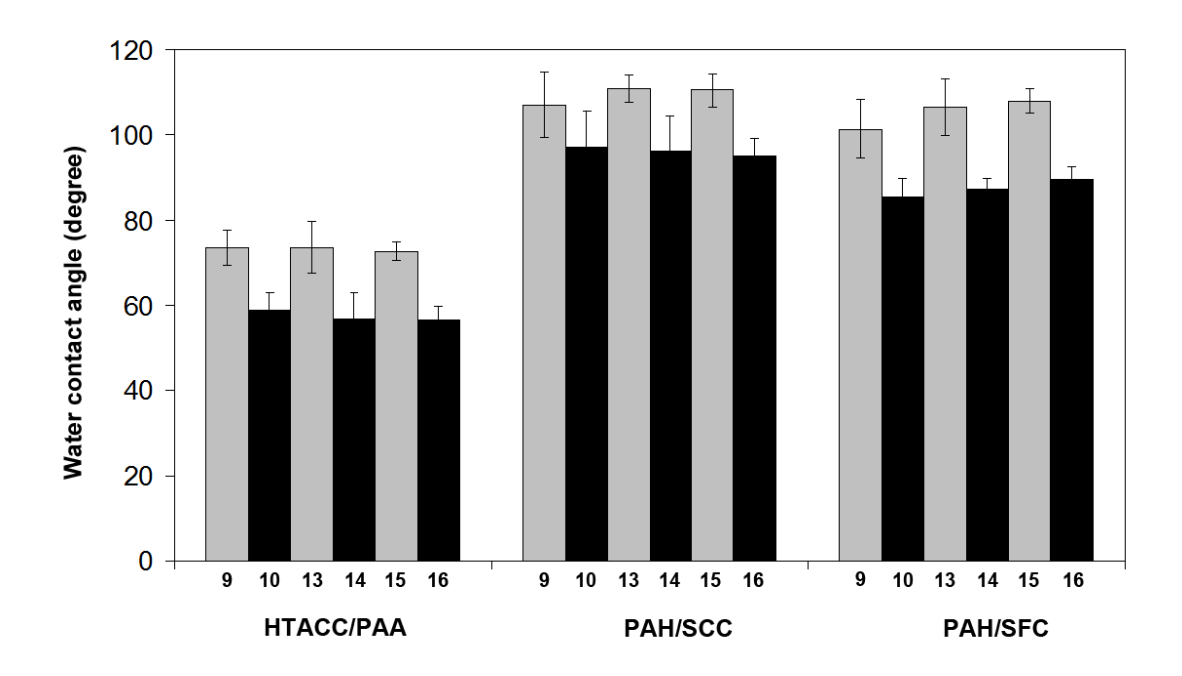


Figure 5. Water contact angle of multilayer films assembled on treated PET substrates. The number appearing on the horizontal scale represents the number of depositions.

Cell Adhesion and Proliferation. The *in vitro* cytocompatibility of three multilayer systems, on the treated PET substrates was carried out against L929 fibroblasts. To investigate the mitochondrial functions of the cultured L929, reduction of MTT reagent was used as an assay to measure mitochondrial redox activity. MTT reagent is a pale yellow substance that is reduced to a dark blue formazan product when incubating with viable cells by mitochondrial succinate

dehydrogenase in complex II, which plays a critical role in both oxidative phosphorylation and tricarboxylic acid cycle. Therefore, the production of formazan can reflect the level of cell viability. The results shown in Figure 6 are reported in terms of the cell adhesion (after 12 h incubation) and proliferation ratio (after 48 and 96 h incubations) with relative to TCPS. The number appearing on the horizontal scale represented the number of deposition. If the number of layer is odd, the charge of the outermost layer is positive. If the number of layer is even, the charge of the outermost layer is negative.

Considering the HTACC/PAA system, the multilayer film having the even number of layer with PAA as the top layer seems to be more favorable for both cell adhesion and proliferation than those having the odd number of layer with HTACC as the top layer. The effectiveness of PAA in promoting positive cellular responses is equivalent to the TCPS which was used as a positive control. It is generally known that the cell membrane possesses negative charges. The opposite charges of HTACC should lead to a strong attraction with the cells and causes detrimental influence on the cells. The effect is more pronounced after 4 days of incubation. It has been previously reported that HTACC exhibit potent antibacterial activity. ^{7,8} And this may be the reason why it is not a favorable substrate for promoting cell growth and maintaining cell viability.

As opposed to the system of HTACC/PAA, the PAH/SCC multilayer films exhibit the opposite tendency. After 2 and 4 days of incubation, a significant improvement of cell adhesion was observed, especially when the number of layer was equal to 15 and PAH was the top layer. Unlike HTACC, PAH is a weak synthetic polyelectrolyte that has been found to enhance early cell adhesion in the multilayer system of (PSS/PAH)³⁰ when it is the outermost layer of the film. The fact that SCC bears some negative charge, which is the same charge as the cell membrane, can explain why it is unfavorable for cell attachment. Evidently, the hydrophilic nature is not

enough to counteract the charge repulsion. However, the same explanation cannot be applied with PAA. A similar trend was observed in the case of PAH/SFC system. In particular, the 9-layer multilayer film with PAH as the outermost layer gave significantly higher in both cell adhesion and proliferation than the treated PET substrate. The charge repulsion may also account for the inferior cellular responses of the multilayer films having SFC as the top layer. The cellular responses seem to be worse as a larger number of layers were deposited. There may be some influence from the increased roughness (See AFM data).

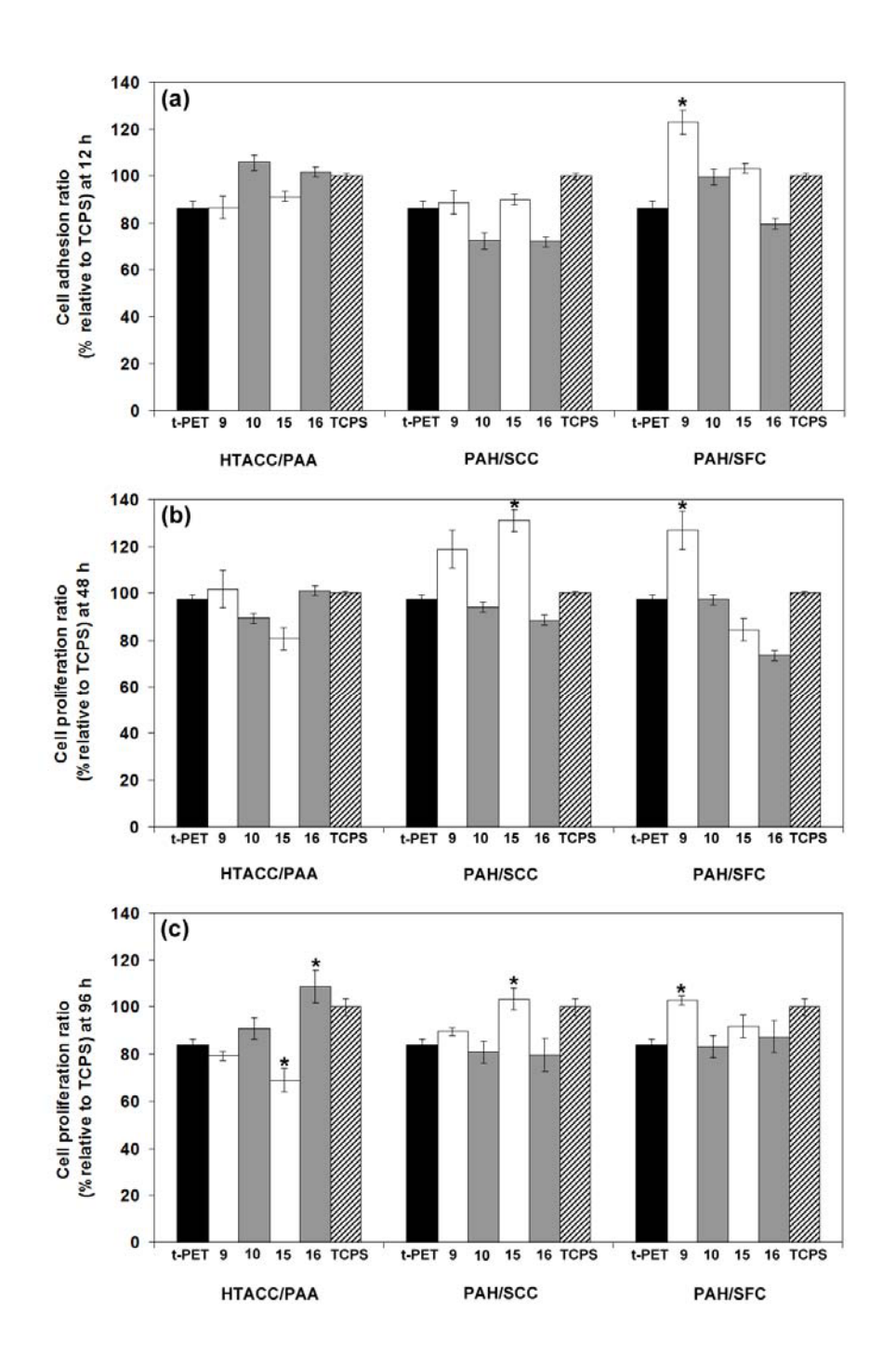


Figure 6. Responses of L929 cells (% relative to TCPS) with a seeding density of 5.0×10^3 cells/well on treated PET substrates with three multilayer systems in terms of (a) cell adhesion ratios at 12 h and cell proliferation ratios at (b) 48 and (c) 96 h. Statistical significance with p < 0.05 is compared with the control (t-PET) (*).

Antibacterial activity of the HTACC/PAA Multilayer Film. HTACC has been known to deliver desirable antibacterial activity when used in the soluble form^{31,32} and chemically grafted or coated on materials.7 Here, we anticipate that a similar antibacterial action can also be achieved when HTACC is deposited as assembled layers on any substrates. In this research, the antibacterial activity of the HTACC/PAA multilayer deposited on the treated PET substrate was tested against the Gram-positive and Gram-negative representative bacteria, S. aureus and E. coli, respectively, in terms of the total number of replication competent (viable) cells as mean colony forming units per volume (CFU/mL). The tested results are displayed in Figure 7 in which the number appearing on the horizontal scale represents the number of depositions. If the number of layers is odd (9 and 15), HTACC was the last layer deposit. If the number of layers is even (10 and 16), PAA was the last layer deposit. In the case of S. aureus, the detrimental effect was detected for the HTACC/PAA multilayer films having 15 and 16 layers. The former seemed to possess greater activity than the latter considering its %antibacterial ratio reached 70.5% as opposed to 57.8% of the latter. This can be expected taking into account that the surface of S. aureus consists of negatively charged teichoic acid within a thick peptidoglycan layer and lacks of an outer membrane. Such characteristic should render the bacterial cell more attractive to and easier to be damaged through the contact-inhibitory mechanism when exposed to the positively charged 15-layer film than the negatively charged 16-layer film.

In contrast, the damaging impact on *E.coli* was observed on the multilayer film having at least10 layers with only a slight odd-even effect was observed between the multilayer film having 15 and 16 deposited layers. The lower antibacterial potency of the multilayer film against *E.coli* than that against *S. aureus* may be explained as a result of the different bacterial membrane structures. Unlike *S. aureus*, *E. coli* has a double protective layer: the outer lipopolysaccharide layer embedded with a number of small channels of porins and the inner peptidoglycan layer (7-8).

nm). The fact that it does not contain the negatively charged entities that can electrostatically interact with HTACC makes it less sensitive to be destroyed by positively charged molecules like HTACC. Although HTACC was not the top layer of the 16-layer HTACC/PAA film, the substrate exhibits favorable cellular responses (See Figure 6), it can introduce a reasonable antibacterial property (~50% antibacterial ratio) against both bacterial strains to the multilayer film. This is a desirable characteristic for biomaterials applications given that the film supported cell attachment and proliferation and at the same time appreciably prevented bacterial growth. Also, it should be emphasized that HTACC can be used as an effective material for antibacterial coating especially against bacterial strains having negatively charged cell membrane, *S. aureus* in this particular case.

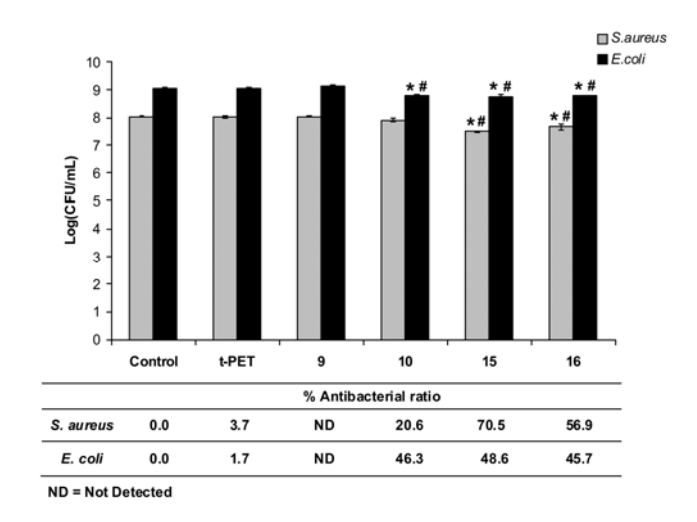


Figure 7. Total replication competent (viable) cell counts of bacteria grown for 24 h in media alone (control) or in the presence of treated PET substrate (t-PET) and multilayer film of HTACC/PAA assembled on treated PET substrate. The number appearing on the horizontal scale represents the number of depositions. Statistical significance with p < 0.05 of the viable count is compared with the control (*) and t-PET (#). Below in the table is the corresponding antibacterial ratio.

Antithrombogenic Properties of the PAH/SFC Multilayer Film. It has been previously demonstrated that SFC in a soluble or a surface-coated form expresses antithrombogenic property^{10,11,33} a necessary feature for the development of materials to be used in contact with blood. This can be derived from the presence of sulfonic acid groups in its structure, the same negatively charged moieties present in heparin (HEP), a well-known and widely used anti-blood coagulation polymeric material. In principle, when a material is in contact with blood, a surface-induced thrombosis is initiated by adsorption of plasma proteins, followed by the adhesion and activation of platelets.²¹ Herein, for the first time, the anticoagulating characteristic of SFC in the assembled form (PAH/SFC) was assessed in terms of amount of adsorbed plasma protein/surface area (mean±S.D.) and platelet adhesion of which results are illustrated together in Figure 8. The investigation was done in comparison with the multilayer films assembled from HEP and the same cationic polyelectrolyte, PAH.

As anticipated, the amount of adsorbed protein on the multilayer film having the odd number of layer with PAH as the top layer (9-layer and 15-layer) was greater than those having the even number of layer with SFC and HEP as the top layer (10-layer and 16-layer). It is generally known that under normal physiological condition at pH 7.4, the human serum carries negative charge due to the presence of albumin, its major protein component having the isoelectric point of $4.8.^{22}$ Thus, the plasma proteins can favorably interact with cationic polyelectrolyte, PAH with a pKa of 9.67^{25} in this particular case, mainly through electrostatic interactions. On the other hand, the amount of adsorbed protein was approximately 31-33% and 48-62% reduced on the assembled films terminating with SFC and HEP (the 10-layer and 16-layer), respectively when compared with that on the treated PET surface. This can be described as a result of the electrostatic repulsion between the negatively charged entities in the SFC and HEP layer and the plasma proteins. It should be emphasized that the negative charges in HEP do not only come from the

sulfonate groups (in the form of –NHSO₃⁻), but also from the sulfate groups (–CH₂OSO₃⁻ and OSO₃⁻) and carboxylate groups (COO⁻). Thereby, there are two negative entities in each repeat unit of HEP. Unlike HEP, SFC used in this investigation only bears 68% of negatively charged sulfonate groups substituted on the chitosan backbone. This is the reason why the ability of the films terminating with SFC in preventing plasma protein adsorption is inferior to that terminating with HEP. It should be noted that the level of antithromboginicity was varied as a function %DS of sulfofurfuryl groups on chitosan backbone in SFC. Upon mixing with 5 mL of whole blood for 15 min, 0.2 mg of SFC having 68%DS (dissolved in 0.85% NaCl(aq)) showed the lowest degree of partial blood coagulation as opposed to the SFC derivative having lower %DS. The real time coagulation of whole blood mixed with SFC having %DS of 68 and 55 can be viewed from Video S1 and S2 in Supporting Information, respectively. In contrast, the blood coagulation of whole blood mixed with the same amount of HEP (Video S3) was entirely suppressed whereas the blood became totally clotted within 3 min of mixing with chitosan (Video S4).

The results from static platelet adhesion assay (Figure 8) are in excellent agreement with the protein adsorption test. Aggregation of adherent platelets at partially activated stage having extensions of pseudopods were apparent on the substrates with high amount of adsorbed plasma proteins such as the treated PET substrate alone or the treated PET substrates with the 9-layer assembled PAH/SFC film. Fewer numbers of platelets adhered with insignificant degree of activation on the assembled PAH/SFC films terminated with SFC (10-layer and 16-layer) than those adhered on the PAH/SFC films terminated with PAH (9-layer and 15-layer). The alternating trend of platelet adhesion was also observed on the assembled PAH/HEP films confirming that the anticoagulant property is surface-dependent with the 16-layer assembled PAH/HEP showing an absolute anti-platelet adhesion. Although SFC is not as effective as HEP in suppressing plasma protein adsorption and platelet adhesion, its anticoagulating property is at

a satisfactory level given that its negative charge density is much less than HEP so that it can be considered as an alternative, nature-derived antithrombogenic material, being capable of forming assembled layer on materials to be used in blood-contacting applications.

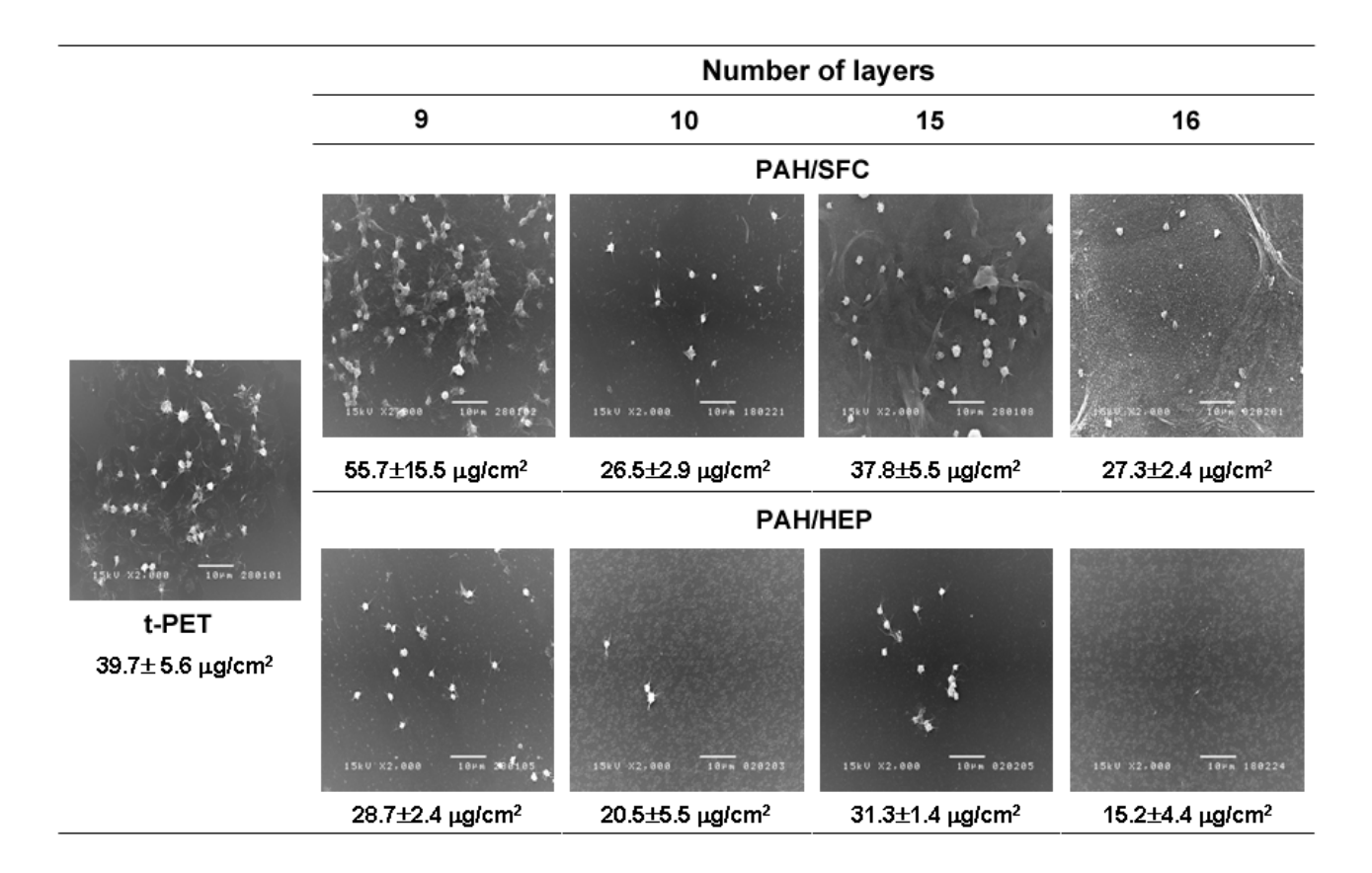


Figure 8. Representative SEM micrographs of treated PET substrates with multilayer systems after exposure to PRP for 1 h. Micrographs shown are representative of at least 10 such fields of view per sample and 3 independent samples. Below each micrograph is the corresponding amount of plasma protein adsorption (μg/cm²) after the substrates were exposed to PPP for 3 h.

Conclusion

QCM analysis suggested that multilayer films of these 3 pairs of polyelectrolytes: (HTACC/PAA), (PAH/SCC) and (PAH/SFC) have been successfully formed by alternate layer-

by-layer adsorption. The stratification of the multilayer films deposited on the plasma-treated poly(ethylene terephthalate) (treated PET) substrates was verified by water contact angle measurements, respectively. As characterized by AFM, the multilayer films can homogeneously cover the substrate and have the ability to smooth-out a rough surface of the treated PET substrates. The *in vitro* cell adhesion and proliferation of fibroblasts showed that the degree of cytocompatibility of the multilayer films depends strongly on the polyelectrolyte used for the assembly process and the last layer deposited. The antibacterial activity of (HTACC/PAA) showed that the multilayer film is able to inhibit the growth of *E. coli* and *S.aureus* which was consistent to cell study. The results from blood compatibility indicated that the (PAH/SFC) multilayer film terminating with SFC can reduce protein adsorption. All above results of this study demonstrated that multilayer film assembled from charged derivatives of chitosan are potential candidates for biomedical applications.

Acknowledgment. This research is financially supported by a Research Team Promotion Grant, the Thailand Research Fund (RTA4780004 and RTA5080004). The authors are indebted to Dr.Xiaodi Su of Institute of Materials Research and Engineering, Singapore for providing a QCM-D facility.

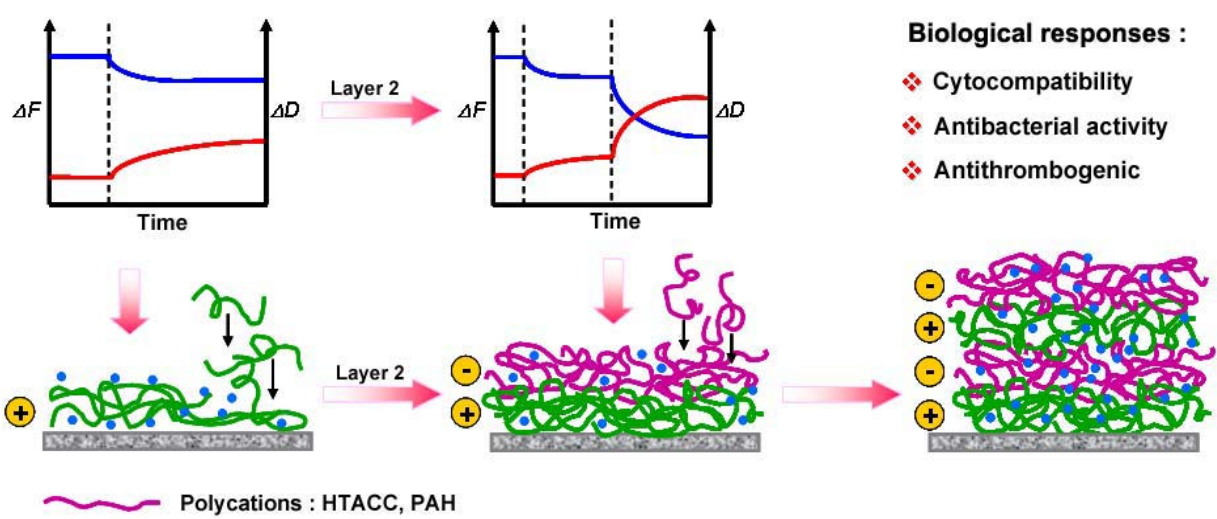
References

- (1) Decher, G. Science 1997, 277, 1232-1237.
- (2) Shahidi, F.; Arachchi, J. K. V.; Jeon, Y.-J. *Trends Food Sci. Technol.* **1999**, *10*, 37-51.
- (3) Sashiwa H, S. H., Shigemasa Y, Ogawa R, Tokura S. *Int. J. Biol. Macromol.* **1990**, *12*, 295-296.
- (4) Shigemasa, Y.; Saito, K.; Sashiwa, H.; Saimoto, H. *Int. J. Biol. Macromol.* **1994**, *16*, 43-49.

- (5) Iwasaki, N.; Yamane, S. T.; Majima, T.; Kasahara, Y.; Minami, A.; Harada, K.; Nonaka, S.; Maekawa, N.; Tamura, H.; Tokura, S.; Shiono, M.; Monde, K.; Nishimura, S. I. *Biomacromolecules* **2004**, *5*, 828-833.
- (6) Rabea, E. I.; Badawy, M. E. T.; Stevens, C. V.; Smagghe, G.; Steurbaut, W. *Biomacromolecules* **2003**, *4*, 1457-1465.
 - (7) Seong, H. S.; Whang, H. S.; Ko, S. W. J. *Appl. Polym. Sci.* **2000**, *76*, 2009-2015.
 - (8) Lim, S. H.; Hudson, S. M. Carbohydr. Res. 2004, 339, 313-319.
 - (9) Kato, Y.; Onishi, H.; Machida, Y. *Biomaterials* **2004**, *25*, 907-915.
 - (10) Amiji, M. M. Colloids Surf. B 1998, 10, 263-271.
- (11) Jayakumar, R.; Nwe, N.; Tokura, S.; Tamura, H. Int. J. Biol. Macromol. 2007, 40, 175-181.
- (12) Vongchan, P.; Sajomsang, W.; Subyen, D.; Kongtawelert, P. Carbohydr. Res. **2002**, 337, 1239-1242.
- (13) Serizawa, T.; Yamaguchi, M.; Matsuyama, T.; Akashi, M. *Biomacromolecules* **2000**, *1*, 306-309.
 - (14) Serizawa, T.; Yamaguchi, M.; Akashi, M. *Biomacromolecules* **2002**, *3*, 724-731.
- (15) Zhu, Y. B.; Gao, C. Y.; He, T.; Liu, X. Y.; Shen, J. C. *Biomacromolecules* **2003**, *4*, 446-452.
- (16) Cai, K.; Rechtenbach, A.; Hao, J.; Bossert, J.; Jandt, K. D. *Biomaterials* **2005**, *26*, 5960-5971.
 - (17) Fu, J.; Ji, J.; Yuan, W.; Shen, J. *Biomaterials* **2005**, *26*, 6684-6692.
 - (18) Liu, Y.; He, T.; Gao, C. Colloids Surf. B 2005, 46, 117-126.
- (19) Channasanon, S.; Graisuwan, W.; Kiatkamjornwong, S.; Hoven, V. P. *J. Colloid Interface Sci.* **2007**, *316*, 331-343.
 - (20) Aoki, N.; Nishikawa, M.; Hattori, K. Carbohydr. Polym. 2003, 52, 219-223.
- (21) Hoven, V. P.; Chombanpaew, K.; Iwasaki, Y.; Tasakorn, P. *J. Appl. Polym. Sci.* **2009**, *112*, 208-217.
 - (22) Lin, W.-C.; Liu, T.-Y.; Yang, M.-C. *Biomaterials* **2004**, *25*, 1947-1957.
 - (23) Sauerbrey, G. Zeitschrift fuer Physik 1959, 155, 206-222.
- (24) Notley, S. M.; Eriksson, M.; Wågberg, L. *J. Colloid Interface Sci.* **2005**, *292*, 29-37.

- (25) Yu, Y.; Wang, F.; Shi, W. Q.; Wang, L. Y.; Wang, W. B.; Shen, J. C. *Chin. Sci. Bull.* **2008**, *53*, 22-26.
- (26) Garg, A.; Heflin, J. R.; Gibson, H. W.; Davis, R. M. *Langmuir* **2008**, *24*, 10887-10894.
- (27) Lvov, Y.; Ariga, K.; Onda, M.; Ichinose, I.; Kunitake, T. *Colloids Surf. A* **1999**, *146*, 337-346.
 - (28) Schlenoff, J. B.; Dubas, S. T. *Macromolecules* **2001**, *34*, 592-598.
- (29) Ladam, G.; Gergely, C.; Senger, B.; Decher, G.; Voegel, J. C.; Schaaf, P.; Cuisinier, F. J. G. *Biomacromolecules* **2000**, *1*, 674-687.
- (30) Boura, C.; Menu, P.; Payan, E.; Picart, C.; Voegel, J. C.; Muller, S.; Stoltz, J. F. *Biomaterials* **2003**, *24*, 3521-3530.
- (31) Kim, J. Y.; Lee, J. K.; Lee, T. S.; Park, W. H. Int. *J. Biol. Macromol.* **2003**, *32*, 23-27.
- (32) Liu, C. X.; Zhang, D. R.; He, Y.; Zhao, X. S.; Bai, R. J. Membr. Sci. 2010, 346, 121-130.
 - (33) Sagnella, S.; Mai-Ngam, K. Colloids Surf. B 2005, 42, 147-155.

Graphic for Table of Contents



Polycations : HTACC, PAH
Polyanions : PAA, SCC, SFC

Supporting Information

Multilayer Thin Film Assembled from Charged Derivatives of Chitosan: Physical Characteristics and Biological Responses

Wilaiporn Graisuwan, Cheeraporn Ananthanawat, Oraphan Wiarachai, Songchan Puthong, Suphan Soogarun, Suda Kiatkamjornwong, Voravee P. Hoven

Page

- 2 Synthesis and Characterization of Charged Derivatives of Chitosan
- 4 **Figure S1.** The mass per unit area for wet films (m_d) determined by QCM-D as a function of layer number for 3 multilayer systems
- Figure S2. Thickness of multilayer film assembled on the thiol-modified gold-coated QCM plate, obtained from QCM analysis as a function of the number of depositions.
- Table S1. Average frequency shift and thickness of deposited multilayer film analyzed by QCM measurements using conventional mode.

Synthesis and Characterization of Charged Derivatives of Chitosan

N-[(2-hydroxyl-3-trimethylammonium)propyl] chitosan chloride (HTACC). Chitosan flakes (0.50 g, 1 equiv. of NH₂) were dissolved in 1 vol. % (v/v) aqueous acetic acid (25 mL) to prepare a 2.0 % (w/v) chitosan solution. GTMAC (1.82 g, 4 equiv.) was added. The reaction was performed at 70°C for 24 h. After the reaction, the solution was poured into the dialysis tubing and dialyzed in deionized water for 5 days and then the solution was lyophilized to obtain a cotton-like white material.

IR (KBr): $v = 1,598 \text{ cm}^{-1}$ (N-H bending of amino groups of chitosan), and 1,480 cm⁻¹ (C-H bending of methyl groups of quaternary ammonium groups)

¹H NMR (D₂O): δ = 2.6 ppm (-NHC<u>H</u>₂-), 3.1 ppm (N⁺-(C<u>H</u>₃)₃Cl⁻), 4.4 ppm (-NHCH₂C<u>H</u>-), and 3.3-4.3 ppm (m, H^{2'},H³, H⁴, H⁵, H⁶, and H^{6'}). Degree of substitution of HTACC calculated from ¹H NMR data was 78%

N-sulfofurfuryl chitosan (SFC). Chitosan flakes (0.50 g, 1 equiv. of NH₂) were dissolved in 1 % (v/v) aqueous acetic acid (25 mL) to prepare a 2.0 % (w/v) solution. Methanol (10 mL) containing 1.0 % (w/v) triethanolamine was slowly added to the chitosan solution. The mixture was stirred for 6 h at ambient temperature. FFSA (2.38 g, 4 equiv.) was slowly added to the chitosan slurry. The reaction was allowed to proceed for 24 h at ambient temperature. As the reaction continued, the Schiff's base thus formed was reduced by a slow addition of sodium borohydride (NaBH₄) (0.70 g, 6 equiv.). After the reduction for 6 h, the Schiff's base slowly dissolved to form a viscous solution. After the reaction, the solution was poured into the dialysis tubing and dialyzed in deionized water for 5 days and then the solution was lyophilized to obtain a cotton-like white material.

IR (KBr): v = 1,237 cm⁻¹ (O=S-O stretching of the sulfonate salt), and 1,040 cm⁻¹ (S=O stretching of sulfonic acid)

¹H NMR (D₂O): δ = 4.4 ppm (-NHC<u>H</u>₂-), 3.3-4.1 ppm (H^{2'}, H³, H⁴, H⁵, H⁶, and H^{6'}), and 6.3-6.7 ppm (=C<u>H</u>₂C<u>H</u>₂=). Degree of substitution of SFC calculated from ¹H NMR data was 68%.

N-succinyl chitosan (SCC). Chitosan flakes $(0.50 \text{ g}, 1 \text{ equiv. of NH}_2)$ were dissolved in 1 % (v/v) aqueous acetic acid solution (25 mL) to prepare a 2.0 % (w/v) chitosan solution. The chitosan solution was diluted with 40 mL of methanol. SA (1.20 g, 4 equiv.) dissolved in a minimum amount of acetone, was then added to the chitosan solution. The mixture was

vigorously stirred for 2 h at ambient temperature. The obtained viscous solution was diluted with 50 mL of water and the pH of the solution was adjusted to 10 using 2 M NaOH solution. After dialysis for 5 days, the solution was lyophilized to obtain a cotton-like white material.

IR (KBr): $\nu = 1,650$ cm⁻¹ (amide I, increase from chitosan), 1,560 cm⁻¹ (amide II, increase from chitosan), and 1,598 (N-H bending of amino groups of chitosan, decrease from chitosan)

 1 H NMR (CF₃COOH/D₂O): δ = 2.2-2.5 ppm (-NHCOC<u>H</u>₂C<u>H</u>₂-), and 3.0-3.8 ppm (m, H^{2'}, H³, H⁴, H⁵, H⁶, and H^{6'}). Degree of substitution of SFC calculated from 1 H NMR data was 44%.

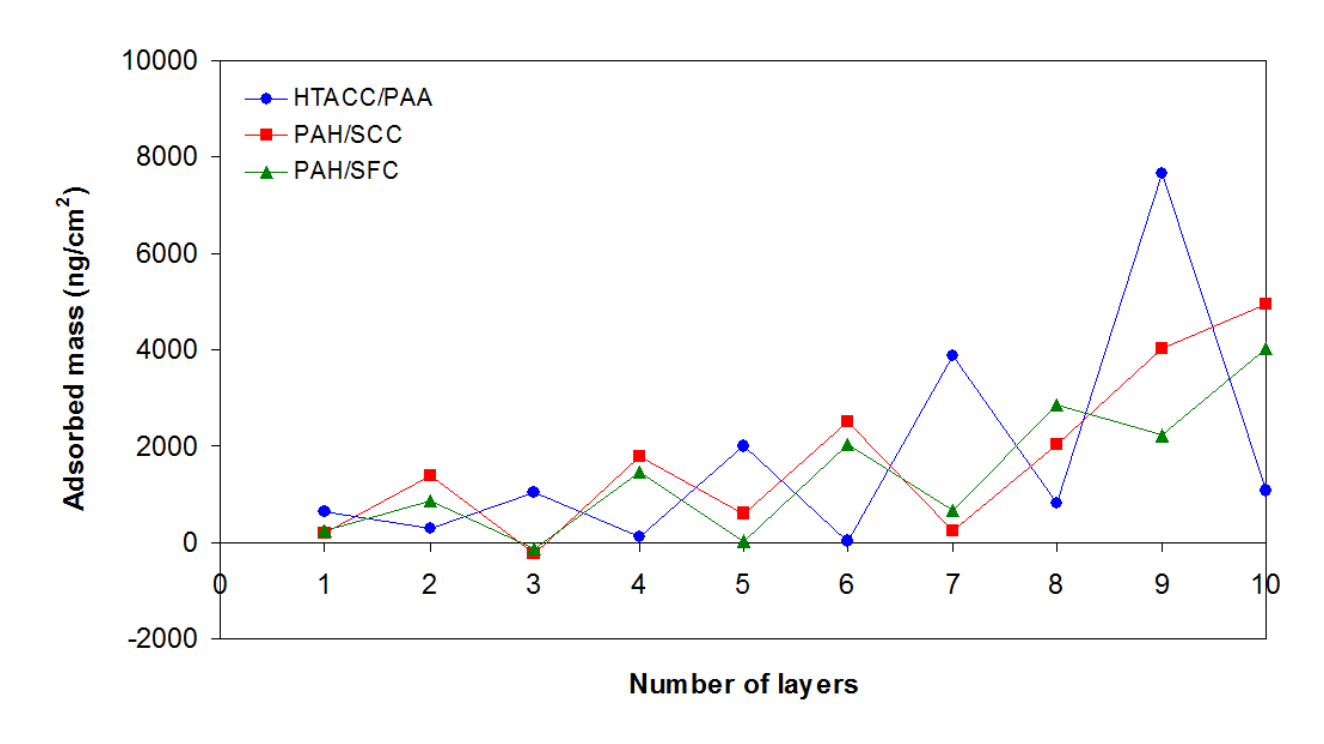


Figure S1. The mass per unit area for wet films (m_d) determined by QCM-D as a function of layer number for 3 multilayer systems

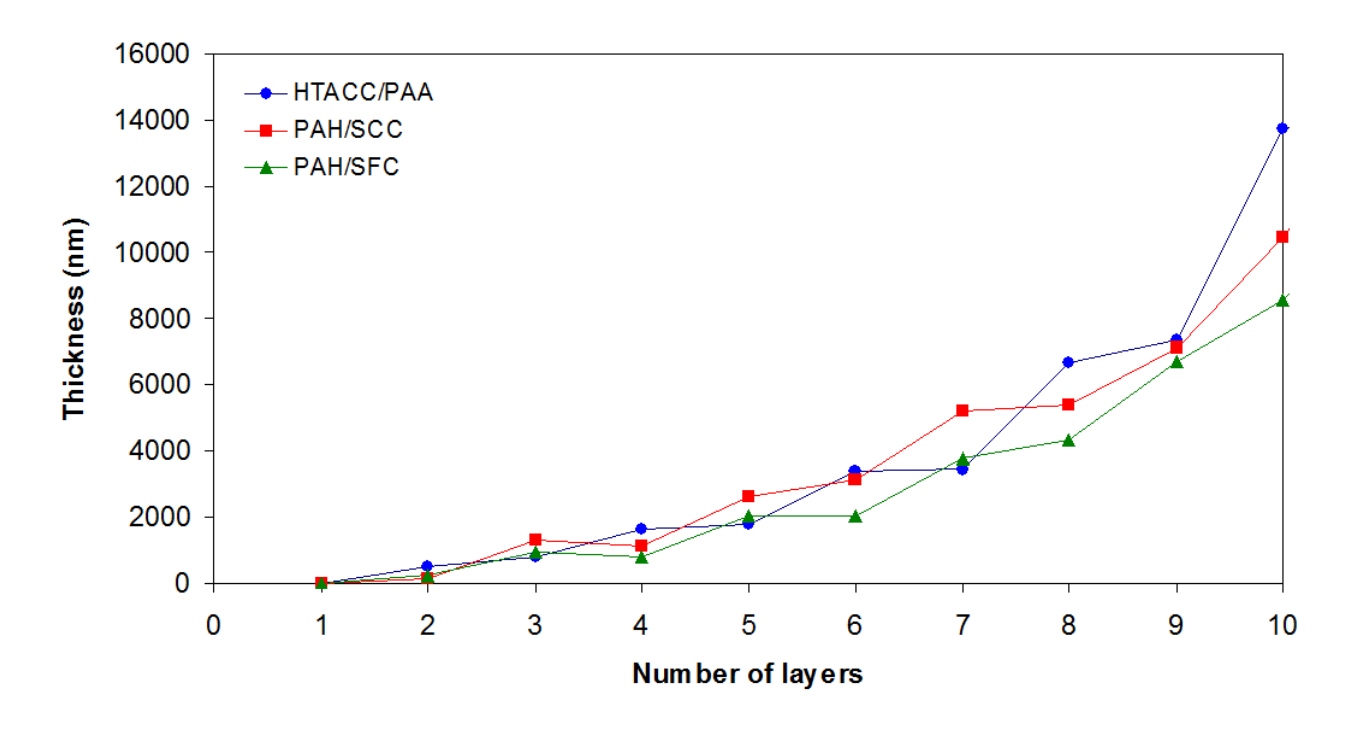


Figure S2. Thickness of multilayer film assembled on the thiol-modified gold-coated QCM plate, obtained from QCM analysis as a function of the number of depositions.

Table S1. Average frequency shift and thickness of deposited multilayer film analyzed by QCM measurements using conventional mode.

Multilayer system	Average $\Delta F_{\rm odd}$ (Hz)	Bilayer thickness, d _{b,odd} (nm)	Average ΔF_{even} (Hz)	Bilayer thickness, d _{b,even} (nm)
HTACC/PAA	81.3	11.9	85.5	12.6
PAH/SCC	142.5	20.9	148.3	21.8
PAH/SFC	81.0	11.9	118.5	17.4

All VDO clips listed below are attached as separated files

Video S1. Real time monitoring for coagulating property of 5 mL whole blood in a closed test tube upon mixing for 15 min with 0.2 mg of SFC having 68%DS, dissolved in 0.85% NaCl(aq).

Video S2. Real time monitoring for coagulating property of 5 mL whole blood in a closed test tube upon mixing for 15 min with 0.2 mg of SFC having 60%DS, dissolved in 0.85% NaCl(aq).

Video S3. Real time monitoring for coagulating property of 5 mL whole blood in a closed test tube upon mixing for 15 min with 0.2 mg of SFC having 55%DS, dissolved in 0.85% NaCl(aq).

Video S4. Real time monitoring for coagulating property of 5 mL whole blood in a closed test tube upon mixing for 15 min with 0.2 mg of HEP, dissolved in 0.85% NaCl(aq).

Video S5. Real time monitoring for coagulating property of 5 mL whole blood in a closed test tube upon mixing for 15 min with 0.2 mg of chitosan, dissolved in 0.85% NaCl(aq).

Draft Manuscript

Kapok II: PRETREATMENT OF KAPOK FIBERS FOR PULPING AND PAPERMAKING

Somporn Chaiarrekij^{a*} Thippawan Hommaivai^b, Kuntinee Suvarnakich^a, and Suda Kiatkamjornwong^a**

^aDepartment of Imaging and Printing Technology, Faculty of Science, Chulalongkorn University, 254 Phayathai Road, Bangkok 10330, Thailand.

*Tel: +662 218 5572; e-mail: huaja@hotmail.com

**Tel: +662 218 5587; Fax: +662 255 3021; e-mail: ksuda@chula.ac.th

^bPulp and Paper Technology Program, Faculty of Science, Chulalongkorn University, 254 Phayathai Road, Bangkok 10330, Thailand.

Abstract

Kapok fibers are naturally coated with wax and cutin which renders them hydrophobic. To obtain fibers that are suitable for pulping, they must first be immersed in tap water for up to three to four weeks which is very time consuming. This research then investigated the effects of fiber pretreatment with sodium hydroxide (NaOH) or lipase for varied immersion times before it was subjected to soda pulping, in comparison with the control fibers that were pretreated by immersion in tap water for 3 weeks. For chemical pretreatment, two doses of NaOH (5 and 10% (w/w) based on the O.D. kapok fiber weight) were used with three immersion times (1, 2 and 3 weeks). For biological pretreatment, a commercial lipase with the enzyme activity of 100 KLU/g with the dosages of 0.25 and 0.5% (w/w) based on O.D. kapok fiber weight was used for three immersion times (1, 3 and 5 hours) of the fibers. After soda pulping and latency removal of the kapok fibers, the pulp and their sheets formed (60 g/m²) from each pretreatment were characterized for the pulping efficiency, and physical and optical properties. It was found that both alkali and lipase pretreatments provided the pulp with the lower lignin content but higher opacity. However, higher tensile and burst strengths were obtained when the pulp was pretreated with NaOH while higher tear resistance was acquired with lipase pretreatment.

Key words: Lipase, Pulping, Paper making, Chemical pretreatment, Biological pretreatment

Introduction

In a previous study of the pulping of kapok fibers for papermaking, it was concluded that kapok fiber can be a quality pulp source for papermaking, especially for strengthening tensile strength of paper (Apirakchaiskul, 2008). However, the idea of using kapok fibers as one of the new potential fiber sources for the demands of the pulp and paper industries is intimidated by the inherent difficulty in soaking the hydrophobic kapok fibers prior to processing them to soda pulping. Indeed, wetting kapok fibers is not easy and practically takes around three weeks for kapok fibers to get wet after being immersed in plain tap water. This is due to the waxy cutin on the fiber surface that provides strong water repellency. So, the pretreatment of kapok fibers before soda pulping is required in order to remove the surface waxy material, and this might also increase the soda pulping efficiency of kapok fibers. In turn, this would make the process more economically and ecologically viable with a lower chemical consumption and/or shorter immersing time and pulping time of kapok fibers.

Fiber pretreatment involves modification of the fibers before the pulping process, and can be divided into two broad types. The first is chemical pretreatment, which utilizes chemicals, typically alkali, such as NaOH or potassium hydroxide (KOH), to digest or soften the material (woodchips or, as in this case, fibers) and to open the fiber surface so that

pulping becomes easier and more efficient. The second broad approach is that of biological pretreatment, which uses micro-organisms or enzymes to digest the woodchips or fibers before processing them by the pulping process. Enzymes that have been used in this method include cellulases, hemicellulases, xylanases, pectinase and cutinase. These micro-organisms and enzymes may react with waxy fiber surface, cellulose, hemicellulose and lignin, including the lignin-carbohydrate complex. This causes the opening of more fiber surfaces to the aqueous environment and therefore provides a better reaction between the fibers and cooking chemicals during the pulping processes.

For biopulping, the fungus *C. subvermispora* has been applied to spruce woodchips for two weeks before processing them in a refiner to produce the mechanical pulp (Scott *et al.*, 1998). The bio-pretreatment of these woodchips provided an energy saving of 24 to 38% during the refining process. Moreover, the bio-treated pulp had a higher strength than that of the control pulp, as indicated by the higher tensile, burst and tear indexes. Although the pulp brightness obtained from the bio-treated pulp was lower than the control pulp, it could, if required, be improved by pulp bleaching. Wax elimination from the surface of cotton fibers was also evaluated using a mixture of mechanical and biological action with cutinase and pectinase (Agrawal *et al.*, 2008). The temperature required for wax elimination decreased from 100 °C, when NaOH was used, to 50 °C, when pectinase was used. In addition, using pectinase with cutinase was able to further reduce the required temperature to 30 °C and the reaction time to 15 min.

In this work, chemical pretreatment using NaOH for kapok fibers was evaluated, along with the biological pretreatment of kapok fibers using lipase. The objectives of the present work are to investigate the effects of these chemical and biological pretreatments on the soda pulping efficiency of the kapok fibers; to determine the optimum condition of each chemical and biological pretreatment of the kapok fibers; and to compare the results from the optimum condition of the chemical pretreatment with those from the biological pretreatment.

Experimental

The kapok fibers sourced in Thailand were subjected to chemical or biological pretreatment. Both pretreated fibers were then pulped by the soda process and analyzed with respect to the control pulp. The control pulp in all cases was derived by replacing the pretreatment stage with simply immersing the fibers in tap water for three weeks. Three replicates were done for all control and pretreated pulps.

Pretreatment of kapok fibers

500 g of Kapok fibers were pretreated by either immersion in tap water for three weeks (control) or chemical (NaOH) or biological (lipase enzyme) pretreatment. For the chemical pretreatment, the kapok fibers were treated with NaOH at 5% or 10% (w/w, based on the oven dried (O.D). kapok fiber weight) in 13 L of tap water for 1, 2 and 3 weeks. For the biological pretreatment, kapok fibers were pretreated with the Lipolase 100L, the commercial enzyme from Novozymes having the enzyme activity of 100 KLU/g (KLU stands for kilo lipase unit) at two different dosages (0.25% and 0.50% w/w, based on O.D. fiber weight) in 13 L of tap water and three times (1, 3 and 5 hours). After the pretreatment, the kapok fibers were washed prior to squeezing out the excess water and cut to 3-5 cm in length before being processed by soda pulping.

Soda pulping of kapok fibers

Kapok fibers with and without the pretreatments were separately pulped using NaOH at 20% (w/w, based on O.D. kapok fiber weight). The liquor-to-wood ratio (L: W) was 17:1 (v/w). The pulping was carried out in an autoclave digester, (UEC-2017A, Universal Engineering, India) with an initial digesting temperature at 40 °C. The pulp matrix was then gradually heated to 120 °C over 30 min. The pulping was proceeded at this temperature for

another 120 min. The pulp was then extensively washed with tap water to remove the excess alkali from the pulp by controlling with a pH meter (Hanna HI 98128, Hanna Instrument, U.S.A.). The net pulp yield and residual alkaline level were then determined.

Kapok pulp at 5% pulp consistency (w/w) was refined twice through a disc refiner, using a 1/100 inch disc gap (Andritz Sprout, U.S.A.). Then, refined kapok pulp was disintegrated at 1.5% pulp consistency (w/w) in a standard disintegrator (Formax T-100, Adirondack, U.S.A.) for 50,000 revolutions in hot water (80 °C) to remove latency.

Evaluation of pulp and paper properties

The chemical composition of each pulp was determined using TAPPI Standard Method T222 om-98 for lignin determination, TAPPI Standard Method T203 cm-99 for alpha cellulose (α -cellulose) determination, and Browning's method for holocellulose determination (Browning, 1963). The amount of hemicellulose was calculated from the difference between the holocellulose content and the alpha cellulose content.

Kappa number, an indication of lignin content in the pulp, was analyzed according to TAPPI Standard Method T236 om-99. Kapok pulp drainage was also determined following the Canadian Standard Freeness (CSF) standard, using a freeness tester (CF/A, Regmed, Brazil) according to TAPPI Standard Method T227 om-04. Kapok pulp was also made into 60 g/m² handsheets on a Rapid-Köthen sheet former (RK-2A KWT, PTI, Austria) according to the ISO Standard Method 5269-2. The brightness and opacity of the handsheets were measured using an optical tester (Color Touch PC, Technidyne, U.S.A.), based on ISO Standard Methods 2470 and 2471, respectively. The tensile, burst and tear strengths were measured using a tensile strength tester (Strograph E-S, Toyo Seiki, Japan), a burst strength tester (SE002P, Lorentzen & Wettre, Sweden), and a tear strength tester (Protear, Thwing-Albert, U.S.A, according to TAPPI Standard Method T494 om-01, T403 om-02, and T414 om-04, respectively.

Results and discussion

Chemical pretreatment of the fibers

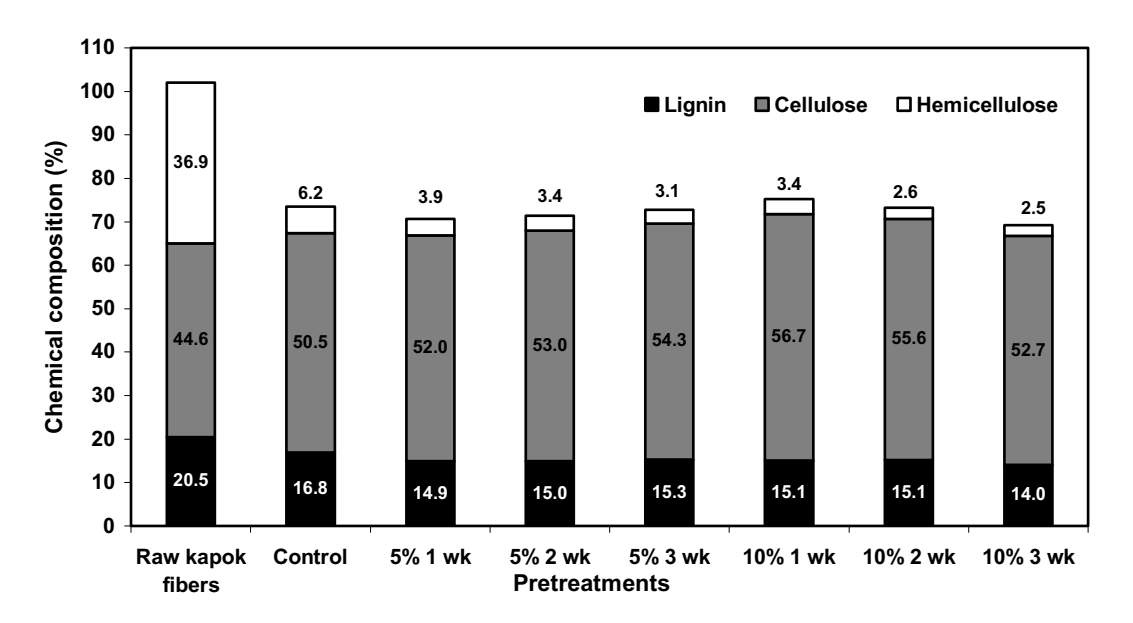


Figure 1. Effects of chemical pretreatment on chemical composition of kapok pulp.

As shown in Figure 1, the analysis of the pulp chemical composition indicated that the alkali pretreated samples had the lower lignin contents than the control pulp since NaOH dissolved the lignin. In addition, NaOH pretreatment was observed to produce a lower hemicellulose content but a higher cellulose content than the control pulp because NaOH partly dissolved the hemicellulose in the pulp leaving the cellulose content mostly intact. It was also noticed that hemicellulose content decreased with the higher dosage and longer alkali pretreatment time. However, cellulose content potentially increased with the higher alkali dosage while the effect of alkali pretreatment time on cellulose content was apparently indistinguishable. The effects of alkali pretreatment dosages and times seemingly have no different impacts on the lignin content of the alkali pretreated pulp except for the extreme case that used the highest alkali dosage with the highest pretreatment time which inevitably provided the lowest lignin content.

Table 1. Effects of chemical pretreatment on pulp yield, residual alkali, and kappa number

Pretreatment condition		Pulp yield	Residual alkali	Kappa number
NaOH dosage	Number of	- (%)	(%)	
(%)	weeks			
0 (Control)	3	76.02 <u>+</u> 1.79	2.00 ± 0.59	108 <u>+</u> 2
	1	73.71 <u>+</u> 0.06	2.90 <u>+</u> 0.14	99 <u>+</u> 2
5	2	75.02 ± 2.25	3.50 ± 0.14	98 <u>+</u> 2
	3	76.00 ± 2.06	3.60 ± 0.28	98 <u>+</u> 1
	1	78.20 ± 1.06	4.00 ± 0.00	116 <u>+</u> 2
10	2	76.08 ± 0.41	4.60 <u>+</u> 0.28	130 <u>+</u> 3
	3	72.66 <u>+</u> 7.17	5.80 ± 0.28	132 <u>+</u> 5

The control experiment as indicated by 0% NaOH dosage was for immersing kapok fibers in tap water for 3 weeks.

The results tabulated in Table 1 indicate that the alkali dosage and pretreatment time used in this study seemed to have a small effect on pulp yield. However, the residual alkali increased with the higher NaOH concentration and longer pretreatment time. The residual alkali levels imply that the alkali consumption during the soda pulping was lower with the alkali pretreated samples than the control. Thus, there was probably less chance for carbohydrate degradation during the pulping leading to the pulp yields comparable to that of the control.

The Kappa numbers of the NaOH pretreated pulp were lower than that of the control pulp only when the lower dosage (5% w/w) of NaOH was used. In contrast, the kappa numbers increased significantly with the higher NaOH pretreatment concentration (10% w/w) and with the longer pretreatment times at this higher dose. Perhaps the presence of cutin interferes with the permanganate oxidation of lignin. At the higher NaOH concentration for the longer pretreatment times, the cutin could be much easier to dissolve during the subsequent soda pulping stage, which might markedly disrupt the permanganate oxidation of lignin.

The results from Table 2 illustrate that the effects of NaOH dosage and pretreatment time on the density were indistinguishable. Opacity typically increased with increasing NaOH dosage and reacting time, the only exception being that seen for the pretreatment with 5% (w/w) alkali for three weeks (Table 2). This might probably cause by the alkali pretreatment which led to the higher fines contents of the pulp and thus could increase light scattering of these handsheets. However, NaOH pretreatment seemed to initially lower the brightness at

the short pretreatment times, and then increase it with the longer treatment times or higher NaOH concentrations. This might be due to the alkali induced darkening effect to render the pulp yellow. Nevertheless, increasing the pretreatment time produced a brighter pulp, which was caused by the result of more wax removed from the fiber surface and so the cooking liquor could penetrate into and react better with more fibers. Thus, more lignin was removed and the pulp became brighter.

Table 2. Effects of chemical pretreatment on density, brightness and opacity

Pretreatment condition		Density	Brightness	Opacity
NaOH dosage (%)	Number of weeks	(g/m^3)	(%)	(%)
0	3	0.72 <u>+</u> 0.03	21.3 ± 0.5	81.2 <u>+</u> 1.0
	1	0.73 ± 0.05	21.0 ± 0.4	85.8 ± 0.6
5	2	0.78 ± 0.04	20.9 ± 0.2	86.1 <u>+</u> 1.5
	3	0.78 <u>+</u> 0.05	21.5 <u>+</u> 0.4	81.2 <u>+</u> 0.4
	1	0.72 ± 0.04	20.0 ± 0.5	86.5 <u>+</u> 1.1
10	2	0.79 ± 0.04	21.2 ± 0.5	88.8 <u>+</u> 1.0
	3	0.76 ± 0.05	22.5 ± 0.5	91.4 ± 0.7

The control experiment as indicated by 0% NaOH dosage was for immersing kapok fibers in water for 3 weeks.

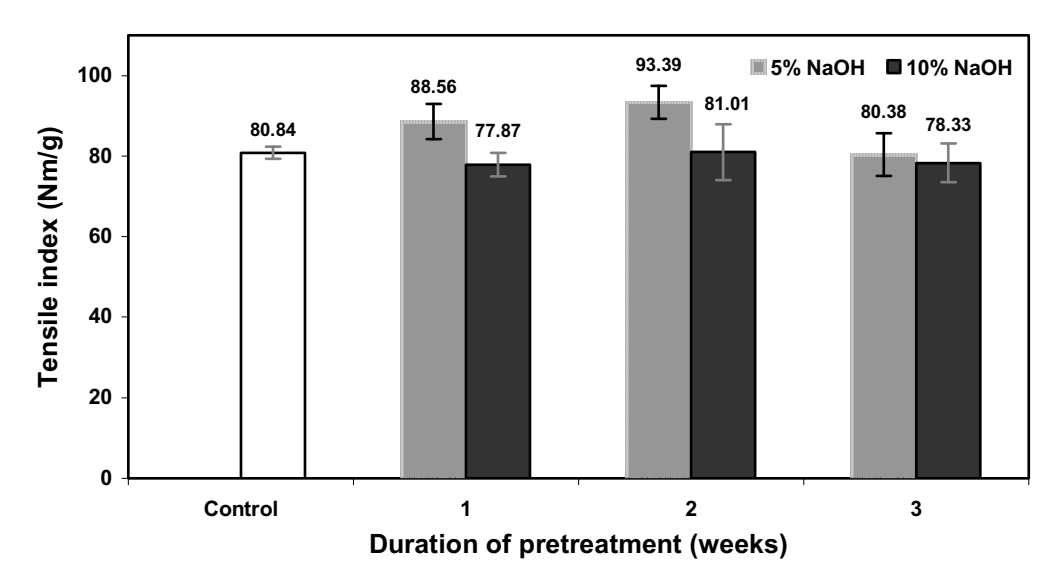


Figure 2. Effects of chemical pretreatment on tensile index.

As shown in Figures 2 and 3, after the pretreatment with the lower concentration of NaOH, the pulp displayed the highest tensile index and burst index, higher than those derived from the control pulp. However, the effects of the NaOH pretreatment time on the tensile index and burst index were somewhat variable but important. The pulp became stronger when it was pretreated with NaOH for two weeks yet three weeks of the pretreatment was detrimental to both the tensile and burst strengths, reducing them to essentially the same level as the control pulp. This could be because NaOH aided in not only removing the fiber surface wax but also attacked the lignin leading to a better fiber bonding in the sheets, at least when pretreated at the optimal NaOH concentration and time. Also, the NaOH led to a higher

cellulose content which might in turn helped increase the fiber strength. However, when too high a NaOH dose was used for a long time, the tensile and burst strengths declined, and this is likely to be due to carbohydrate degradation by the peeling reaction under a strong alkali condition.

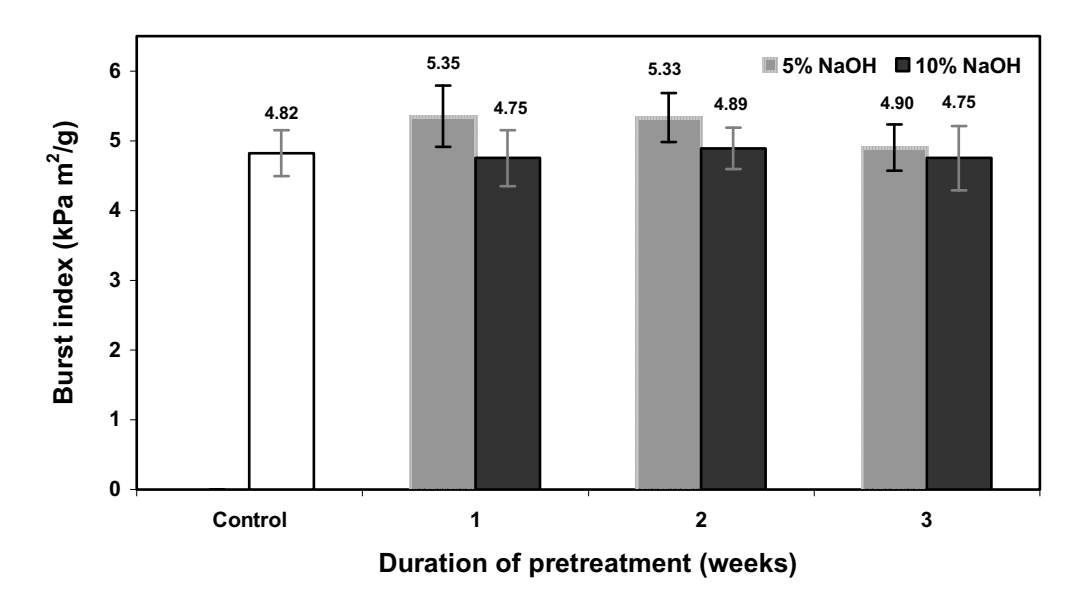


Figure 3. Effects of chemical pretreatment on burst index.

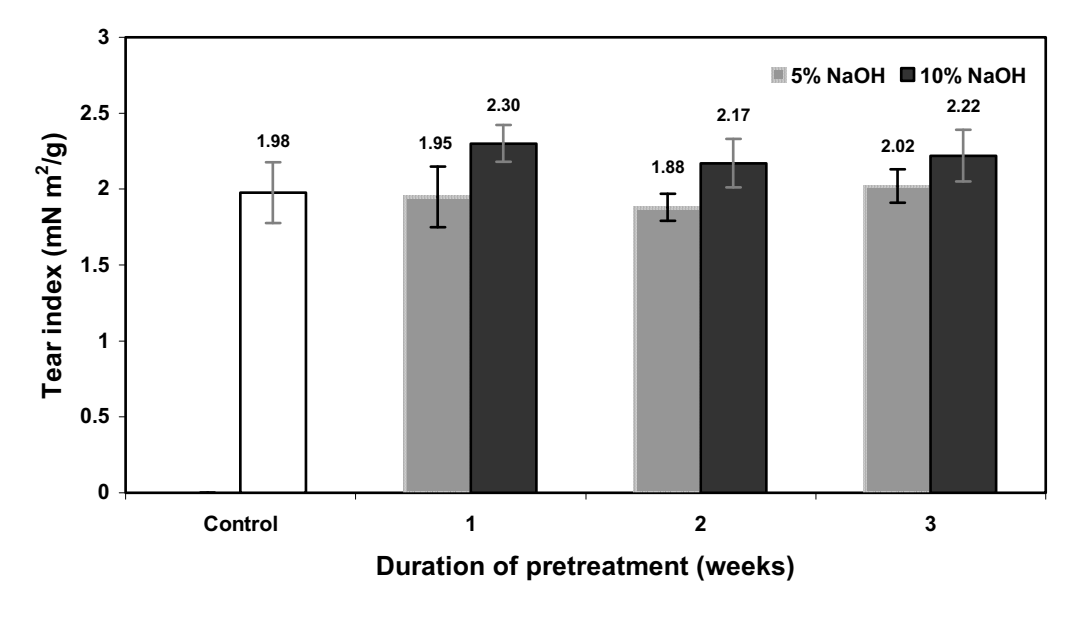


Figure 4. Effects of chemical pretreatment on tear index.

The pulp pretreated with the higher concentration (10% w/w) of NaOH potentially provided a higher tear index (Figure 4), which is opposite to the cases for the tensile and burst indexes. Generally, in contrast to tensile and burst strengths, tear resistance depends mostly on the strength of individual fibers rather than the strength of inter-fiber bonding. The higher NaOH concentration produced pulp with the higher cellulose content but the lower

hemicellulose contents (Figure 1), which might increase the fiber strength and then tear strength of the pulp as a whole.

Based on the overall results, pretreatment of the kapok fibers with NaOH at 5% (w/w) for two weeks was selected as the optimal condition. Under these pretreatment conditions, the kapok pulp provided the highest tensile strength with the lowest kappa number. Burst and tear strengths were acceptable and it also gave a suitable residual alkali level which was in the optimal range for pulping.

Biological pretreatment of the fibers

Pretreatment of the kapok fibers with lipase beneficially resulted in a lower lignin content than that seen in the control pulp, whilst the lignin content was further reduced with the higher lipase dose (Figure 5). Likewise, the hollocellulose contents were lower in pulp pretreated with any lipase dose than that seen in the control, suggesting that the lipase had reacted with the wax at the kapok fiber surface. This might then cause the fiber surface to open more and allow greater access to NaOH during the soda pulping. That the resulting holocellulose and especially alpha cellulose of the lipase pretreated pulps were lower implies that the cellulose was attacked more than was the hemicellulose after the lipase pretreatment. It was also noticed that the effects of the pretreatment time on the chemical composition were more evident only in the case of higher dosage of lipase as indicated by the lower lignin and cellulose contents but the higher hemicellulose content with the longer pretreatment time.

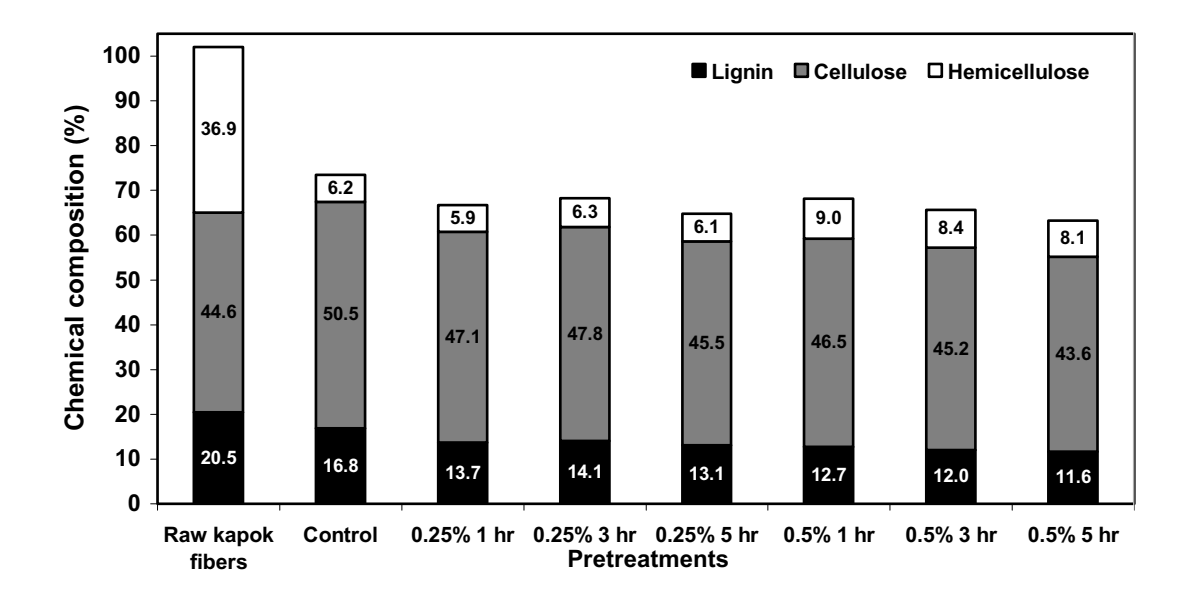


Figure 5. Effects of lipase pretreatment on chemical composition of kapok pulp.

Table 3 reveals that the lipase pretreated pulps gave a lower pulp yield than that of the control pulp, and the yield decreased with a higher enzyme dosage and pretreatment times. The residual alkali content was lower in the lipase-pretreated samples and was minimal after two-hour exposure. This also implied that the alkali consumption during the soda pulping stage was higher following the lipase pretreatment. The lipase pretreated pulp also produced a slightly lower kappa number, compared to that of the control, at the low lipase dose; but at the higher lipase dose, it was lower than the control only after a three-hour exposure. The kappa number and pulp yields obtained indicated that lipase eventually reacted with cutin at

the fiber surface and caused the surface to open for the alkali to react with the kapok fibers more easily in the pulping stage.

It should also be noted that the lipase enzyme pretreated pulp gave a lower pulp yield and residual alkali content than did the NaOH pretreated pulp (Tables 1 and 3). Thus, the enzyme pretreatment provided a better accessibility of the kapok fibers for the NaOH in the pulping reaction than did the NaOH pretreatment.

Table 3. Effects of lipase pretreatment on pulp yield, residual alkali, and kappa number

Pretreatment condition		Pulp yield	Residual alkali	Kappa
Lipase dosage	Number of	(%)	(%)	number
(%)	hours			
0 (Control)	504	76.02 <u>+</u> 1.79	2.00 ± 0.59	108 <u>+</u> 2
	1	70.52 <u>+</u> 1.04	1.60 <u>+</u> 0.57	106 <u>+</u> 0
0.25	3	72.10 ± 0.12	0.80 ± 0.00	105 <u>+</u> 2
	5	68.73 <u>+</u> 1.70	1.05 <u>+</u> 0.07	107 <u>+</u> 0
	1	71.59 <u>+</u> 1.70	1.20 ± 0.00	108 <u>+</u> 3
0.50	3	69.22 <u>+</u> 1.07	0.90 ± 0.14	108 <u>+</u> 3
	5	66.92 ± 1.68	1.25 ± 0.07	105 ± 3

The control experiment as indicated by 0% NaOH dosage was for immersing kapok fibers in tap water for 3 weeks

Table 4. Effects of lipase pretreatment on density, brightness and opacity

Pretreatment condition		Density	Brightness	Opacity
Lipase dosage	Number of	(g/m^3)	(%)	(%)
(%)	hours			
0	504	0.72 ± 0.03	21.3 <u>+</u> 0.5	81.2 <u>+</u> 1.0
	1	0.68 ± 0.03	22.7 ± 0.7	87.7 <u>+</u> 1.1
0.25	3	0.67 ± 0.04	22.2 ± 0.7	87.1 <u>+</u> 1.2
_	5	0.71 ± 0.02	22.8 <u>+</u> 0.7	88.3 <u>+</u> 1.4
	1	0.65 ± 0.02	22.2 <u>+</u> 0.8	88.9 <u>+</u> 1.3
0.50	3	0.70 ± 0.03	23.0 ± 0.7	87.6 <u>+</u> 1.3
	5	0.70 ± 0.03	22.3 ± 0.6	85.4 <u>+</u> 1.9

The control experiment as indicated by 0% NaOH dosage was for immersing kapok fibers in tap water for 3 weeks

Lipase pretreatment hardly impacted sheet density but provided the pulp with a higher brightness and opacity as compared to the control pulp (Table 4). Higher brightness of lipase pretreated pulp was caused by a higher level of lignin removal while higher opacity might probably be caused by higher fines contents which then increased the light scattering coefficients of these handsheets. This might implied that lipase pretreatment improved accessibility of the kapok fibers for NaOH in pulping reaction. However, the effects of enzyme dosage and treatment time on density, brightness and opacity seemed to be very small.

When comparing the effects of the lipase pretreatment on the density, brightness and opacity to those of the NaOH pretreatment, it was found that both pretreatments provided

essentially the same effects on the density and opacity, but the lipase pretreatment potentially produced a higher brightness level.

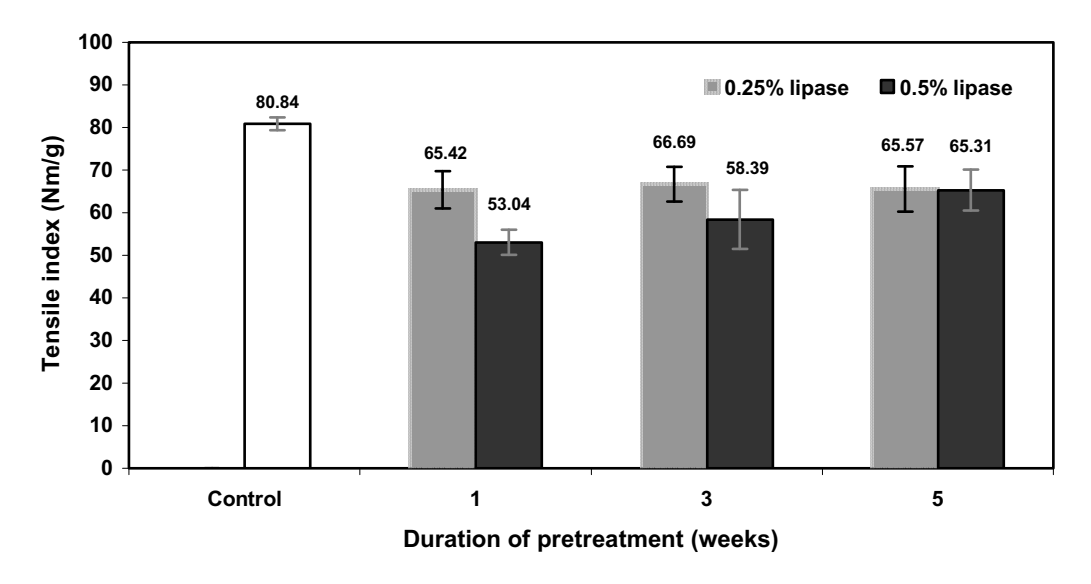


Figure 6. Effects of lipase pretreatment time on tensile index.

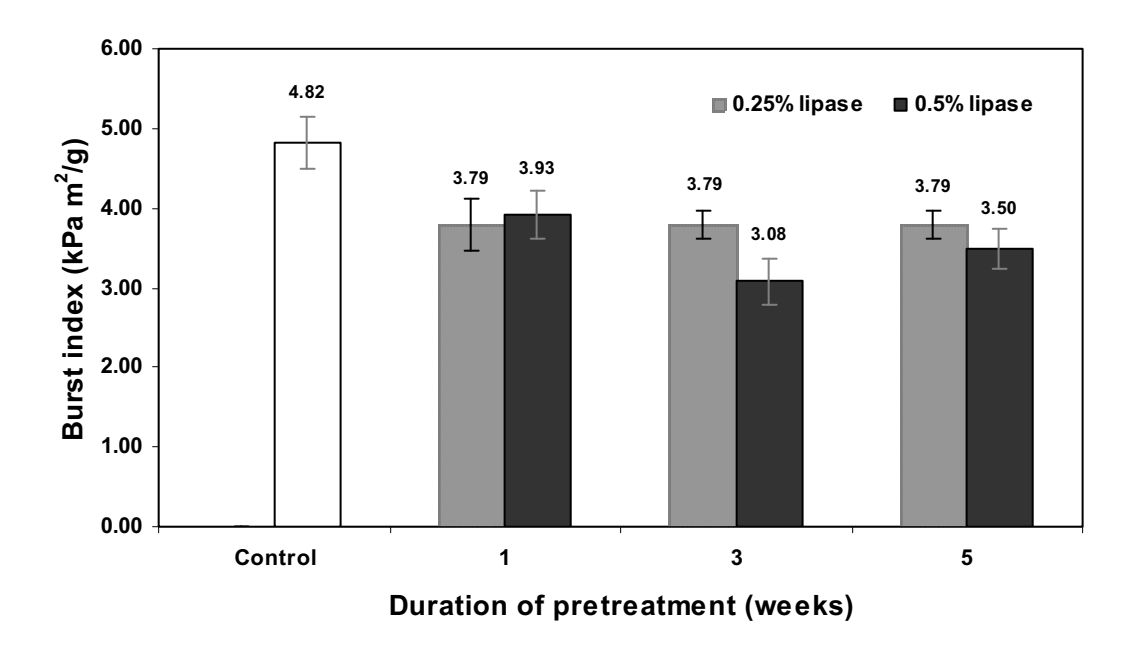


Figure 7. Effects of lipase pretreatment time on burst index.

The tensile and burst strengths of all lipase pretreated pulp were lower than those of the control pulp (Figures 6 and 7). This could be because the cellulose content was lower whilst the hemicellulose content was higher for the lipase pretreated pulp (Figure 5). Thus, the individual fiber strength of the enzyme pretreated pulp might be diminished due to the lower cellulose content and this might decrease the tensile and burst indexes. It should also be noted that these tensile and burst strength of lipase pretreated pulp typically decreased with pretreatment at the higher lipase dose, while effects of the longest enzyme treatment time on the tensile and burst index.

The lipase pretreated pulp gave lower tensile and burst strengths than that of the NaOH pretreated pulp (Figures 2 and 3 compared to Figures 6 and 7), which emphasizes that the enzyme pretreatment could provide a better accessibility of the NaOH into the kapok fibers in the pulping stage than did the NaOH pretreatment.

Unlike the tensile and burst indexes, the tear index of the lipase pretreated pulp was surprisingly higher than that of the control pulp, and this was more markedly at the higher lipase dose, although the preincubation time at both lipase doses seemed irrelevant (Figure 8).

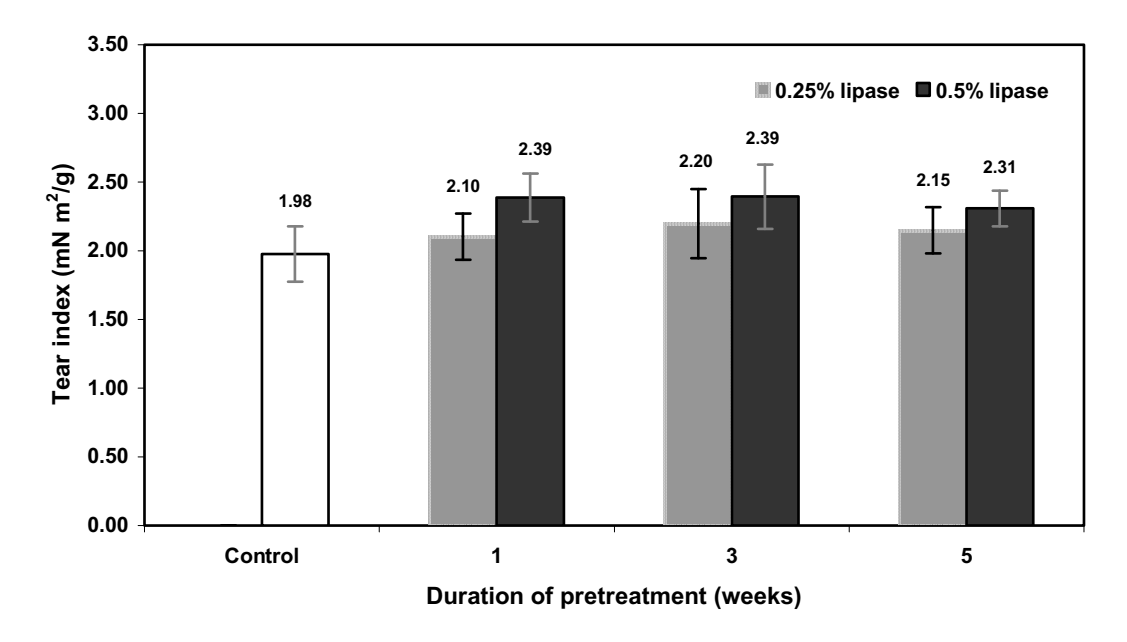


Figure 8. Effects of lipase pretreatment on tear index.

Based on the overall results, the biological pretreatment with a lipase dosage of 0.25% (w/w), based on the O.D. fiber weight, for three hours was selected as the optimal condition, since at this condition the kapok pulp provided the highest tensile strength and pulp yield with the lowest kappa number and residual alkali content.

Overall comparison between the chemical and biological pretreatments

Based on the results obtained from both the NaOH and lipase pretreatments in comparison with respective control pulp, the pulp and paper properties obtained at the optimal conditions for each of the pretreatments are summarized in Table 5. The optimal conditions for the alkali pretreatment was NaOH at 5% (w/w) based on the O.D. fiber weight for two weeks, whilst those for the lipase pretreatment was a lipase dose at 0.25% (w/w) based on O.D. fiber weight, for three hours.

The benefits of both chemical and biological pretreatments are the lower kappa number and higher opacity obtained compared to that of the control pulp. Perhaps the pretreated kapok pulp has more opened structures and more fines content which could lead to the higher light scattering and opacity.

The advantages of using the alkali pretreatment are better tensile and burst indexes. The residual alkali content of the chemical pretreatment was also higher than that of the control and lipase enzyme pretreated pulps, which implied that the alkali content in the pulping reaction can be decreased in future work. The lower kappa number also indicated that the cooking liquor could penetrate through the kapok fibers and react with a greater proportion of the total number of reaction sites.

The advantages of utilizing the lipase pretreatment were the lower kappa number with the higher tear index, brightness and opacity. Finally, it was recommended that mechanical or physical parameters such as a proper mixing and suitable reaction temperature for the lipase enzyme, which were not evaluated and optimized here, might be selectively employed for the biological pretreatment in order to increase the rate of enzyme reaction at the kapok fiber surface.

Table 5. Comparison of the control, alkali (chemical) and lipase (biological) pretreatments of kapok fibers

Pulp and paper properties	Control	NaOH	Lipase
		pretreatment	pretreatment
Lignin (%)	16.8 <u>+</u> 0.3	15.0 ± 0.2	14.1 <u>+</u> 0.2
Cellulose (%)	50.5 ± 0.0	53.0 ± 0.2	47.8 <u>+</u> 1.0
Hemicellulose (%)	6.2 ± 0.2	3.4 ± 0.0	6.3 ± 0.9
Pulp yield (%)	76.02 <u>+</u> 1.79	75.02 <u>+</u> 2.25	72.10 <u>+</u> 0.12
Residual alkali (%)	2.00 ± 0.59	3.50 ± 0.14	0.80 ± 0.00
Kappa number	108 <u>+</u> 2	98 <u>+</u> 2	105 <u>+</u> 2
Tensile index (N m/g)	80.8 <u>+</u> 1.5	93.4 <u>+</u> 4.1	66.7 <u>+</u> 4.0
Burst index (kPa m ² /g)	4.82 ± 0.33	5.33 ± 0.35	3.79 ± 0.18
Tear index (mN m ² /g)	1.98 <u>+</u> 0.20	1.88 <u>+</u> 0.09	2.20 ± 0.25
Density (g/m ³)	0.72 ± 0.03	0.78 ± 0.04	0.67 ± 0.04
Brightness (%)	21.3 <u>+</u> 0.5	20.9 <u>+</u> 0.2	22.2 <u>+</u> 0.7
Opacity (%)	81.2 <u>+</u> 1.0	86.1 <u>+</u> 1.5	87.1 <u>+</u> 1.2

The control experiment as indicated by 0% NaOH dosage was for immersing kapok fibers in water for 3 weeks

Conclusions

Chemical (NaOH) and biological (lipase enzymatic) pretreatment of kapok fibers were shown to be beneficial to the soda pulping of kapok fibers, because the immersing time and NaOH consumption could be reduced. The pretreated pulp also had a lower kappa number and higher opacity. The chemical pretreatment with NaOH should be employed when increases in tensile and burst index are demanded, whilst the biological pretreatment with lipase is more attractive when the tear resistance of sheets is desired. Combining both chemical and biological pretreatments is also supposition since both treatments can provide beneficially synergistic effects to the soda pulping of kapok fibers.

Acknowledgements

This research is fully financially supported by the Research Team Aided Grant from the Thailand Research Fund and the Commission of Higher Education under the Contract number RTA5080004. Some research facilities provided by the Product and Technology Development Center of Siam Cement Group Paper Company Limited are also gratefully appreciated.

References

Apirakchaiskul, A., "The Use of Kapok Fiber to Improve Strength of Paper", M.S. Thesis, Department of Imaging and Printing Technology, Faculty of Science, Chulalongkorn University, 2008.

Scott, G.M., Akhtar, M., Lentz, M.J., Kirk, T.K., and Swaney, R., "New Technology for Papermaking: Commercializing Biopulping", TAPPI Journal, 81(11), 1998, 220-225.

Zhang, W., Okubayashi, S., and Bechtoid, T., "Fibrillation Tendency of Cellulosic Fibers-Part 3. Effects of Alkali Pretreatment of Lyocell Fiber", Carbohydrate Polymers, 59(2), 2005, 173-179.

Browning, B. L. (1963). Methods in Wood Chemistry, Interscience Publishers, New York.

Comments to Archan Somporn: More corrections are needed. Suda

Draft Manuscript

Colloids and Surfaces A: Physicochemicals and Engineering Aspects

Manuscript Number:

Title: Microencapsulation of menthol by crosslinked chitosan via porous glass membrane emulsification technique and their controlled release properties

Article Type: Research Paper

Keywords: Microcapsules; chitosan; menthol; SPG membrane emulsification; encapsulation

Abstract: Chitosan encapsulated menthol microcapsules were successfully prepared by the oil-in-water emulsion process using Shirasu porous glass (SPG) membrane emulsification technique. The SPG membrane with a membrane pore size of 5.2 µm was found to be suitable for a high viscosity dispersion phase containing light mineral oil. The effect of operating pressure, the amount of menthol loading and crosslinking time on the size and size distribution of microcapsules were systemically investigated. The size of the menthol-loaded chitosan microcapsules was strongly dependent on the mean pore size of the SPG membrane and the amount of menthol loading in the dispersion phase. The average diameter of emulsion droplets of 28.3 µm with a coefficient of variation of 24.7% was obtained. Increasing the menthol loading in the dispersion phase from 5 to 10 wt% of chitosan decreased the emulsion droplets with a broad droplet size distribution. The crosslinked microcapsule size and size distribution of the o/w emulsion droplets decreased with increasing crosslinking time. The mechanism of menthol release was a diffusion control which depended on the proportion of amino group in chitosan-to-tripolyphosphate and crosslinking time.

Microencapsulation of menthol by crosslinked chitosan via porous glass membrane emulsification technique and their controlled release properties

Roongkan Nuisin $^{\rm a)}$, Jaruwan Krongsin $^{\rm b)}$, Supaporn Noppakundilograt $^{\rm c)}$, Suda Kiatkamjornwong $^{\rm c)*}$

Short running title: Microencapsulation of menthol by crosslinked chitosan via porous glass membrane

Suda Kiatkamjornwong

Address: Department of Imaging and Printing Technology, Faculty of Science,

Chulalongkorn University, Bangkok 10330, Thailand

Telephone: +66-02-218-5587 E-mail: ksuda@Chula.ac.th

^{a)} Department of Environmental Science, Faculty of Science, Chulalongkorn University, Bangkok 10330, Thailand

b) Multidisciplinary Program of Petrochemistry and Polymer Science, Faculty of Science, Chulalongkorn University, Bangkok 10330, Thailand

^{c)}Department of Imaging and Printing Technology, Faculty of Science, Chulalongkorn University, Bangkok 10330, Thailand

^{*}Corresponding author

Abstract

Chitosan encapsulated menthol microcapsules were successfully prepared by the oil-in-water

emulsion process using Shirasu porous glass (SPG) membrane emulsification technique. The

SPG membrane with a membrane pore size of 5.2 µm was found to be suitable for a high

viscosity dispersion phase containing light mineral oil. The effect of operation pressure, the

amount of menthol loading and crosslinking time on the size and size distribution of

microcapsules were systemically investigated. The size of the menthol-loaded chitosan

microcapsules was strongly dependent on the mean pore size of the SPG membrane and the

amount of menthol loading in the dispersion phase. The average diameter of emulsion

droplets of 28.3 µm with a coefficient of variation of 24.7% was obtained. Increasing the

menthol loading in the dispersion phase from 5 to 10 wt% of chitosan decreased the emulsion

droplets with a broad droplet size distribution. The size and size distribution of o/w

crosslinked microcapsules decreased with increasing crosslinking time.

Keywords: Microcapsules; chitosan; menthol; SPG membrane emulsification; homogenizing

1. Introduction

Menthol is a cyclic terpene alcohol with three asymmetric carbon atoms. Among the optical isomers, menthol is the one that occurs most widely in nature and it is endowed with the peculiar property to be a fragrance and flavor compound. For this reason, it is widely used as flavoring for toothpaste, oral hygiene and personal care products [1]. Menthol is generally available in the form of crystals or granules with a melting point of 41–43°C. However, its high volatility and whisker growth are the very important problems concerning its applications and shelf life. The microencapsulation method is an accountable and appropriate technique to solve these problems [2]. Chitosan is derivatized by deacetylation of chitin. Chitosan has been used in many applications because of its biocompatibility, biodegradability, non-toxicity and antibacterial activity [3]. Chitosan can form microcapsules by various methods such as spray drying, emulsification/solvent evaporation, ionotropic gelation, coacervation techniques, and so on. It can prevent loss of volatile flavors, and enhance stability of the flavor core materials [2]. The capsule is kept stable during the release time. However, the size of the microcapsules prepared by these methods is difficult to control, and the size distribution is thus very broad [4].

In conventional emulsification devices, such as high-pressure homogenizer, mechanical stirring, and rotor-stator systems, these methods produce rather polydisperse emulsions and consume high energy [5]. A membrane emulsification system produces emulsions by permeating a dispersed phase into a continuous phase through a membrane having a uniform pore diameter. The membrane emulsification method makes it possible to produce monodisperse emulsions and consume less energy [6, 7]. The most commonly used microporous membrane for the emulsification is a Shirasu Porous Glass (SPG) membrane. The SPG membrane is made from SiO₂–Al₂O₃, with a very narrow pore size distribution. It was fabricated by Nakashima and Shimizu [8] via a series of sophisticated heat treatments,

an induced phase separation created a bi-continuous structure of CaO-B₂O₃, and SiO₂–Al₂O₃. Commercially, the pore sizes ranging from 0.1 to 18.0 μm have been available. The SPG membrane is inherently hydrophilic and it is much easier to get the monodisperse oil-inwater (o/w) emulsions than water-in-oil emulsion (w/o) due to the presence of negatively charged silanol groups on the surface [9]. Kiatkamjornwong et al. [10] had successfully prepared the microcapsules of chitosan (0.5–40 μm in diameter) by the conventional stirring method in which chitosan is the shell of microcapsules encapsulating the core material of menthol. The size distribution of the conventional method is rather polydisperse and thus a better technique of porous glass membrane emulsification can remedy the large size distribution to a narrow size distribution of microcapsules.

In this study, the SPG membrane emulsification method was applied to prepare menthol-loaded sodium tripolyphosphate crosslinked chitosan microcapsules. The effects of membrane pore size, the amount of menthol loading and crosslinking time were investigated on the microcapsule size and size distribution. Release kinetics of menthol from microcapsules correspondence to crosslinking time, concentration, and molar ratio of amino and tripolyphosphate were studied.

2. Experimental

2.1 Materials

Chitosan (Sea fresh Chitosan Lab Co., Ltd., Bangkok, Thailand) with a degree of deacetylation of 95% with a viscosity-average molecular weight (\overline{M}_{ν}) of 100,000 g/ mol was used as received. Sodium tripolyphosphate (TPP, Merck, Hohenbrunn, Germany) was used as a crosslinker. Light mineral oil (Hopewell International Co., Ltd., Thailand) was used as an oil phase. Menthol with a molecular weight of 156.27 g/mol (Hong Huat Co., Ltd., Thailand) was used as an encapsulating material. Poly(oxyethylene-2-stearyl ether) (Brij 72,

Greensville Co., Ltd., Thailand) was used as an oil-soluble surfactant. Sodium dodecyl sulfate (SDS, Merck, Germany) and cetyl stearyl alcohol (Kao Co., Ltd., Thailand) were used as a surfactant and a co-surfactant, respectively. Poly(vinyl alcohol), PVA-220, (Kuraray Co., Ltd., Japan) with 87-89% of hydrolysis degree was used as a stabilizer.

2.2 Apparatus

A miniature kit for emulsification with an SPG module was purchased from Kiyomoto Co., Ltd (Japan). A tubular porous glass membrane with the size of 2 cm length and 1 cm diameter was installed in the module. The dispersed phase (oil phase) was stored in a Teflon vessel (20 ml) which was connected to nitrogen gas inlet, the continuous phase (water phase) containing a mixture of SDS and PVA in a 250-ml beaker was stirred at 300 rpm with a magnetic bar to prevent creaming of the droplets. With an optimum pressure of nitrogen gas, the dispersed phase can permeate through the uniform pores of the membrane into the continuous phase to form droplets. The droplets were then stabilized by the PVA and SDS dissolved in the continuous phase.

2.3 Preparation of chitosan microcapsules

The procedures of preparing oil-in-water emulsion of chitosan/menthol microcapsules were manufactured as follows: continuous phase was composed of 50.0 g of deionized water, 0.05 g of sodium dodecyl sulfate, then pour 1w/v% chitosan solution in acetic acid 1v/v%. Oil phase consist of 5.0 g of mineral oil, the solution were then mix using high speed homogenizer at 6000, 10000, 14000 and 16000 rpm for 30-120 minutes. The mixture was continuous stirred at 400 rpm to prevent the coagulation.

2.3.1Preparation of chitosan microcapsules via SPG emulsification

The SPG membrane with an average pore size of 1.4 and 5.2 μm was used for the emulsification. The preparative condition for the emulsification is shown in Table 1. The

SPG membrane was pre-wetted in the aqueous phase. Menthol was dissolved in a mixture of light mineral oil, surfactant and co-surfactant by heating up to 40-43°C and was used as a dispersed phase. The aqueous phase where PVA and SDS had been dissolved was used as a continuous phase. The oil phase permeated through the uniform pores of the SPG membrane by the pressure of nitrogen gas into the aqueous phase to form the o/w emulsion. Sodium tripolyphosphate (TPP) solution was slowly dropped into the o/w emulsion to crosslink the chitosan droplets by stirring at 200 rpm for 1 to 5 h. Finally, the chitosan microcapsules were collected and washed repeatedly two times with petroleum ether and acetone by centrifugation at 3000 rpm, and then the microcapsules were freeze dried. A pressure used was slightly above the critical pressure. In this study, the ranges of the permeation pressures at 48.9 to 88.8 kPa for the 1.4 μm pore size, and 14.1 to 67.0 kPa for the 5.2 μm membrane pore size were used.

Insert Table 1

2.3.2 Preparation of chitosan microcapsules via double emulsion methods

Primary and secondary emulsions in a ratio of 1:1 were mixed and stirred in mild condition of 200 rpm for 1 hr. Sodium tripolyphosphate (TPP) with various concentration of 1, 5, 10, and 15% was dropped into the mixture as crosslinking agent. Varying amount of amino group of chitosan to TPP of 2:1, 4:1, 6:1, and 8:1, the mixtures were then stirred at 400 rpm using different time interval of 30, 60, 90, and 120 minutes. The pH was adjusted to 3, 5, 7, and 9 using acetic acid and sodium hydroxide solution. A simple flowchart for the preparation of chitosan microcapsules by the double emulsion is shown in Fig. 1.

Insert Figure 1

2.4. Characterization of chitosan microcapsules

2.4.1. Measurement of size distribution of the droplets

Droplets before and after the crosslinking were observed with an optical microscope. Diameters of approximately 150 droplets were measured to calculate the average diameter. The number average diameter $(\overline{d_e})$ was calculated according to eq. (1). The coefficient of variation (CV) was determined using the formula in eq. (2).

$$d_e = \frac{\sum_{t=1}^n d_t}{N} \tag{1}$$

$$CV = \left(\sum_{i=1}^{n} \frac{\left(d_i - \overline{d}_e\right)^2}{N}\right)^{1/2} / \overline{d}_e$$
 (2)

where, d_i is the diameter of each droplet, N is total number of the droplets measured, and $\overline{d_e}$ is the number average diameter of the droplets.

2.4.2 Observation of morphology of the microparticles

Morphology of the emulsion microparticles was observed using an optical microscope (model BH2, Olympus Optical Co., Ltd, Tokyo, Japan).

2.4.3 Controlled release study

The 5 ml of prepared chitosan microcapsules were transferred to 15 ml test tube and centrifuged at 3000 rpm for 30 minutes. The creamy layer was separated from aqueous layer, and then transferred to vacuum oven at 30°C for 12 hr. The encapsulation efficiency was calculated as shown in eq.3. Release profiles were calculated in term menthol release (%) with time as shown in eq. 4. All samples were assayed in triplicate for 60 hr.

Encapsulation efficiency =
$$\frac{W_m - W_0}{W_m} \times 100$$
 (3)

Release
$$(\psi) = \left[\frac{W_m - W_m(t)}{W_m - W_0}\right] \times 100$$
 (4)

where, W_m is the weight of dried microcapsule after vapor evaporation, $W_{(t)}$ is the weight of microcapsules in a 40°C oven at time t (hr). The samples were weight at different time interval of 1, 3, 5, 7, 12, 24, 48, and 60 hr. The W_o is the weight of microcapsules after menthol evaporated in a 120°C [11, 12].

2.5 Release kinetic studies of menthol from microcapsules

The release profile of menthol from chitosan microcapsules was studied using the release (%) calculated from eq. 4. The release data of microcapsules were analyzed following mathematical models: Zero-order kinetic; first-order kinetic; Higuchi equation (square-root of time equation) [13]; Baker-Lonsdale equation; Hixson-Crowell; and Ritger-Peppas equation [14], as shown in Table 2. Linear regression value has been used for calculation the correlation coefficient (R²) in order to predict the release behavior from microcapsules.

Insert Table 2

3. Results and discussion

3.1. Effect of the pore size of membrane on the droplet size and size distribution

The SPG membranes with the average pore diameter of 1.4, and 5.2 μ m were used to prepare the o/w emulsion. The uniform emulsion droplets were prepared, and the average diameter ($\overline{d_e}$) of 10.2 and 19.6 μ m for the membrane pore sizes of 1.4 and 5.2 μ m obtained. It was found that the diameter of droplets in the o/w emulsion was approximately 8 and 4 times the diameters of membrane pore. The dispersed phase containing light mineral oil without menthol as an additive was difficult to permeate through the SPG membrane pore size of 1.4 μ m. The possible cause was occurred from the high viscosity of light mineral oil. Furthermore, due to the high molecular weight of PVA stabilizer used, the PVA molecules were covered onto the membrane surface and plugged the pores, the oil phase was thus

retained and could not be permeated. As a resulted, the SPG membrane pore size of $5.2~\mu m$ was used for further studied.

3.2. Effect of the amount of menthol loading on droplet size and size distribution

The menthol dissolved in the dispersed phase affected the o/w emulsion. The permeation pressure decreased from 7.4 kPa to 2.5 kPa and 0.6 kPa when increasing the amount of menthol from 0 to 5 and 10 wt%, respectively. The hydrophilic in the disperse phase increased with increasing the amount of menthol loading in disperse phase. The hydroxyl group of menthol enhances the hydrophilicity of the oil phase, thus to permeate it easily through the hydrophilic pore wall of the SPG membrane. The permeation pressure was then decreased. Optical micrographs and the histogram of size distribution of the droplets in oil phase at different amounts of menthol loadings are shown in Fig. 2. Without the menthol, an average diameter of emulsion droplets of 28.3 μm with the CV of 24.7% was obtained. When the amounts of menthol loading in the disperse phase increased from 5 to 10 wt%, the average diameters of emulsion droplets decreased from 24.2 to 16.8 μm with the CV of the droplets increased from 34.4 to 57.6%. The size distributions expressed as histograms in Figure 2 a-c) indicate that more menthol loading in the dispersed phase produced the smaller size droplets in the range of 10 μm. This effect is caused by the increases in hydrophilicity of the hydroxyl groups when increasing the menthol loadings.

Insert Fig. 2

Insert Fig.2a, Fig 2b, Fig 2c

3.3. Effect of crosslinking time on the size and size distribution

Chitosan as the shell of o/w emulsion droplets was crosslinked with TPP solution. TPP was dissociated into OH^- and $P_3O_{10}^{5-}$ anions. The positively charged amino group of chitosan reacted with $P_3O_{10}^{5-}$ anions to form crosslinking bonds [15]. The crosslinked microcapsule

sizes of the o/w emulsion droplets decreased from 47.4 to 27.6 µm with increasing crosslinking time (Fig. 3) due to the increase of crosslink density of chitosan-TPP matrix [16]. The less crosslinking time of 1 h could not form the small droplet size for the subsequence process in this research. Very interestingly, the longer crosslinking time gave the narrow size distribution.

Insert Fig. 3

3.4Preparation of microcapsules via conventional homogenizing method

The preparation of o/w emulsion with narrow size distribution by SPG emulsification technique is that the o/w emulsion should be stable with a narrow emulsion droplets size distribution. Since, the oil phase composed of chitosan with different amount of menthol, a hydrophilic properties was reviewed. Therefore, it is necessary to find a condition where a large amount of chitosan can be maintained and performed microcapsules. The ultrasonic homogenizer was used with high homogenizing rate. The effects of homogenizing speed, time, and chitosan concentration were studied.

3.4.1 Effect of homogenizing speed

Chitosan microcapsules with broad coefficient of variation of 55.9% were obtained using the lower homogenizing speed of 6000 rpm. Increasing the homogenizing speed from 14000 to 16000 rpm, the microcapsules with CV of 38.9 and 39.7%, were obtained, respectively. However, the homogenizing speed at 10000 rpm was found the lowest CV% of 31.5. The phase separation of emulsion was observed at the beginning of emulsification process approximately within 1 hr after the homogenizing process. As shown in Table 3, the homogenizing speed of 10000 rpm was selected for further study since the emulsion droplets in size of $39.1\pm12.3~\mu m$.

Insert Table 3

3.4.2 Effect of homogenizing time

Chitosan microcapsules was prepared and used as a secondary emulsion for combination with a primary emulsion obtained via SPG emulsification process. The homogenizing speed of homogenizer was used at 10000 rpm. The effect of homogenizing time of 30, 60, 90, and 120 second were studied. As shown in Table 4, the emulsion droplets with coefficient of variation of 30.8 and 34.8% were obtained with homogenizing time of 30 and 60 second, respectively. The broad droplets size distribution was reviewed comparison with using the homogenizing time of 60 and 120 second. The coefficient of variation of 24.8 and 24.6% was calculated. The short period of homogenizing time, the droplets disruption with less stability occurred. The micelles formation was unstable. The oil droplets distribution related to the stirring time that affected to the micelles of oils in water phase was reviewed [10]. An increasing in stirring time from 90 to 120 minute, an emulsion droplets size was increased from 39.8±9.9 to 41.2±10.1 µm. The stirring time of 90 second were then selected for further studies.

Insert Table 4

3.4.3 Effect of chitosan concentration

Preparation of chitosan microcapsules was prepared with various concentration of chitosan in acetic acid solution. As shown in Table 5, the amount of chitosan was varied from 1, 1.5, and 2.0 w/v% of acetic acid. It was found that the emulsion droplets of chitosan in size of 17.9±8.1, 17.0±6.3, and 16.7±6.9 μm was obtained, respectively. The 1.5 w/v% chitosan solution in acetic acid was considered as a suitable concentration for further experiment since the viscosity is concerned for emulsification processing [17].

Insert Table 5

3.5 Preparation of menthol encapsulated chitosan microcapsule

Menthol encapsulated microcapsules was prepared via double emulsion method. The emulsions from SPG emulsification using SPG membrane pore size of 5.2 μm as a primary, and high-speed homogenizer at 14,000 rpm for 90 minutes as secondary emulsion was prepared. The miscibility of two emulsions was studied in terms of size and encapsulation efficiency. In this experiment, the primary emulsion of 24.2±8.3 μm was mild stirred with secondary emulsion of 17.0±6.3 μm, and left for 1 hr. The emulsion droplets in size of 31.0±8.5 μm was obtained and the narrow coefficient of variation observed as shown in Table 6. It was found that the small size of secondary emulsion was diffused and absorbed into the primary emulsion, the swelling droplets obtained with narrow size distribution. The mechanism is followed the non-destructive swelling [18]. Since, the less thermodynamics stability of secondary emulsion tend to migrate to the more stable droplets of primary emulsions, the absorption were then occurred.

Insert Table 6

3.5.1 Effect of pH on size and size distribution of microcapsules

The effects of pH adjusted solution onto size and size distribution of swollen microcapsules was studied. The pH in ranges of 5 to 7 was preferred for the use of microcapsules in further application as an additive in leave-on conditioners. The pH values of 3.6, 5.0, 7.0, and 8.9 were studied. As shown in Fig. 4, the droplets size of microcapsules tend to decreased with increasing coefficient of variation at pH of 3.6 (Figure 4a, and 4b). The affects of microcapsules degradation may results from the non-crosslinked chitosan molecules dissolved from microcapsule at low pH. The pH of 5.0, 7.0, and 8.9 in emulsions were adjusted using sodium hydroxide. The menthol encapsulated chitosan microcapsules in size of 26.8, 28.6, and 28.0 µm were obtained, respectively. The narrow emulsion size

distribution as increasing pH was reviewed. The coefficient of variation of 20.6, 23.7, and 30% was calculated. Then, the workable pH for microcapsules in further uses was considered in ranges of 5 to 7.

Insert Figure 4a

Insert Figure 4b

3.6 Efficiency of encapsulation and controlled release of menthol from microcapsule

The efficiency of encapsulation and controlled release of menthol from microcapsules were studied as follows:

3.6.1 Effects of crosslinking time

Menthol encapsulated chitosan microcapsules were prepared via double emulsion, 5 w/w% sodium tripolyphosphate (TPP) as crosslinking agent. The crosslinking time was varied for 30, 60, 90, and 120 min. The encapsulation efficiency profiles of microcapsules were graphically presented in Figure 5. The results revealed that the menthol encapsulated in chitosan microcapsules was increased with increasing crosslinked time. The order of menthol encapsulated in microcapsules was 9.9±0.1, 35.6±0.1, 35.5±1.0 and 36.1±0.3% when the crosslinking time of 30, 60, 90 and 120 min, respectively. The encapsulation pattern indicated that the menthol was released and controlled by the thickness of microcapsule wall. The ionic interaction between a negatively charged counterion of tripolyphosphate and a positively charged amino group of chitosan was an important role on degree of crosslinking [16]. Encapsulation efficiency of menthol in microcapsules was retained when the longer period of crosslinking time was applied. The release of menthol was very slow which could be due to the thickness of chitosan wall. Figure 6 shows release behavior of menthol from chitosan microcapsules prepared with TPP solution as ionic crosslinking agent at various crosslinking times.

15

Insert Fig. 5

Insert Fig. 6

3.6.2 Effects of crosslinking concentrations

Figure 7 shows release behavior of menthol from chitosan microcapsules prepared with tripolyphosphate solution at various concentrations. As previously described, the amount of crosslinking agent influenced the ionic-crosslinking density of TPP-chitosan. As shown in Figure 7, the encapsulation efficiency of menthol was improved by the increasing amount of TPP concentration. The amount of TPP solution of 1, 5, 10, and 15 w/w% was applied, the encapsulation efficiency values of 14.8±7.8, 36.1±0.3, 38.1±1.7 and 37.7±3.3% were obtained. The higher the amounts of TPP is, the thicker the microcapsule walls became. Figure 8 shows the effect of the TPP as the crosslinking agent on the release behavior of menthol. There was a release 95% of menthol at 60 hr in 1 w/w% TPP-chitosan microcapsules. The amount of TPP of 5, 10, and 15 w/w%, the amount of menthol releasing from microcapsules were 46.1±1.5, 43.8±2.3, and 38.3±2.5, respectively. The higher concentration of TPP, the lower amount of menthol released from chitosan microcapsules. It depends on the crosslinking density of TPP-chitosan.

Insert Fig. 7

Insert Fig. 8

3.6.3 Effects of molar ratio of amino group in chitosan to tripolyphosphate

Encapsulation efficiency increases with increasing the molar ratio of amino group in chitosan to TPP, as shown in Figure 9. The effects of molar ratio of amino group in chitosan to tripolyphosphate of 2:1, 4:1, 6:1, and 8:1 to encapsulated efficiency of menthol was carried out. Chitosan microcapsules with encapsulated efficiency of 47.5±3.5, 52.7±0.5, 67.0±1.5 and 69.2±1.3% was obtained, respectively. In Figure 10, the comparative releasing

profile of menthol from chitosan microcapsules decreased with increasing amount of molar ration of amino group to TPP. The menthol diffusion was reduced after 12 hours. It was found that the amount of menthol releasing of 34.0±2.0, 22.9±2.9, 18.4±2.9 and 16.2±2.8% obtained when the molar ratio of amino group-to-TPP of 2:1, 4:1, 6:1, and 8:1, respectively. The slope of releasing profiles for all molar ratio of amino and tripolyphosphate increased at the initial stage and declined after 60 hr. From the graph, the release rate of menthol could find slows down when the molar ratio of amino and tripolyphosphate increases. The chitosan wall membrane almost completely seals up when increasing degree of crosslinked.

Insert Fig. 9

Insert Fig. 10

3.7 Release kinetics studies of menthol from microcapsules

The release kinetics of menthol from various conditions based upon crosslinking time, crosslink concentration, and molar ratio of amino and tripolyphosphate was determined by comparing their respective co-relation coefficients. Various models and equations of zero order, first order, Higuchi, Hixson-Crowell, Baker-Lonsdale, and Ritger-Peppas [19, 20] have been used after linearization to predict mechanisms of menthol release. Ritger-Peppas plots were found to be the highest linearity with correlation coefficient greater than that of the other kinetics as shown in Fig. 11a-c. The results indicating that the menthol release mechanism from these chitosan microcapsules was diffusion controlled with diffusion index (n) calculated from slope. In Table 7, the n values revealed that the releasing menthol was found from spherical capsules. The diffusion index n was ≤ 0.43 , which indicates a Fickian diffusion, and $0.43 \leq n \leq 1.00$ indicates a non-Fickian [19]. The value of "n" in Ritger-Peppas is approximately 0.5, which implies that the menthol follows non-Fickian transport.

The resulted demonstrated that the transportation of menthol was controlled by crosslink density [21]. The crosslinking density increases, the value of n was increased.

Insert Fig. 11

Insert Table 7

4. Conclusion

Chitosan as the wall membrane material, menthol as volatile core material microcapsules were prepared using high speed homogenizer and SPG membrane emulsification techniques. The effects of membrane pore size, the amount of menthol loadings and crosslinking time were affected to size and size distribution of droplets. The uniform-sized chitosan microcapsules can also be prepared when the membrane pore size used was 5.2 µm; the higher amount of menthol gave the smaller mean diameter of the emulsion droplets with narrow size distribution. The longer crosslinking time, the smaller microcapsules with a narrow size distribution was produced. The emulsion droplets with average size of 31.0±8.5 µm and coefficient of variation of 27.4% were obtained. The suitable pH for microcapsules stability was found at pH in range of 5 to 7. To control release of menthol by changing manufacturing conditions of crosslinking time, amount of tripolyphosphate, and molar ratio of amino group in chitosan to tripolyphosphate were studied. The resulted indicated that encapsulation efficiency and release properties of menthol were depended on the crosslinking time, amount of tripolyphosphate, and molar ratio of amino group to tripolyphosphate. The menthol release curve shows an exponential release normally at a higher rate in the beginning. Non-Fickian diffusion was described behavior of menthol release from microcapsules. The diffusion patterns were found to be dependent on the crosslinking density.

Acknowledgements

The authors thank the Thailand Research Fund for funding the research under the Senior Scholarly Consolidation Grant no. RTA5080004. Research facilities from the Department of Imaging and Printing Technology are highly appreciated.

References

- [1] N. Galeotti, L. Di Cesare Mannelli, G. Mazzanti, A. Bartolini, C. Ghelardini, Menthol: a natural analgesic compound. Neurosci. Lett. 322 (2002) 145–148.
- [2] A. Soottitantawat, K. Takayama, K. Okamura, D. Muranaka, H. Yoshii, T. Furuta, M. Ohkawara, P. Linko, Microencapsulation of l-menthol by spray drying and its release characteristics. Innovat. Food Sci. Emerg. Tech. 6 (2005) 163–170.
- [3] M. Rinaudo, Chitin and chitosan: Properties and applications. Prog. Polym. Sci. 31 (2006) 603–632.
- [4] W. Wei, L.Y. Wang, L. Yuan, X.D. Yang, Z.G. Su, G.H. Ma, Bioprocess of uniform-sized crosslinked chitosan microspheres in rats following oral administration. Eur. J. Pharm. Biopharm. 69 (2008) 878–886.
- [5] G.T. Vladisavljevic, H. Schubert, Preparation and analysis of oil-in-water emulsions with a narrow droplet size distribution using Shirasu-porous-glass (SPG) membranes. Desalination 144 (2002) 167–172.
- [6] M. Yasuno, M. Nakajima, S. Iwamoto, T. Maruyama, S. Sugiura, I. Kobayashi, A. Shono, K. Satoh, Visualization and characterization of SPG membrane emulsification. J. Membr. Sci. 210 (2002) 29–37.
- [7] S.M. Joscelyne, G. Trägårdh, Membrane emulsification a literature review. J. Membr, Sci. 169 (2000), 107–117.

- [8] T. Nakashima, M. Shimizu, Porous glass from calcium alumino boro-silicate glass. Ceramics 21 (1986), 408.
- [9] G.T. Vladisavljevic, I. Kobayashi, M. Nakajima, R.A. Williams, M. Shimizu, T. Nakashima, Shirasu Porous Glass membrane emulsification: Characterization of membrane structure by high-resolution X-ray microtomography and microscopic observation of droplet formation in real time. J. Membr. Sci. 302 (2007) 243–253.
- [10] S. Kiatkamjornwong, S. Phansomboon, V. Hoven, Chitosan microencapsulation of menthol and its controlled release, The Journal of the Royal Institute of Thailand 34 (2009) 337–371.
- [11] C.P. Chang, T.K. Leung, S.M. Lin, C.C. Hsu, Release properties on gelatin-gum Arabic microcapsules containing camphor oil with added polystyrene. Colloids Surf. B Biointerfaces 50 (2006) 136–140.
- [12] W.C. Hsieh, C.P. Chang, Y.L. Gao, Controlled release properties of chitosan encapsulated volatile citronella oil microcapsules by thermal treatments. Colloids Surf. B Biointerfaces 53 (2006) 209–214.
- [13] T. Higuchi, Mechanism of sustained-action medication. Theoritical analysis of rate of release of solid drugs disperse in solid matrices. J. Pharm. Sci. 52 (1963) 1145–1149.
- [14] R.W. Korsmeyer, R. Gurny, E. Doelker, P. Buri, N.A. Peppas, Mechanisms of solute release from porous hydrophilic polymers. Inter. J. Pharm. 15 (1983) 25–35.
- [15] F.M. Hsieh, C. Huang, T.F. Lin, Y.M. Chen, J.C. Lin, Study of sodium Tripolyphosphate-crosslinked chitosan beads entrapped with *Pseudomonas putida* for phenol degradation, Process Biochem. 43 (2008) 83–92.
- [16] J.A. Ko, H.J. Park, S.J. Hwang, J.B. Park, J.S. Lee, Preparation and characterization of chitosan microparticles intended for controlled drug delivery. Inter. J. Pharm. 249 (2002) 165–174.

- [17] L.Y. Wang, G.H. Ma, Z.G. Su, Preparation of uniform sized chitosan microspheres by membrane emulsification technique and application as a carrier of protein drug. J. Control. Release 106 (2005) 62–75.
- [18] G.H. Ma, M. Nagai, S. Omi, Synthesis of uniform microspheres with higher content of 2-hydroxyethyl methacrylate by employing SPG emulsification Technique followed by swelling process of droplets. J. Appl. Polym. Sci. 66 (1997) 1325–1341.
- [19] P.L. Ritger, N.A. Peppas, A simple equation for description of solute release I. Fickian and non-Fickian release from non-swellable devices in the form of slabs, spheres, cylinders or discs. J. Control. Release 5 (1987) 23–36.
- [20] K. Shi, Y. Jiang, M. Zhang, Y. Wang, F. Cui, Tocopheryl succinate-based lipid nanospheres for paclitaxel delivery: Preparation, characters, and in vitro release kinetics. Drug Delivery 17(1) (2010) 1–10.
- [21] R.V. Kulkarni, B.S. Mangond, S. Mutalik, B. Sa, Interpenetrating polymer network microcapsules of gellan gum and egg albumin entrapped with diltiazem–resin complex for controlled release application. Carbohydr. Polym. 83 (2011) 1001–1007.

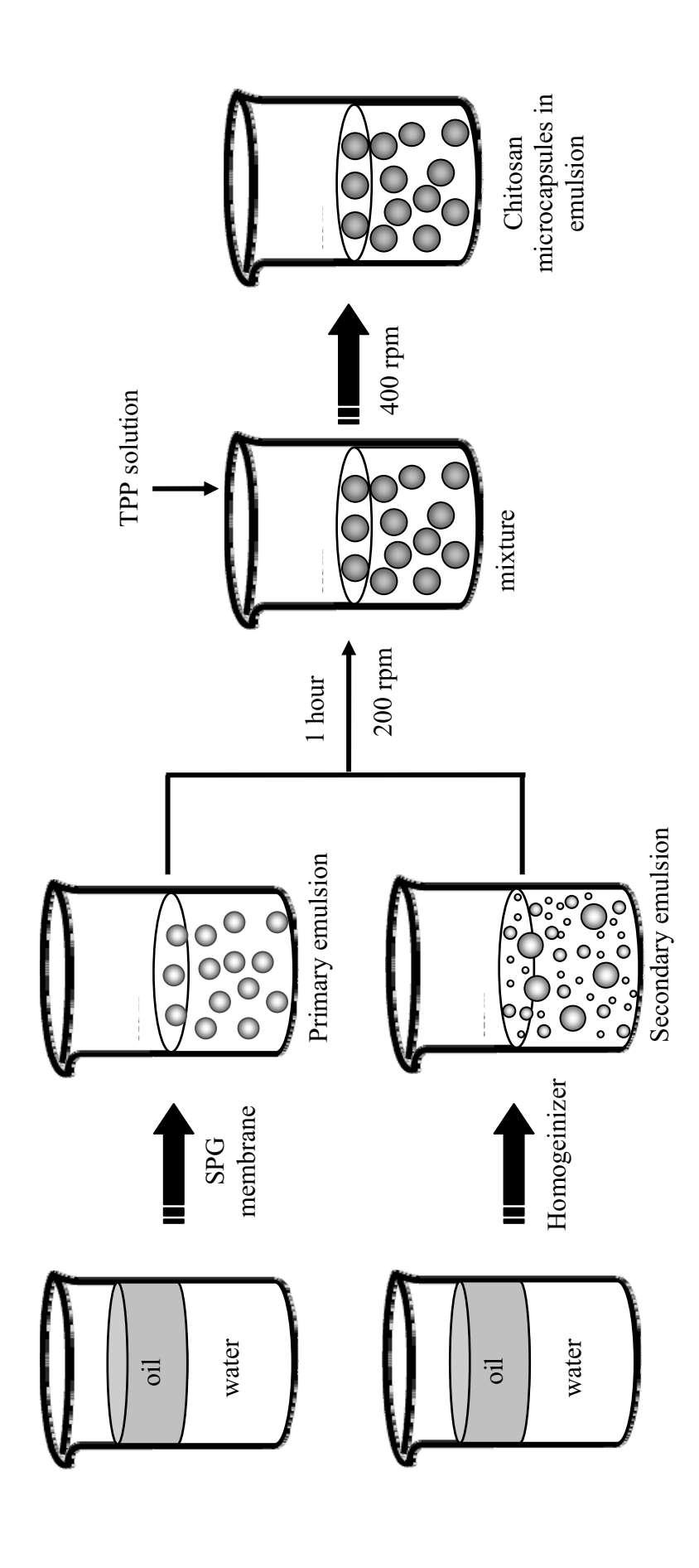


Figure 1 Flowchart for preparation of chitosan microcapsules by double emulsification

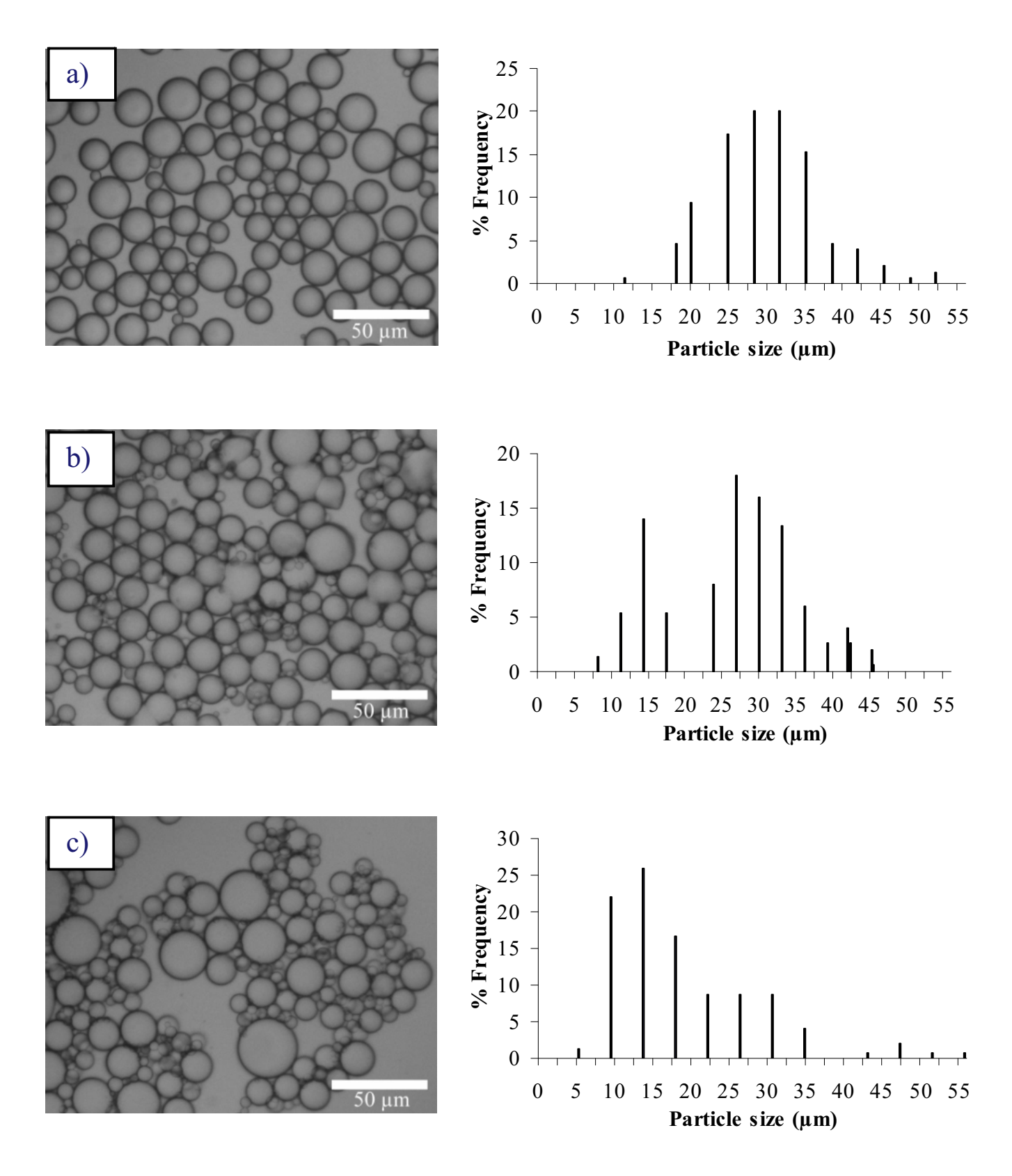


Figure 2 Optical micrographs (left) and histograms of the size distribution (right) of o/w emulsion with different amounts of menthol loadings for a) without menthol, b) 5 wt% menthol, c) 10 wt% menthol

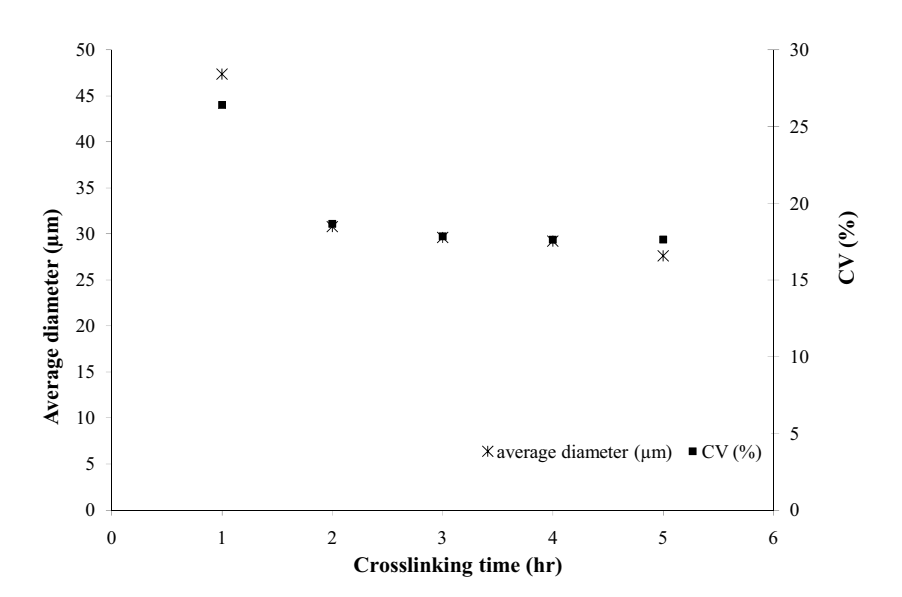


Figure 3 Relationship between the crosslinking time, the average size and the coefficient of variation

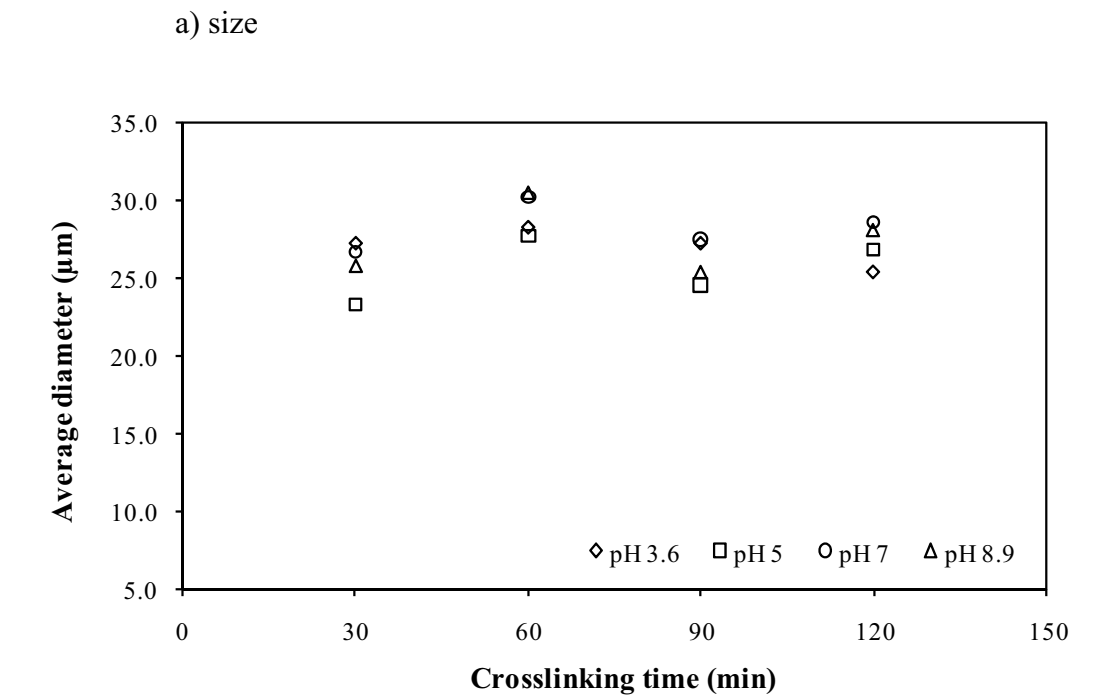


Figure 4 Relationship of microcapsules with different pHs: a) size, b) coefficient of variation

b) coefficient of variation

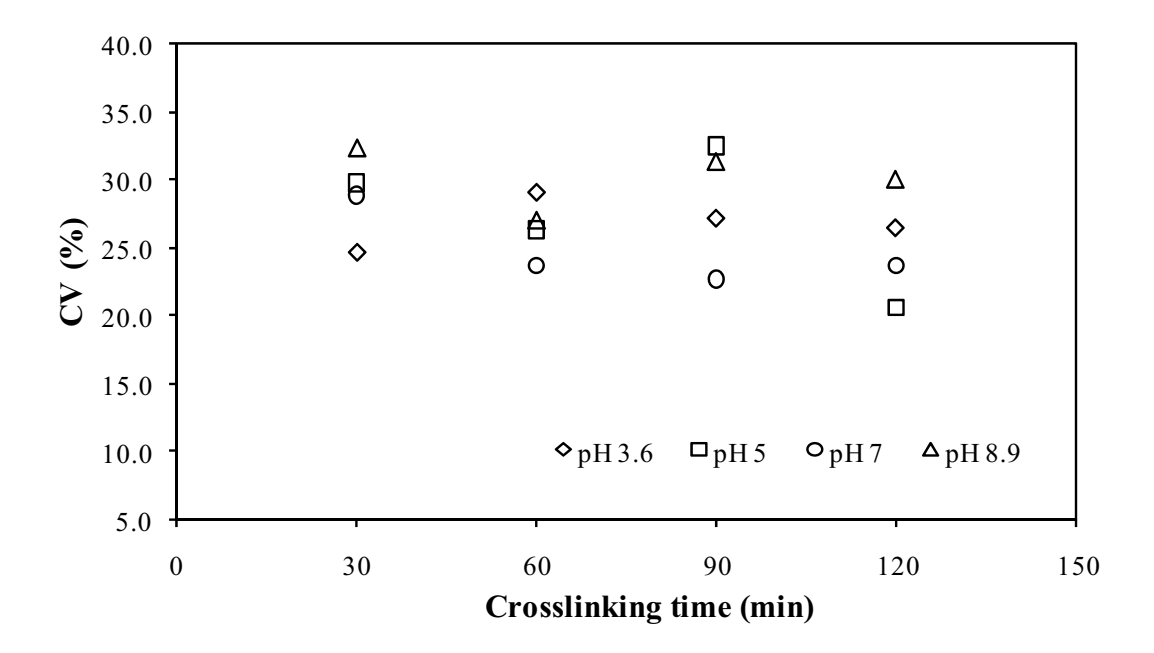


Figure 4 Coefficient of variation Vs. crosslinking time at various pHs

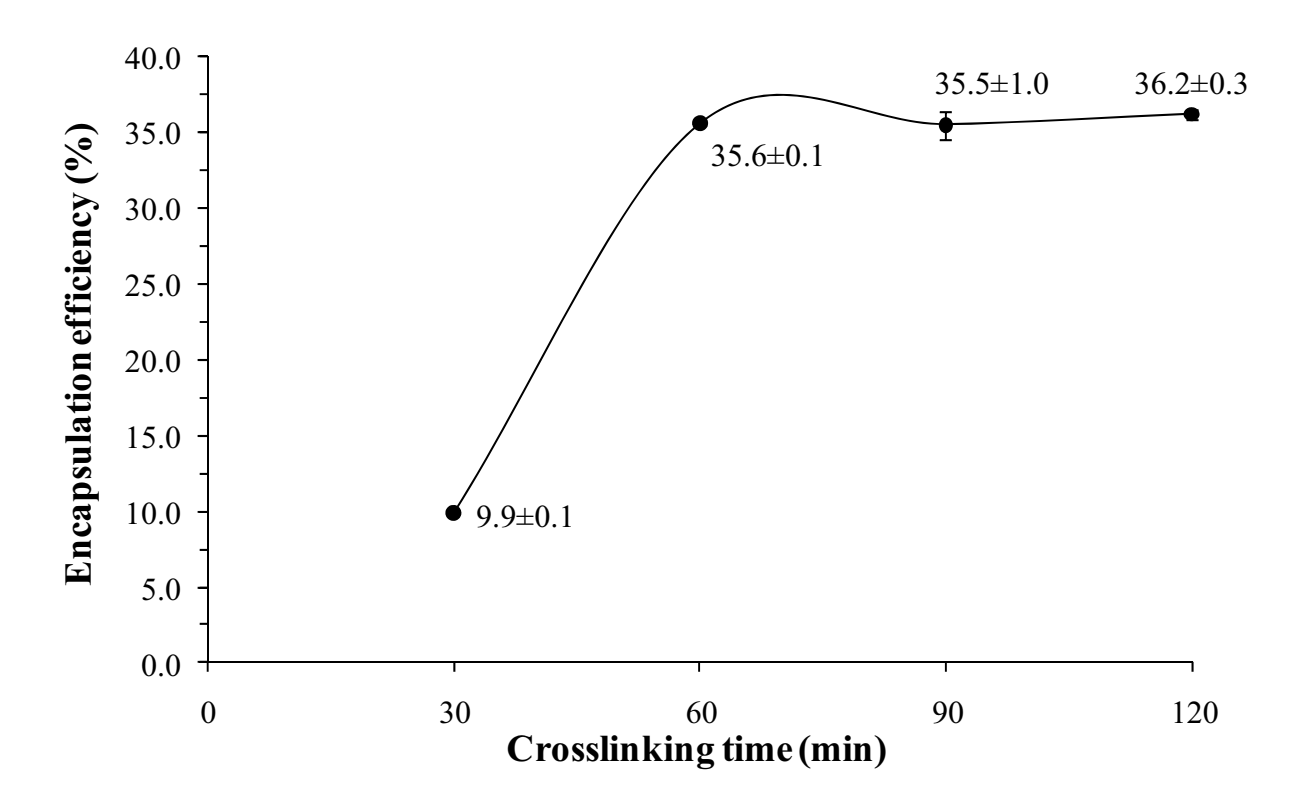


Figure 5 Encapsulation efficiency curves of menthol at 72 hr with various crosslinking times with 5w/w% of TPP, and molar ratio of amino group in chitosan to TPP of 1:1.

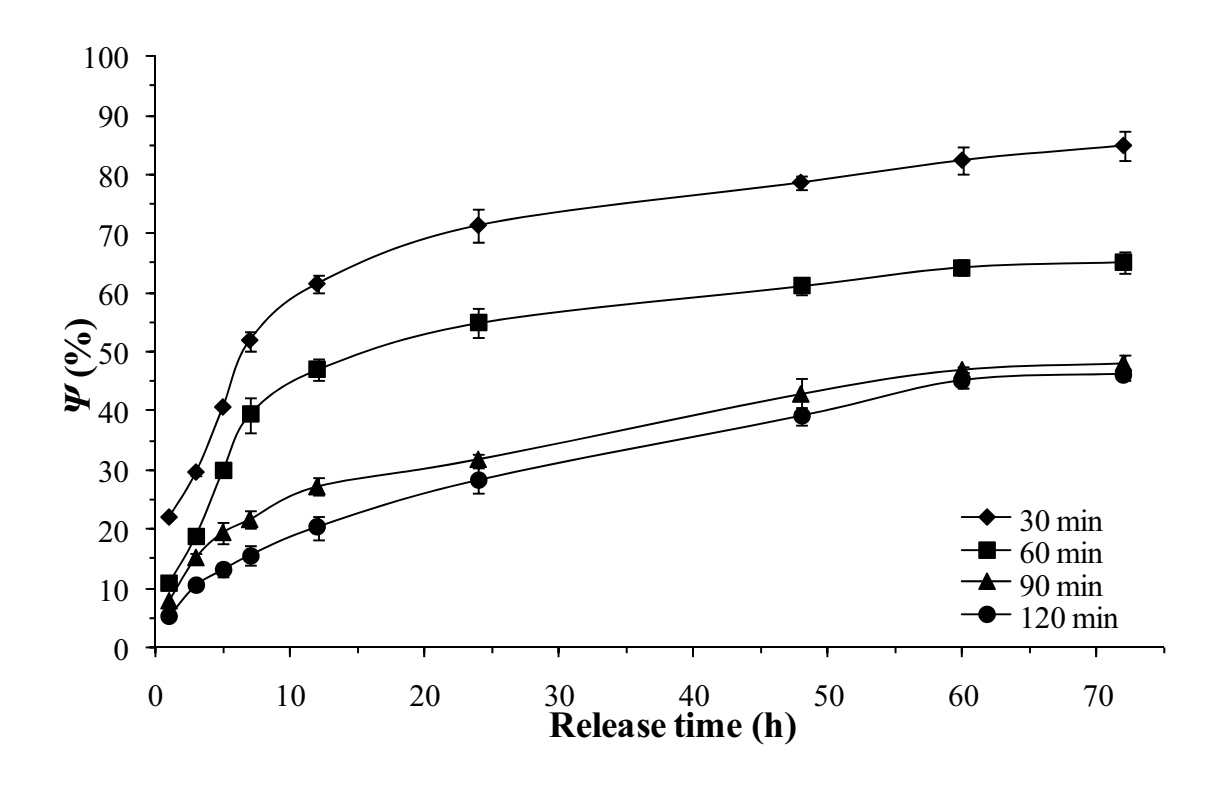


Figure 6 Comparative curves of menthol at 72-hr release, the chitosan amino group-to-TPP mole ratio of 1:1 at various crosslinking times

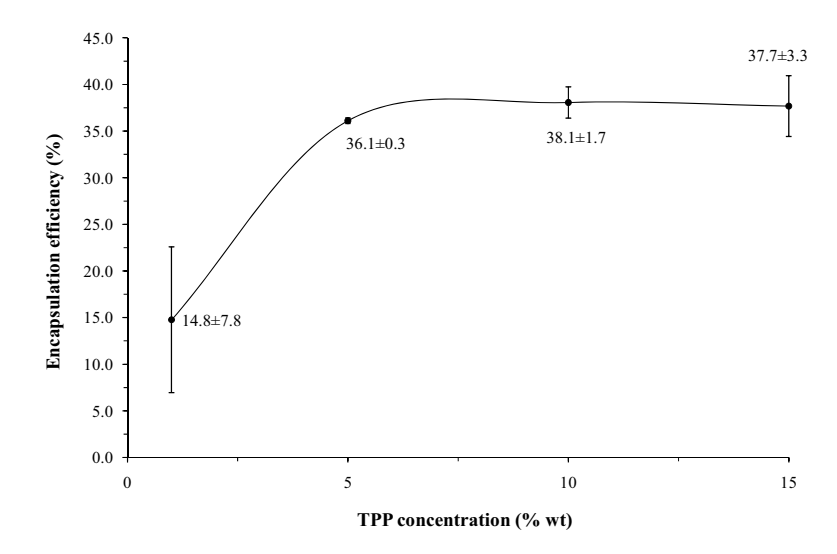


Figure 7 Menthol releasing curve at 72 hr with various TPP concentrations

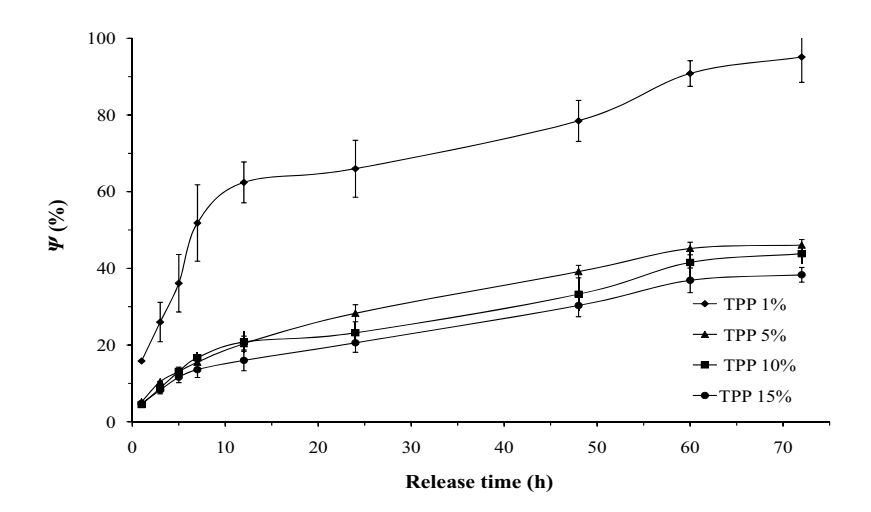


Figure 8 Menthol release curves as a function of TPP concentrations at the crosslinking time of 120 min.

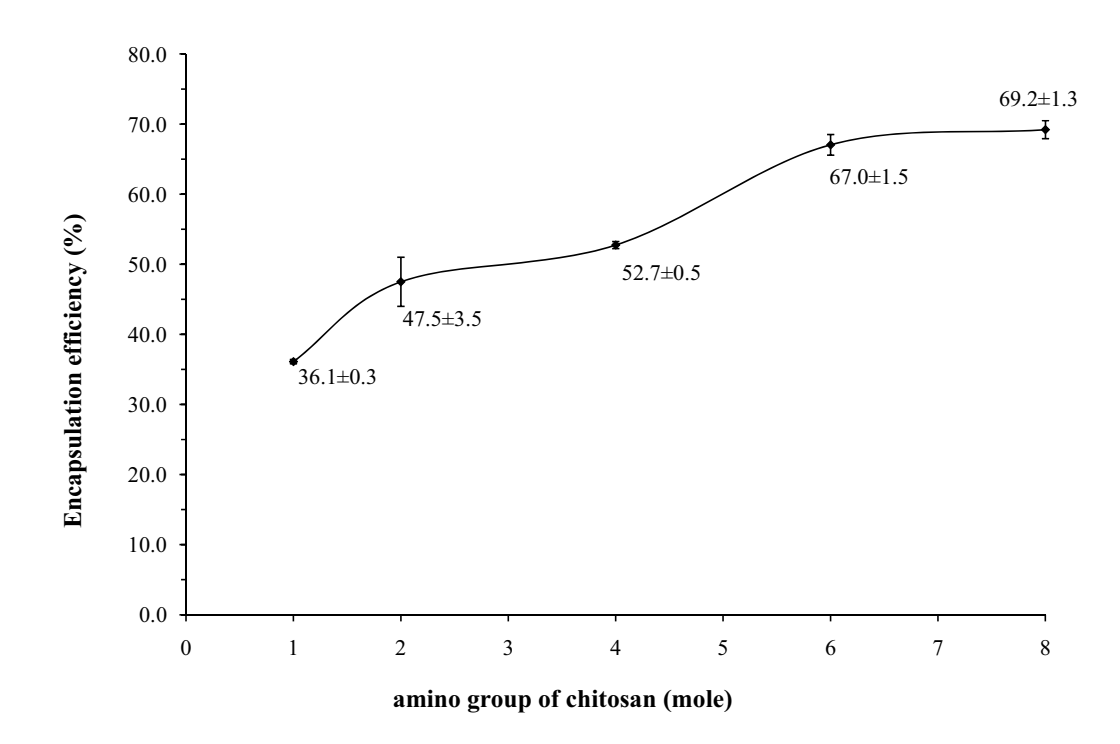


Figure 9 Encapsulation efficiency curve of menthol at 72 hr at various molar ratios of amino group in chitosan, 5 w/w% TPP at a crosslinking time at 120 min.

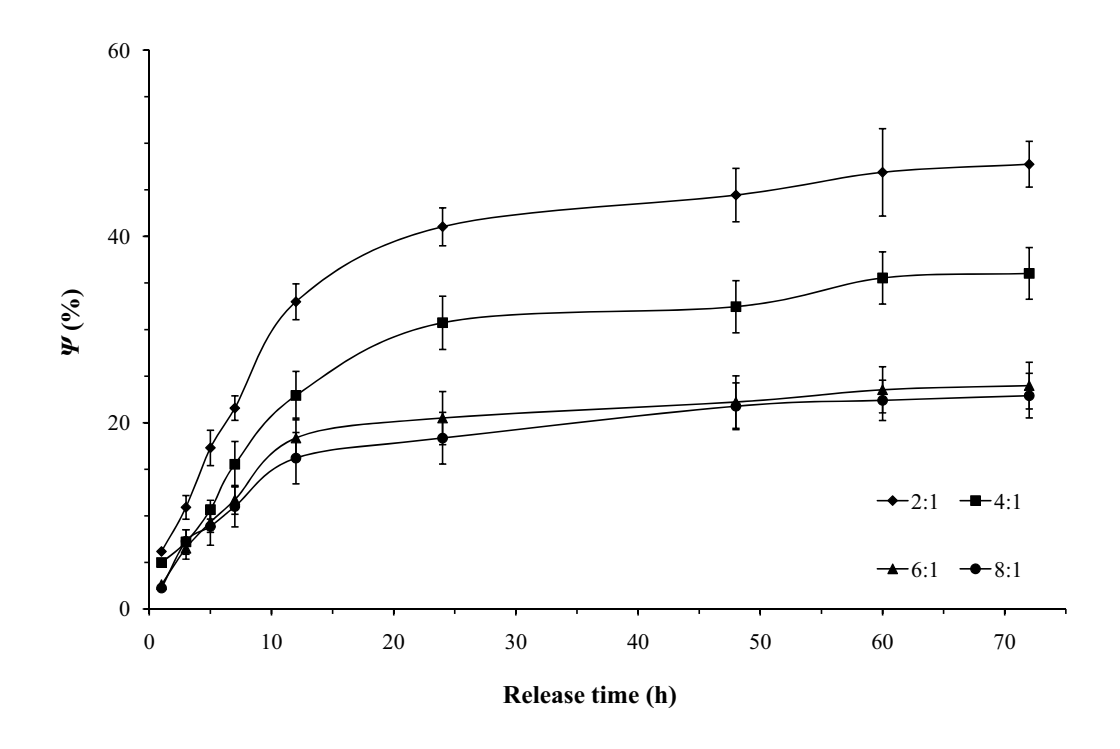
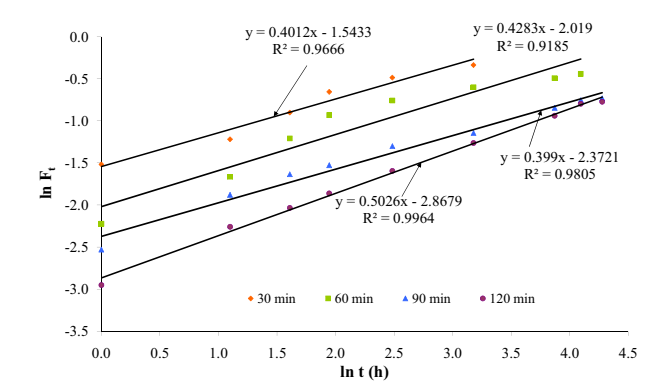
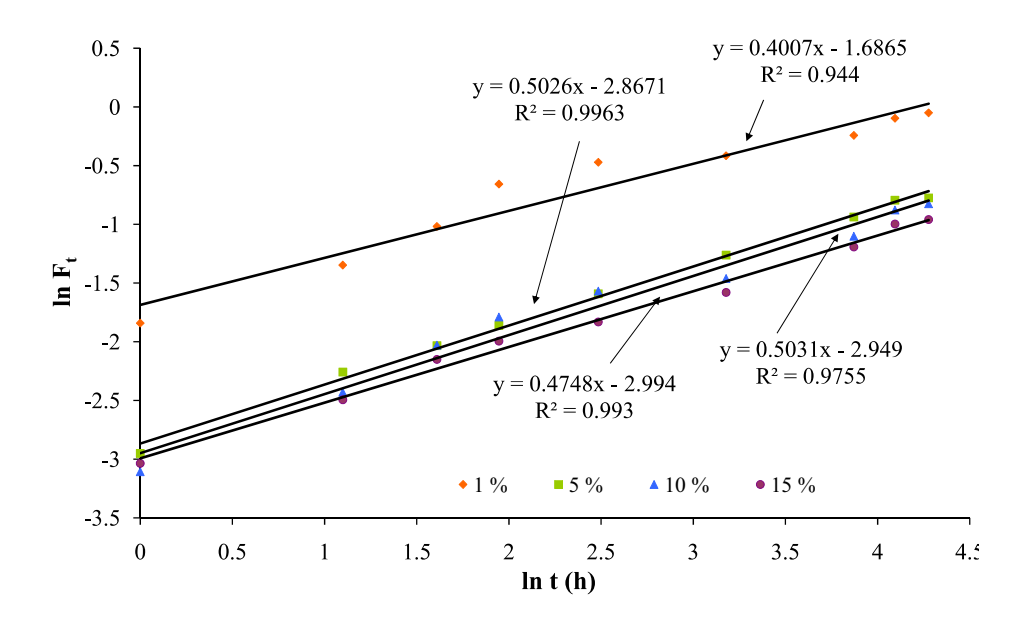


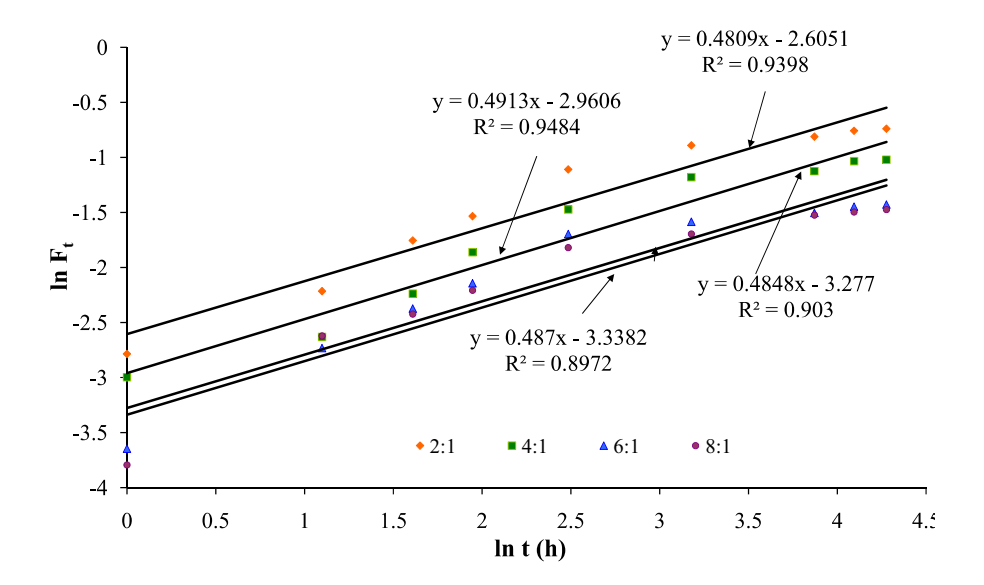
Figure 10 Effect of release time at the function of molar ratios of amino group in chitosan to TPP with 120 min crosslinking time



a) crosslinking time



b) concentration of TPP



c) molar ratio of an amino group to TPP

Figure 11 Linear regression of Ritger-Peppas models for release kinetics of menthol; a) crosslinking time, b) concentration of TPP, and c) molar ratio of an amino group to TPP

Table 1 A recipe for the o/w emulsion

Component	Weight (g)
Continuous phase	
water	220
	20
chitosan solution (1% w/v in 1 M acetic acid)	3.0
PVA	
SDS	1.5
Disperse phase	
light mineral oil	20
_	0.5-2.0
menthol	0.5
Brij 72	
cetyl-stearyl alcohol	0.5

Table 2 The o/w emulsion droplets (without menthol) obtained by two pore size membranes

Particle property	-	pore size (μm)	
1 1 2	1.4	5.2	
Number average diameter, $\overline{d_e}$ (µm)	10.2	19.6	
CV (%)	10.1	11.5	

Table 3 Size and size distribution of emulsion with different homogenizing speeds

Run no. ^a	Speed (rpm)	$\overline{d_e}$ (µm) ±SD	CV (%)
D001	6000	62.6±34.9	55.9
D002	10000	39.1±12.3	31.5
D003	14000	20.2±7.9	38.9
D004	16000	30.5±12.1	39.7

^a Chitosan solution 1 w/v% of 2 M acetic acid, the amount of chitosan was 10.0 g.

Table 4 Size and size distribution with various homogenizing times

Run no.	Time (second)	$\overline{d_e} \pm SD (\mu m)$	CV (%)
T30	30	38.7±11.9	30.8
T60	60	38.7±13.5	34.8
T90	90	39.8±9.9	24.8
T120	120	41.2±10.1	24.6

Table 5 Size and size distribution of microcapsules with various chitosan concentrations

Run no.	Chitosan concentration	$\overline{d_e}$ ±SD	CV (%)
	(% w/v)	(µm)	
CH1	1.0	17.9±8.1	45.6
CH1.5	1.5	17.0 ± 6.3	37.1
CH2	2.0	16.7±6.9	41.0

Table 6 Size and size distribution of emulsion droplets prepared with double emulsion method

Conditions	$\overline{d_e} \pm SD (\mu m)$	CV (%)
Primary emulsion	24.2±8.3	34.4
Secondary emulsion	17.0±6.3	37.1
Double emulsion	31.0±8.5	27.4

Primary emulsion was prepared using homogenizing speed at 14,000 rpm for 90 minutes.

Secondary emulsion using SPG pore size having 5.2 micrometers.

Table 7 Mathematical models for controlled release kinetics understudy

Model	Equations	X	у
Zero-order	$Q_t = Q_0 + k_0 t$	Q_{t}	t
First order	$\log Q_{t} = \log Q_{0} + kt/2.303$	$log \; Q_t$	t
Higuchi	$Q_t = k_H t^{1/2}$	Q_{t}	t ^{1/2}
Baker-Lonsdale	$3/2[1-(1-F_t)^{2/3}]-F_t = kt$	$3/2[1-(1-F_t)^{2/3}]-F_t$	t
Hixson-Crowell	$(1-F_t)^{1/3} = 1-kt$	$(1-F_t)^{1/3}$	t
Ritger-Peppas	$Ln F_t = ln k + n ln t$	ln F _t	ln t

Table 8 Release exponent (k), diffusion index (n), and correlation coefficient (R^2) from the linear regression using Ritger-Peppas model with $\ln F_t = k + n \ln t$

Condition	k	R ²	n
Crosslinking time (min)			
30	-1.5433	0.9666	0.4020
60	-2.0190	0.9185	0.4283
90	-2.3721	0.9805	0.3990
120	-2.8679	0.9964	0.5026
Concentration of TPP (%)			
1	-1.6865	0.9440	0.4007
5	-2.8671	0.9963	0.5026
10	-2.9490	0.9755	0.5031
15	-2.9940	0.9930	0.4748
Molar ratio of CS:TPP			
2:1	-2.6051	0.9398	0.4809
4:1	-2.9606	0.9484	0.4913
6:1	-3.2770	0.9030	0.4848
8:1	-3.3382	0.8972	0.4874

Draft Manuscript

2	Synthesis and Characterization of Water Swellable Natural Rubber Composite
4	
5	
6	Charoen Nakason ¹ *, Yeampon Nakaramontee ¹ , Azizon Kaesaman ¹ , Wiyong
7	Kangwansukpamonkon, and Suda Kiatkamjornwong ² **
8	
9	¹ Center of Excellence in Natural Rubber Technology, Department of Rubber
10	Technology and Polymer Science, Faculty of Science and Technology, Prince of
11	Songkla University, Pattani, 94000, Thailand;
12	¹ *e-mail:ncharoen@bunga.pn.psu.ac.th
13	² Multidisciplinary Program of Petrochemistry and Polymer Science,
14	Department of Imaging and Printing Technology, Faculty of Science,
15	Chulalongkorn University, Bangkok, 10330, Thailand;
16	² **e-mail: <u>ksuda@chula.ac.th</u>
17	
18	
19	
20	
21	
22	
23	
24	
25	
26	
-	

Synthesis and Characterization of Water Swellable Natural Rubber Composites

28

30

31

32

33

34

35

36

37

38

39

40

41

42

43

44

45

46

27

29 ABSTRACT

A superabsorbent polymer (SAP) based on cassava starch-g-polyacrylamide (CSt-g-PAM) was prepared by a reactive batch processing using a specially designed batch reactor. SAP composites (SAPCs) were prepared from the CSt-g-PAM by blending with 20 phr of bentonite clay to increase the water absorbency of the SAP from 605 g/g up to 730 g/g for the SAPC. Water swellable natural rubber (WSNR) was then prepared by blending high-ammonia natural rubber (HANR) latex, or dry blending either epoxidized natural rubber (ENR) or maleated natural rubber (MNR) with the SAPC, coupled with poly(ethylene oxide) (PEO) and/or trimethylol propane trimethacrylate (TMPTMA). The curing, mechanical and morphological properties and the water absorbency of the different WSNRs were characterized. The WSNRs with both 10 phr PEO and 2 phr TMPTMA gave a higher mechanical strength and water absorbency. Increasing the PEO loadings to 20 or 40 phr rendered a higher absorbency but with a lower mechanical strength. A higher scorch time and cure time with a lower crosslinking density and cure rate index were found in the MNR based WSNRs compared with the WSNRs derived from the unmodified NR or ENR. The ENR base WSNR exhibited the highest water absorbency with lower mechanical strength compared with the unmodified NR base WSNR.

47

48

49

Keywords: Water swellable natural rubber, Superabsorbent polymer composite, Poly(ethylene oxide), Trimethylol propane trimethacrylate coupling agent.

50

INTRODUCTION

52

53

54

55

56

57

58

59

60

61

62

63

64

65

66

67

68

69

70

71

72

73

74

75

76

Superabsorbent polymers (SAPs) have been synthesized by modifying the molecular structure of cassava starch (CSt), and thus has gained in interest since such CSt based SAPs are claimed to be biodegradable products [Nakason, Wohmang, Kaesaman & Kiatkamjornwong, 2010; Lanthong, Nuisin & Kiatkamjornwong, 2006]. In contrast, most of the current SAPs are synthetic polymers that have a poor biodegradability that then leads to environmental problems upon their disposal. The development of starch-based SAPs could potentially be used to solve this problem. Potential applications of starch-based SAPs are fairly diverse and include, amongst others, personal care products, fire-fighting gels and agricultural uses [Willette & Finkenstadt, 2006]. Starch-based SAPs are developed by grafting starch with unsaturated hydrophilic monomers, such as acrylic acid (AA), acrylamide (AM) [Nakason, Wohmang, Kaesaman & Kiatkamjornwong, 2010; Lanthong, Nuisin & Kiatkamjornwong, 2006; Willette & Finkenstadt, 2006; Athawale & Lele, 1998; Karadage, Uzum & Saraydin, 2005; Lostafa, 1995] and ε-caprolactone [Chen, Ni, Bian, Qiu, Zhang & Chen, 2005], by a chemical initiated radical chain copolymerization [Athawale & Lele, 2000; Chen, Park & Park, 1999], or by using γray irradiation [Kiatkamjornwong, Mongkolsawat & Sonsuk, 2002]. A reactive extrusion process has been used to prepare starch-based graft copolymers [Carr, Kim, Yoon & Stanley, 1992; Yoon, Carr & Bagley, 1992]. Starch-g-polyacrylamide (St-g-PAM) has been successfully prepared using a co-rotating twin screw extruder [Willette & Finkenstadt, 2003, Finkenstadt & Willette, 2005], but the maximum water absorbency capacity of the St-g-SAPs obtained using this process was relatively low at only approximately 300 times their dry weight [Carr, Kim, Yoon & Stanley, 1992]. However, our previous work based on the reactive blending process [Nakason,

Wohmang, Kaesaman & Kiatkamjornwong, 2010] with a specially designed batch reactor gave St-g-SAPs with a higher maximum water absorbency capacity at ~ 730 times their dry weight.

In recent years, the development of water swellable (natural) rubbers (WS(N)Rs) has been developed. WS(N)Rs are functional polymers that expand their volume up to more than 1.5 times their original weight by absorbing surrounding water. They can be used as a sealing material or in calking applications, preventing water leakage from pipes or blocking connections in civil constructions, such as subways and subsea tunnels [Park & Kim, 2001].

Any given WS(N)R is typically prepared by dispersing SAP particles in common hydrophobic rubbers, such as chloroprene rubber [Wang, Li & Chen, 1999; Liu, Ding, Zhou & Chen, 2006], chlorohydrin rubber [Zhang, Zhang, Wang, Liu, Liu & Chen, 1999; Zhang, Zhang, Wang, Liu, Liu & Chen, 2000] and NR [Park & Kim, 2001, Wang, Zhang, Dong, Chen & Tan, 2002]. This special type of rubber possesses not only the properties of general rubber, such as a high mechanical strength, set and resilience properties, but also has high water absorbency. These properties are due to the presence of the crosslinking network in the rubber and water absorbing material.

A specially designed batch reactor was used to prepare St-g-PAM based SAPs via reactive processing, based on the optimum conditions found in Nakason *et al*. [2010]. In this work, SAP composites (SAPCs) of the St-g-PAM mixed with bentonite clay were prepared and later blended with NR and other important ingredients. That is, each WSNR was prepared by mixing SAPC particles with the NR, poly(ethylene oxide) (PEO) and trimethylol propane trimethacrylate (TMPTMA). Each ingredient was then compounded and cured by the sulfur vulcanization system. The effects of the addition of SAPC, PEO and TMPTMA on the water absorbency, curing, mechanical

and morphological properties of the resulting WSNR compound and vulcanizate were then investigated.

104

105

106

107

108

109

110

111

112

113

114

115

116

117

118

119

120

121

122

123

124

125

126

102

103

2. EXPERIMENTAL

2.1 Materials

High ammonia (HA) NR latex having a dried rubber content of approximately 60% was manufactured by Yala Latex, Co., Ltd (Yala, Thailand). Epoxidized natural rubber (ENN)) with 25% mol epoxide (i.e., Epoxyprene 25 (ENR-25)) was manufactured by Muang Mai Guthrie Public Co., Ltd. (Surathani, Thailand). Maleated natural rubber (MNR) was prepared in-house by blending the rubber air-dried sheet (manufactured by Khuan Pun Tae Farmer Co-operation, Phattaluang, Thailand) with 8 phr of maleic anhydride at 150 °C using an internal mixer (Brabender Plasticorder, model PLE331, Brabender OHG Duisburg, Germany) at a rotor speed of 60 rpm. Details of the preparation and characterization procedures of MNR are described by Nakason and Saiwari [2008]. CSt, used as a polymer substrate, was obtained from Siam Starch (1966) Co., Ltd., Rayong, Thailand. AM, used as a grafting monomer, and N, N'methylenebisacrylamide, used as a crosslinker were from Fluka (Buchs, Switzerland). Potassium persulfate, used as a free radical initiator, was obtained from Asia Pacific Specialty Chemicals Ltd., (Seven Hills, Australia). Hydroquinone, used as a free radical scavenger, was from Merck (Darmstadt, Germany). Sodium lauryl sulfate was prepared in-house by reacting lauric acid (Imperial Industrial Chemicals (Thailand) Ltd.) with sodium hydroxide (BDH, England). For the preparation of SAPCs, bentonite clay, grade SAC-1, was from Thai Nippon Chemical Industry, Co., Ltd.,

(Samut Sakhon, Thailand), and TMPTMA, used as a coupling agent for functional

groups, was obtained from Behn Meyer Chemical Co., Ltd, Rayong, Thailand. PEO was from Alkox E-30, Meisei Chemical Works, Ltd., Kyoto, Japan, and was used to enhance the water absorbing properties of the rubber. Zinc oxide (white seal) and stearic acid, used as the activators in the sulfur vulcanization system, were supplied by Metoxide Thailand Co., Ltd. (Pathumthani, Thailand) and Imperial Industry Chemical Co., Ltd. (Pathumthani, Thailand), respectively. *N*-tert-butyl-2-benzothiazyl sulphenamide (TBBS), used as an accelerator, was manufactured by Flexsys America L.P. (Reliance Technochem Co., Ltd., Bangkok, Thailand). Sulfur, used as a curing agent, was manufactured by Ajax Chemical Co., Ltd. (Auckland, New Zealand).

Figure 1 A illustrates Infrared spectra of the major raw materials (a) poly(ethylene oxide), (b) starch-g-polyacrylmide and bentonite 20 phr, and (c) TMPTMA. The neat natural rubber peaks (not shown here) contained the following peaks: 3224 cm⁻¹ (w), v_{O-H} OH (moisture in the rubber); 3037 cm⁻¹ (s) v_{-C-H} ; 2960, 2916 and 2850 cm⁻¹, v_{-C-H} ; 1661 cm⁻¹, v_{C-C} ; 1447 and 1375 cm⁻¹, ρ_{C-H} ; 833 cm⁻¹ v_{C-H} on cis C=C of polyisoprene, or δ_{-C-H} polyisoprene. For the neat PEO, the following peaks were found. 3450 cm⁻¹, v_{-OH} (hydration of PEO); 2889 cm⁻¹, v_{-CH} ; 1632 cm⁻¹, v_{-C-C} ; 1467 cm⁻¹, $\delta_{asH-C-H}$; 1360 cm⁻¹, δ_{sH-C-H} ; 1149 cm⁻¹, v_{-C-C-C} ; 916, 842 cm⁻¹, ρ_{CH_2} (guache) (Manoratne, Rajapake &Dissanayake, 2006; Zain & Arof, 1998). For the neat TMPTMA, 2980, 2920, 2900 cm⁻¹, v_{-CH} (ali); 1870 cm⁻¹, v_{-C-C} (w); 1720 cm⁻¹, v_{-C-C-C} (s); 1640 cm⁻¹, v_{-C-C-C} (m); 1480 cm⁻¹, δ_{-C-H} .

2.2 Preparation of Cassava Starch-Graft-Polyacrylamide Superabsorbents (CSt-PAM SAPs) and Associated Composites (SAPCs) by Reactive Blending

CSt-PAM was prepared by reactive batch processing using a specially designed batch reactor, with the preparation and characterization as described before [1]. The SAPC loaded with 20 phr of bentonite clay was prepared from the CSt-PAM according to the described procedures [1].

2.3 Preparation of WSNR

The HA concentrated NR latex was first mixed with the SAPC loaded with 20 phr bentonite clay and 2% (w/w) of SDS surfactant for 1 h at room temperature, and then the mixture was aged for another 24 h to allow it to reach equilibrium. The mixture was then cast into 10 x 10 cm thin films and dried at room temperature for 24 h followed by in a hot air oven for another 24 h at 40 °C. The ENR and MNR derived WSNRs or called modified WSNRs were produced by a dry blending process with the internal mixer at 40 °C and a rotor speed of 60 rpm, with the formulation and mixing schedule shown in Table 1.

2.4 Influence of PEO and TMPTMA loadings on properties of WSNRs

WSNR composites from the CSt-PAM SAP loaded with 20 phr bentonite clay were prepared according to the procedure described in section 2.3. Each dried composite was mixed at 50 °C using the internal mixer (capacity of 80 cm³) at a rotor speed of 60 rpm following the formulations shown in Table 2. In this work, the properties of the WSNR composites and also with the addition of PEO with or without the coaddition of TMPTMA were investigated.

2.5 Water absorbency

Each WSNR composite (0.1 - 0.5 g) was immersed in distilled water (250 mL) for 24 h at ambient temperature (25 - 30 °C) to reach equilibrium swelling. The residual water was removed by filtration through an 80-mesh stainless steel screen with the WSNR composite left on the screen for at least 1 h to drain off the unabsorbed water. During this period, the screen was gently shaken with a declining angle of 15 - 20° to ensure that most of the unabsorbed water was separated. The water absorbency was determined by weighing the fully swollen WSNR and its dried composite as follows:

$$Water\ absorbency\ (g/g) = \frac{(W_1 - W_0)}{W_0} \tag{1}$$

where W_0 is the weight of the dried WSNR and W_1 is the weight of the swollen WSNR. In this work, the water absorbency of the WSNR composites before vulcanization (rubber compound) and after vulcanization (rubber vulcanizate) was carried out.

2.6 Cure characterization

A rotorless rheometer (Rheo Tech MD+, Tech Pro, Inc., from Cuyahoya Falls, U.S.A.) was used to determine the curing characteristics of the rubber composites at $160~^{\circ}$ C with 1° arc and 60~min. The optimum cure time (tc_{90}) and scorch time (t_{s1}), the minimum and maximum torque (M_L and M_H , respectively), and delta torque (M_H - M_L) were determined from the curing curves. Cure rate index (CRI) was measured based on ASTM D5289 and the formula for the calculation is shown below.

199 CRI =
$$100/t_{c90}-t_{s1}$$
 (2)

where t_{s1} is the time required to increase one unit torque from the minimum torque, t_{90} is the time required to reach 90% of the total cure.

Vulcanizates with a thickness of approximately 550 ± 50 µm were then prepared by compression molding at 160 °C according to the determined optimum cure time (tc₉₀). The mechanical, morphological and water absorbency properties of the composite vulcanizates were investigated.

2.7 Infrared Spectroscopic Analysis

The existence of the functional groups of the rubber samples and raw materials was investigated by Fourier Transform Infrared Spectroscopy (FT-IR; System 2000, Perkin Elmer, U.S.A.). The dried sample and KBr powder were mixed, ground, pressed, and then subjected to the FT-IR spectrometry.

2.8 Microstructure studies

Scanning electron microscopy (SEM) (model JSM-6510LA, Jeol Ltd., Akishima, Japan) was used to characterize microstructures of the cryogenic fractured surfaces of the WSNR composites. The samples were coated with a thin layer of gold under vacuum before characterization.

2.9 Thermal properties analysis

Thermal behavior of the WSNR composite at different PEO contents was investigated using differential scanning calorimetry (DSC) (Mettler Toledo DSC823e/400, USA) and thermogravimetric analysis (TGA) (Mettler Toledo). In the case of DSC, the powder sample sealed into the aluminum pan was heated up at the rate of 10 $^{\circ}$ C min⁻¹ from -50 to 100 $^{\circ}$ C. During the heating, nitrogen gas (N₂) was

flowed into the furnace at a flow rate of 20 cm³ min⁻¹ for 5 min. In TGA, the samples were put inside alumina pans hanged in the heating furnace. The weight of remaining material was recorded while the furnace was heating from 25 °C to 500 °C at a rate of 10 °C min⁻¹. Oxygen (O₂) was fed into the furnace at 20 cm³ min⁻¹ as a purge gas.

2.10 X-ray diffraction analysis

X-ray diffraction measurements of WSNR composite at different PEO contents were carried out using an X-Ray Diffractometer: Bruker AXS Germany (Model D8 Advance with the target and wavelength (CuK $_{\infty}$ radiation, $\lambda=0.15406$ nm, 40 kV, 30 mA). The X-ray diffraction (XRD) patterns were recorded from 5° to 80° with an increment of 0.02 degree in a 2θ mode at a scanning rate of 1° min⁻¹. The dried composite powder was mounted on a sample holder with smooth double-sided adhesive tape.

2.11 Mechanical properties

Dumbbell shaped specimens were prepared from a sheet of the rubber vulcanizates by die cutting according to ASTM die type C. The stress-strain behavior of the vulcanizates was then investigated using a universal tensile testing machine (Hounsfield Tensometer, model H 10KS, Hounsfield Test Equipment Co., Ltd, Surrey, U.K.) at a speed of 500 mm/min and an initial gauge length of 25 mm, according to ASTM D412. The tensile strength and elongation at break were then determined based on the stress-strain behavior.

3. RESULTS AND DISCUSSION

3.1 IR studies

250

251

261

- The materials derived were investigated for IR spectroscopic information to look for some interaction. Figure 1 B illustrates the peaks of the unmodified NR synthesized with bentonite-modified SAP and compounded with PEO with/without TMPTMA, the additional peaks are found as follows.
- Sample A [NR+bentonite]: one can see the peak at 3318 cm⁻¹ v(-OH) of Si-OH group; the peak at 1646 cm⁻¹ for deformation vibration of the interlayer water in the clay; the peak at 1263 cm⁻¹ ρ_s (-Si-CH₃), peaks at 1100 cm⁻¹ v(-Si-O) in-plane, and 1030 cm⁻¹ v(-Si-O) out-of-plane (Alabarse, Conceição, Balzaretti, Schenato & Xavier, 2011; Paluszkiewicz, Holtzer & Bobrowski, 2008; Madejova, Janek,
- Sample B ([NR+ bentonite + PEO (10 phr)]: the additional peak at 3318 cm⁻¹ ν (-OH) of Si-OH group; 873 cm⁻¹ ρ (Al-Fe-OH) bentonite.

Komadel, Herbert & Moog, 2002; Özcan & Özcan, 2004).

- Sample C [NR+ bentonite + PEO (10 phr) + TMPTMA (2 phr)]: the additional peaks were found as follows: 3318 cm⁻¹ ν (-OH) of Si-OH group; 1725 cm⁻¹ ν (C=O) TMPTMA, and 1145 cm⁻¹ ν (C-O-C) PEO.
- Sample D [NR+ bentonite + PEO (20 phr) + TMPTMA (2 phr)]: additional peaks were found: 3318 cm⁻¹ v(-OH) of Si-OH group; 1725 cm⁻¹ v(C=O) TMPTMA; 1637 cm-1 v(C=O) PEO; 1342 cm⁻¹ δ_s CH₂ PEO; and 1143 cm⁻¹ v(C-O-C) PEO.
- 270 **Sample E** [NR+ bentonite + PEO (40 phr) + TMPTMA (2 phr)]: additional 271 peaks were found: 3318 cm⁻¹ v(-OH) of Si-OH group; 1725 cm⁻¹ v(C=O) TMPTMA;

1360 cm $^{-1}$ δ_{S} (CH $_{2}$) PEO; 1145 cm $^{-1}$ v(-C-O-C) PEO; 916, 842 cm $^{-1}$, $\rho_{CH_{2}}$ (guache)

(Manoratne, Rajapake &Dissanayake, 2006; Zain & Arof, 1998).

Sample F [ENR+ bentonite + PEO (10 phr) + TMPTMA (2 phr)]: 3318 cm⁻¹ ν (-OH) of Si-OH group; 1725 cm⁻¹ ν (C=O) TMPTMA; 1539 cm⁻¹???; 1342 and 1360 cm⁻¹ δ_s CH₂ PEO; 1144 cm⁻¹ ν (C-O-C) PEO; 962, 946 and 873 cm⁻¹ ν (oxirane ring) epoxide (Zong-Qiang, He-Ping, Qi-Fang & Guang, 2008; Yoksan,2008)

Sample G [MNR+ bentonite + PEO (10 phr) + TMPTMA (2 phr)]:)]: 3318 cm⁻¹ v(-OH) of Si-OH group; 1793 cm⁻¹ v(C=O) succinic anhydride rings; 1723 cm⁻¹ v(C=O) succinic acid (hydrolysis of succinic anhydride ring); 1146 cm⁻¹, v(C-O-C) PEO; 872 cm⁻¹ v(oxirane ring) maleic anhydride (Saelao & Phinyocheep, 2004; Nakason, Kaesaman & Supasanthitikul, 2004; Vicente, Campos, Bordado & Ribeiro, 2008).

3.1 Influence of PEO and TMPTMA on Curing Properties

The curing curves of the WSNR composites and those with the addition of PEO with and without the co-addition of TMPTMA reveal that all of the composites have a curing equilibrium state (the plateau curves), with equilibrium being obtained with 20 min (Figure 2). Furthermore, the NR-based composites alone (i.e. without PEO and TMPTMA) showed the longest delayed action at the beginning of the curing with the longest scorch time of 4.0 min (Table 3). Incorporation of 10 phr PEO produced a significantly shorter scorch time (1.43-fold) of the composites due to reactivity of PEO with polar functinal groups in the composite system. Moreover, co-incorporation of 2 phr TMPTMA with the PEO induced only a slight reduction in the scorch time compared with the one without PEO and TMPTMA, and much less than

with the addition of the same content (10 phr) of PEO alone. This is attributed to the fact that, besides the role of crosslinking agent, TMPTMA could react with the TBBS accelerator and delay the scorching of the materials while a shorter scorch time resulted from the incorporation of the PEO. In this scenario then, these two effects overshadow and compensate each other with a net unchanged scorch time. Basically, the addition of zinc oxide (ZnO) as an activator for the sulfur vulcanization of rubbers enhances the vulcanization efficiency and vulcanizate properties and reduces the vulcanization time. The co-addition of 2 phr TMPTA and 10 phr PEO reduced the scorch time by 1.11-fold compared to that with no addition, but to a lower extent than the addition of 10 phr PEO alone (Table 3). Moreover, the incorporation of 10 phr PEO and 2 phr TMPTMA also slightly decreased the crosslinked density ($M_{\rm H}$ - $M_{\rm L}$) and the cure rate index (CRI), by significantly decreasing both the minimum and the maximum torque, of the rubber composites.

3.2 Influence of PEO and TMPTMA on Water Absorbency

Figure 3 illustrates the water absorbency capabilities of the WSNR composites and vulcanizates, either alone or with the addition of 10 phr PEO with or without the coaddition of 2 phr TMPTMA. With each given blend system, the WSNR composite compounds exhibited a higher water absorbency (e.g. 2.6-fold to 4.7-fold higher at two days of immersion) than that of the corresponding vulcanizate at all time points. This is attributed to the crosslinked structure that is formed in the rubber vulcanizates and provides a lower free volume for water to enter into the bulk of the rubber. As a result of the hydrophilic nature of PEO, its incorporation at 10 phr rendered a higher water absorbency capacity of the products. Furthermore, the PEO contributed to a better dispersion of the SAP and SAPC in the rubber matrix. The highest water

absorbency was obtained in the WSNR containing both 10 phr PEO and 2 phr TMPTMA. The hydrophilic nature of both PEO and TMPTMA has the capability to form a strong hydrophilic network with NR, SAP, PEO and SAPC to generate the highest water absorbency.

321

322

323

324

325

326

327

328

329

330

331

332

333

334

335

336

337

338

339

340

341

342

343

344

345

Three PEO loadings (10, 20 and 40 phr) at a fixed concentration of 2 phr TMPTMA used to prepare WSNR composite compounds and their associated vulcanizates are shown in Figure 4. The water absorbency capabilities of these vulcanized and unvulcanized WSNR composites differed, where as expected, at each given loading of PEO, the water absorbency capabilities of the unvulcanized composite compounds were higher than those of the corresponding vulcanizates at all time points of water immersion (e.g. from 1.4-fold to 2.6-fold after two days immersion). The water absorbency of the unvulcanized composite compounds with and without PEO differed, showing a slightly decreasing trend with increasing immersion times of longer than 6 days in the absence of PEO, but remained constant (10 phr PEO) or continued to increase (20 & 40 phr PEO) after six days of immersion. Probably the SAP was prone to be eluted from the composite compounds into the water phase due to lack of interaction between the different phases of the composite compounds. Certainly, increasing the PEO loading to 20 and 40 phr increased the water absorbency at each time point of water immersion and lead to increasing water absorbency with increasing water immersion times. A corresponding trend, but with a lower magnitude, was observed for the water absorbency in the vulcanizates. This suggested a stronger network because of the interaction between the polar functional groups and the reactive groups of different components in the composites. The WSNR composite vulcanizates showed the highest water absorbency capacity of 530% (w/w) at a PEO loading of 40 phr after 14 days of water immersion.

3.3 Influence of PEO and TMPTMA on Mechanical Properties

The tensile strength and elongation at break of WSNR composite vulcanizates decreased and increased slightly, respectively, with increasing water immersion time (Table 4). This suggests that a certain portion of the water sensitive SAP or SAPC still present in the composites is not damaged by a long-term immersion in water, and so the strength of these materials can potentially be used in damping conditions. It was also noted that the inclusion of 10 phr PEO to the vulcanizates significantly (1.24-fold to 1.1-fold at 0 to 14 days immersion time, respectively) increased the elongation at break but had only a marginal affect on the tensile strength due to the presence of the crosslinked network that is capable of a higher elongation. In contrast, the co-addition of 2 phr TMPTMA with 10 phr PEO to the WSNR composite vulcanizates and compounds resulted in the highest tensile strength properties, but essentially the same elongation at break values (Table 4). The WSNR with PEO or with PEO plus TMPTMA showed the same trend of a decreasing tensile strength with increasing water immersion time and an opposite but weaker trend for the elongation at break.

The influence of the PEO loading levels on the tensile strength and elongation at break of the WSNR composite vulcanizates is shown in Table 4, respectively. As expected, for all four PEO loadings (0, 10, 20 and 20 phr), increasing the water immersion time rendered a decreasing trend of the tensile strength, which is attributed to the swelled hydrophilic components of the WSNR composites. At any given immersion time larger than 2 days, the composite loaded with 10 phr PEO exhibited the highest tensile strength and that with a PEO of 40 phr exhibited the lowest strength. The tensile strength of the WSNR composites with different PEO loadings could then be ranked as follows: 10 phr > 0 phr > 20 phr > 40 phr. The WSNR composite vulcanizate loaded with 10 phr PEO is presumed to have the appropriate

amount to react and interact between the different components. Wang et al [1999] found that when increasing the amount of PEO in the blends, it could not only decrease the intermolecular forces of the NR phase functioning as a plasticizer, but also produced more flaws in the rubber phase and also increase the low crosslinking density moieties. The mechanical properties thus decreased in which they found coincided with the decreases in crosslinking density.

The elongation at break (Table 4) is increased by incorporation of PEO into the WSNR composite vulcanizate at all three levels examined (10, 20 and 40 phr vs. 0 phr), but to essentially the same extent for all three PEO inclusion levels at any water immersion time. However, the WSNR composite vulcanizates without PEO exhibited the lowest extension capability. It is likely that the swelling network of PEO could lubricate the WSNR composite system to gain more extensibility. These properties then mean that these WSNR composite vulcanizates can likely be used for sealing and caulking applications.

3.4 Influence of PEO and TMPTMA on Morphological Properties

SEM micrographs of the WSNR composite vulcanizates with PEO loadings at 20 and 40 phr before and after immersion in water for 14 days show clear differences in morphologies in Figure 5a and 5c and Figure 5b and 5d, respectively. The white particulates and agglomerates of SAP, SAPC, PEO and ZnO are clearly observed as particulate in nature before immersing in water (Figure 5a and 5b), but after immersion in water for 14 days, a large number of holes were seen while the white particulates or agglomerates had disappeared (Figure 5c and 5d). The higher (40 phr) PEO loaded WSNR composite vulcanizates (Figure 5 d) had larger holes in the surface after a long time immersion in water, suggesting that some of the PEO, SAP

and SAPC, the hydrophilic nature materials, were removed from the composites. This appearance could be related to the inferior mechanical strength of the WSNR composites (Table 4).

3.5 Thermal properties analysis

Figure 6A shows the DSC curves of WSNR composites with different contents of PEO in which the WSNR composite without PEO exhibited no peak while two transition peaks at approximately –12 °C and 38 °C were observed when the PEO contents were 20 and 40 phr, respectively. The first peaks may be caused by PEO which was well-dispersed and interacted with the WSNR composites whereas the second peak might be caused by the phase separation due to the excess PEO content. The intensity of PEO peaks at 38 °C increased with increasing amounts of PEO loading in the WSNR composite (Figure 6A (c, d)). This result indicates that the crystallization of PEO in the WSNR composite is strictly confined.

Thermal stability is an ability of a material to maintain its physical properties when being exposed to high temperatures. The TGA curves in Figure 6B show that the neat PEO in curve (a) is the most thermally stable material, whereas the WSNR composites having higher PEO content (Figure 6B (c, d)) are more stable materials than the WSNR composite without PEO (Figure 5B (b)). This is additional evidence that the PEO crystalline phases were dispersed in the polymer matrix in the XRD work to be discussed below.

3.5 Effect of PEO amount loaded in unmodified WSNR on mechanical properties

The XRD patterns of bentonite, PEO and SAP (all starting materials for preparing WSNR), unmodified WSNR composites in the different contents of PEO,

and the modified NR are graphically represented in Figure 6. The XRD pattern of bentonite was found at 6.02° with a d-spacing value of 14.7 Å, while those of PEO at 19.6° and 23.7° had the d-spacing values of 4.5 and 3.8Å. The starch-g-PAM had only one intense peak at 22.1° with a d-spacing of 4.0Å. Table X illustrates the effect of PEO and TMPTMA loadings on XRD pattern. The XRD pattern of WSNR composite without PEO (Figure 7 (a)) showed a strong peak at $2\theta = 9.54^{\circ}$ which involves that the layers of bentonite were partially exfoliated in the polymer matrix. The absence of diffraction peaks for WSNR composite with PEO 10 phr (Figure 7 (b)) suggests that the bentonite clay has been totally exfoliated and dispersed in the polymer matrix to form a nanocomposite structure. The WSNR composites with various contents of PEO (Figure 7 (c, d)) produced the peaks at approximately $2\theta =$ 19.2° and 23.3° correspond to the 011 and 210 planes of the crystalline structure of PEO in the polymer composite [Wang, Li & Chen, 1999]. The intensity of the characteristic PEO peaks increased more intensely with increasing amounts of PEO loadings in the WSNR composite, in comparison with the WSNR composite with less PEO loadings (Figure 7 (b, c)). Thus, mechanical properties of the swollen rubber samples decreased with an increase in the amount of PEO as mentioned above due to increases in the absorbed water.

439

440

441

442

443

444

445

421

422

423

424

425

426

427

428

429

430

431

432

433

434

435

436

437

438

3.6 Influence of NR Type on Curing Properties.

The curing curves of the WSNR composites derived from three different types of rubber bases (NR, ENR and MNR) revealed that the unmodified NR and the ENR exhibited broadly similar curing characteristics (Figure 8) and a broadly similar scorch time (Table 4). Likewise, the curing curves revealed they reached an equilibrium state by about 10 min for NR to 20 min for ENR. In contrast, the curing

curve of the MNR containing WSNR compound exhibited a very slow and delayed action, not beginning to cure until after some 10 min and then proceeding slowly such that equilibrium was still not attained after 60 min, a characteristic marching curve, where only a slight increase in the torque with increasing time was observed. In addition, the MNR compounds exhibited a significantly longer scorch time (3.3- and 3.83-fold) and cure time (3.19- and 4.46-fold) than did the ENR and NR vulcanizates, respectively, together with the lowest cure rate index (2.92- and 5.71-fold) and crosslinked density (2.53- and 2.17-fold, respectfully) (Table 3). This effect is induced by the remaining maleic anhydride, and maleic acid from the reaction with moisture, which then react with the TBBS accelerator. As a direct consequence there is insufficient TBBS accelerator left for the vulcanization process leading to the inferior curing characteristics. Also seen in Figure 8 and Table 4 is that the ENR compound exhibited the longest cure time and the lowest cure rate index compared with the unmodified NR compound. However, the ENR compound gave the highest crosslinked density. This could be caused by the chemical interaction from the polar functional groups in ENR molecules with the blend components, and the coupling reaction among the blend components with TMPTMA.

463

464

465

466

467

468

469

470

446

447

448

449

450

451

452

453

454

455

456

457

458

459

460

461

462

3.7 Influence of the NR Type on Water Absorbency

The water absorbency of the WSNR composite compounds and vulcanizates derived from NR, ENR and MNR show marked differences (Figure 9). In all cases the water absorbency of the WSNR composites increased with increasing immersion time and were still increasing after 14 days of water immersion (the longest time point assayed), although this was less marked for the vulcanized samples than the unvulcanized ones. The modified NR (i.e., ENR and MNR) showed a markedly

higher (from 2.8- and 3.4-fold to 2.0- and 2.5-fold higher for ENR and MNR at two and 14 days immersion, respectively) water absorbency of the WSNR composite compounds (unvulcanized) than NR. Indeed, ENR showed the highest water absorbency followed by MNR and the unmodified NR showed by far the lowest water absorbency and this trend was maintained over the entire 14 days of water immersion. This is attributed to the stronger chemical interactions and bonding between the modified NR, PEO and SAPC that are assisted by the TMPTMA. However, note that although the vulcanizates showed the same trend of water absorbency and the same ranked order of ENR > MNR > NR, a lower level of water could enter into the crossliked structure of the vulcanizates and the difference in magnitude between the three different rubber types was less marked than in the non-vulcanized samples. Thus, the water absorbency of the ENR based WSNR vulcanizate showed the highest value with the maximum value at approximately 600 wt% for the vulcanizate.

3.8 Influence of type of natural rubber on Mechanical properties

The tensile strength and elongation at break of the WSNR vulcanizates derived from the NR, ENR and MNR show clear differences (Table 6). As with the higher water absorbency, the WSNR of ENR and MNR showed a dramatic reduction in the tensile strength. It is possible that some NR molecules might be degraded during the modifying process. Additionally, a number of polar functional groups along the chain of NR that form weak linkages, such as –C-O, and -O-O-, are removed in the modification process. The elongation at break of the WSNR vulcanizates increased slightly with increasing immersion time, but the ENR- and MNR-based WSNR vulcanizates yielded lower elongation at break values that were still within the range

of good extensibility of the rubber vulcanizates. Therefore, it is concluded that the ENR and MNR base WSNR vulcanizates exhibited a superior water absorbency but

One can see that the peak intensity at 873 cm⁻¹ in (e) and (f) for the inclusion of 10 phr PEO decreased sharply which is in agreement with the XRD and thermal properties. As mentioned by Wang et al (1999) that increases in PEO content had a significant effect on the crystallinity of the vulcanized rubber, i.e., the PEO contents higher than 10 phr are not used in the process and cause increases in water absorption which reduce tensile strength.

CONCLUSION

SAPs of CSt-g-PAM were prepared by a reactive batch process using a specially designed batch reactor. The SAPCs were then prepared with the addition of 20 phr bentonite clay to the SAP mixture. WSNRs were prepared by blending HANR latex, or dry blending of ENR or MNR, with the SAPC alone or with the addition of various loadings of PEO with or without the co-addition of 2 phr TMPTMA. The WSNR compounds and vulcanizates with PEO and TMPTMA gave the highest mechanical strength and water absorbency. A PEO loading of 10 phr gave the highest mechanical strength and water absorbency compared with the WSNR without PEO. Increasing the PEO loading increased the water absorbency and lowered the mechanical strength, with the lowest tensile strength being observed at a 40 phr PEO loading. The curing behavior of the WSNR depended on the NR type. The highest scorch time and cure time with the lowest crosslinked density and cure rate index were obtained in the MNR based WSNR, whilst the ENR based WSNR exhibited the highest water absorbency but with a lower mechanical strength than that of the WSNR made from the unmodified NR.

ACKNOWLEDGEMENTS

The authors are indebted to the Thailand Research Fund for funding the research project under the Research Team Aid (Grant no. RTA5080004). Sincere thanks and appreciation are given to the Prince of Songkla University (Pattani Campus) and Chulalongkorn University for provision of the research facilities. Language editing from Publication Consultation Unit of the Research Division, Faculty of Science, Chulalongkorn University, is acknowledged.

527

528

520

REFERENCES

- Alabarse, F. G.; Conceição, R. V.; Balzaretti, N. M.; Schenato, F.; Xavier, A. M.
- 530 (2011). In-situ FTIR analyses of bentonite under high-pressure. Applied Clay
- 531 *Science 51*, 202-208.
- Athawale, V.D, Lele, V. (1998). Graft copolymerization onto starch. II. Grafting of
- acrylic acid and preparation of its hydrogels. *Carbohyd. Polym.*, **35**, 21.
- Athawale, V.D., Lele, V. (2000). Thermal Studies on Granular Maize Starch and its
- Graft Copolymers with Vinyl Monomers. *Starch/Starke*, **52**, 205.
- 536 Carr, M. E., Kim, S., Yoon, K. J., & Stanley, K. D. (1992). Graft polymerization of
- cationic methacrylate, acrylamide, and acrylonitrile monomers onto starch by
- reactive extrusion. *Cereal Chem*, **69**, 70–75.
- 539 Chen, J., Park, H., and Park, K. (1999). Synthesis of superporous hydrogels:
- 540 hydrogels with fast swelling and superabsorbent properties, *J Biomed Mater*
- 541 *Res*, **44**, 53.
- Chen, L., Ni, Y., Bian, X., Qiu, X., Zhang, X., Chen, X. A novel approach to grafting
- polymerization of ε-caprolactone onto starch granules (2005). *Carbohyd*.
- 544 *Polym.*, **60**, 103.

545 Finkenstadt, V.L., Wilett, J.L. (2005). Reactive Extrusion of Starch-Polyacrylamide Graft Copolymers: Effects of Monomer/Starch Ratio and Moisture Content 546 Karadag, E; Uzum, OB; Saraydin, D. (2005). Water uptake in chemically crosslinked 547 poly(acrylamide-co-crotonic acid) hydrogels, Mater Design, 26 (4), 265–270. 548 Kiatkamjornwong, S., Mongkolsawat, K., Sonsuk, M. (2002). Synthesis and property 549 characterization of cassava starch grafted poly[acrylamide-co-(maleic acid)] 550 superabsorbent via y-irradiation *Polymer*, **43**, 3915. 551 Lanthong, P., Nuisin, R., Kiatkamjornwong, S. (2006). Graft copolymerization, 552 characterization, and degradation of cassava starch-g-acrylamide/itaconic acid 553 superabsorbents Carbohyd. Polym. 66, 229. 554 Liu, C., Ding, J., Zhou, L., Chen, S. (2006). Mechanical properties, water-swelling 555 behavior, and morphology of water-swellable rubber prepared using 556 crosslinkedsodium polyacrylate J. Appl. Polym. Sci., 102, 1489. 557 Madejova, J., Janek, M.; Komadel, P., Herbert, H.-J., Moog, H. C. (2002) FTIR 558 analyses of water in MX-80 bentonite compacted from high salinity salt solution 559 systems. Applied Clay Science 20, 255-271. 560 561 Manoratne, C. H.; Rajapakse, R. M. G.; Dissanayake, M. A. K. L. (2006). Ionic Conductivity of Poly(ethylene oxide) (PEO)-Montmorillonite (MMT) 562 563 Nanocomposites Prepared by Intercalation from Aqueous Medium. International Journal of Electrochemical Science, 1, 32-46. 564 Mostafa, K.H.M. (1995). Graft polymerization of acrylic acid onto starch using 565 potassium permanganate acid (redox system) J. Appl. Polym. Sci., 56, 263. 566 Nakason, C., Saiwari, S. (2008). Effect of Grafted Maleic Anhydride Content 567

Recyclability of Dynamically Cured Maleated Natural Rubber/Polypropylene

Blends. J. Appl. Polym. Sci., 110, 4071.

568

- Nakason, C., Wohmang, T., Kaesaman, A., Kiatkamjornwong, S. (2010). Preparation
- of cassava starch-graft-polyacrylamide superabsorbents and associated
- composites by reactive blending *Carbohyd. Polym.*, **81**, 348.
- Özcan, A. S., Özcan, A. (2004). Adsorption of acid dyes from aqueous solutions onto
- acid-activated bentonite. *Journal of Colloid and Interface Science* 276, 39-46.
- Paluszkiewicz, C., Holtzer, M., Bobrowski, A. (2008). FTIR analysis of bentonite in
- moulding sands. *Journal of Molecular Structure* 880, 109-114.
- Park, J.H., Kim, D. (2001). Preparation and characterization of water-swellable
- natural rubbers J. Appl. Polym. Sci., **80**,115.
- Wang, C., Zhang, G., Dong, Y., Chen, X., Tan, H. (2002). Study on a water-
- swellable rubber compatibilized by amphiphilic block polymer based on
- poly(ethylene oxide) and poly(butyl acrylate). J. Appl. Polym. Sci., 86, 3120
- 582 (2002).
- Wang, G., Li, M., Chen, X. (1999). Effects of fillers on mechanical properties of a
- water swellable rubber *J. Appl. Polym. Sci.* **72**, 577.
- Willet, J.L., Finkenstadt, V.L. (2003). Preparation of starch-graft-polyacrylamide
- copolymers by reactive extrusion, *Polym. Eng. Sci*, **43**, 1666.
- Willette, J.L., Finkenstadt, V.L. (2006). Reactive Extrusion of Starch–Polyacrylamide
- Graft Copolymers Using Various Starches. *J. Polym. Environ*, **14**, 125.
- Yoksan, R. (2008). Epoxidized Natural Rubber for Adhesive Applications. *Kasetsart*
- 590 *Journal: Natural Science* 42, 325 332.
- Yoon, D. J., Carr, M. E., & Bagley, E. B. (1992). Reactive extrusion vs. batch
- preparation of starch-g-polyacrylonitrile. J. Appl. Polym. Sci., 45, 1093–1100.
- Zain, N. M.; Arof, A. K. (1998). Structural and electrical properties of poly (ethylene
- oxide)-cadmium sulphate complexes. Materials Science and Engineering: B 52,
- 595 40-46.

596	Zhang, G., Zhang, Z., Xie, F., Hu, X., Luo, X. Chen, X. (2000). Chlorohydrin water
597	swellable rubber compatibilized by an amphiphilic graft copolymer. I. Synthesis
598	and characterization of compatibilizer PVA-g-PBA J. Appl. Polym. Sci., 75,
599	977.
600	Zhang, Z., Zhang, G., Li, D., Liu, Z., Chen, X. (1999). Chlorohydrin water-swellable
601	rubber compatibilized by an amphiphilic graft copolymer. II. Effects of PVA-g-
602	PBA and CPA on water-swelling behaviors, J. Appl. Polym. Sc.i, 74, 3145.
603	Zhang, Z., Zhang, G., Wang, C., Liu, D., Liu, Z., Chen, X. (2001). Chlorohydrin
604	water-swellable rubber compatibilized by an amphiphilic graft copolymer. III.
605	Effects of PEG and PSA on water-swelling behavior, J. Appl. Polym. Sci., 79,
606	2509
607	Zong-Qiang, Z.; He-Ping, Y.; Qi-Fang, W.; Guang, L. (2008). Effects of Coagulation
608	Processes on Properties of Epoxidized Natural Rubber. Journal of Applied
609	Polymer Science 109, 1944-1949.